UNIVERSITÄT DER BUNDESWEHR MÜNCHEN
Fakultät für Elektrotechnik und Informationstechnik

Development and Characterization of a Propulsion System for CubeSats based on Vacuum Arc Thrusters

Mathias Pietzka

Vollständiger Abdruck der von der Fakultät für Elektrotechnik und Informationstechnik der Universität der Bundeswehr München zur Erlangung des akademischen Grades eines

Doktor-Ingenieurs
(Dr.-Ing.)

genehmigten Dissertation.

Vorsitzender:	Prof. Dr.-Ing. Andreas Knopp Universität der Bundeswehr München
1. Gutachter:	Prof. Dr.-Ing. Jochen Schein Universität der Bundeswehr München
2. Gutachter:	Prof. Dr. Michael Keidar The George Washington University

Die Dissertation wurde am 22.02.2016 bei der Universität der Bundeswehr München eingereicht und durch die Fakultät für Elektrotechnik und Informationstechnik am 01.07.2016 angenommen. Die mündliche Prüfung fand am 04.07.2016 statt.

Abstract

Within this PhD thesis the development of an innovative propulsion system for small satellites, especially so called CubeSats is described. The intended formation flight of such satellites requires a precise attitude control and fine positioning system. The mass (≤ 1.3 kg), size ($100 \times 100 \times 100$ mm^3) and power (≈ 2 W) limitations of these satellites are challenging for an efficient propulsion system. One of the most promising concepts is the so called Vacuum Arc Thruster (VAT). Thereby, an electric discharge is initiated between two galvanically separated electrodes, an anode and a cathode, which leads to the erosion of the cathode surface. From the ejection of this material a thrust in the range of μN is produced at a specific Impulse of around 1000 s. However, up to now these values have been validated only under laboratory conditions without consideration of spacecraft limitations and requirements.

Apart from the technical challenges of CubeSat integration, several principle issues have yet to be solved. These are the improvement of the unreliable ignition process, the feeding of the cathode material which is used as propellant, a uniform erosion of the cathode and the reduction of macroparticles which occur due to high localized heat loads. For the investigation of these effects and possible solutions, a comprehensive test environment was built consisting of a torsional thrust balance, an ion current density detector array and a high speed imaging system. Thereby it is possible to measure thrust, ion current density distribution and ion velocity as well as to observe the evolution of the plasma plume and the cathode spot movement optically in the range of μs.

For arc initiation the so called "triggerless" ignition was implemented. Thereby, a conductive layer is applied to the insulation between anode and cathode which allows to reduce the necessary ignition voltage. However, this layer is eroded during thruster operation. An inwards sloped conical anode geometry enables a re-deposition of this layer with macroparticles from the cathode material and reduces spacecraft contamination. Titanium is chosen as cathode material because of its high feasibility as VAT propellant. A thrust-to-power ratio of around 12 μN/W given by literature was validated in laboratory tests. To facilitate a long lifetime, i. e. around 10^6 pulses for a typical Δv of 7.5 m/s, a reliable feeding system was developed. Depending on the space, mass and power budget of the given satellite two feeding mechanisms can be used: A highly precise piezoelectric actuator which allows movements in the range of μm and a shape memory effect spring which uses the discharge current as energy source. The thus developed thruster has an outer diameter of 8.5 mm and a mass below 20 g. Due to the feeding system, a thruster length of around 30 mm is required which easily fits into the rail structure of a CubeSat.

To meet the limitations and requirements of a typical CubeSat, a novel Power Processing Unit (PPU) was developed. Based on earlier attempts with an inductive energy storage this PPU uses an inductor to produce a voltage peak in the range of 1 kV for ignition. A capacitor is used as energy storage which allows pulse energies of up to 0.7 J and pulse lengths of up to 4 ms under the restrictions of a CubeSat. However, the maximal possible pulse repetition rate is limited to 1.4 Hz. To allow short periods of higher pulse energies (up to 2.7 J) a Li-Po battery was implemented. The ignition coil, which has been optimized in terms of a reduced production of parasitic magnetic fields, is bypassed during discharge to achieve a smooth discharge of the capacitor. An additional switch separates the VAT from the PPU to allow a charging of the capacitor without losses due to the conductive layer. Overall, the electric system has been miniaturized down to one PCB of 90×90 mm and a mass of 150 g. EMI is reduced by constructive measures like a splitting of power lines to several layers and the use of shielded wires. Four thrusters can be alternately operated by the PPU.

For an improvement of thrust, specific impulse and erosion behavior a magnetic focusing system was implemented. Initially, the inductor of the PPU was used as field coil based on earlier work in literature. Due to the novel PPU design an additional coil with a low inductance but a high field strength was integrated into the circuit. Thereby, inductive losses have been reduced as well as the size and mass of the coil. It was found that, depending on the position of the coil, thrust can be increased by around 50 % or decreased by around 30 % and that the cathode spot movement is massively increased. Thereby, the local heat load and thus the production of macroparticles is reduced. This may help to prevent fusing of anode and cathode and to condition the re-deposition of the conductive layer.

Zusammenfassung

In der vorliegenden Arbeit wird die Entwicklung eines innovativen Antriebssystems für Kleinstsatelliten beschrieben. Der Formationsflug sogenannter CubeSats erfordert ein präzises Lage- und Positionsregelungssystem, das die Beschränkungen hinsichtlich Masse ($<$ 1,3 kg), Größe ($100 \times 100 \times 100$ mm^3) und Leistung ($\approx$ 2 W) erfüllt. Eines der erfolgversprechendsten Konzepte ist der sogenannte Vacuum Arc Thruster (VAT). Dabei wird eine elektrische Entladung zwischen zwei galvanisch getrennten Elektroden erzeugt. Dies führt zur Erosion des Kathodenmaterials wodurch ein Schub im μm-Bereich bei einem spezifischen Impuls von ca. 1000 s erzeugt wird. Bei den meisten bisherigen Entwicklungen wurden die Beschränkungen und Anforderungen eines Satelliten nicht berücksichtigt.

Abgesehen von den technischen Herausforderungen bei der Integration in einen CubeSat müssen einige grundlegende Probleme gelöst werden. Neben der Verbesserung des Zündprozesses und der Nachführung des als Reaktionsmasse genutzten Kathodenmaterials sind dies eine gleichmäßigere Erosion der Kathode und die Verringerung von Makropartikeln, die durch lokale Erhitzung entstehen. Dazu wurde umfangreiche Testumgebung bestehend aus einer Schubmesswaage, einem Ionenstromdichtedetektor und einem Hochgeschwindigkeitsbildaufnahmesystem aufgebaut. Dadurch ist es möglich Schub, Ionenstromdichteverteilung und Ionengeschwindigkeit zu messen bzw. die zeitliche Entwicklung der Plasmawolke und die Bewegung der Kathodenfußpunkte optisch im Bereich von μs zu beobachten.

Durch die sogenannte "triggerless" Zündung wird die erforderliche Zündspannung verringert indem eine leitfähige Schicht auf die Isolation zwischen Anode und Kathode aufgebracht. Allerdings wird diese Schicht beim VAT Betrieb erodiert. Eine nach innen konisch geformte Anode begünstigt nicht nur die Erneuerung dieser Schicht, sondern verringert auch die Kontamination des Satelliten. Als Kathodenmaterial wird Ti mit einem Schub-zu-Leistungsverhältnis von ca. 12 μN/W verwendet. Um eine lange Lebensdauer (ca. 10^6 Pulse für ein typisches Δv von 7,5 m/s) zu erreichen, wurden zwei Nachführsysteme unter der Berücksichtigung der Raum-, Masse- und Leistungsbeschränkungen des Satelliten entwickelt: Zum einen ein hochpräziser Piezo-Aktuator, der Bewegungen im μm-Bereich erlaubt, und eine Formgedächtnisfeder, die mithilfe des Entladungsstromes aktiviert wird. Der hier entwickelte VAT hat einen Außendurchmesser von 8,5 mm, eine Länge von ca. 30 mm und eine Masse von 20 g.

Des Weiteren wurde eine innovative Power Processing Unit (PPU) entwickelt. Die für die Zündung erforderliche Spannungsspitze im kV-Bereich wird dabei mit einer Induktivität erzeugt, während die Pulsenergie in einem Kondensator gespeichert wird. Unter den Leistungsbeschränkungen eines CubeSats sind damit Pulsenergien bis 0,7 J und Pulslängen bis 4 ms bei einer maximalen Pulsfrequenz von 1,4 Hz möglich. Für eine kurzzeitige Erhöhung der Pulsenergie (bis 2,7 J) wurde ein Li-Po-Akku integriert. Die EMV-optimierte Zündspule wird während der Entladung überbrückt, um eine gleichmäßige Entladung des Kondensators zu erreichen. PPU und VAT werden während der Ladezeit voneinander getrennt um Verluste durch Stromfluss über die leitende Schicht zu vermeiden. Die PPU wurde auf einer quadratischen Platine mit 90 mm Seitenlänge und einer Masse von 150 g untergebracht. Elektromagnetische Interferenzen werden durch konstruktive Maßnahmen reduziert. Die PPU ermöglicht den abwechselnden Betrieb von vier Triebwerken.

Für die Verbesserung von Schub, spezifischen Impuls und Erosionsverhalten wurde ein magnetisches Fokussiersystem integriert. Basierend auf früheren Veröffentlichungen wurde zunächst die PPU-Induktivität als Feldspule verwendet, die jedoch im weiteren Verlauf durch eine zusätzliche Spule mit einer niedrigen Induktivität und einer hohen Feldstärke ersetzt wurde, um die induktiven Verluste als auch die Größe und die Masse der Spule zu verringern. Abhängig von der Position der Spule konnte der Schub um 50 % erhöht bzw. um 30 % verringert werden. Die Beweglichkeit der Kathodenfußpunkte konnte darüber hinaus stark erhöht werden. Dadurch wird die lokale Temperaturbelastung und dementsprechend die Produktion von Makropartikeln reduziert. Dies soll das Risiko eines Kurzschlusses von Anode und Kathode verringern und es ermöglichen, die Erneuerung der leitenden Schicht zu steuern.

Danksagung

Ohne die großartige Unterstützung meiner Kollegen und meiner Familie wäre diese Arbeit nie vollendet worden. Daher möchte ich mich an dieser Stelle für den fachlichen und moralischen Rückhalt und nicht zuletzt für das entgegengebrachte Verständnis recht herzlich bedanken.

Mein besonderer Dank gilt meinem Doktorvater Herrn Prof. Dr.-Ing. Jochen Schein, der mir die Bearbeitung eines interessanten und herausfordernden Themas ermöglicht hat. Er hat mich stets mit wertvollen Ratschlägen unterstützt und meiner Kreativität unbegrenzten Freiraum gelassen.

I would like to thank Prof. Dr. Michael Keidar who has agreed to act as second supervisor. Especially his research on the magnetically enhanced Vacuum Arc Thruster was a major source of inspiration for my own work.

Darüber hinaus bedanke ich mich ganz herzlich beim Vorsitzenden des Promotionsausschusses, Prof. Dr.-Ing. Andreas Knopp, für die reibungslose Durchführung des Promotionsverfahrens und die sehr angenehme Gestaltung der Prüfung.

Besonderer Dank gilt auch Herrn Dr.-Ing. Günter Forster für die fachliche und vor allem auch die moralische Unterstützung. Mit seiner ruhigen gelassenen Art hat er immer wieder dafür gesorgt, dass ich nicht den Mut verloren haben und weiter dran geblieben bin.

Weiterhin bedanke ich mich bei Herrn Dr.-Ing. Stephan Zimmermann und Herrn Dr.-Ing. Jochen Zierhut ganz herzlich, die bei technischen Problemen jeglicher Art stets mit Rat und Tat zur Stelle waren. Ohne ihre Hilfestellung wäre vieles schwieriger gewesen.

Bei meinen Vorgängern Dr.-Ing. Sebastian Lange, Dr.-Ing. Ben Bachmann und Dr.-Ing. Erwan Siewert bedanke ich mich für die fachliche Unterstützung besonders am Anfang meiner Arbeit und vor allem auch, dass sie mir als wichtige Wegweiser für meinen eigenen Weg gedient haben.

Ich bedanke mich auch vielmals bei Herrn Dr.-Ing. Karsten Hartz-Behrend insbesondere für seine unschätzbare Hilfe bei verschiedensten administrativen Angelegenheiten. Meinen zeitweisen Büropartnern Herrn Dr.-Ing. Jörg Schaup und Herrn Dr. Igal Kronhaus danke ich für die gute Zusammenarbeit.

Ein besonders herzliches Dankeschön gilt meinen Laborkollegen Frau Dr.-Ing. Marina Kühn-Kauffeldt und Herrn M.Sc. Marvin Kühn für das gute Miteinander trotz räumlicher Einschränkungen und die vielen fachlich wertvollen Diskussionen und Anregungen.

Vielen Dank auch an meine Kollegen und Nachfolger auf dem Weg zur Promotion, Dipl.-Ing. Stefan Kirner, Dipl.-Ing. Stefan Eichler, M.Sc. Michal Szulc, M.Sc. Alexander Atzberger und Dipl.-Ing. Matthias Bredack, für die unzähligen Lösungsvorschläge, die vielen Diskussionen über alle möglichen fachlichen und fachfremden Themen und vor allem auch dafür, dass der Spaß bei der Arbeit nicht zu kurz gekommen ist. Ich wünsche Euch noch viel Erfolg auf Eurem Weg!

Natürlich hätte diese Arbeit nicht ohne die tatkräftige und professionelle Unterstützung unserer Institutswerkstatt gelingen können. Daher gilt ein ganz besonders herzliches "Vergelt's Gott" unserem Werkstattleiter, Herrn Ulrich Bayrle und seinem Team bestehend aus Martin Goretzki, Alejandro Javier Madina Cerda, Hermann Karl, Tobias Kisthardt und Alexander Mai.

Außerordentlicher Dank gilt Frau Dagmar Bergel und Frau Cornelia Budach für die Erledigung unzähliger administrativer Angelegenheiten sowie Herrn Günter Haderer für die Unterstützung in computertechnischen Belangen und Herrn Walter Wagner für die unzähligen Beschaffungsmaßnahmen.

Weiterhin bedanke ich mich bei Herrn Anton Lebeda und allen Mitarbeitern der Firma Apcon Aerospace & Defense GmbH für die professionelle Zusammenarbeit im Rahmen des Projektes IASV. Diesbezüglich gilt mein Dank auch den Kollegen aus Würzburg, M.Sc. Philip Bangert, Dipl.-Inform. Stefan Busch, M.Sc. Alexander Kramer und Herrn Dieter Ziegler.

Ein ganz besonderer Dank gilt meiner Freundin Katrin für ihre moralische Unterstützung und ihre unglaubliche Geduld. Meinem Bruder David danke ich dafür, dass er mir immer mal wieder gezeigt hat, dass es auch noch ein Leben neben der Arbeit gibt. Ein ganz besonders herzliches Dankeschön gebührt seiner Freundin Theresa für das mehrfache und sehr sorgfältige Korrekturlesen meiner Arbeit.

Mein größter Dank gilt schließlich meinen Eltern, Irmgard und Jürgen, die meinen Werdegang erst möglich gemacht haben. Leider war es meinem Vater nicht mehr vergönnt, das Ende meiner Arbeit mitzuerleben. Papa, ich vermisse Dich sehr.

Contents

Introduction

Since the beginning of spaceflight, a rapidly increasing number of satellites for communication, navigation, reconnaissance and scientific missions have been launched to satisfy mankind's needs for information, entertainment and knowledge. It is unquestionable that new concepts are necessary to overcome the financial restrictions of conventional space missions. One idea is the utilization of several small satellites instead of one satellite. A given amount of small specialized satellites deployed by one launch vehicle as secondary payload could fly in formation, therefore building up a big network of satellites with different scientific instruments or communication hardware working together. The equipment of several satellites of such a constellation with similar instrumentation gives a redundancy against e. g. launch failure or meteorite collisions. However, due to the small dimensions of each satellite the possibility of meteorite collisions is reduced and the lower sensibility to atmospheric drag allows operation in low earth orbit (LEO) which is also an important factor in terms of cost reduction. This gives institutions like universities, small enterprises and amateur radio associations with limited financial budgets the opportunity to launch their own satellites, for instance for hardware testing or within student projects.
To set limits for such projects, the so called CubeSat was set as international standard by Stanford University and the California Polytechnic State University (CalPoly) [Mehrparvar et al. 2014]. The base design is a cubical satellite with an edge length of 100 mm and a maximum mass of 1.33 kg as well as miscellaneous material definitions for the structure. Examples for the use of this standard known as one unit (1U) CubeSat are CUTE-I of Tokyo Institute of Technology, one of the first in 2003, and UWE-3 of Wuerzburg University in 2013 [Nakaya et al. 2003], [Busch and Schilling 2012]. To extend the capabilities of such satellites, it is possible to merge several CubeSats together. Common combinations are 2U- and 3U-CubeSats. Examples for this are QuakeSat of Standford University (3U, 2003) and the proposed SOMP2 of Dresden Technical University (2U) [Long et al. 2002], [Baertling 2015]. While the development of small satellites is not limited to these standards, it is an excellent, cost efficient base for future satellites and their subsystems like communication, control, remote sensing and propulsion systems. The proposed formation flight requires a precise and reliable fine positioning system which can operate under the restrictions given by such small satellites. Assuming a typical 1U-CubeSat like UWE-3 with only about 200 g and around a fourth of its internal space left for additional systems, this is a very challenging task considering that only around 2 W of

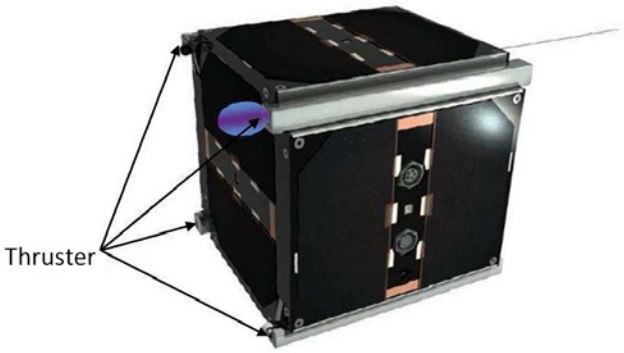

Figure 1: Concept for VAT implementation on a CubeSat like UWE-3 (Universitaet Wuerzburg Experimentalsatellit 3) [Kronhaus et al. 2013] and [Pietzka et al. 2013].

electrical power at a mean bus voltage of 4 V can be consumed by the propulsion system - provided that all other systems are in standby mode [Kronhaus et al. 2013]. Moreover, the miniaturization of tanks, valves and pipes suffers from unreliable parts, breaking during launch, leakage and freezing. Therefore, the use of gaseous or liquid propellants is not reasonable at the current state of development. These issues could be eliminated by the use of solid propellants. Chemical propulsion systems with solid propellants are no option due to a very low specific impulse (I_{sp}) and inability to turn off after ignition. In addition, the CubeSat Design Specifications prohibit the use of any pyrotechnical propulsion system [Mehrparvar et al. 2014]. Therefore, only a few electric propulsion concepts are left for the proposed task.

One of these concepts is the so called Vacuum Arc Thruster (VAT) which was firstly introduced by [Qi et al. 1998] and [Schein et al. 2001] as small satellite propulsion system. Its origin could be found in a physical vapor deposition process mostly known as cathodic arc deposition. Thereby, an electric field is built up between two electrodes which are insulated against each other [Boxman et al. 1995]. When the field strength reaches a critical level, an arc discharge is initiated between anode and cathode. Several processes like Joule heating and ion bombardment lead to an explosive erosion of the cathode material. The resulting metal vapor leads on its own or after an interaction with a working gas to the deposition of a functional layer on a substrate material. Since fast particles with a high density compared to the surrounding space are ejected, it is obvious that at least a small thrust is thereby generated. With this idea in mind, several groups are now successfully working world wide on the modification of this process as propulsion system (e. g. [Keidar et al. 2005], [Lun et al. 2010], [Fuchikami et al. 2013]). The main issues are the constructive adaption to the needs of spaceflight such as thermal and mechanical stress, the reliability of the ignition process, the propellant supply and the development of a high efficient power supply. All possible solutions are challenged by the special restrictions of small satellites mentioned above (see figure 1).

Most of the research conducted up to now in the field of VATs has been focused on the

physical properties of the thruster, i. e. the measurement of erosion rate, thrust and specific impulse of different cathode materials [Polk et al. 2008], the optimization of the thruster geometry or the pulse length [Lun and Law 2015] and the manipulation of the plasma with external electrical or magnetic fields [Keidar et al. 1997], [Tang et al. 2005]. A significant part of most publications is also dedicated to innovative or improved diagnostic methods. Therefore, there is a huge set of material data and measurement systems. This work is based on this knowledge and does not intend to provide another list of material data or an additional new diagnostic system. Instead, it aims to take VAT development to the next level: An actual CubeSat with a reliable fine positioning and attitude control system. In the meantime, this goal has already been achieved by BRICSat-P, a 1.5U-CubeSat of the United States Naval Academy [Hurley et al. 2015]. However, little is known about this mission and military restrictions may prohibit the future publication of technical and scientific data. In contrast to the 1.5 units of BRICSat-P, the potential host satellite of the VAT system described in this thesis consists of only one unit which makes the space and mass issue much more challenging. In the following, a possible solution for this task will be presented.

After a short overview on the technical background of CubeSats and formation flight as well as on possible propulsion systems with a special emphasis on electrical spacecraft engines in chapter 1 follows a thorough excursion into the theoretical principles of vacuum arcs. The 2nd chapter closes with the application of vacuum arcs as thrust source and shows important stages of VAT development together with a description of remaining challenges. The diagnostic systems used for the control of the thruster development within this thesis are explained in chapter 3. Together with simple electrical measurements, thrust and beam profile have been investigated.

The VAT development itself is divided into two parts. Chapter 4 introduces the new power processing unit which has been designed for the limitations of a CubeSat especially in terms of low power supply. It will become obvious that this is also a challenge for the geometrical dimensioning of the print circuit board as well as for the size and mass of the used components. The latter is no big issue for the actual thruster, which is however strictly limited in size and installation position. This will be one part of chapter 5, which in general shows possible thruster designs for a CubeSat with a special focus on an optimal cathode consumption and the reduction of satellite contamination. Another important topic of this chapter is the supply of the propellant with different innovative methods. The improvement of the directional characteristic of the plasma plume by the application of an axial magnetic field will be described in chapter 6.

Finally, the results of the development done within this thesis will be presented in chapter 7. The performance of power processing unit and thruster will be merged together and the suitability for CubeSat integration will be discussed. Since this highly ambitious aim could not be reached alone with the results presented here, an outlook for future research will be given. Possible topics are alternative geometries, other cathode materials and further improvement of the ignition process.

Chapter 1

Background

This chapter covers thematic background of this thesis. The main application areas of the proposed propulsion system are small satellites, especially CubeSats. The specifications and their basic design are subject of the first section as well as a preview of future small satellite constellations. In the second section, a selection of potential actuator solutions for this goal will be described. Thereby, it will become obvious that currently only electric propulsion systems are able to fulfill the requirements of formation flight. Therefore, this chapter closes with an introduction of electric propulsion systems with a focus on CubeSat applications.

1.1 Low-Cost Satellite Constellations

The concept of small satellites is almost as old as satellite development itself. The first satellite which could be referred to as nanosatellite was Vanguard 1, alias "Grapefruit", with a diameter of 165 mm and a mass of 1.47 kg [Easton and Votaw 1959]. It was the fourth satellite in space after Sputnik 1, Sputnik 2 and Explorer 1 and it was the first satellite with solar panels. In 1999, the California Polytechnical State University (CalPoly) and Standford University began to develop design specifications for the so called Cube Satellite or in short CubeSat, based on the experience with earlier student satellites like OPAL and SAPPHIRE [Kitts and Twiggs 1998], [Martin et al. 1999]. [Heidt et al. 2000] and [Puig-Suari et al. 2001] introduced the basic design concept for the construction of CubeSat class picosatellites and a standard deployer mechanism for the implementation in different launch vehicles. Although it was not intended to set a standard for other satellite projects, it became exactly that in the following years. By today, there have been 13 revisions of the so called CubeSat Design Specifications of CalPoly [Mehrparvar et al. 2014]. Apart from the educational aspect, CubeSats have a wide range of applications: Communication, earth observation, remote sensing, test of new equipment and scientific experiments, e. g. for biological research. Future missions to moon and mars are planned.

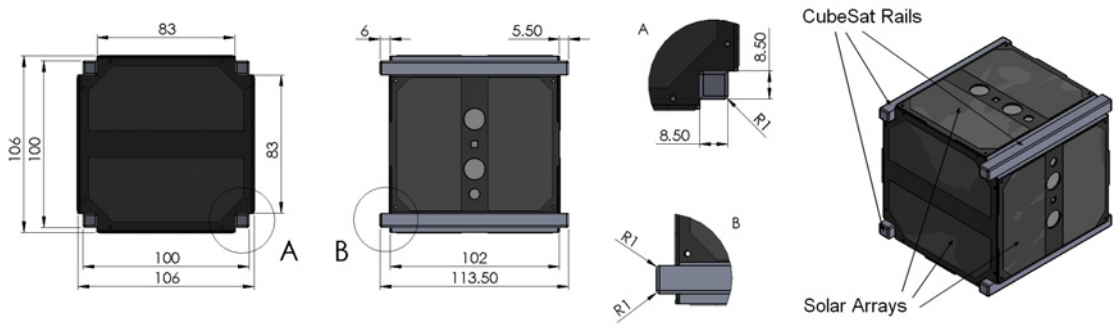

Figure 1.1: Typical dimensions of a 1U-CubeSat using the example of UWE-3, based on [Busch and Schilling 2012]. The CubeSat structural assembly consists basically of four rails (grey) and six side panels (yellow) which are usually equipped with solar arrays.

1.1.1 Cube Satellites

The key features of the CubeSat concepts are a compact, modular design, so called CubeSat Units, and a deployment mechanism, the so called P-POD or Poly-Picosatellite Orbital Deployer, which allows the use of a wide variety of launch vehicles. One CubeSat unit is defined as a cubic satellite with a side length of around 100 mm and a maximum mass of 1.33 kg [Mehrparvar et al. 2014]. Important are the outer dimensions and the material properties of the components which are in contact with other CubeSats or the P-POD during launch and deployment in orbit. Figure 1.1 shows the geometrical limitations of a 1U-CubeSat.

The geometrical specifications concern mainly the four rails, which are designed to give a smooth glide off the deployment system and to act as structural base for the interior subsystems and the six side panels. The front planes of these rails have mechanical contact to other satellites in the P-POD, only damped by springs to lead of vibrational stress during launch. Each P-POD can be filled with three CubeSats of one unit in size, so called 1U-CubeSats. For deployment with this mechanism, a CubeSat can have at max three units, although more units are possible with other deployment systems, e. g. 12 units [Rotteveel 2014]. A selection of different sizes of CubeSats is illustrated in figure 1.2.

To avoid static potential differences, the aluminum rails must have an anodized surface. The design of the six side panels is only limited in its dimensions. Apart from that they can be equipped with various sensors or other systems, although in most cases they are used as basis for solar arrays. While a 1U-CubeSat limits the possible payloads and test systems massively, for bigger satellites a large variety of designs for different mission goals had been developed in the last years. They all have in common that they fit into the design specifications of the CubeSat program.

A very important part of the whole concept is the P-POD, which is able to deploy up to three 1U-CubeSats from the launch vehicle into orbit. It was developed according to the

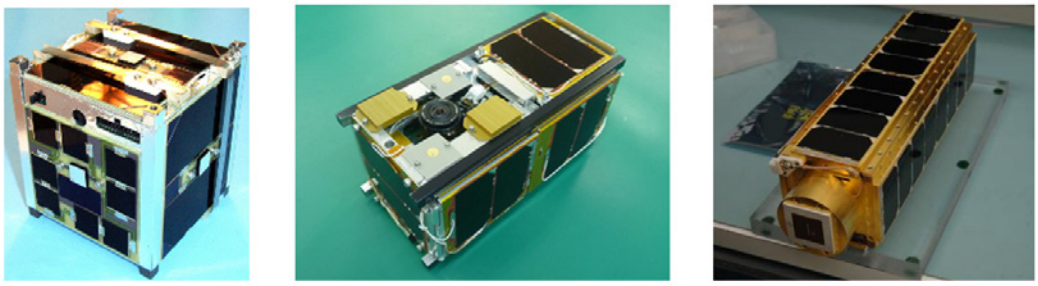

Figure 1.2: Selection of different CubeSats with one, two and three units. Left: BEESAT-1 was the first CubeSat of the Technical University of Berlin and demonstrated an attitude control system based on micro reaction wheels [Trowitzsch 2008]. Middle: Raiko, an Earth observation satellite by the universities of Wakayama and Tohoku with different camera systems [Yoshida 2012]. Right: Standford's PharmaSat 1, equipped with autonomous biological experiments [Beasley 2009].

experiences with earlier student satellites, especially OPAL [Kitts and Twiggs 1998]. In principle, it is only a canister of about 400x20x20 mm which can be mounted easily on many governmental or commercial launch vehicles as secondary pay load. The satellites are released over a hatch on one front plane of the deployer. The necessary momentum is applied by a big spring which pushes the three CubeSats out of the canister when the hatch is opened (see figure 1.3).

A rail system with very smooth surfaces allows the satellites to glide of the P-POD with very low friction. All satellites are connected via wires to a control system which monitors their vital systems and initiates the deployment procedure. The number of P-PODs in one launch vehicle and therefore the number of CubeSats is determined by the launch provider. If one of the satellites fails during launch or deployment, all other satellites in the given P-POD could be harmed. Therefore, any CubeSat has to be designed in a way that avoids damage to all other involved systems. The positioning order of the three satellites

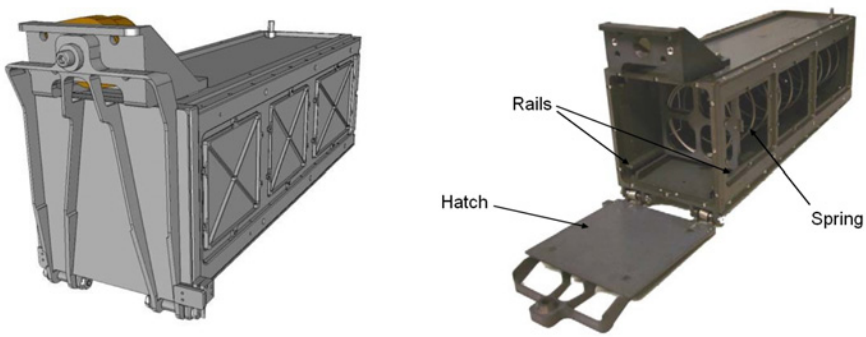

Figure 1.3: Left: The Poly-Picosatellite Orbital Deployer (P-POD), as shown in the CubeSat Design Specifications [Mehrparvar et al. 2014]. Right: Each P-POD can deploy up to three 1U-CubeSats, which are ejected with the help of a spring [Nugent et al. 2008].

inside one deployer is decided by the failure potential of each satellite, i. e. the most "dangerous" leaves the P-POD last so that it cannot block the other two if it gets stuck [Bangert 2015].
As it will matter later in this work, even if all six planes of a 1U-CubeSat are fully equipped with solar arrays it can supply only a very low level of electrical power ($\sim$ 2 W [Kronhaus et al. 2013]). Therefore, an efficient energy concept is necessary for the satellite and its payloads. Modern 3.3 V ICs allow the limitation of the bus voltage to around 4 V. So, apart from the restrictions in space and mass, the capabilities for additional subsystems are very limited with regard to their power supply. This limits the abilities of a 1U-CubeSat. The possibility of bigger satellites with up to three units without bigger issues in terms of transport and deployment gives the opportunity to use heavier, bigger and more power consuming payloads, since the core systems of a 1U-CubeSat, which require around 4/5 of one unit in space and mass, does not change much on bigger satellites. Current designs for 3U-CubeSats allow up to 12 W of power consumption at the same bus voltages [Park et al. 2015]. This enhances the capabilities of a multi-unit CubeSat compared to a 1U-CubeSat drastically, although it is a bigger challenge to deploy a highly sophisticated picosatellite in orbit than a nanosatellite. The common definition of both goes along with its mass: Satellites bigger than 1 kg are referred to as nanosatellites while smaller ones can be called picosatellites [Rycroft and Crosby 2002].
One of the most interesting challenges of satellite and space probe development since the very beginning is the operation of a formation of several spacecrafts. This is especially interesting for CubeSats. A "swarm" of small satellites, each with very limited capabilities, could merge their individual abilities like long range communication, remote sensing, astrogation or geophysical observation to a cluster which then can cope with a bigger, more expensive conventional single satellite. Moreover, it is possible to combine the antennas of several individual satellites to create a virtual antenna array, thus enhancing communication or sensing capabilities [Martin et al. 2001].

1.1.2 Formation Flight

First attempts of formation flight have been started early in the famous "space race". With the rendezvous maneauvers of Wostock and Gemini capsules, both opponents made experience with the difficile control of spacecraft relative to another in orbit. Interestingly, Gemini 12 and Apollo 11 astronaut Buzz Aldrin wrote his doctoral thesis on this topic [Aldrin 1963]. The development of satellite constellations started some years later with the idea to allow long range communication and to have a bigger area of sight in observation missions, both military and scientific [Larson and Wertz 1999]. This has become an important concept, especially for navigation systems like GPS and communication systems like Iridium. The orbits of these constellations have approximately the same altitude but different inclinations, i. e. different angles relative to the Equator [Larson and Wertz 1999]. All satellites are independent from each other and have been

deployed individually. Nevertheless, each satellite has the ability to control its position for station keeping and its attitude for data transfer. Later, with better actuators, short ranged formations came into consideration. A satellite formation is given if all satellites within this constellation are working together as a single functional unit and share their capabilities for one common objective [Alfriend et al. 2009]. These satellites usually fly in close proximity in the same orbit (e. g. in LEO with a distance of 1500 km [Kronhaus et al. 2013]). However, formations with big distances between the satellites, which fly on individual, not necessarily earthbound orbits (e. g. LISA on heliocentric orbits with a distance of around 5 million km [LISA Mission Science Office 2007]), are also possible. An example for a satellite formation is illustrated in figure 1.4.

Several concepts for scientific missions in different earth orbits have been developed. Although these concepts are already very challenging, a new record breaking idea became visible: With LISA (now known as eLISA/NGO) and LISA Pathfinder gravitational wave phenomena should be observed [LISA Mission Science Office 2007]. At first it was planned to station three satellites around one of the Lagrange points near earth. All three probes have to be positioned in a very exact way to each other so that they can act as a very big and therefore highly precise interferometer. This intention requires a highly precise position and attitude control. But also smaller and cheaper missions carried out by small student satellites are planned [Martin et al. 1999]. Although they are not so

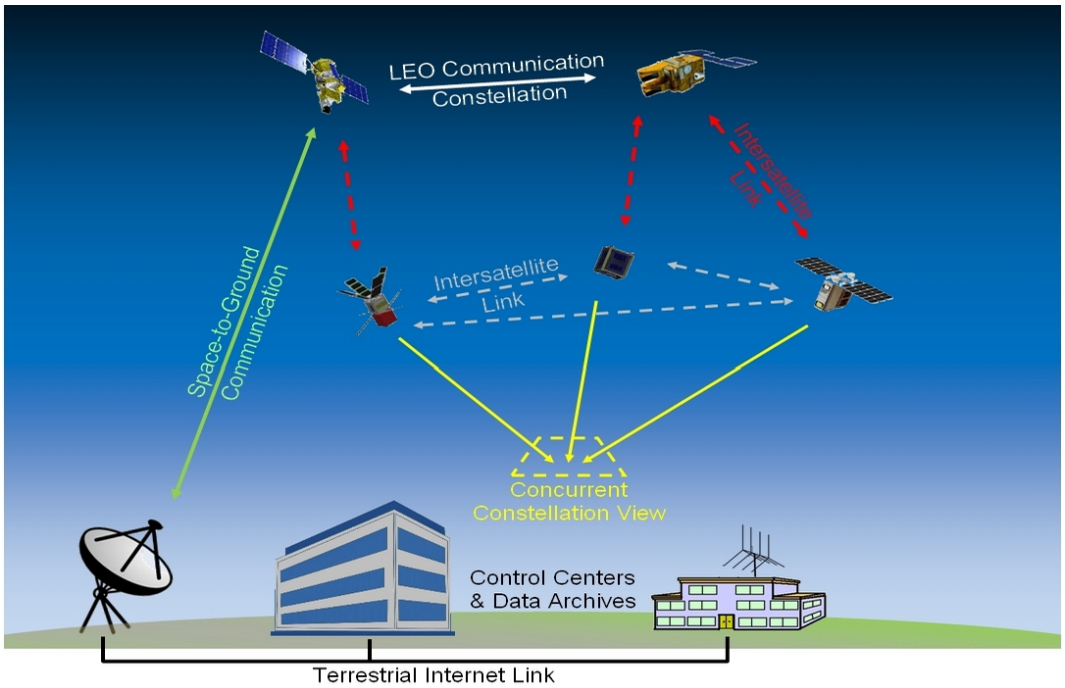

Figure 1.4: Illustration of a satellite constellation with several instances, based on [Martin et al. 1999]. The formation flight of small satellites with distances of only some hundred km requires highly precise propulsion systems.

prestigious and important as governmental or commercial missions, they also need very precise actuators.
Beginning with simple attitude determination systems (ADS) which were only able to measure deviations from the desired attitude, increasingly effective attitude determination and control systems (ADCS) have been developed in the meantime. Usually the attitude is determined with a gyroscope, a sun sensor or star tracker or a magnetometer [Larson and Wertz 1999]. This measurement results in an input for a control loop which gives output to an actuator. Basically, there are the following types of actuators for attitude and orbit control: Reaction wheels and gyroscopes, magnetic torquers, solar sails and thrusters. Reaction wheels are well established actuators for attitude control. A torque applied by a motor driven flywheel forces the satellite to rotate in the different direction to conserve the angular momentum. Thus, rotational motions are possible to change the satellite's attitude without the application of thrust. Reaction wheels are usually big and heavy devices, but miniaturized systems for one axis control have been successfully implemented in CubeSats, [Oland and Schlanbusch 2009], [Li et al. 2013]. A more elegant method are magnetic torquers or "magnetorquers" which are consisting of an electromagnetic coil. If a current is running through this coil, a magnetic field occurs which interacts with the magnetic field of the earth. The resulting counter-force leads to a torque which allows rotational attitude control. Due to their simple and robust assembly they have become a popular attitude control mechanism for CubeSats, [Gerhardt and Palo 2010] [Busch et al. 2015]. These systems are relatively sensible to electromagnetic interference. Moreover, like reaction wheels they do not allow orbital or position control maneuvers. For this intention reaction control systems, i. e. thrusters, or solar sails are necessary.

1.1.3 Propulsion Systems for Small Satellites

The development of low thrust propulsion systems for miniaturized satellites started already before the introduction of the CubeSat. The Vacuum Arc Ion Thruster (VAIT) for example was introduced as propulsion for small satellites by [Qi et al. 1998] just before the first version of the CubeSat Design Specifications. In principle, the integration of any kind of propulsion system into a spacecraft of any size is a huge challenge [Mueller et al. 2010]. There is never enough space, mass or power available. But these parameters are nowhere as limited as in a small satellite. A propulsion system is usually defined by its thrust and propellant demand. In the 1729s English translation of Newtons "*Philosophiae Naturalis Principa Mathematica*" by Andrew Motte the third axiom *actio est reactio* states that

"*To every action there is always opposed an equal reaction; or the mutual actions of two bodies upon each other are always equal, and directed to contrary parts.*" [Newton et al. 1729]

In other words: If a body is emitting some kind of (gaseous or liquid) material it is propelled

in the opposite direction. The force or the thrust of this process is determined by how much mass is emitted within a given time and its velocity, i. e. by the propellant flow $\frac{dm}{dt} = \dot{m}$ and the effective exhaust velocity v_e [Jahn 1968]:

$$F(t) = T = \dot{m} v_e. \tag{1.1}$$

The performance of a propulsion system is often expressed as total impulse since it gives the change in momentum, resulting from the acting force over a certain time:

$$I = \int_{t_0}^{t_1} T dt. \tag{1.2}$$

From the thrust equation follows that the thrust can be either increased by a higher propellant flow or by a higher exhaust velocity. Obviously, it is more efficient to use a system with a higher exhaust velocity than a higher mass flow. A measure for the efficiency of a given propulsion system is the specific impulse I_{sp}, which is the exhaust velocity normalized to the gravitational acceleration on earth g_0:

$$I_{sp} = \frac{v_e}{g_o}. \tag{1.3}$$

This means that the higher the specific impulse, the higher is the propellant efficiency and the lower the propellant demand for a certain thrust. The total change in velocity for a given maneuver is called Δv. Its dependency on exhaust velocity and mass demand can be expressed with the Tsiolkovsky rocket equation [Tsiolkovsky 1903]:

$$\Delta v = v_e ln \frac{m_0}{m_1} \tag{1.4}$$

The calculation of the required Δv is part of the mission design and will therefore not be covered further within this work. But from this equation it can be concluded that for a defined Δv the necessary propellant mass again depends on the exhaust velocity. The chart in figure 1.5 gives a general overview on spacecraft propulsion systems.

Classical, propulsion systems are based on chemical thrusters, especially on hot gas thrusters [Larson and Wertz 1999]. Thrust is generated by the chemical, exothermal reaction on solid, liquid or gaseous propellants. The exhaust flow of chemical propulsion (CP) systems is usually expanded by a Laval nozzle. Thereby, very high thrust (up to 1000 kN) can be achieved, unfortunately at very low specific impulse (150 – 450 s) [Larson and Wertz 1999]. Longer operation is therefore only possible by the use of more than one stage. This is a huge drawback for CubeSat applications together with leakage and freezing issues in miniaturized propellant supply systems [Harmann et al. 2013]. Moreover, dangerous, i. e. explosive and corrosive, materials are prohibited from CubeSat application [Mehrparvar et al. 2014]. Nevertheless, some systems are in development but mostly for the upper limit of small satellites, e. g. like the Busek green monopropellant thruster for a 4 kg CubeSat with a thrust up to 500 mN and a specific impulse of

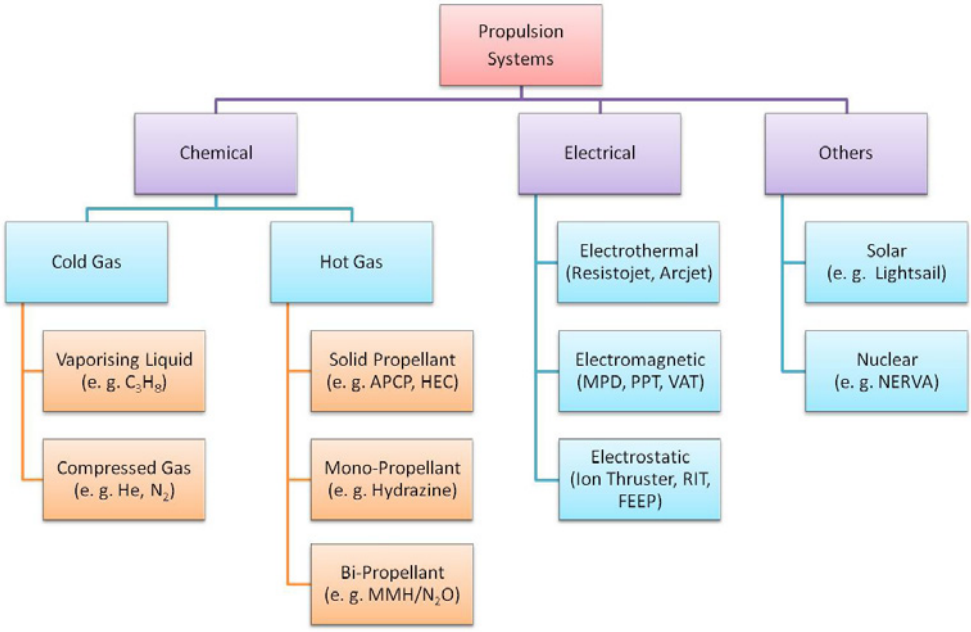

Figure 1.5: Classification of propulsion systems according to [Larson and Wertz 1999] and [Goebel and Katz 2008]. For CubeSat positioning and attitude control currently only cold gas thruster, some electrical propulsion systems and possibly lightsails are suitable.

220 seconds [Williams 2012]. Cold gas thrusters on the other hand are operating without chemical reaction. The propellant which can be either gaseous or liquid is stored in a pressured tank and then released through a valve into a nozzle. Because of this comparable safe operation and a relatively high thrust up to some mN they are currently considered as possible method for initial orbit correction maneuvers just after deployment [Kvell et al. 2014], [Pellegrino et al. 2015]. According to [Mehrparvar et al. 2014], pressured components inside a CubeSat are limited to 1.2 bar which limits the operation time of such thrusters and the specific impulse mentioned in connection with CubeSats is very low (below 100 s), although the thrust reaches an order of about 100 mN [Cardin et al. 2003], [Arestie et al. 2012]. Finally, from the equations above it can be concluded that chemical thrusters have a very low propellant efficiency and would therefore need very much space and mass which both are very rare aboard a CubeSat.
As alternative to chemical propulsion systems, solar sails have been proposed for long time orbital and interplanetary maneuvers [Biddy and Svitek 2012]. From the solar constant ($E_{solar} = 1.367$ kW/m^2) a solar radiation pressure of $p_{rad} = E_{solar}/c = 9.1$ μN/m^2 can be derived, assumed that the reflection is perpendicular to the plane of the sail. Hence, a minimum surface of around 1 m^2 is necessary to achieve sufficient thrust for attitude and position control maneuvers, which results in a very complex deployment mechanism and subsequently a high failure possibility, like NASA's Nanosail-D2 demonstrated [Katan and Lanning 2012]. Due to their nature, solar sails are not suitable for attitude control, but since they do not need any further energy sources they might be a good option

for future orbital and interplanetary missions. Nuclear propulsion systems are currently no option since there are numerous issues which prohibit CubeSat or even small satellite applications: The handling is difficult, the propellant is radioactive and usually also toxic which is incompatible with CubeSat regulations and up to now there is no adaption which can cope with the space and mass restrictions of a small satellite. Nevertheless, there is an early stage NASA concept for the implementation of a nuclear cryogenic propulsion stage into a massively clustered CubeSat platform, i. e. a combination of several hundred satellites [Robertson et al. 2013].
Apart from chemical propulsion systems and some rather unconventional concepts, this leaves only electric propulsion (EP) systems for CubeSat application. Within the next section it will be shown that these have some important advantages compared to the classical concepts and that there are already some EP systems proposed for CubeSat missions.

1.2 Electric Propulsion

Based on the pioneering work of Konstantin E. Tsiolkovsky and Robert H. Goddard [Choueiri 2004], the first working electric propulsion system was the so called ion rocket built by [Kaufman 1961]. Only a few years later in 1964, the feasibility of such an EP system was demonstrated for the first time in space aboard SERT-1 with a successful 31 minutes operation [Cybulski et al. 1965]. From that on, various types of EP systems have been developed and around 70 satellites and probes haven been launched by now. The main advantage compared to classical chemical propulsion systems is the higher exhaust velocity of the propellant (a better term would be reaction mass, but propellant has become standard) and the therefore higher specific impulse [Osiander et al. 2006]. This means that for a given propellant mass an EP can operate much longer than a chemical thruster. Typically the I_{sp} reaches some 1000 s, while the thrust ranges up to some 100 mN at most, which is the big disadvantage apart from some very far concepts (e. g. VASIMR [Chang-Díaz 2001]). Therefore, EP systems are usually used for maneuvers without time constraint, e. g. orbit raise, station keeping, de-orbiting and attitude control of satellites as well as interplanetary probes like Deep Space 1 and Hayabusa [Sovey et al. 2001], [Kuninaka et al. 2007]. The latter may need a very long execution time, but the necessary reaction mass is many times smaller than for chemical propellants.

1.2.1 Fundamentals

Other than in chemical rocket engines, the thrust of an EP system is not generated by a chemical reaction within the propellant or between two propellants, but by the application of electrical energy to the propellant which itself is chemically not reactive. However, the properties of the reaction mass are important for specific impulse, mass flow and thrust [Goebel and Katz 2008]. Classical propellants are Ar, Cs, He, Hg, In, and Xe. Both CP and EP systems need additional components for propellant storage and delivery. For an

EP system these components do not need much space and mass, but in contrast to CP it needs a power processing unit (PPU) where the thrust energy comes from. The importance for the decision whether to choose a CP or an EP system can be expressed by

$$m_{PPU} = \frac{T\alpha}{T/P}, \tag{1.5}$$

where the mass of the PPU m_{PPU} is depending on the thrust T, the specific mass α which determines how much mass is necessary at a certain average power and the thrust-to-power ratio T/P which defines how much thrust is possible at a given average power [Osiander et al. 2006]. Hence, it is obvious that a higher thrust requires a heavier and therefore bigger PPU which also increases the power demand. This could also be shown by

$$T = \frac{2P_{in}\eta}{v_e}. \tag{1.6}$$

This means that the thrust is inversely proportional to the exhaust velocity at a given input power P_{in} and a system efficiency η. It could also be followed from the equations for thrust and Δv that

$$\frac{\Delta v}{\Delta t} \propto \frac{1}{v_e}. \tag{1.7}$$

Therefore, apart from e. g. the VASIMR drive mentioned above, an EP system is only reasonable for missions without time constraint and for small spacecraft where the efficiency and reliability of CP systems is currently very poor.

Usually, EP systems are classified either as an electrostatic, electromagnetic or electrothermal type [Jahn 1968]. The already mentioned ion rocket or ion thruster is an electrostatic propulsion system and could be seen as classic of EP [Kaufman 1961]. Other adaptions are the Radiofrequency Ion Thruster (RIT) and the Hall Effect Thruster (HET) [Goebel and Katz 2008]. The functional principle of the ion thruster is illustrated in figure 1.6.

The plasma is generated within a discharge chamber: Electrons are produced by a cathode within the propellant gas and accelerated by an electric field until they have enough energy to produce secondary electrons from atomic collisions. The thereby generated ions are then accelerated by the acceleration grid to generate thrust [Jahn 1968]. Usually, noble gases like argon or xenon are used for this. An important component is the neutralizer which has the task to generate electrons to neutralize the exhaust gas. Otherwise this would lead to a negative charging of the spacecraft.

To avoid the disadvantage of an additional component, electromagnetic propulsion systems have been invented where the acceleration is achieved by magnetic fields. Typical adaptions are the magnetoplasmadynamic thruster (MPD) and its subtype VASIMR (Variable Specific Impulse Magnetoplasma Rocket) [Haag et al. 2007]. The plasma generation itself is performed in the same way as in electrostatic thrusters [Chang-Díaz 2001]. Unfortunately, the high magnetic field densities which are necessary for the acceleration and guidance of the plasma may interfere with the spacecraft electronics.

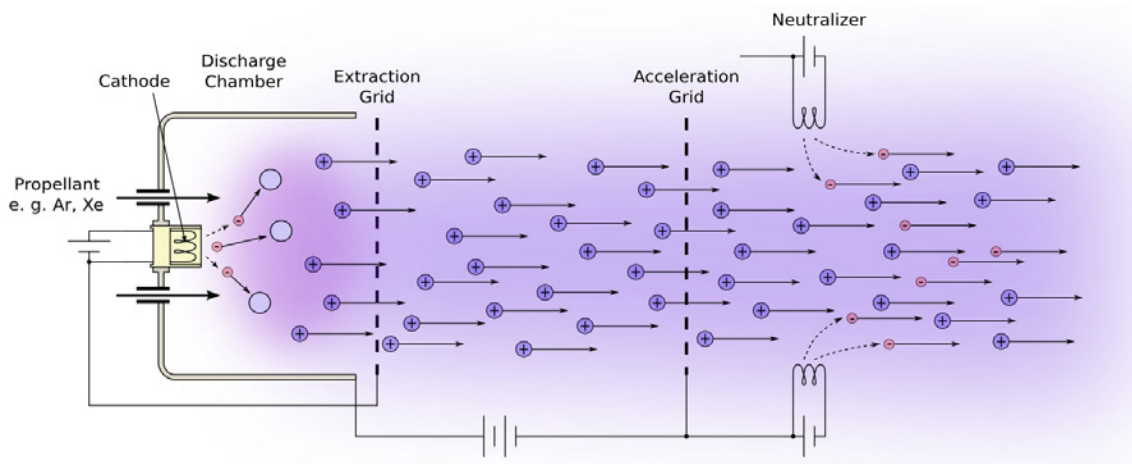

Figure 1.6: Functional Principle of the ion thruster, based on [Jahn 1968]. A propellant gas like Ar or Xe is ionized by electrons which are emitted from a cathode. The ions are then accelerated by a negatively biased grid and generate thereby thrust. To avoid a negative charging of the spacecraft a neutralizer is used to neutralize the exhaust gas.

The last category contains electrothermal propulsion systems, i. e. arcjets and resistojets. Like ion thrusters, especially resistojets have a long heritage in space propulsion [Auweter-Kurtz et al. 1996]. They consist simply of a chamber where the propellant is heated by an electric resistance and a Laval nozzle where such accelerated plasma is expanded into space. In an arcjet the heating is achieved by the initiation of one or more electric arcs. Both concepts require relatively high input power and a high thermal resistance.

All these typical representatives of EP have one big disadvantage for the use in small satellites: They work with gaseous or liquid propellants and need therefore pressured tanks, heating systems, pipes and valves which need much space and mass. Such components are difficult to miniaturize and tend to the same failures as the above mentioned CP systems. Most of the described EP systems require relatively high input power which is also a drawback for small satellite applications. Although there have been attempts to adapt ion thrusters and RIT for such satellites (e. g. the μNRIT [Feili et al. 2009]), other concepts have proven to be much more promising.

1.2.2 Current Development

Basically, the development of EP systems for CubeSats has focused on three types: Field Electric Emission Propulsion (FEEP), Pulsed Plasma Thruster (PPT) and Vacuum Arc Thruster (VAT) [Scharlemann et al. 2011]. Each of these systems has its individual assets and drawbacks which will be addressed in the following. The concept with the longest heritage and therefore with the most sophisticated stage of development is the PPT. The first known spacecraft equipped with a PPT was the Soviet mars probe Zond 2 in 1964/65. Four years later the second PPT equipped spacecraft named LES-6 was

successfully launched by the USAF [Hamidian and Dahlgren 1973]. Since then several PPT systems have been tested by the US and Soviet/Russian space agencies. The first attempt to use miniaturized PPTs for small satellites came at the beginning of the 21st century [Spanjers et al. 2002]. A successful integration of micro PPT systems to small satellites like FalconSat-3 (50 kg) or PROITERES (30 kg) has already been achieved [Saylor and France 2008], [Ozaki et al. 2011]. The working principle is very simple and is very similar to the VAT: Between two electrodes a high voltage is applied to erode material from the PTFE insulation in between. The main challenges hereby are the generation of high voltage pulses, the ignition process and the feeding of the eroded material [Scharlemann et al. 2011]. In contrast to the VAT, higher voltages have to be applied to achieve a uniform erosion of the insulation. This is due to a necessarily thicker wall thickness of the insulation and the unavailability of a conductive layer on the insulation surface (see chapter 2). Moreover, the propellant is limited to PTFE or liquid PTFE [Barral et al. 2014]. However, up to $1.8 \cdot 10^6$ pulses have been achieved with PPT systems for 2U-CubeSats as illustrated in figure 1.7 [Ciaralli et al. 2013]. A proper implementation has up to the date of this thesis not been achieved, possibly due to the space and mass demand of the high voltage power supply and the feeding mechanism.

Another interesting option is the FEEP thruster. Introduced by [Tajmar 1999], the FEEP system has even been considered as highly precise position adjustment system for LISA. Unfortunately, the requirements could not be met as ESA examination showed, although the FEEP concept has some advantages compared to PPT and VAT: It can produce a continuous thrust instead of pulses and a very high specific impulse can be achieved [Scharlemann et al. 2011]. The core of the system is a porous tungsten needle which is filled with indium or mercury. The capillary effect prevents the needle from leaking. If a high voltage of several kV is applied to a grid in front of this needle, charged particles will be sucked out of the pores and accelerated into space. Since the required electrical cur-

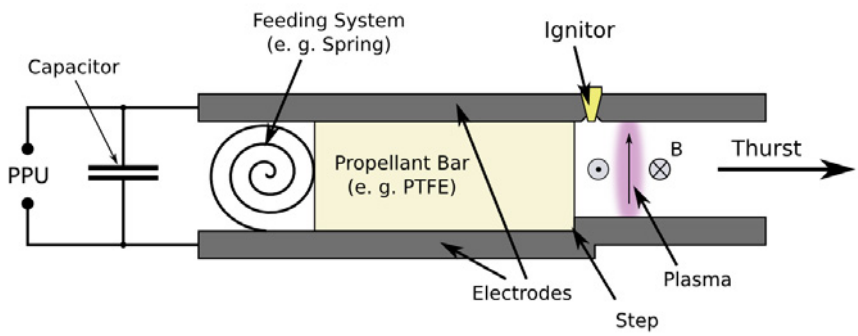

Figure 1.7: Working principle of a Pulsed Plasma Thruster (PPT), based on [Hamidian and Dahlgren 1973]. A voltage is applied between two electrodes. This leads to the erosion of the PTFE insulation in between. The ejection of the eroded particles generates thrust in the range of μN to mN.

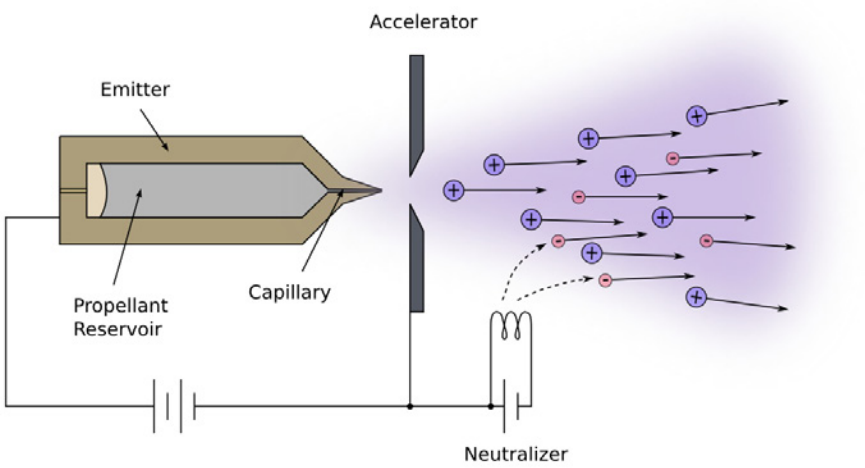

Figure 1.8: Functional Principle of Field Electric Emission Propulsion, based on [GG Phase A Study Team 2000]. Between a porous W needle and an acceleration grid a voltage is applied which leads to the extraction of charged particles. Usually In or Hg is used as propellant. The capillary effect prevents the material from leaking out of the needle.

rent is very low (some hundred μA), a continuous operation is possible even with a power budget of below 10 W. Like in all electrostatic EP concepts, a neutralizer is necessary to avoid a negative charging of the spacecraft. This and the miniaturization of the PPU are currently serious challenges on the path to CubeSat integration [Bock et al. 2014]. An overview on FEEP for CubeSats is given in figure 1.8.

The last option is the so called Vacuum Arc Thruster introduced by [Schein et al. 2001], for small satellites and firstly proposed especially for CubeSats by [Rysanek et al. 2002]. A detailed explanation of this EP concept will be given in the next chapter.

Chapter 2

Vacuum Arcs

The vacuum arc thruster is one of only a few suitable propulsion concepts for the attitude and orbit control of small satellites. This chapter starts with the physical background of vacuum arcs, their initiation behavior, the inter-electrode plasma and the surface processes which are essential for the understanding of this propulsion concept. Following that, the basics of their use as thrust source will be introduced with a special consideration of thrust and specific impulse. The chapter closes with an overview on previous realizations and how critical factors like arc initiation, plasma plume control and reliability are treated.

2.1 Theoretical Background

The research and application of vacuum arcs is mostly concentrated on the deposition of thin films [Gilmour and Lockwood 1972], [Dolotov et al. 1974]. Many contributions to the explanation of vacuum arc phenomena have also been accomplished within the research of vacuum switches, where arcing can be a serious issue [Lafferty et al. 1980]. While most modern thin film deposition processes are based on different methods, there is still interest in the further development, e. g. for the coating of flexible synthetics with biocompatible titanium oxide layers for medical applications [Kauffeldt et al. 2012]. Another possible application is utilization of the plasma expansion for influencing the boundary layer of air foils and turbine blades [Kronhaus and Scharnowski 2015]. The latter is in an even earlier stage as propulsion development, but may be an interesting alternative to dielectric barrier discharges and fluidic actuators.
Nevertheless, the basic principle is always the same: A discharge between two electrodes separated by a vacuum or a low pressure environment leads to the ejection of highly ionized plasma into the surrounding area. For the initiation of the arc a high electric field between the two electrodes is required, which leads to a negative charge building up at the cathode and a positive charge at the anode. When the field reaches a critical value, electrons are emitted by the cathode and fly towards the anode. Within the subsequently following arc which acts as conducting medium between the electrodes, cathode material is eroded

[Mesyats 1998]. As a result, a plasma plume is formed by the ionized metal vapor and expands into free space. The ion density, their velocity and the ion current fraction depend on the physical properties of the used cathode material and the applied energy. Collisions and excitations between particles within the plasma occur only in the first hundred μs (depending on the input energy) when the density is extremely high ($\sim 10^{24}$ cm^{-3}).

2.1.1 Electron Emission and Cathode Spots

In reality the surface of both electrodes is not exactly smooth. Instead, they have a certain roughness due to small craters, protrusions or inclusions. The application of an electric field leads to a reduction of the material's work function. A minimal field strength of around 10^9 V/m is required [Mesyats 1998]. This process is influenced by the mentioned irregularities. Especially tips lead to a local amplification of the electric field and to a further lowering of the work function until electrons can leave the surface by field emission or thermionic emission [Anders 2008]. In case of field emission, the applied electrical energy leads to a higher quantum-mechanical tunneling probability by the reduction of the work function. The emission of electrons due to their thermal energy on the other hand is also enhanced by the applied field. A sufficient temperature is achieved by Joule heating of the emission region which follows from a current density of around 10^{10} A/m^2 [Coulombe and Meunier 1997].
The most probable mechanism for the erosion of the cathode material is the explosive vaporization of the tip due to rapid overheating when a critical current density of about 10^{12} A/m^2 is reached [Dyke and Trolan 1953]. In connection with the designation Explosive Electron Emission (EEE) for the processes explained above, the erosion regions are often called Ectons [Mesyats 1998] or Cathode Spots [Anders 2008]. While Joule heating is the dominant heating mechanism during arc breakdown, ion bombardment becomes the more important reason for cathode heating within the lifetime of the cathode spot (up to microseconds). Depending on the discharge current their usual size ranges from 1 μm to 100 μm [Boxman et al. 1995]. Spots generated at the beginning of the discharge are smaller and move with a velocity of 100 to 300 m/s along the cathode–anode interface. Whether the cathode surface is oxidized/contaminated or clean, they are categorized as Type 1 or Type 2 spots. To add some confusion, an additional classification scheme could be found in literature: The fast moving Type 1 and 2 spots are grouped within the designation Type 1, while slow moving spots which usually occur in discharges longer than 100 to 200 μs are called Type 2 spots. Moreover, there is a Type 3 existing that was found on semiconductors and semi-metals which have a lower electric conductivity than metals [Anders 2008]. The heating of the cathode spot area leads to a reduction of the local resistivity, which thereby enhances the further spot production. Type 3 spots have a lower velocity than other spot types and they have the tendency to stay in the same position for a significant time, which leads to deeper craters [Anders 2008]. Figure 2.1 shows cathode spots of different sizes.

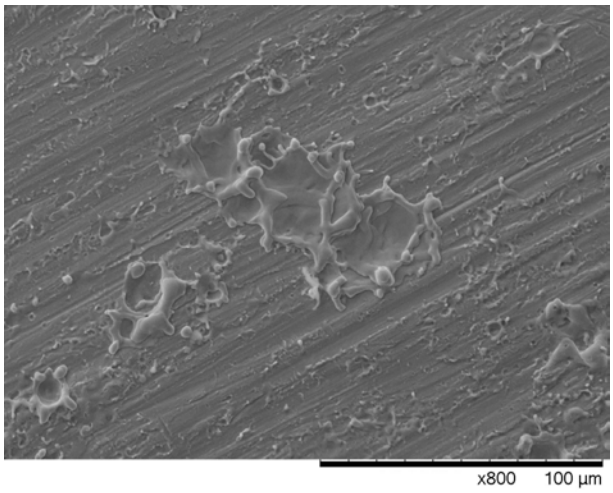

Figure 2.1: Surface of a Ti cathode, acquired with a SEM (Scanning Electron Microscope) at a magnification factor of x800. Different sizes from around 10 to 40 μm of cathode spots are visible along the path of the arc. Longer residence times lead to bigger spots with more molten material around, resulting from the higher energy input

The erosion leads to the creation of craters on the cathode surface which are growing during the spot lifetime. As a result, Joule heating decreases up to the point where the temperature is not sufficient to maintain evaporation and electrode emission. Finally, the cathode spot extinguishes. As long as energy is supplied to the cathode new cathode spots can arise at protrusions nearby these extinct spot regions. For the interesting type of vacuum arc with an arc current of up to a hundred ampere the cathode is the dominant origin of the plasma material. The anode on the other hand is only important as conserving counterpart to the cathode, since it only collects the emitted electrons and does not contribute significantly to the vacuum arc material. This is only happening at higher currents in the region of kA [Boxman et al. 1995].

2.1.2 Plasma Processes

Eventually, a plasma is formed from the material evaporated from the cathode spot region. Several different and partially interacting processes lead to the creation and sustainment of this plasma. The plasma right in front of the cathode could be divided in cathode spot surface, a positive sheath region, a pre-sheath or ionization region and the actual arc plasma region [Lun 2008]. Figure 2.2 gives a simplified overview of this model.

Together with the fast moving electrons, much slower neutral atoms are ejected by the explosive evaporation of the cathode spots. The cathode region becomes positive due to the loss of electrons. Thus a positive sheath is built in front of the cathode where the potential drops from the now positive charged cathode surface to the negative edge of the sheath. The accelerated electrons have enough kinetic energy to cross this zone and to ionize neutrals from the evaporated cathode material within the adjacent pre-sheath which is

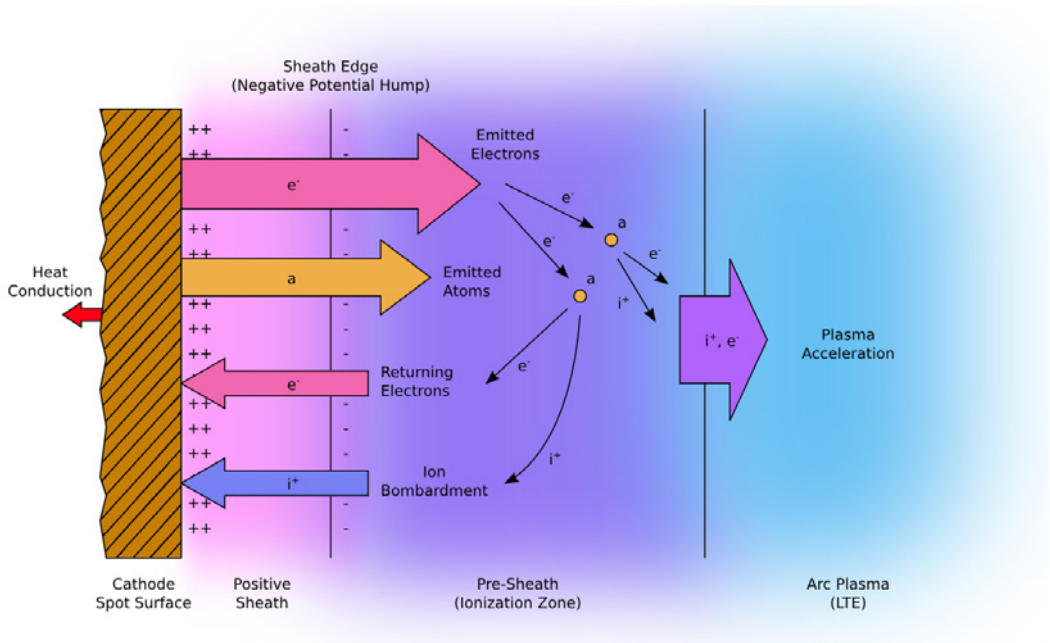

Figure 2.2: Schematic illustration of the processes in the transition region between cathode spot and arc plasma based on [Lun 2008]. The plasma can be divided in cathode spot surface, a positive sheath region, a pre-sheath and the arc plasma.

therefore also called ionization zone. Further interactions between electrons and ions within the pre-sheath can cause higher charge states depending on arc energy and pulse length. Due to the positive cathode potential some ions are attracted back and form a sheath of positive charges at the cathode surface. This process is enhanced by the accelerating effect of the positive sheath region. The ion bombardment leads to an additional heating of the cathode. A total heat flux of around 10^9 to 10^{13} W/m^2 is typical [Boxman et al. 1995]. The resulting heat load for a given cathode size is important for the material choice as well as for the thruster geometry. Hence, an estimation will be given in chapter 5.
The ions which can leave the pre-sheath are forming a quasi-neutral plasma which is accelerated away from the cathode. Only around 7 to 12 % of the electrical discharge current which results from electron flow between cathode and anode and the ion flow to the cathode is converted into the ion current flux of the expanding plasma [Kimblin 1974], [Tuma et al. 1978], [Cohen et al. 1989]. Together with the electromagnetic force ($\mathbf{j} \times \mathbf{B}$) produced by the discharge current and Joule heating, several mechanisms lead to the acceleration of the plasma plume. From the explosive evaporation of cathode material a high pressure gradient is resulting ($\sim 10^7$ Pa). Moreover, ions are repelled by the positive sheath in front of the cathode and the interaction between the fast, high energetic electrons (around 1 keV) and slow ions lead to a momentum transfer to the ions (20 – 200 eV) [Boxman et al. 1995]. Thus, the particles are expanded from the high dense ($\sim 10^{24}$ m^{-3}) zone in front of the cathode into a low-density plasma jet with a velocity of around 10^4 to

10^5 m/s, depending on the physical properties of the cathode material [Dethlefsen 1968]. In addition, depending on the material properties and the applied energies, so called macroparticles are produced inevitably. From materials with a low melting point liquid droplets of molten metal are ejected, because the boiling point is reached by the applied energy before EEE occurs. Very brittle materials like Mo or W tend to break under high thermal loads, thus creating also small non-ionized particles. Unfortunately, these particles are much slower than ions (only around 10^2 m/s) and leave the cathode region under a relatively flat angle ($\sim 20 - 30°$ relative to the cathode plane) [Kutzner and Miller 1989]. Moreover, in case of a very close distance between anode and cathode together with an solid interface, macroparticles tend to increase the possibility of a short circuit of both electrodes. This ultimately ceases operation since no further arc can be initiated without a separation of both electrodes.

2.1.3 Technical Implementation and Application

The plasma jet expands into the surrounding area with an ion current distribution which can be approximated with a cosine or exponential fit function [Tuma et al. 1978], [Heberlein and Porto 1983], [Cohen et al. 1989]. During the expansion of the plasma plume, the ion density decreases inversely proportional with r^2, where r is the distance from its origin. By putting a substrate into the plasma beam, a thin layer of cathode material is deposited on its surface. Various coating systems and layer compositions have been developed and studied since the beginning of vacuum arc PVD [Anders 2008]. The application of magnetic filters can be used to focus the plasma beam as well as to filter macroparticles from the deposition zone and by the addition of a reactive gas like O_2 or N_2, oxidic or nitridic layers could be composed. More innovative applications are the use of a vacuum arc as ion source for heavy ion fusion as proposed by [Qi et al. 1997] and the use as thruster for small spacecraft, which will be further explained in the following section. A typical setup for a vacuum arc PVD system is illustrated in figure 2.3 a).

An important issue for all applications is the initiation of the vacuum arc. Up to now only an electric field, generated by a potential difference between anode and cathode, was mentioned as starting point of the arc. As mentioned above, the minimal field strength required for arc initiation in vacuum is located in the region of 10^9 V/m. This is a big challenge even for industrial PVD processes. Various methods for arc initiation have therefore been developed [Anders et al. 1998]. The most reliable method is the electrode separation or contact ignition technique where anode and cathode are simply moved apart, thus creating a very high current density on a view protrusions and subsequently a sufficiently high electric field. Based on this a trigger electrode can be used which touches the cathode and is immediately removed, leading to the same effect. The trigger motion can be achieved by a spring mechanism, an electromagnetic or pneumatic actuator, or even manually. However, this method is prone to fusing since the trigger electrode is usually a thin pin which also suffers from erosion. Moreover, both mechanisms have very low repetition rates (up to 1

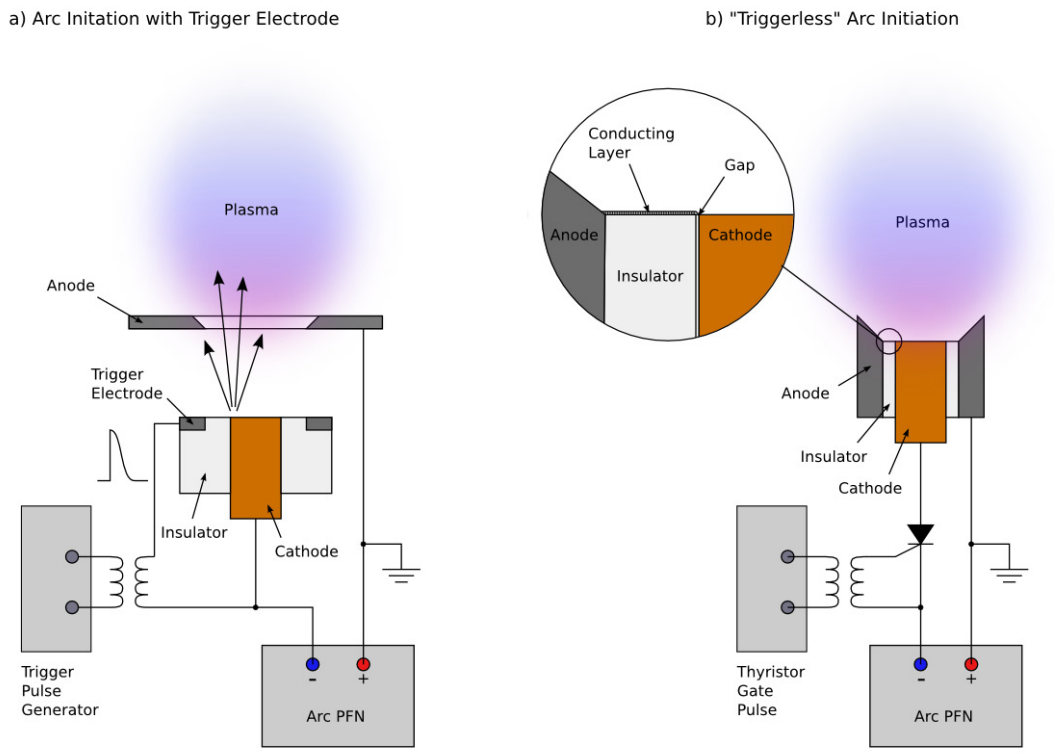

Figure 2.3: Left: Schematic illustration of a conventional vacuum arc deposition system with trigger electrode. Right: Vacuum arc source with "triggerless" arc initiation according to [Anders et al. 2000]. The insulator between anode and cathode is coated with a conducting layer. This allows arc initiation at relatively low voltages (some hundred volts to a few kV).

Hz [Boxman et al. 1995]). Thus, mechanical trigger methods are usually used only for continuous discharges, where the arc is maintained by a DC current source.
A suitable method for pulsed operation with high repetition rates (up to some kHz) is the use of a stationary trigger electrode in proximity of the cathode. Both electrodes are thereby separated by a thin insulation (figure 2.3 a)). By the application of a sufficiently high voltage (some kV), a surface flashover occurs which is then relieved by the arc discharge between anode and cathode by an electrical switch [Anders 2008]. This process can be facilitated by the deposition of a conductive layer (e. g. a pencil mark) on the surface of the insulator which leads to a lowering of the resistance between cathode and trigger electrode. Unfortunately, the layer is also explosively eroded by Joule heating due to the high energy input and will become increasingly useless. Moreover, a contamination of the plasma beam may occur which is a serious issue for the deposition of very pure coatings. Nevertheless, this procedure was used as basis for the so called "triggerless" arc initiation which was introduced by [Anders et al. 1998] especially for low-voltage discharges.
As illustrated in figure 2.3 b), the trigger electrode is replaced by the real anode. The surface of the insulator is coated with a conductive layer which in principle could be made

of any conducting material. In most cases graphite simply applied by a pencil is used, e. g. [Schein et al. 2001], [Lun 2008] or [Fuchikami et al. 2013]. Since only a small gap of some μm is separating cathode and the combination of anode and conductive layer, a resistance of only some kΩ is achieved. Therefore, a relatively small high voltage of some kV or below is sufficient to achieve a breakdown at the gap, thus shortcutting both electrodes [Anders et al. 1998]. The resulting current leads to a heating of the conducting material by Joule heating. This causes an explosive evaporation of weak points within the conductive layer. Thereby, a small cloud of conducting vapor is produced between anode and cathode, leading to a new low-resistance path for the electron flow between cathode and anode. Hence, a vacuum arc can arise as explained above. This simple mechanism is the basis for the development of the vacuum arc thruster [Schein et al. 2001].
The last trigger method worth mentioning is the arc initiation by a laser beam. Thereby, the laser beam is focused on the cathode surface with a focal diameter of around 150 μm [Siemroth and Scheibe 1991]. This enhances the probability of arc initiation when the power density applied by the laser reaches around 10^{11} W/m^2. Unfortunately, this requires a very powerful and therefore big and expensive laser which obviously exceeds the limitations of space application. However, the physical processes on the surface may be of interest for the further development of a propulsion system. The laser does not necessarily need to evaporate the cathode surface [Mesyats 1998]. Instead, it may be sufficient to force an evaporation of the gas layer adsorbed on the cathode surface. This can be achieve by laser radiation but also by other thermal loads.

2.2 Vacuum Arc Thruster

The use of vacuum arcs as propulsion system was considered first by [Gilmour 1966] and [Dethlefsen 1968], based on the knowledge that from the electrode regions of an arc source plasma jets with velocities up to 10^5 m/s were ejected. Later [Qi et al. 1998] introduced the so called Vacuum Arc Ion Thruster (VAIT) where a vacuum arc is used as plasma source for an ion thruster. The big advantage compared to common ion thrusters would have been the use of a solid reaction mass, Bismuth, to avoid a complicated liquid or gaseous propellant supply system with all its problems like freezing or leaking. However, as explained in the last chapter ion thrusters require a neutralizer. Fortunately, especially for low thrust applications like attitude control and fine positioning of small satellites, additional electrical acceleration systems are possibly not required. Revisiting the original concept, [Schein et al. 2001] introduced the VAT as propulsion system for small satellites.

2.2.1 Basic Concept

Several geometries have been described in literature which could be allocated in three basic groups: A coaxial [Gilmour 1966], [Schein et al. 2001], a planar [Rysanek et al. 2002], [Lun 2008] and a ring or hollow electrode design

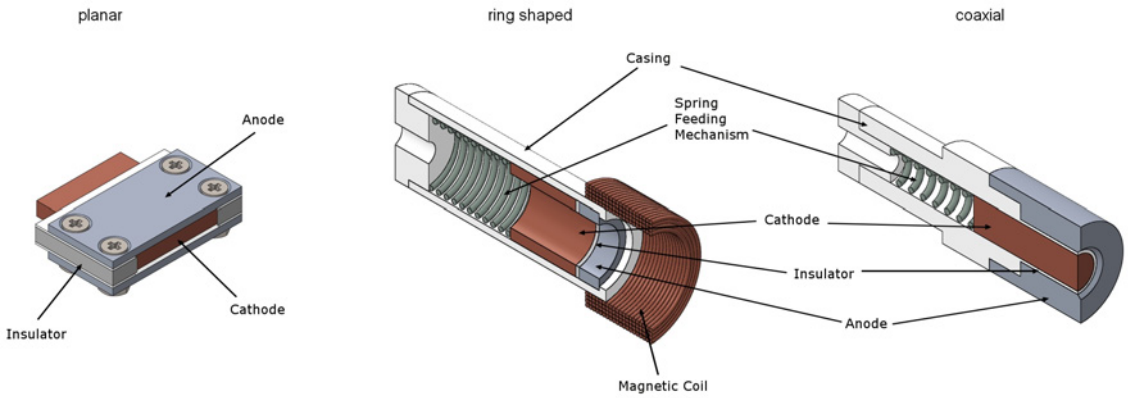

Figure 2.4: Illustration of the most common vacuum arc thruster geometries: Planar (left), ring (middle) and coaxial (right) electrode setup [Rysanek et al. 2002], [Keidar et al. 2005], [Schein et al. 2007]. All geometries require a propellant feeding system (e. g. a spring) for a suitable lifetime.

[Keidar et al. 2005], [Schein et al. 2007] (see figure 2.4). The advantage of the coaxial design is the well-defined location of thrust production compared to the planar thruster where the arc can arise at any point of a broad contact area [Lun 2008] and the accurate expansion direction of the plasma plume compared to the ring thruster, where the expansion direction has to be controlled by an external magnetic field [Keidar et al. 2005].

All concepts have in common that anode and cathode are separated by a solid insulator and not by vacuum as it is the case in many PVD systems. Due to the required high resistance against high voltages and temperatures, alumina is used mostly in literature, e. g. [Schein et al. 2001], [Keidar et al. 2005]. This limits the minimal thickness and is also a weak point regarding mechanical loads during takeoff. Thiner but more flexible materials like Kapton or Mica have also been tested, but turned out to be very prone to erosion during operation [Lun 2008]. For the anode, in principle any conductive material could be used. In practice Al and Cu are used mostly because both have a very good conductance and a good machinability.

The above mentioned conversion of cathode material into a plasma jet leads not only to the creation of a momentum in the opposite direction, i. e. thrust, but also to consumption of the cathode material which therefore can be referred to as propellant or reaction mass (see figure 2.5). The mass flow or erosion rate depends on the applied pulse energy and on the material properties. Hence, thrust can be controlled within a limited range. Typically, the thrust ranges between some nN and some 100 μ while the specific impulse lies between some 64 s for Cd and 1666 s for Cr [Polk et al. 2008]. However, the consumption of the propellant reduces the ignition probability and declines the discharge behavior, since the distance between anode and cathode surface becomes longer and the cathode surface properties are changing rapidly. Therefore, a reliable feeding mechanism is necessary. For the coaxial thruster design a simple spring mechanism was introduced by [Schein et al. 2001]

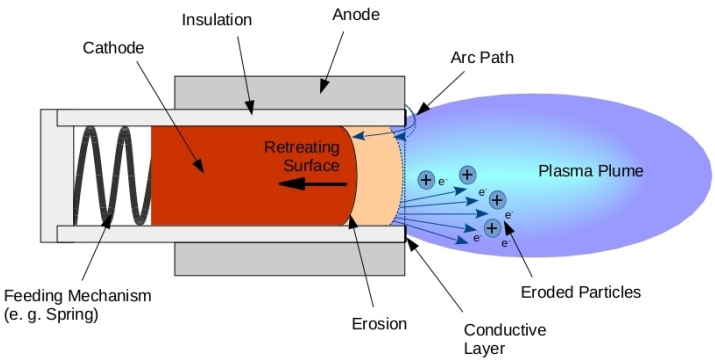

Figure 2.5: Working principle of the Vacuum Arc Thruster: Charged particles from the eroded cathode material are forming a quasi-neutral plasma plume with an inside pressure of around 10^7 Pa. This leads together with electromagnetic ($\mathbf{j} \times \mathbf{B}$) and thermal forces (Joule heating) to the ejection of the particles (ion velocity $\sim 10^4$ m/s) and subsequently to the production of thrust. The cathode surface would retreat against the exhaust direction without a feeding system. The gap between conductive layer and cathode becomes larger until the distance is too big for the further arc initiation.

and [Rysanek et al. 2002]. Unfortunately, this mechanism was not developed far enough for satellite integration and in the following literature no continuative and functional concepts have been described. One exception is the ring electrode thruster introduced by [Keidar et al. 2005].

Another challenge for satellite integration is the supply of sufficient power for arc initiation and arc sustainment. The application of an off-the-shelf HV-regulator would lead to relatively space consuming power supply, e. g. [Sekerak 2005] or [Lun 2008], which requires also enough input current. A pure capacitive power circuit would require (physically and electrically) big capacitors which are also beyond CubeSat limitations. Although it is necessary to apply high voltages for breakdown, the plasma itself can be sustained with relatively low voltages in the range of 15 to 32 V (depending on the material) as long as current could be provided by the power supply [Polk et al. 2008]. Based on this fact, [Schein et al. 2002] designed a simple and efficient Power Processing Unit (PPU) which generates very short pulses with ignition voltages in the range of some kV and enough pulse current for an arc of several hundred μs from an input voltage of around 24 V by the use of a so called Inductive Energy Storage (IES).

As shown in figure 2.6, the IES circuit consists basically of an inductance connected to a external power supply and a fast acting (up to some hundred ns) high voltage switch, e. g. an IGBT or MOSFET. The inductance is charged as long as the circuit is closed by the switch. When the switch is opened again a rapid increase of the voltage U between anode and cathode occurs, which is proportional to the product of inductance L and the temporal change of the electrical current in the circuit dI/dt. If the voltage peak is sufficient for an electric breakdown a vacuum arc is initiated. Figure 2.7 shows the voltage and current characteristics of a typical arc discharge achieved by a PPU with IES.

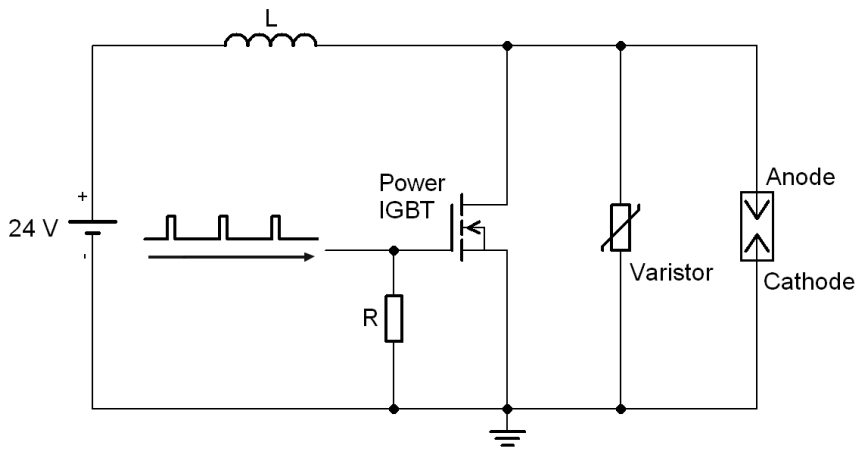

Figure 2.6: Schematic of the PPU concept of [Schein et al. 2002] with inductive energy storage (IES). The inductor L is charged as long as the IGBT is activated. After that, a high voltage peak occurs which leads to the ignition of the vacuum arc.

The current profile is of nearly triangular shape, while the arc voltage stays more or less constant after the ignition peak as long as a current is running. Pulse length and discharge current are depending on voltage, inductance and its saturation current. The typical pulse length for an IES PPU with an inductance of around 200 μH and a saturation current of 9 A is up to 400 μs at an input voltage of 24 V while currents up to 50 A could be achieved (although the exemplary pulse in 2.7 reaches only 9 A). Practically, this is only possible if the power source can provide currents in the region of some Ampere continuously as long as thruster operation is required. A CubeSat cannot provide such current and voltage levels [Kronhaus et al. 2013]. Figure 2.8 shows early realizations of VAT systems by the Alameda Applied Sciences Corporation (AASC).

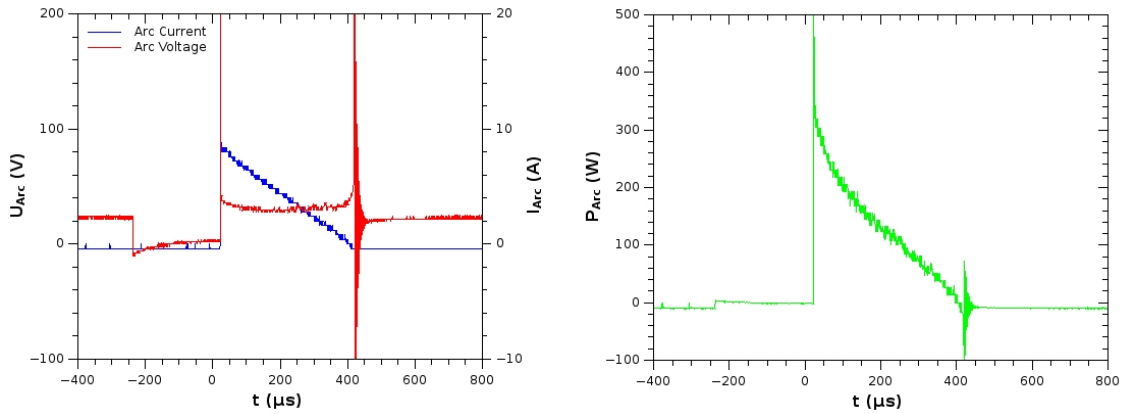

Figure 2.7: Left: Arc voltage U_{Arc} and arc current I_{Arc} achieved with an IES PPU at an Input Voltages of 24 V. Right: From the Power $P_{Arc} = U_{Arc}I_{Arc}$ the pulse energy could be derived by integrating over duration of the pulse (here around 50 mJ).

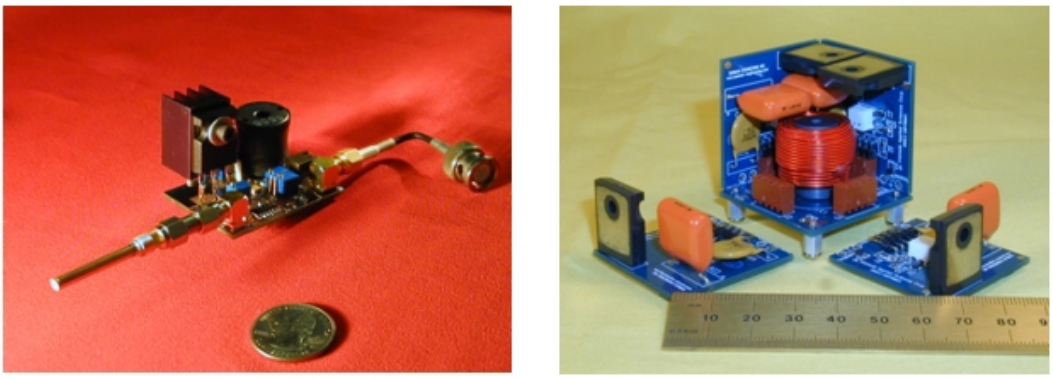

Figure 2.8: Early Prototypes of VAT propulsion systems for small satellites based on IES PPUs [Alameda Applied Sciences Corporation 2011].

The original VAT concept is essentially depending on the already explained "triggerless" arc initiation [Schein et al. 2001]. Therefore, a reliable conductive layer is necessary which works as long as the satellite mission lasts. This is still an issue since the usually used graphite layer on the surface of the insulation withstands some 1000 pulses before it is eroded or welding occurs [Lun and Law 2015]. Other materials like Cu, Ti or W have shown almost the same failure possibility. However, experiments with higher pulse energies and repetition rates showed that the inevitable re-deposition of cathode material can lead to a "healing" of the conductive layer [Anders et al. 2000]. Usually this re-deposition is unwanted since it contaminates the satellite, which is especially a problem for the solar arrays.

2.2.2 Thrust and Specific Impulse

The origin of the thrust, i. e. the creation of the plasma plume, was already explained in section 2.1. As it was also mentioned, apart from the input energy thrust and specific impulse are depending on the properties of the cathode material. Actually, there is a close connection between the atomic mass of the material and the theoretical achievable performance of the thruster [Polk et al. 2008]. Figure 2.9 shows the predicted specific impulse and total efficiency for various cathode materials as function of the atomic mass.

The atomic structure has a significant influence on efficiency and specific impulse since this determines the ion fraction, i. e. how many charge states will occur and how they are distributed, as well as the erosion rate. The erosion rate $[E_r] = \mu\text{g/C}$ determines the mass flow $\dot{m}$ and hence the required amount of reaction mass for a certain thrust at a given discharge current I_{Arc} [Polk et al. 2008]:

$$\dot{m} = E_r I_{Arc}. \tag{2.1}$$

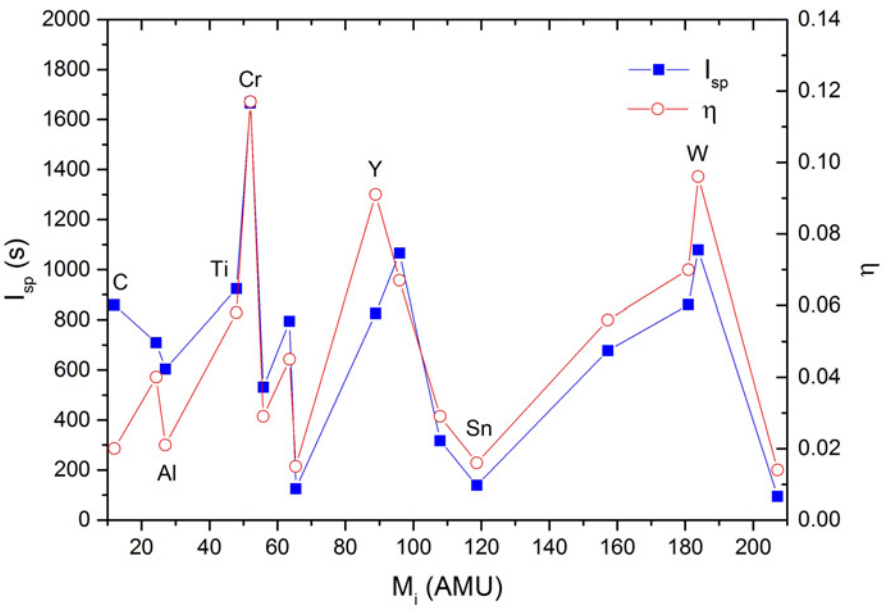

Figure 2.9: Theoretical specific impulse I_{sp} and total efficiency η of various cathode materials, based on [Polk et al. 2008].

The current I_{Ion} related to one ion can be written as sum of the currents I_Z which is the flux of ion in different charge states Z:

$$I_{Ion} = \sum_Z I_Z = I_{Ion} = f_{Ion} I_{Arc} \tag{2.2}$$

Higher charge states lower the efficiency of the thruster because they partially consume the energy needed to achieve and sustain the plasma. Moreover, only a fraction f_{Ion} between 7 and 12 % of the discharge current is converted into ion current which is deciding for thrust and I_{sp} which gives the following expression

$$\dot{m}_{Ion} = \frac{f_{Ion} I_{Arc} m_{Ion}}{e} < Z^{-1} > \tag{2.3}$$

for the ion mass flow rate $\dot{m}_{Ion}$ if m_{Ion} is the mass of the ion, e the charge of an electron and $< Z^{-1} >$ the mean inverse charge state which is defined as

$$< Z^{-1} >= \sum_Z \frac{f_Z}{Z}, f_Z = \frac{I_Z}{I_{Ion}}. \tag{2.4}$$

Literature shows that the charge state distribution is almost constant within the expanding plasma except in the direct vicinity of the cathode. At arc currents of up to 60 A, which are typical for thruster applications, only within the first 100 μs significant changes where observed [Anders et al. 2005]. However, this could be influenced by the application of external magnetic fields [Anders and Yushkov 2002]. Thus the fraction of the total ion

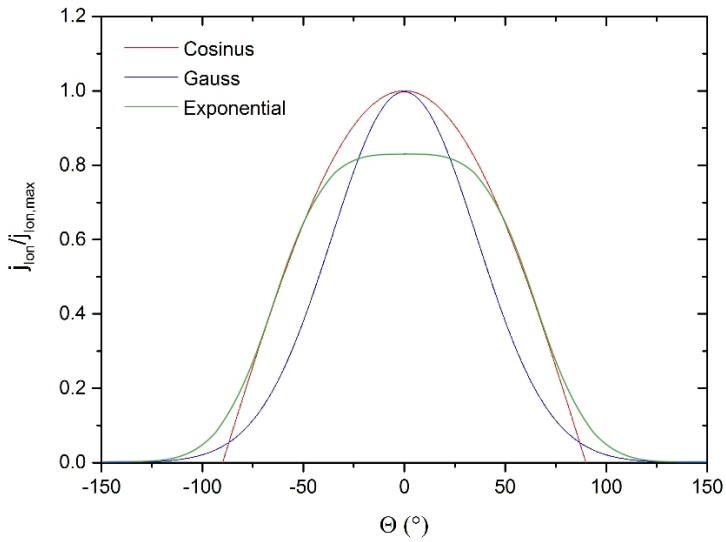

Figure 2.10: Examples for a Cosinus, an exponential and a Gauss fit function normalized to the peak ion current density as predicted by literature, e. g. [Polk et al. 2008]. Θ is the angle from the surface normal.

mass loss can be written as

$$F_{Ion} = \frac{f_{Ion} m_{Ion} < Z^{-1} >}{eE_r}. \tag{2.5}$$

The geometry of the expanding plasma plum could be fitted best with a Cosinus, exponential or Gauss function (see 2.10) as measurements of ion density distribution have shown [Tuma et al. 1978], [Heberlein and Porto 1983], [Kutzner and Miller 1989], [Cohen et al. 1989]. A cosine beam profile is the simplest approach to model the ion current density distribution $j_{Ion,P}$ at a distance r from the cathode and an angle Θ from the surface normal and can be described by

$$j_{Ion,P}(r, \Theta) = \frac{j_{Ion,C} \cos\Theta dA}{\pi r^2}. \tag{2.6}$$

Thereby, $j_{Ion,C}$ is the ion current flux from the cathode surface. However, measurements showed that ion can also be found at angles greater than 90° where the cosine distribution naturally ends [Kutzner and Miller 1989]. This ion current backflow could be adequately addressed by using an exponential distribution:

$$j_{Ion,P}(r, \Theta) = \frac{2 j_{Ion,C} dA}{\sqrt{\pi} r^2 k \mathrm{erf}(2\pi/\kappa)} \exp(-[2\pi(1 - \cos\Theta]^2/\kappa). \tag{2.7}$$

The spread of the distribution can be adjusted with the constant factor k. With $j_{Ion,C} = f_{Ion} I_{Arc}$ follows the mass flow rate for ions at distance r and angle Θ, created by erosion of the surface element dA [Polk et al. 2008]:

$$\dot{m}_{Ion,P}(r, \Theta) = \frac{m_{Ion} j_{Ion,P}}{e} < Z^{-1} > . \tag{2.8}$$

Further assumptions apart from a constant ion fraction distribution are a constant ion velocity v_{Ion} and a constant discharge voltage U_{Arc} which is dominated by the cathode fall for a given material [Polk et al. 2008]. The last both parameters vary only weakly with the charge state and the anode geometry. With the ion mass flow, the performance of the thruster could be estimated. Following [Polk et al. 2008], the differential thrust resulting from an ion flux from the cathode area dA_C through area dA_A on the anode exit plane is given by

$$dT = d\dot{m}_{Ion,P}(r,\Theta)(v_{Ion}\cos\Theta)(\cos\Theta dA_C). \tag{2.9}$$

By inserting $m_{Ion,P}$ and integrating over dA_C and dA_A follows

$$T = \frac{M_{Ion} f_{Ion} I_{Arc} v_{Ion}}{e} < Z^{-1} > C_{Thrust}(\overline{L}, \overline{r}_C). \tag{2.10}$$

This is the theoretical thrust achieved by all ions eroded from the cathode or radius r_C which leaves the anode plane with velocity v_{Ion}. C_T is the so called thrust correction factor which was introduced by [Polk et al. 2008] to address the plume divergence and the deposition of cathode material on anode walls. Thereby, a uniform discharge current density is assumed over the cathode surface, i. e. $j_{Arc} = I_{Arc}/\pi r_C^2$. The derivation of C_T can be found in [Polk et al. 2008] who gives a value of 0.67 for a cosine distribution and of 0.64 for a exponential distribution, with a spread factor of $k = 4.5$ which is a good assumption for typical vacuum arcs. Now it is possible to calculate the theoretical specific impulse:

$$I_{sp} = \frac{T}{\dot{m}_T g} = \frac{F_i v_{ion} C_T}{g}. \tag{2.11}$$

With the applied discharge power $P = I_{Arc} U_{Arc}$ the total efficiency is given as

$$\eta = \frac{T^2}{2\dot{m}_T P} = \frac{M_{Ion}^2 f_{Ion}^2 v_{Ion}^2 C_T^2 (< Z^{-1} >)^2}{2e^2 E_r U_{Arc}}. \tag{2.12}$$

And finally the thrust-to-power ration can be written as

$$T/P = \frac{m_{Ion} f_{Ion} v_{Ion} C_T}{e U_{Arc}} < Z^{-1} > . \tag{2.13}$$

Thus, together with measured material data an analytical examination of different cathode materials relating to their viability as reaction mass can be conducted. A large selection of possible cathode materials and their theoretical performance can be found in [Polk et al. 2008]. This model helps also to interpret the results from thrust measurement and ion current density detection. However, deviations from the theoretical model can be expected and have actually been found in experiments [Lun and Law 2015]. Possible reasons are, for example, influences by the thruster geometry and heat loads around or above the melting points of anode and cathode, which can lead to melting and therefore a higher number of macroparticles as well as electromagnetic and electrothermal accelerating effects [Polk et al. 2008].

In practice, most surveys used Al, Cu, Ti and W as cathode material, e. g. [Schein et al. 2001], [Tang et al. 2005], [Sekerak 2005] or [Lun 2008]. Apart from the obviously good machinability of Al and Cu, a good discharge behavior of Ti (i. e. reliable arc initiation, only a few macroparticles, low fusing tendency) was decisive for this as well as very good predicted performance of W (I_{sp} = 1064 s). Additional materials of interest are Graphite [Fuchikami et al. 2013], [Lun and Law 2015], Cr and Mo on the high melting point side and Sn and In on the low melting point side. However, apart from the choice of the most suitable material several other issues still have to be solved.

2.2.3 Topics for Research

Although the VAT has been shown to be a viable option for CubeSat propulsion, there are still some working areas. One of the most important issues is the erosion of the conductive layer if "triggerless" arc ignition is used [Lun 2008]. In fact, the ablation of this layer is essential for the functionality of the thruster. It is therefore necessary to find a solution which allows a long-time operation. Possible directions of research are the development of a more resistant layer in terms of thermal and mechanical loads, or the investigation of mechanisms that lead to the replacement or "healing" of this layer.
The uniformity and reproducibility of the ignition process and the afterwards burning plasma is still an issue which is connected to the geometry of the electrodes, the length of the pulse and the application of additional means like electric or magnetic fields, which may consume additional power. If the pulses are too short, only the edges of the cathode are eroded. When longer pulses are applied the arc plasma can move to the middle of the cathode, leading therefore to an even erosion of the surface. However, long pulses could lead to an overheating of the electrodes as well as high repetition rates which result again in a reduced thruster performance.
A purely technical challenge is the integration of the thruster into a CubeSat and the development of a reliable propellant supply system. The coaxial geometry has some advantages compared to other concepts. Especially the precise localized origin of the thrust is an important feature of such a setup [Schein et al. 2001]. But, on the other hand this limits also the amount of available reaction mass at a time. Since thrust is produced from the erosion of cathode material, some kind of feeding mechanism is necessary to replace the consumed reaction mass [Schein et al. 2001]. Most emphasis was previously laid on a simple spring mechanism which has yet to be adapted to CubeSat requirements. Various other methods like electro-motors, shape memory alloy and pieco actuators may be possible, although additional power is required for this. Together with the adaption of the geometrical design to a CubeSat, this is an important task for this thesis.
Further attention has to be set on the avoidance or at least reduction of satellite contamination. This is a serious matter, especially for the solar array which otherwise will lose efficiency if their surface is covered with a metallic coating. One possible solution is a geometrical shielding which on the other hand lowers the net thrust if too much of

the plasma plume is shadowed. Another measure is the application of an external axial magnetic field which has shown to be capable of improving thrust and specific impulse [Keidar et al. 2005], [Tang et al. 2005]. However, it has to be verified if this is possible and reasonable under the power limitations of a CubeSat.
These limitations are also the reason for the further development of the PPU. Common methods like the use of a PFN or an IES consume too much power and are usually too large and heavy for CubeSat conditions, although there had been some efforts to reduce size and mass, particularly by [Schein et al. 2002] and [Lun 2008]. But these concepts did not pay attention to power supply capabilities of a CubeSat and an appropriate operation scheme which will be one focus of this thesis, together with the just mentioned working areas.

Chapter 3

Experimental Setup

The further development of the VAT system for CubeSats requires a sound knowledge of its physical properties as well as of the operational characteristics of the improved or altered components. Hence, accompanying the development of PPU and VAT several diagnostic methods have been used to measure the electrical operation parameters, the ion current density distribution, the thrust and the erosion rate as well as to visualize the propagation of plasma plume and macroparticles. These methods will be described after a brief introduction of the test environment with the vacuum system in the center.

3.1 Basic Assembly

Within this work, a comprehensive test environment consisting of electrical measurements, ion current density detection, thrust measured and high speed imaging has been constructed. It has to be pointed out that these instruments should not be mistaken with highly precise or innovative diagnostic systems. In fact, they are meant to build a multi-functional test bed which allows the control of the development progress. The core is a vacuum system which consists primary of a vacuum chamber, a turbomolecular pump, a rotary vane pump and several pressure gauges. The basic requirement was a minimum pressure of around 10^{-5} Pa to allow test conditions like in a 400 – 600 km LEO. The inner dimensions were chosen to allow the installation of a thrust balance and the use of other diagnostic systems like ion current detectors and mirror systems for high speed imaging. Therefore, numerous flanges for feedthroughs and vacuum windows have been implemented. Figure 3.1 shows an image of the experimental setup within the vacuum chamber.

The vacuum chamber has a volume of 243 l and is made from stainless steel. To achieve a leakage as low as possible, copper fittings have been chosen, with exception of the main door which has a Viton fitting for a fast access. Fore-vacuum is achieved with a Pfeiffer Duo 20M rotary vane pump which has a pumping speed of up to 24 m^3/h [Pfeiffer Vacuum GmbH 2011a]. For a reduction of acoustic and mechanic vibrations,

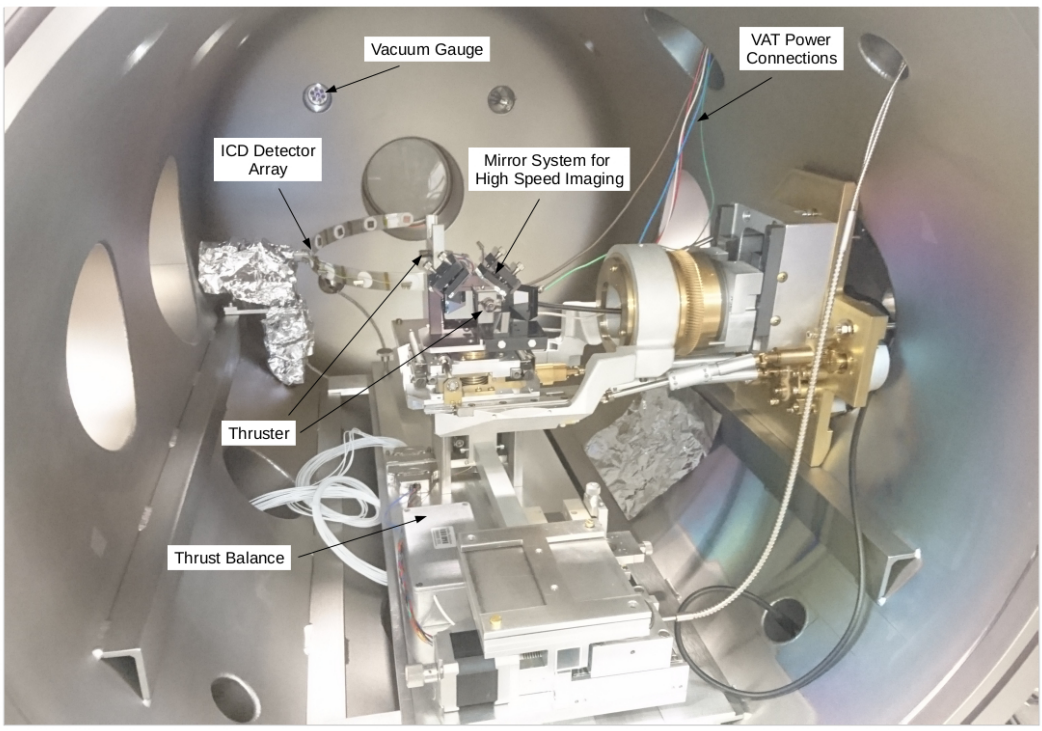

Figure 3.1: Image of the interior of the vacuum chamber. In the front, the mirror setup for high speed imaging is visible. The ion current density detection system can be found in the background. The thrust measurement system is mounted on the rack at the bottom.

it is housed with a noise insulation cover and the flexible hose to the turbomolecular pump is guided through a sandbox which enhances the reduction of mechanical vibrations. As it will be described later, together with the heavy chamber assembly these measures lead to a noise of only around 500 nN during thrust measurement. The main vacuum is achieved with a Pfeiffer HiPace 700 turbomolecular pump with a pumping speed of 685 l/s for N_2 [Pfeiffer Vacuum GmbH 2011b]. To allow experiments in the region of 10 Pa with and without gas supply, the turbomolecular pump can be circumvented with a bypass pipeline. In addition, a gate valve allows the separation between vacuum chamber and turbomolecular pump.

The pump stand allows an evacuation to 10^{-4} Pa in less than one hour, provided that the outgassing rate of the components within the chamber is low. This pressure correlates to an altitude of around 400 km which is sufficient for thruster testing. A confirmation of this statement can be given by calculating the mean free path λ of particles at this pressure under the assumption of a Maxwell distribution [Jousten 2008]:

$$\lambda = \frac{k_B T}{\sqrt{2}\pi d^2 p} \tag{3.1}$$

With the Boltzmann constant $k_B = 1.381 \cdot 10^{-23}$ J/K, an estimated ambient temperature $T = 300$ K, a gas particle diameter $d = 3 \cdot 10^{-10}$ for air molecules and a typical pressure

of $p = 10^{-4}$ Pa follows that the mean free path is around 100 m, which is a hundred times the chamber length. Therefore, the probability for collisions outside the plasma plume is extremely low. For long duration experiments, a lower pressure can be achieved with longer pumping times and with the help of a heating cable which allows to bake out up to a wall temperature of around 80°C.

For vacuum pressure control a Pfeiffer PKR 251 Full Range Gauge and a Balzers (now Pfeiffer) IKR 261 Cold Cathode Gauge were installed. The PKR 251 combines a mechanical Pirani gauge for rough vacuum and cold cathode sensor for high and ultra-high vacuum which provides a display range of $5 \cdot 10^{-7}$ to 10^5 Pa [Pfeiffer Vacuum GmbH 2011d]. The IKR 261 on the other hand is equipped only with the latter sensor type which allows measurements between 10^{-7} and 1 Pa [Pfeiffer Vacuum GmbH 2011c]. This gives an overlapping measurement range and allows especially in the lower regions a validation of the vacuum by two independent systems.

Every measurement, whether if it is thrust, ion current density or the high speed imaging of the plasma plume was accompanied by monitoring of the electrical parameters of VAT and PPU. All measurement values were monitored with LeCroy 2- and 4-channel oscilloscopes at a sampling rate of 100 kS/s. Figure 3.2 shows a schematic overview of the electrical measurement setup. The redundant acquisition of current and voltage is conditioned by the circuit design of the improved PPU, which will be introduced in the next chapter. Due to the use of an arc initiation method based on IES and the "triggerless" technique, a high voltage peak has to be generated for ignition. The level of this peak is determined by the coil inductance, its charging time and apparently by the condition of the conductive layer, whereas the voltage after ignition is primarily depending on the cathode material [Anders et al. 2000]. Together with discharge current and pulse length, it is possible to determine pulse energy and impedance of the discharge circuit. Furthermore, the magnitude of the produced thrust seems to be connected to the length of the pulse [Lun and Law 2015]. Hence, the time-resolved measurement of discharge voltage and current may help to adjust the optimal operation parameters of PPU and VAT.

Since PPU and VAT are physically separated during charging by an additional electronic switch (see chapter 4), it is necessary to measure the charging voltage of the storage capacitor parallel to the power source with additional voltage probe directly at the PPU input connection. The charging current of the inductor is measured with a current probe directly on the input line for the same reason. From these values the power consumption and the peak pulse repetition rate can be determined as well as the optimal operation of the inductor. A charging beyond the saturation current lowers the efficiency of the circuit massively, as will be discussed in the next chapter.

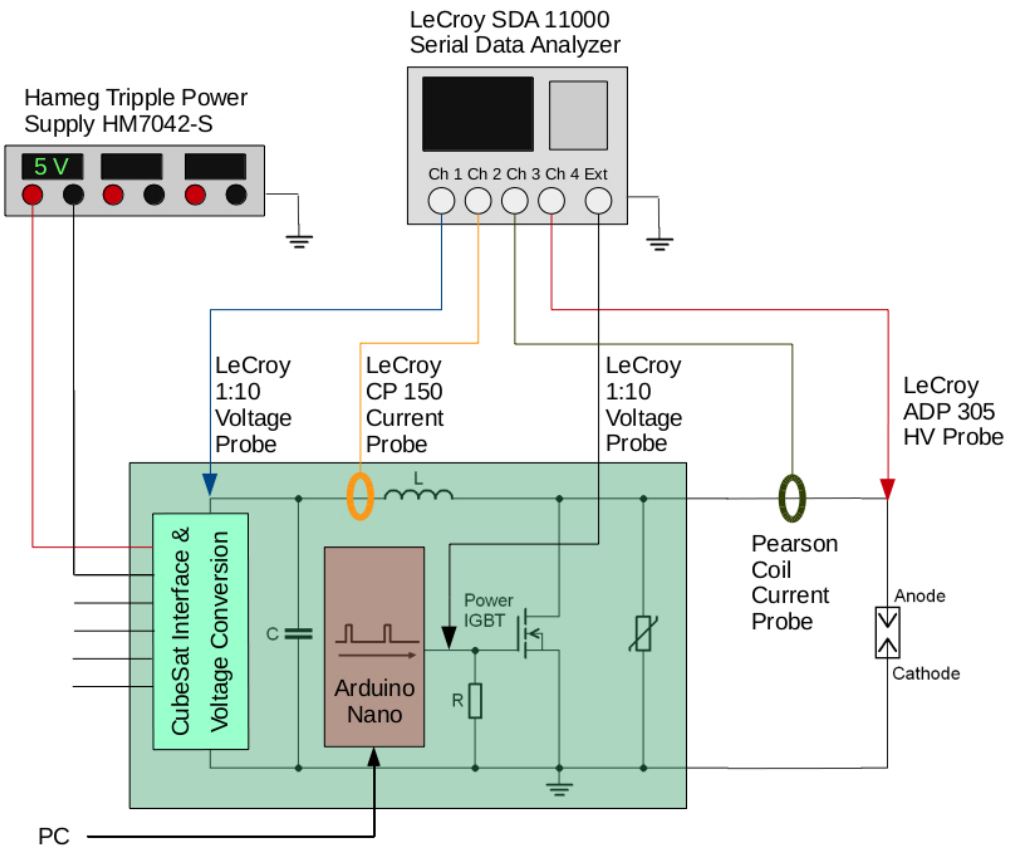

Figure 3.2: Electrical measurement setup as it was used in all development stages. Input voltage and inductor current are measured for the optimization of the PPU. Output voltage and current allow the determination of the arc energy as well as the investigation of the discharge behavior. A detailed description of the finally used PPU design follows in chapter 4.

3.2 Ion Current Density Distribution

For the characterization of the plasma plume produced by vacuum arcs several interesting diagnostic methods have been developed. One of the most used procedures is the measurement of the ion current with an electric probe, e. g. [Cohen et al. 1989], [Kutzner and Miller 1989]. Not only the angular distribution of the emitted ion flux but also the spatial development of the plasma beam and the velocity of the ions have been investigated, e. g. [Yushkov et al. 2000], [Roy et al. 2009]. Therefore, a huge database on the behavior of vacuum arc plasma could be used for further research. Moreover, this method allows a relatively precise valuation of the produced thrust based on theoretical models like [Sekerak 2005] and [Polk et al. 2008]. As a result, within this thesis a simple ion collector setup has been developed for the validation of the thrust balance described in the next section as well as for the investigation of the influence of different thruster geometries and external magnetic fields on the ion beam.

3.2.1 Detector Assembly

Since detailed values for typical ion velocities of vacuum arcs with comparable energies have been published already (cf. [Yushkov et al. 2000], [Polk et al. 2008], [Lun and Law 2015]), it is not intended here to build a precise setup for velocity measurement. Instead, the main focus has been laid on the angular detection of the ion current density distribution (ICDD) and on the derivation of the ejected ion mass. Nevertheless, a rough estimate of the ion velocity is possible. Based on the setup of [Anders and Yushkov 2002], the ion current density is simply detected by a planar probe after a given travel length in front of the thruster. Other approaches like [Sekerak 2005] or [Lun 2008] used a Faraday Cup. In both assemblies the ion collector is biased with a negative voltage which lies in the ion saturation regime (usually around -60 V to -90 V). Therefore, it is unlikely that electrons from the plasma plume are attracted to the probe and create artifacts in the measurement signal. Moreover, the chamber and the supporting structure of the probe is thoroughly grounded. The further use and development of this setup by [Roy et al. 2009] and [Kauffeldt 2010] has validated this assumption. Hence, for simplicity of the assembly the measurements were conducted without a Faraday Cup. Further assumptions are that ion velocity and charge state distribution are constant over the length of the drift region (150 mm) which is well supported by literature, e. g. [Anders and Yushkov 2002] or [Polk et al. 2008]. The ion current is measured via a shunt resistor on the positive side of the probe power supply. With the measured voltage U_P and the shunt resistance R_s the ion current I_{Ion} is simply given by Ohm's law:

$$I_{Ion} = \frac{U_P}{R_s}. \tag{3.2}$$

Within the given pulse energies of the VAT, a resistance of 100 Ω is adequate since typical ion currents are in the range of several 100 mV as shown below. A buffer capacitor of 10 μF is connected parallel to the power supply to stabilize the bias voltage [Kauffeldt 2010].

Figure 3.3 shows the complete setup of the detector system. To allow a real time acquisition of the angular ICDD in front of the thruster, an array of nine planar probes has been mounted on a semicircle of aluminum in front of the thruster. Each probe is quadratic, has an area of 1 cm^2 and is insulated by PTFE plates and an alumina tube against the aluminum arch. The angular arrangement of the probes can be seen in figure 3.3. Over all, an angle of almost 170° is covered along a semicircle which has its origin in the center of the cathode surface. Thereby, all probes have the same distance to the thruster. In addition, it is possible to rotate the probe array around the axis of the cathode surface normal. The pivot bearing is thereby attached behind the probe at the 0°-position. This allows a mapping of the ICDD in the full hemisphere in front of the thruster, averaged over several pulses with a very high precision. For the acquisition of the data a PicoScope 4824 High Resolution 8 Channel Oscilloscope is used, set to a sampling rate of 100 kHz. This setup is influenced by a detector assembly developed by [Kronhaus et al. 2013]. Thereby, 16 planar probes were mounted inside a hemispherical aluminum bowl and read out with

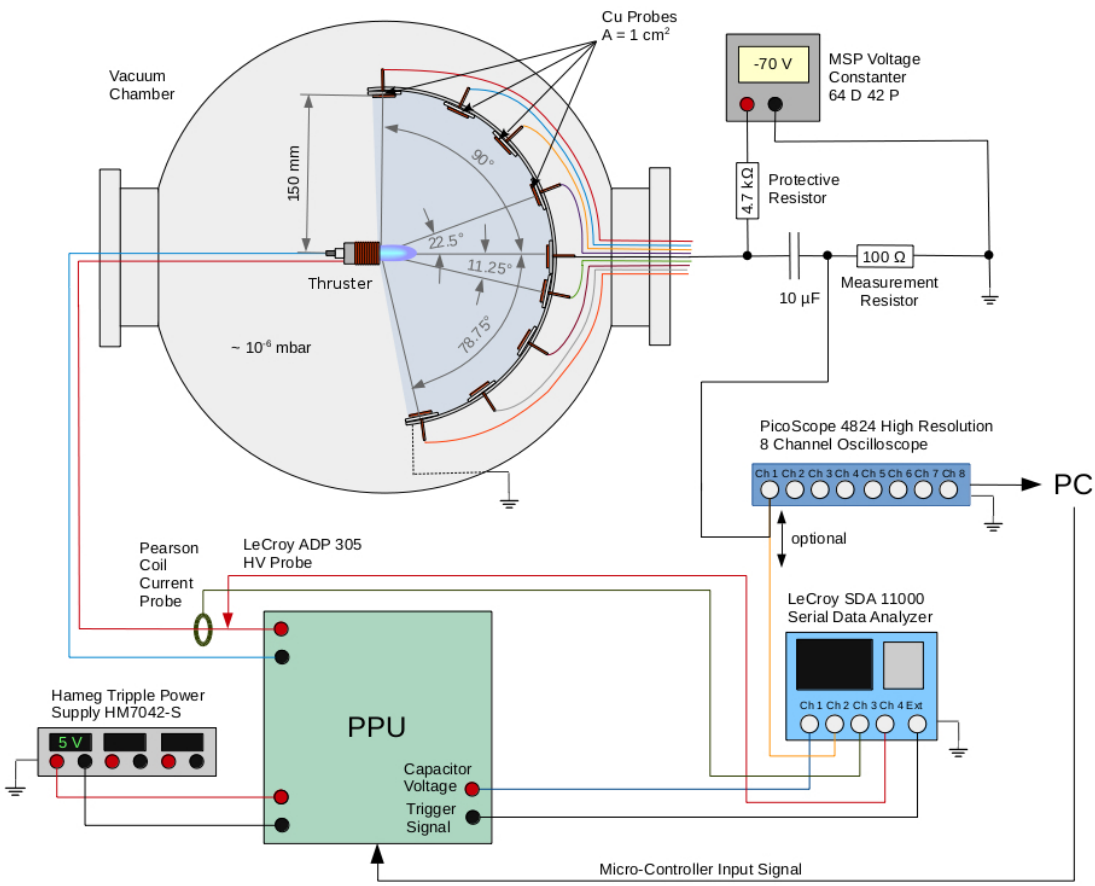

Figure 3.3: Setup for the ion current density measurement with a field of view of 168.25° in front of the thruster. The Cu probes are mounted on an aluminum arch which is rotatable around the axis formed by thruster and central probe. All systems have one common ground to avoid grounding issues. The measurement circuit is illustrated exemplary for one probe.

a multiplexer circuit. However, the acquisition system only allowed to read out one probe per pulse and prevented optical process control.

3.2.2 Preliminary Considerations

For a reliable and repeatable measurement it is necessary to characterize the measurement setup thoroughly. At first it was tested if the above described shielding of the probe cables is sufficient to avoid the reception of parasitic signals. To proof this, another thruster which was not in the angle of view of the probes was operated. As it turns out, only during the HV switching processes of the PPU significant noise is detected. By this it is verified that no ground loop was generated due to cabling errors or the like. Figure 3.5 shows the detected noisy signal of the reference thruster.

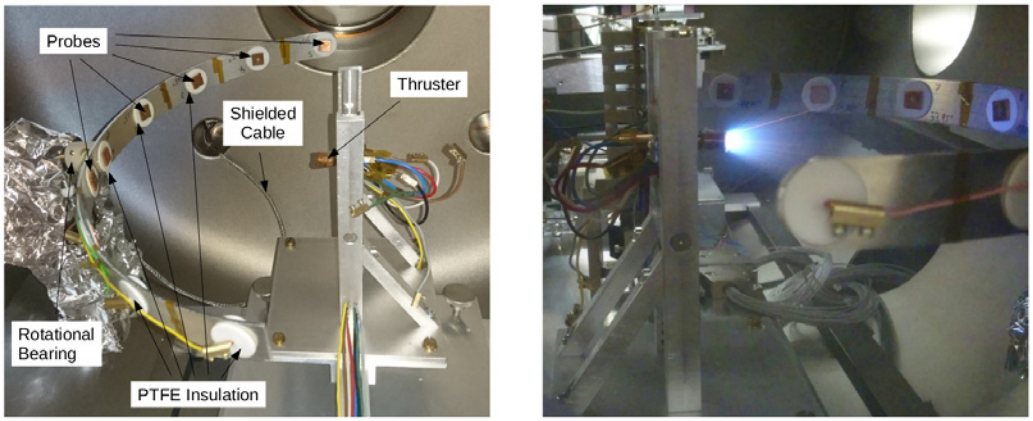

Figure 3.4: Left: An image of the ICDD detection system. The connection cables to the feedthrough are shielded to prevent artifacts by EMI noise. The supporting structure is covered with aluminum foil for the same reason and to prevent a coating of the moving parts. The cables between the structure and the probes are covered by the aluminum arch. Right: Picture taken during thruster operation. The divergence of the plasma beam is clearly visible.

Another important issue is finding the optimal bias voltage. Several effects may influence the results as described e. g. by [Lun 2008]. If the negative voltage is too large ions will be accelerated by the probe array, thus leading to wrong estimations of their velocity. A too low negative voltage on the other hand may fail to prevent electrons which will distort the signal, too. This was tested by measuring the ion velocity for different bias voltages. According to [Anders and Yushkov 2002], the ion velocity can be estimated by the product of drift length s_d (= 150 mm) and the time delay t_d between an arc current maximum and the corresponding maximum of the ion current density signal:

$$u_{Ion} = \frac{s_d}{t_d} \tag{3.3}$$

Unfortunately, very noisy signals may occur depending on the cathode material (macroparticles) and possible contaminations of the affected thruster geometry. Therefore, not all thruster configurations allow a reliable velocity determination. As it turns out, Cu produces very clean signals. Hence, the ion velocity of Cu was measured for several bias voltages. As literature suggested, -70 V are appropriate for the intended ICDD detection [Lun 2008]. However, only a weak acceleration effect was observed (figure 3.6). A significant effect is visible not before -100 V. Possible distortion by secondary electrons generated by the ion impact on the probe surface can also be neglected [Byon and Anders 2003], [Anders et al. 2005], [Lun 2008]. Based on these assumptions it is possible to measure the ICDD of different VAT configurations and to derive a rough estimation for the thrust.

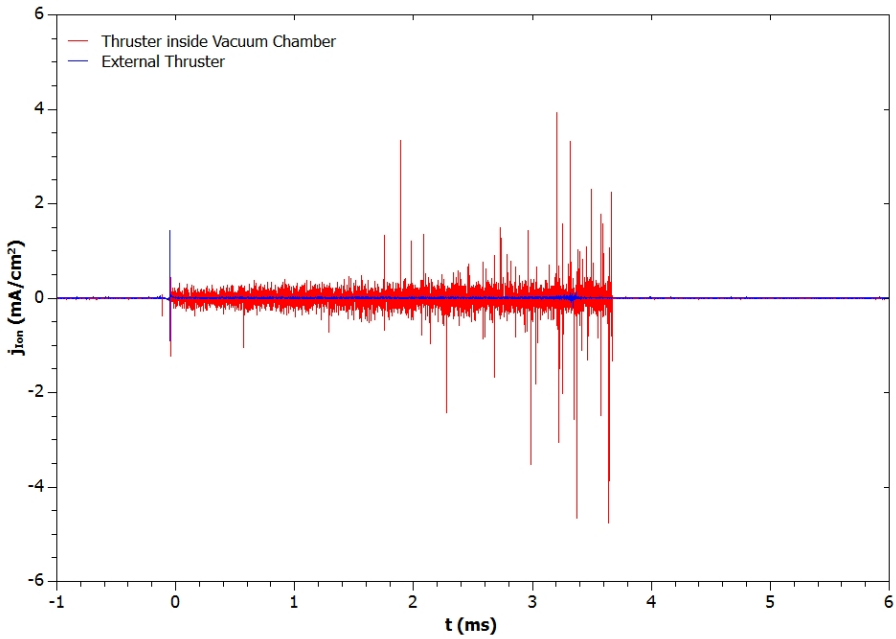

Figure 3.5: Background Signal generated with a thruster out of sight of the probe array. The red signal in the background is produced by a thruster inside the vacuum chamber at a distance of 0.5 m from the probe array. A thruster fired at the outside of the chamber produces almost no interference (blue signal in the front).

3.2.3 Data Analysis

The evaluation of the acquired data has been conducted using Origin 9.1 which allows a fast and precise data processing. Depending on the noise level of the ion current density signals, a reliable filtering algorithm is required. Therefore, a fast Fourier transformation (FFT) analysis was conducted to investigate which frequencies of the signal are actually connected to ion current measurement. With this knowledge, a FFT low pass filter was subsequently applied to the measured signal. An example for this is illustrated in figure 3.7.

The now smoothed signal allows the evaluation of the ion velocity as explained above as well as the investigation of the beam profile by processing the signal of all nine channels. For this the peak ion current density $j_{Ion,max}$ of each channel was determined from the filtered signal. To allow a first comparison with other measurements regarding e. g. chances in the thruster geometry, a Gauss fit has been applied which is simpler than the exponential fit introduced by [Polk et al. 2008] and nevertheless seems accurate enough for the given task [Kutzner and Miller 1989], [Sekerak 2005]. Figure 3.8 shows a typical beam profile produced by a Cu cathode.

The thrust can be calculated with help of the model of [Polk et al. 2008]. Since ion current is measured, the product of ion fraction and arc current $f_{Ion}I_{Arc}$ becomes simply

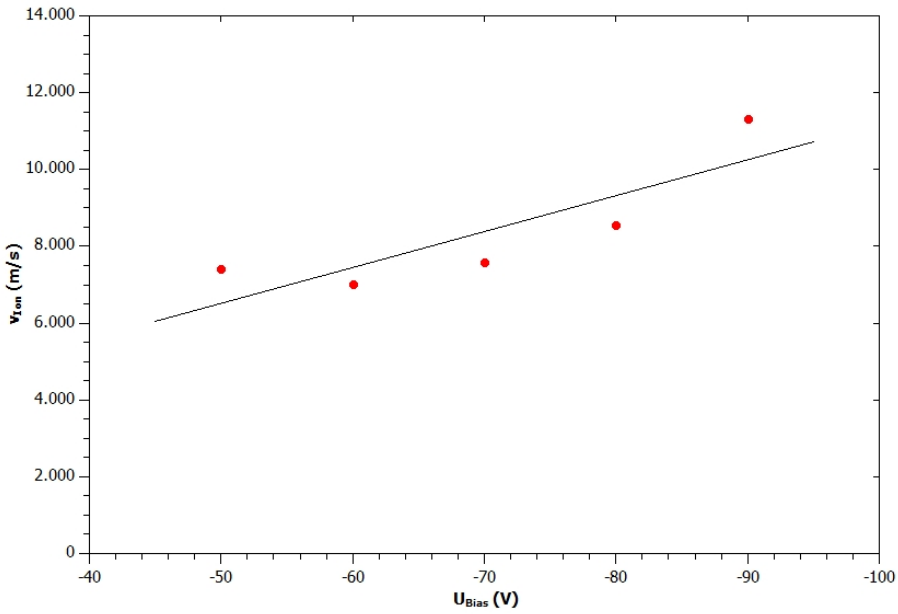

Figure 3.6: Impact of different bias voltages on the ion velocity of a Cu cathode. Between -50 and -90 V no significant change is visible. All ion current measurements described in this work were conducted with a bias voltage of -70 V.

I_{Ion} and the formula from chapter 2 reads as

$$T = \frac{m_{Ion} I_{Ion} u_{Ion}}{e} < Z^{-1} > C_T. \tag{3.4}$$

However, actually an ion current density was measured with a probe of a given surface area thus the ion current I_{Ion} equals the ion current density j_{Ion} divided with a correction factor C_P. The ion current was detected by a surface element of 1 cm^2 of the hemisphere ($r = 15$ cm $\rightarrow A = 2\ \pi r^2 = 1413.72$ cm^2) in front of the thruster and thus only 0.07 % of the actually emitted ion current is covered by one probe. Therefore, the thrust equation is changed to

$$T = \frac{m_{Ion} j_{Ion} u_{Ion}}{e C_P} < Z^{-1} > C_T. \tag{3.5}$$

Moreover, the thrust is not achieved by a continuous emission of ions. Due to pulsed operation it is more convenient to speak of an impulse bit I_{bit}, e. g. μNs. The ion current is therefore replaced by the number of charges collected by the probes per pulse:

$$Q_{Ion} = \int_{t_0}^{t_1} I_{Ion} dt \text{ or } Q_{Ion} = \frac{1}{C_P} \int_{t_0}^{t_1} j_P dt \tag{3.6}$$

The resulting equation for the impulse bit can than be written as

$$I_{bit} = \frac{m_{Ion} Q_{Ion} v_{Ion}}{e C_P} < Z^{-1} > C_T = \frac{m_{Ion} u_{Ion}}{e C_P} \int_0^t j_P dt < Z^{-1} > C_T. \tag{3.7}$$

The ion velocity v_{Ion} was already estimated above and the values for the ion mass m_{Ion} as well as their inverse charge state $< Z^{-1} >$ can be drawn from [Polk et al. 2008]. Thus, a

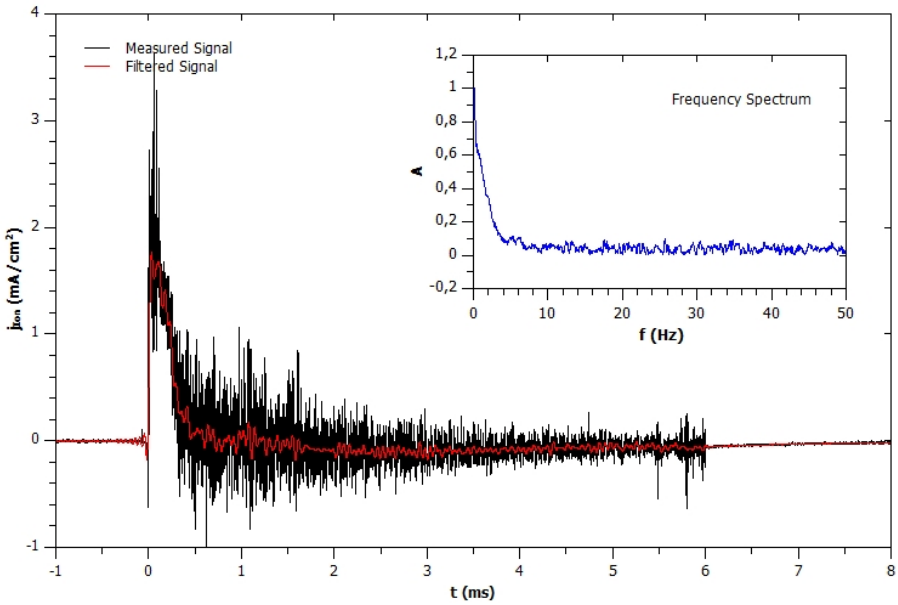

Figure 3.7: The original measurement signal of a Ti cathode is very noisy (black). From the FFT spectrum (blue), a cut off frequency could be derived which then allows the smoothing with a FFT low pass filter (red). The frequency spectrum shows no significant amplitude values above 10 Hz which was therefore chosen as cut off frequency.

qualitative verification of the thrust measured directly with the thrust balance described below is now possible.

3.3 Thrust Measurement

Obviously, the thrust is the most interesting parameter of a propulsion system. Different regions of expected thrust require different measurement methods. For this work very low thrust values of some μN have to be acquired, which is a very challenging measurement range. Various different concepts have been developed for this intention. An early approach for a torsional thrust balance by [Ziemer 2001] at JPL (NASA Jet Propulsion Laboratory) had already a very high precision of 0.1 μN but required a vacuum chamber of 2m diameter. Another possible arrangement is a classic pendulum with or without reference system [Lun 2008], [Luna et al. 2011]. All these approaches were relatively complex. Therefore, [Marhold and Tajmar 2005] developed a much simpler rotational pendulum setup. A second generation version of this kind of thrust balance has been chosen for the measurements within this work.

3.3.1 Mechanical Setup

The used thrust balance was built by the then Austrian Research Centers GmbH (ARC) which merged partially into the Fotec AG in Wiener Neustadt in the meantime. Before-

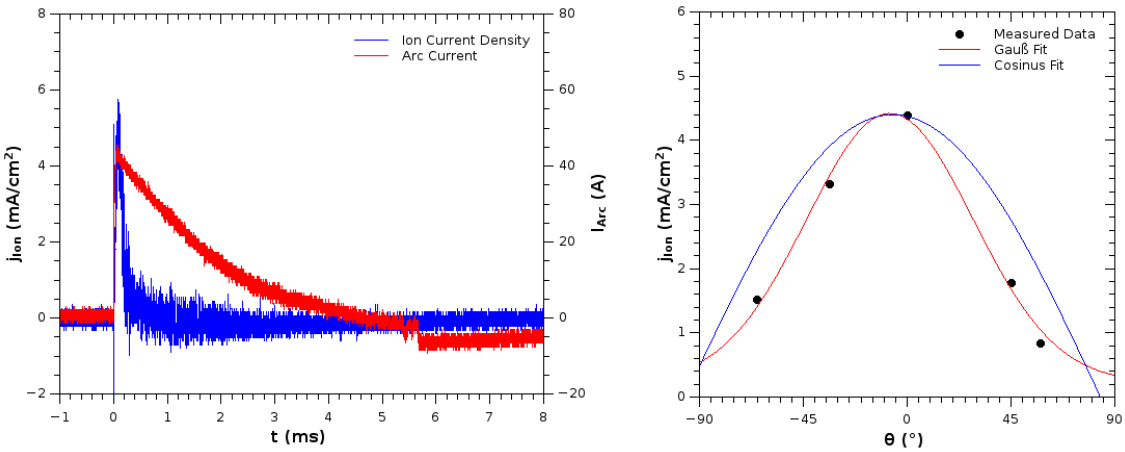

Figure 3.8: Left: Result of an ion current density measurement of a Cu thruster with a cathode diameter of 2 mm and an input voltage of 40 V. Right: Distribution of the peak ion current densities of a Cu thruster measured at different angles at a distance of 150 mm. As literature predicts both a Gauss profile and a Cosinus function can be fitted.

hand, it has to be pointed out that it is not the newest version, since in the last years several improvements had been applied: A liquid metal connection on the rotational axis of the balance which has also been adapted for this work [Seifert et al. 2013], a bluetooth data connection [Bock et al. 2014] and the implementation of an interferometric distance sensor [Hey et al. 2015]. During this work a new impulse response model was developed by[Kramer 2014] which revealed that the original model overestimates the actual thrust. Figure 3.9 shows the modified version of the thrust balance used within this thesis.

The functional principle is very simple: As shown in figure 3.10, the thruster is mounted on one of the two tables (yellow) which are attached to a lever (green). The lever is supported by a central pivot (blue) so it can rotate around the vertical axis. The other table (dark grey) has to be equipped with a counter weight equal to the thruster assembly to avoid additional loads on the pivot and a displacement due to gravitational forces [Seifert 2008]. For the same reason it is necessary to adjust the balance exactly using a water level. The displacement of the lever is measured with an optical sensor (red). A torsional spring inside the central pivot counteracts the deflection of the lever.

The vacuum environment prevents damping by air friction which would otherwise lead to a damping of the oscillations induced by thruster operation. Therefore, below the second table an eddy current brake with a strong Neodym magnet is installed as damping system [Seifert 2008]. By the movement of the table currents are induced which lead to a damping of the oscillations. Since the displacement x is assumed to be very small the small angle approximation $\Theta \approx \frac{180 \cdot x}{r \cdot \pi}$ can be applied (with distance r between the pivot axis and the location of the optical sensor). Then the torque M is given by

$$M = F \cdot r = k \cdot \Theta = \frac{180 \cdot k \cdot x}{r \cdot \pi}. \tag{3.8}$$

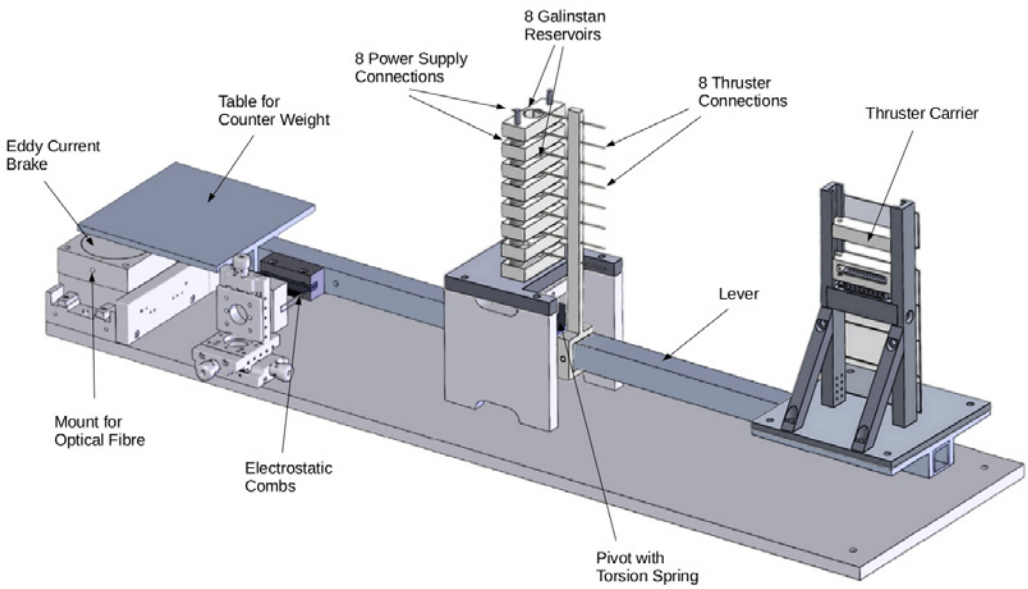

Figure 3.9: Modified ARC thrust balance with liquid metal connection in the rotational center adapted from [Seifert et al. 2013] and thruster mount on the right table. The original layout was taken from the technical documentation of the balance [Seifert 2008].

Hence, the force F applied by the thruster against the spring with the constant k can be calculated with

$$F = \frac{180 \cdot k \cdot x}{r^2 \cdot \pi}. \tag{3.9}$$

For the determination of the thrust delivered per pulse only the displacement x, the lever length $r = 0.32$ m and the spring constant k are necessary. The latter can be derived from the frequency ν of the free oscillation of the system without thruster assembly and counter weight:

$$\nu = \frac{1}{2\pi}\sqrt{\frac{k}{J}} \rightarrow k = (2\pi \cdot f)^2 \cdot J. \tag{3.10}$$

The moment of inertia $J = 5.739 \cdot 10^{-2}$ kgm^2 was determined by the manufacturer from the CAD data of the system [Seifert 2008]. Thus, the spring constant can be calculated to $k = 2.80 \cdot 10^{-3}$ Nm/$^\circ$ and the force of the thruster is only depending on the displacement x:

$$F \approx 3.133 \frac{\mathrm{N}}{\mathrm{m}} \cdot x. \tag{3.11}$$

This force respectively the thrust can be drawn from the software of the manufacturer. However, by reading out the signal of the optical sensor it is also possible to acquire the original displacement signal. A typical measurement of three pulses is illustrated in figure 3.11.

Apart from the use of the natural frequency of the assembly there is a second possibility to calibrate the thrust balance. By the application of a known electrical force to the

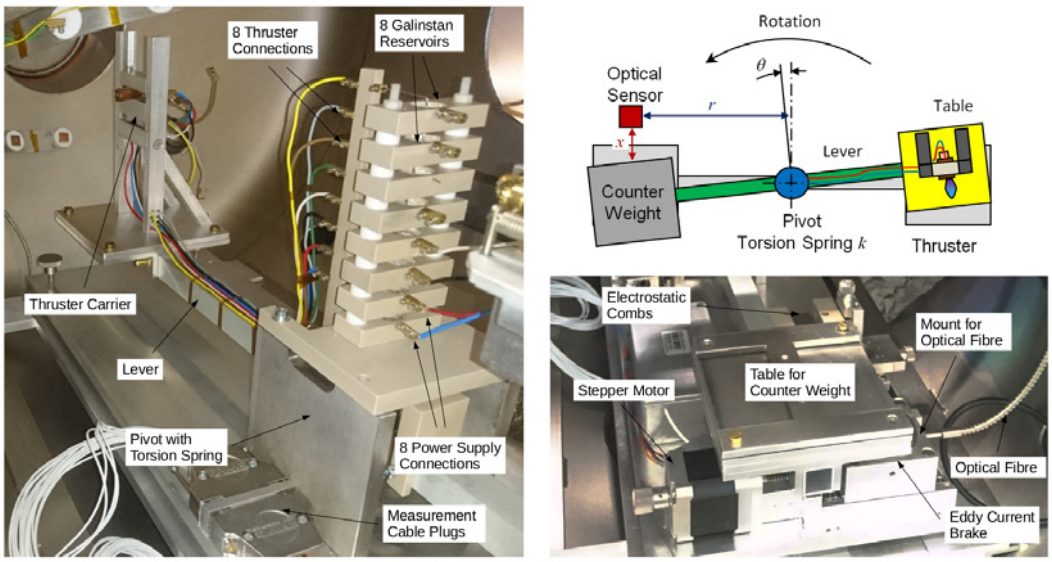

Figure 3.10: Images from the ARC thrust balance inside the vacuum chamber. The functional principle is schematically illustrated on the upper right. The firing of the thruster leads to a rotational movement of the lever around the vertical axis against a torsion spring in the central pivot. From the displacement x measured by an optical sensor the thrust can be calculated.

lever via electrostatical combs (see figure 3.9), a verification of the first method is feasible. For this the software of the manufacturer has a calibration function which is important for the elimination of a possible off-set. The whole assembly and especially the torsion spring underly thermal fluctuations and have therefore to be held in thermal equilibrium after some settling time. The stepper motor, visible on the lower right image in figure 3.10, allows the adjustment of the optical fiber aperture and is also controlled by the manufacturer software.

As already mentioned, an electric connection by wires between the vacuum feedthrough and the thruster leads to an indeterminable change of the spring constant, leaving the whole model worthless. This issue has been addressed by adapting a liquid metal connector directly on the rotation axis introduced by [Seifert et al. 2013]. As it is shown in figures 3.9 and 3.10, eight reservoirs have been mounted on the central frame of the balance. Each reservoir is made of PEEK and is filled with Galinstan, an alloy of Ga, In and Sn (lat. Stannum) which is liquid at room temperature and has an electrical conductivity of $3.46 \cdot 10^6$ S/m [Karcher et al. 2003]. On the left side each reservoir is directly connected to the wires from the feedthrough. The pole mounted on the right side of the pivot is equipped with eight rectangular bent connection pins which dip with their vertical parts into the center of the corresponding reservoir. Each pin is carefully aligned with the vertical axis. The other ends of these pins are then connected to the thruster carrier. Like in the original design, the additional weight on the right lever side has to be balanced by a corresponding counter weight on the left side.

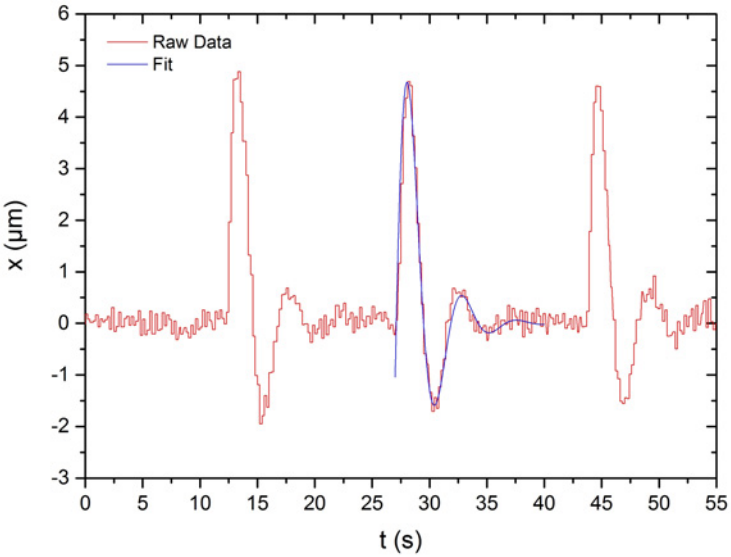

Figure 3.11: Typical measurement signal of three pulses with a Cu cathode acquired from the optical sensor with LABVIEW. The blue fit is determined with the method described by [Kramer 2014]. From that the thrust can be calculated.

As shown in figure 3.12, the tested thruster is mounted to a carrier on the table opposite to the optical measurement setup (see figure 3.10). Limited by the dimensions of this carrier and by the power connections, up to four thrusters of typical CubeSat size may be installed. An easy-to-mount adapter was developed based on a D-Sub connector to allow handling without any wiring work inside the chamber. Instead, all thrusters can be connected as needed outside the chamber. The adapter is then simply be plugged to the carrier on the thrust balance.

Typical D-Sub connectors usually have a current and voltage limit of around 5 A and 500 V AC (RMS) for one minute [NorComp 2005]. However, during VAT operation only very short pulses are generated and the cross section of their pins corresponds to the cross section of the cables ($\sim$ 0.8 mm^2). A comparison to a thruster connected directly with cable to the PPU has shown that the additional resistance by the D-Sub connector can be neglected. For an optimal space usage inside the chamber, this carrier is also used for the ICDD setup which is located directly in front of the thrust balance. Thereby, a simultaneous measurement of thrust and ion current density is possible.

3.3.2 Data Processing

The static model of the manufacturer does not take into account that each thruster setup has an individual momentum of inertia $J = m \cdot r^2$ corresponding to its mass m and its distance r from the pivot [Seifert et al. 2013]. Thus, the frequency ν respectively the natural frequency $\omega_0 = 2\pi \cdot \nu$ of the system is variable. The damping coefficient γ of the system is also neglected. Hence, this model is only valid for the approximation of a static

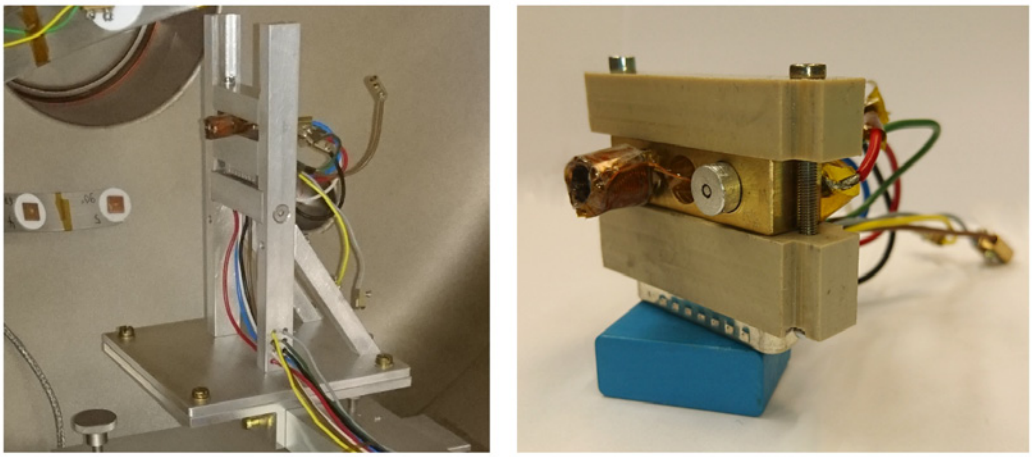

Figure 3.12: Probe carrier developed for a mounting on the ARC thrust balance. The power supply for the thruster(s) is achieved via SUB-D connection.

force F but not for pulsed operation. Therefore, [Kramer 2014] developed a new dynamic model especially for VAT testing which takes these factors into consideration. As it can be seen in figure 3.11, an oscillation with an overshoot in the negative direction occurs after the positive displacement resulting from the thrust pulse. Without the influence of the thruster this behavior can be described as damped harmonic oscillation by the following differential equation:

$$\ddot{x}(t) + \gamma\dot{x}(t) + \omega_0^2 x(t) = 0. \tag{3.12}$$

This system is disturbed by the force applied by the thruster. Since the achieved pulse is very short ($\sim 0.1 - 10$ ms), the force F can be introduced as direct excitation $f = a \cdot \delta(t - t')$ at time t' with the characteristic of a Dirac delta distribution [Kramer 2014]. a determines thereby the magnitude of the applied thrust. The resulting inhomogeneous differential equation is given as

$$\ddot{G}(t - t') + \gamma\dot{G}(t - t') + \omega_0^2 G(t - t') = a \cdot \delta(t - t'). \tag{3.13}$$

Thereby, $G(t - t')$ denotes the Green's function of the differential equation, i. e. its impulse response. The solution of this equation is then [Ziemer 2001]

$$G(t - t') = a \cdot \Theta(t - t') \cdot \exp(-\frac{\gamma(t - t')}{2}) \cdot (\frac{\sin(\omega_1(t - t'))}{\omega_1} \tag{3.14}$$

with $\omega_1 = \sqrt{\omega_0^2 - (\frac{\gamma}{2})^2}$. ω_0^2 and γ are system parameters which should not change during repeated thruster operation. Thus, the thrust balance can be calibrated for the thruster assembly mounted at a time by solving this optimization problem [Kramer 2014]. For the measurement setup used by [Kramer 2014] e. g. a damping constant $\gamma = (1.204 \pm 0.001)$ (rad·s)$^{-1}$ and a natural frequency $\omega_0^2 = (3.835 \pm 0.001)$ (rad $\cdot$ s^2)$^{-1}$ was determined in contrast to 5.593 (rad $\cdot$ s^2)$^{-1}$ given by the manufacturer. An experimental verification

with known masses on the two tables showed that this deviation is owed to the additional mass of the thruster carrier. With these results it is now possible to compute the actual thrust form equation 3.14. A byproduct is a much lower uncertainty compared to the original model (± 0.671 μN vs. ± 3.785 μN) [Kramer 2014].

3.4 High Speed Imaging

For the further investigation of the plasma plume shape and the influence of thruster geometry and external magnetic fields, high speed imaging was applied. As shown earlier it is possible to visualize the movement of the cathode spots by the use of very high frame rates [Kirner 2011], [Pietzka et al. 2011]. However, the interesting phenomena take place within a time interval of 1 μs to 10 ms, which makes it difficult to observe the whole pulse with one parameter set. The high speed imaging system HOBAS (HOchgeschwindigkeits-BildaufnahmeSystem) allows acquisition rates up to 10^6 fps (frames per second) with very short exposure interval in the range of some hundred ns [Kirner 2011]. However, the number of images is limited to ten. This restricts the overall acquisition period, e. g. at 10^5 fps respectively 10 μs between two images only 100 μs will be recorded. In addition, the assembly and adjustment of the whole system is very extensive. However, since the main interest is put on the propagation of the plasma plume over the whole pulse length it was decided to use a commercial high speed camera, which, as shown in the following, provides a sufficient acquisition rate for this goal.
The camera chosen for this intention is a 12 bit pco.dimax HS4 which allows up to 2277 fps at 2000×2000 pixel respectively 46,746 fps at 320×200 pixel and has a minimal exposure time of 1.5 μs [PCO AG 2015]. This camera is mounted outside the vacuum chamber 2 m in front of the thruster. A 5-axis positioning stage allows the precise alignment of the thruster carrier within the limitations of the vacuum viewport. For focusing an objective with a focal length of 100 mm is used [Carl Zeiss AG 2015]. To achieve acquisition rates of around 62,500 fps, a frame of around 280×80 pixel has been chosen. With the help of a mirror setup (see figure 3.13), the lamellar image format allows the mapping of a three side view of the thruster.

By this mirror setup not only the front of the thruster can be acquired but also a side and the top view. This assembly requires a precise adjustment of the four mirrors which has to be carried out during the time where the vacuum chamber is open. The position relative to the camera aperture (x-, y-, z-axis translation, tilting around x-axis and rotation around z-axis) can be conducted during vacuum operation with the 5-axis positioning stage. For this five bellow sealed rotary feedthroughs have been installed to the vacuum chamber. To avoid overexposure a neutral density filter with 3.0 % transmittance ([Edmund Optics Inc. 2015] is positioned in front of the thruster. The filtering value is not important since no quantitative measurements are intended.
The camera uses an internal ring buffer which allows up to 653,411 images at 320×200

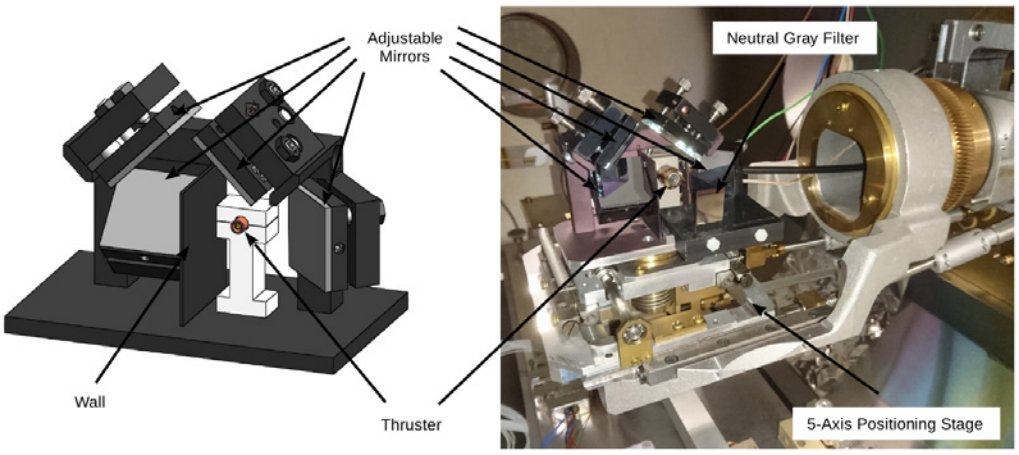

Figure 3.13: Left: Mirror setup used for high speed imaging. This allows the simultaneous acquisition of front, top and side view of the vacuum arc for the investigation of the plume propagation and the cathode spot movement. Right: Mounting of the mirror setup on a 5-axis positioning stage inside the vacuum chamber.

pixel, which is equal to a data volume of 36 GB [PCO AG 2015]. Triggering is achieved with the switching signal of the PPU. As described later, the micro-controller of the PPU generates a 5V-TTL signal which is compatible for the synchronization interface of the pco.dimx HS4. These images are then processed for the investigation of the plasma propagation.

Before the acquisition of real image sequences, several images had been taken with an ordinary digital camera and the life image mode of the high speed camera to proof the working principle and to check the proper adjustment of the mirrors and the thruster within the image frame. Figure 3.14 shows two exemplary recordings. For the further processing a

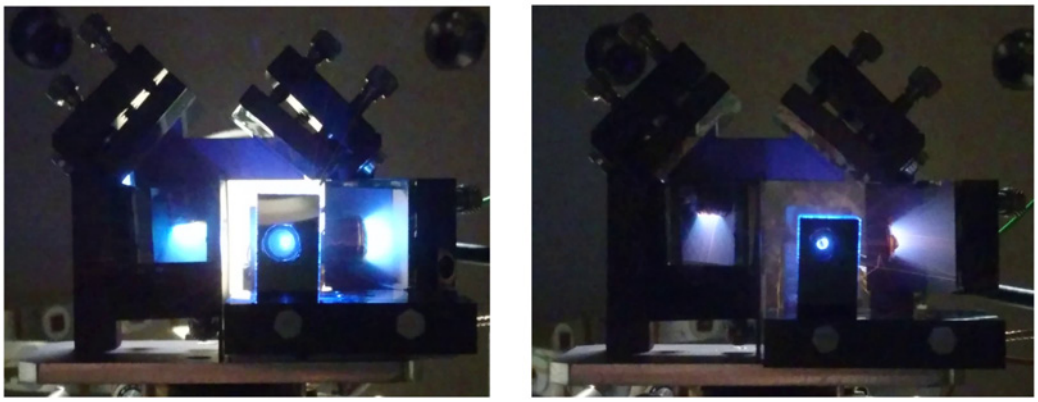

Figure 3.14: Two images of the mirror setup during thruster operation. Both images were taken with an ordinary digital camera for proof of principle.

Delphi program is used which allows the precise filtering of the necessary images from the stored image sequence. With the help of a reference image of the picture it is possible to assign the acquired mirror images to the right position. The program allows also to rotate and to flip the side and top view for right orientation. Since there are only three views of the plasma plume, it is not appropriate to speak of a three-dimensional real-time image acquisition system. But for the qualitative investigation of the plasma plume this approach is sufficient, considering the additional effort for the acquisition of a real 3D-imaging system. An exemplary evaluated image sequence from a Ti thruster is presented in figure 3.15

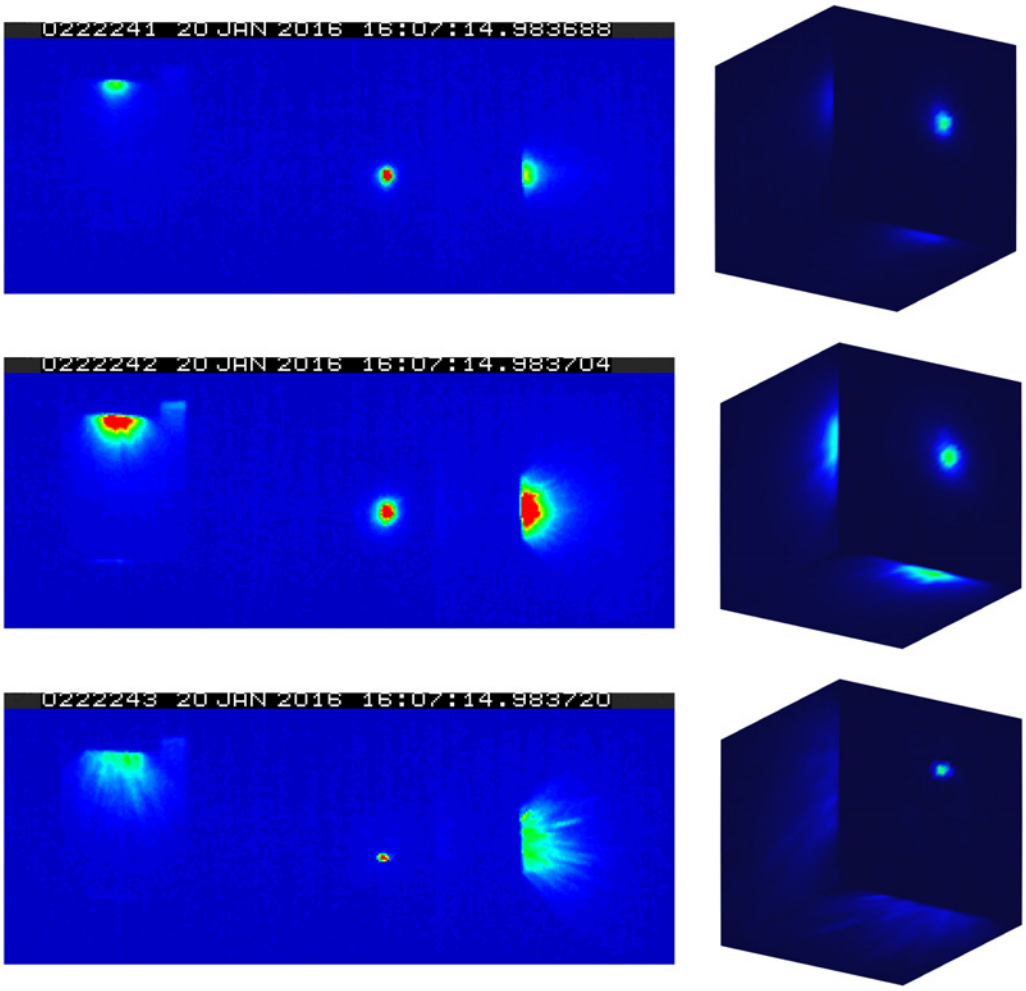

Figure 3.15: Development of a Ti vacuum arc in proximity of the cathode after initiation. In this example a Ti cathode was used which was surrounded by a Neodym ring magnet (see chapter 6). The acquisition speed was 62,500 fps, which gives a difference between each image of 16 μs as it is visible from the last two digits of the time stamp.

3.5 Outlook

Apart from the presented and actually used measurement systems, further methods have been described in literature. For the mechanical measurement of thrust, e. g. [Ziemer 2001], [Marhold and Tajmar 2005] and [Luna et al. 2011] developed different types of thrust balances. [Yushkov et al. 2000], [Lun 2008] and [Zhuang et al. 2012] described methods for the measurement of ion velocity u_{Ion}, ion mass flow $\dot{m}_{Ion}$ and ion current density distribution from which thrust, I_{sp} and plume shape can be determined. Together with the monitoring of the electrical parameters of an EP system a thorough characterization regarding performance and efficiency is possible.
A further method for the characterization of the plasma plume is based on the optical investigation via high speed imaging: Assuming a rotational symmetry of the plasma plume, it should be possible to derive the plasma temperature from the image data. [Bachmann 2013] showed a possible solution for this intention. Thereby, two lateral images of atmospheric Ar arcs typical for Tungsten Inert Gas (TIG) welding have been acquired by high speed imaging. Like in the present case both images had a difference angle of 90°. Between plasma source and camera, two different wavelength filter had been installed which allowed the determination of the plasma temperature by the application of the Saha equation and Abel inversion. Although this method requires a thorough spectroscopic examination for the selection of the right wavelength filter, it may be an interesting option for further research.
Another method came to mind during the characterization of the vacuum system: The operation of the thruster leads to a temporal change of vacuum pressure as illustrated in figure 3.16.

Assuming that at the usual operation level of vacuum of around 10^{-4} Pa a local equilibrium between throughput q_P of the vacuum pump and leakage rate q_L of the vacuum system is reached, i. e. $q_P = q_L$, the ejected cathode material could be seen as additional leakage q_T:

$$q_P - q_L = q_T \tag{3.15}$$

Both q_P and q_L can easily be determined by a thorough characterization of the vacuum system, e. g. [Pietzka 2010]. The number of additional particles ΔN yielded by the thruster is given by the ideal gas law:

$$pV = Nk_BT \rightarrow \Delta N = \frac{\Delta pV}{k_BT}. \tag{3.16}$$

where Δp is the measured pressure change, V the chamber volume (= 243 l), T the room temperature (≈ 300°C) and $k_B = 1.381 \cdot 10^{-23}$ J/K the Boltzmann constant. Assuming further that all ions recombine with electrons before they are detected by the pressure sensor and that within this simple model ions only occur in charge state 1 ΔN could equally be divided into electrons and ions, therefore ΔN_{Ion} and subsequently the mass of

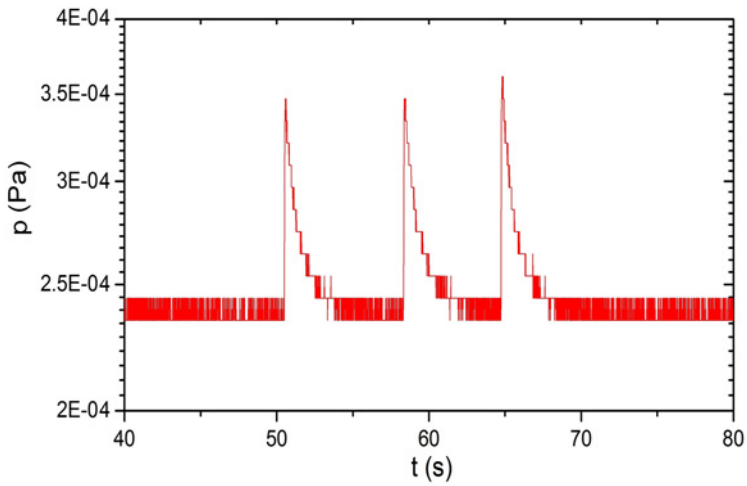

Figure 3.16: Variation of the vacuum pressure during thruster operation. With the help of a thorough characterized vacuum chamber (pumping and leakage rate) and a model of the wall losses, an estimation of the ejected propellant mass may be possible.

all yielded particles could be written as

$$\Delta N_{Ion} = \frac{1}{2}\Delta N \rightarrow \Delta m_{Ion} = \frac{1}{2}\Delta N m_{Ion}. \tag{3.17}$$

Unfortunately, there are some serious inaccuracies with this simple model: Usually there are more charge states for a given cathode material which have to be considered. Moreover, most of the eroded material will never reach the pumps because it is deposited onto the chamber walls. In addition, it is not certain if only cathode material is responsible for the pressure change. Contaminations and oxidation of the surface may lead to a distortion of the measurement. Therefore, a spectroscopic investigation of the plasma plume is necessary. Finally, this model is only applicable for pulsed propulsion systems with a very low thrust. However, a further development of this procedure might be interesting.

Chapter 4

Electric Power Supply

One of the most crucial components of an electric propulsion system is the power processing unit. Like other thruster types, the VAT needs much higher voltages for operation than a satellite can supply without further measures. This chapter starts describing the special requirements and restrictions of the adaption to CubeSats. Subsequently, the generation of the required ignition voltage is described together with possible solutions for energy storage under satellite conditions. The next section focuses on the voltage conversion from satellite bus to power processing unit, the interface components and the operation control system. Concluding this chapter, performance and integration considerations of a PPU for CubeSats will be discussed.

4.1 Requirements and Restrictions

The compact design of CubeSats is limiting the size, mass and available power of any potential electric propulsion system drastically. CubeSats typically use a 3.3 V logic which allows a very energy efficient application of microcontrollers and other electronic parts. Subsystems for communication and navigation as well as pay loads for remote sensing or scientific experiments can therefore be built smaller, lighter and with a lower power demand than with common 12 V components. Although it is possible to generate higher voltages with the solar arrays of a 1U-CubeSat, it is more reasonable to use voltages in the region of 3.5 to 4.5 V. Thus, an efficient yet compact power processing unit (PPU) is necessary.
The restrictions used for the VAT development described in this work were given by the 1U-CubeSat concept for the successor of UWE-3 (Universitaet Wuerzburg Experimentalsatellit 3), where the propulsion system is powered by an unregulated voltage of 3.7 to 4.2 V [Busch and Schilling 2012], [Kronhaus et al. 2013]. A permanent maximum current of 0.5 A can be drawn from the electric power system (EPS). Therefore, the average power is limited to 2 W which is typical for CubeSats of this size. A 3U-CubeSat with similar basic components but consisting of three instead of one unit can provide up to 12 W at the same bus voltage [Park et al. 2015]. Therefore, the PPU should be scalable without

bigger changes for an easy implementation into other CubeSats or other small satellites. Both the limitation of voltage and current are a serious challenge for VAT operation aboard a CubeSat. The voltage needs to be converted to much higher levels since all EP systems described in chapter 1 which could be possibly integrated into CubeSats need voltages in the kV region. Even if the VAT needs the HV only for arc initiation, a highly efficient conversion unit is required between the satellite's EPS and the PPU. In contrast to PPT or FEEP, the VAT only needs a HV peak for the arc initiation, while the following plasma discharge can be sustained at relatively low voltages, i. e. 15 to 32 V depending on the cathode material [Polk et al. 2008]. However, the discharge will only last as long as a sufficient current level can be maintained by the PPU. Hence, it is not only necessary to generate a short HV peak ($\lesssim 1\ \mu$s) for ignition and the required voltage level for the given cathode material, but also a current distribution which allows a sufficiently long discharge. This can be clarified by calculating how many electric charges Q are required for the erosion of enough cathode material for a certain thrust $T = \dot{m}v_e$. Assuming that only ions have a significant contribution to the thrust, the exhaust velocity v_{ex} equals the ion velocity v_{ion}. The total erosion rate or mass flow $\dot{m}_T$ is the product of constant erosion rate E_r of the cathode material and the arc discharge current I_{Arc} [Polk et al. 2008]

$$\dot{m}_T = E_r I_{Arc}. \tag{4.1}$$

For an assumed discharge current of 10 A a mass flow rate of 0.30 mg/s can be calculated for Ti ($E_r = 30\ \mu$g/C, $v_{Ion} = 16{,}700$ m/s). Usually there occur more than one charge state ($\rightarrow F_i = 0.815$ for Ti) and due to the plasma plume profile only about 67 % contribute to the actual thrust ($C_T = 0.67$). Moreover, only around 10 % of the discharge current are converted into ion current ($f_{Ion} = 0.1$). Thus, the thrust is given as

$$T = \dot{m}_T v_{Ion} F_{Ion} f_{Ion} C_T \tag{4.2}$$

or $T = 2.72$ mN for the given example. However, this equation applies only for continuous erosion and thrust production. Therefore, the discharge current has to be constant, which is simply not possible on a CubeSat. As mentioned above, the average power of a 1U-CubeSat is around 2 W whereas in this example a power level of $P = 21.3\ \text{V} \cdot 10\ \text{A} = 213$ W or an average energy of 213 J would be necessary. Therefore, a VAT has to be operated in pulse mode with rectangular or – more realistic – with a more or less triangular current profile, thus it is more adequate to talk of impulse bits ($[I_{bit}] = \mu$Ns) than of thrust. The eroded mass per pulse m_t is then given by the erosion rate E_r and the number of electrical charges Q_{Arc} per pulse:

$$m_T = E_r Q_{Arc} = E_r \int_{t_0}^{t_1} I_{Arc}(t)dt. \tag{4.3}$$

For the exemplary CubeSat mentioned above an average energy of 2 J per second could be assumed. If the conversion to PPU voltage level has an efficiency of 100 % and assuming

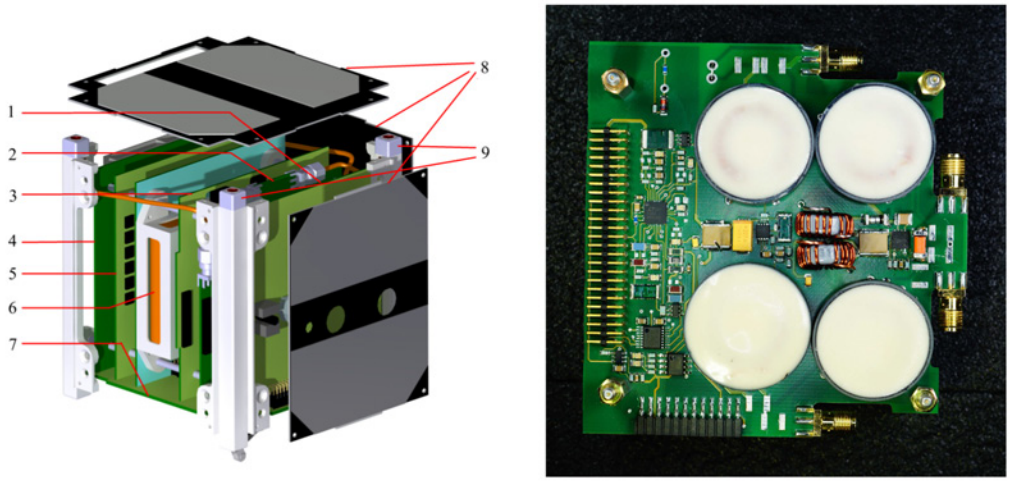

Figure 4.1: Left: The constricted room of the successor to the 1U-CubeSat UWE-3 [Kronhaus et al. 2013]. The PPU is labeled with "2" and the four VATs with "9". Right: PPU prototype especially fabricated for this satellite by Apcon Aerospace & Defense GmbH.

that there is no loss due to the ignition pulse, a possible triangular pulse would have a discharge current of 40 A and a pulse length of around 4.75 ms (U_{Arc} = 21 V for Ti). From this it can be calculated that Q_p = 95 mC. For an erosion rate of 30 μC follows an eroded mass of around 2.85 μg. The corresponding impulse bit for an ion velocity of u_i = 16,700 m/s is then I_{bit} = 2.6 μNs. If the thruster is operated at maximum repetition rate of 1 Hz only 2.6 μN of average thrust could be expected. Of course it is possible to split the average energy per second into several weaker pulses with a higher repetition rate. This assumption gives a rough limit of the possibilities within the limitations of a 1U-CubeSat. In reality, additional penalties have to be taken into account: The conversion from 4 V EPS voltage to minimal operation voltage given by the cathode material is associated with electrical losses, and the production of the breakdown voltage (some hundred V to KV) reduces the actual available pulse energy. Moreover, as it will become clear in the following sections, a higher operation voltage than the theoretical burning voltage of the given cathode material is required to sustain a stable plasma. Therefore, the calculated thrust should be seen as ideal value which is not accessible in reality. The impulse bit can be increased at the expense of the peak repetition rate. A possible solution could be the implementation of an additional storage device like an accumulator. This would allow higher currents for a limited time and therefore higher pulse energies and subsequently higher thrust. However, this implies that the thruster operation time or the number of possible pulses is limited by the battery capacitance. Therefore, an alternating operation scheme has to be applied where a certain interval of thruster operation is interrupted by battery charging.

Figure 4.1 shows the interior of an exemplary CubeSat and a PPU prototype. Apart

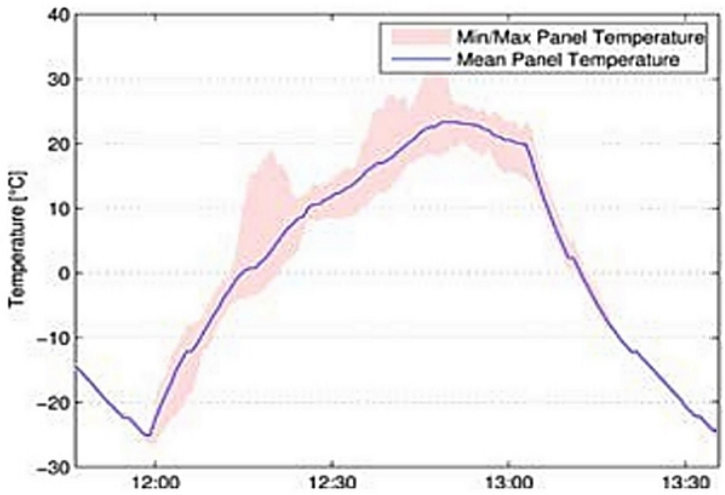

Figure 4.2: Variation of the mean temperature measured on the six side panels of the 1U-CubeSat UWE-3 [Bangert et al. 2014]. The satellite needs around 90 minutes for one orbit in which the temperature changes between -25 and +29°C.

from the electrical restrictions there are also limits in terms of mass and space budget as well as of mechanical and thermal resistance. The design of a 1U-CubeSat like UWE-3 allows the integration of printed circuit boards (PCB) of around 90 x 90 mm side length [Busch and Schilling 2012]. The height of the electric components on the PCB is limited by space which is left after the integration of the other subsystems. Also depending on the CubeSat interior, the mass is more or less massively restricted. The proposed successor for UWE-3 e. g. allows a PCB height of around 15 mm and a total VAT system mass of 200 to 250 g [Kronhaus et al. 2013]. The interface, which means the mechanical parts of the electrical connection as well as the control protocol, may also be determined by the CubeSat developer. A description of the mechanical and thermal requirements which usually have to be respected can be found within the CubeSat Design Specifications and the General Environmental Verification Standard of the NASA [Mehrparvar et al. 2014], [NASA 2013].

Additional information for the boundary conditions can be retrieved from successful CubeSat missions and simulations. Aboard UWE-3 e. g., a temperature variation from -25 to +29°C was measured (see figure 4.2) which could also be expected for future UWE missions [Rathinam et al. 2015].

4.2 Energy Processing

Various PPU types have been used for vacuum arc generation within laboratory constraints: Typically, pulse forming networks (PFN) and power supplies equipped with high voltage capacitors were used. The first approach is a combination of several inductor-capacitor stages which provide pulses with voltages in the kV region and rectangular current pulses

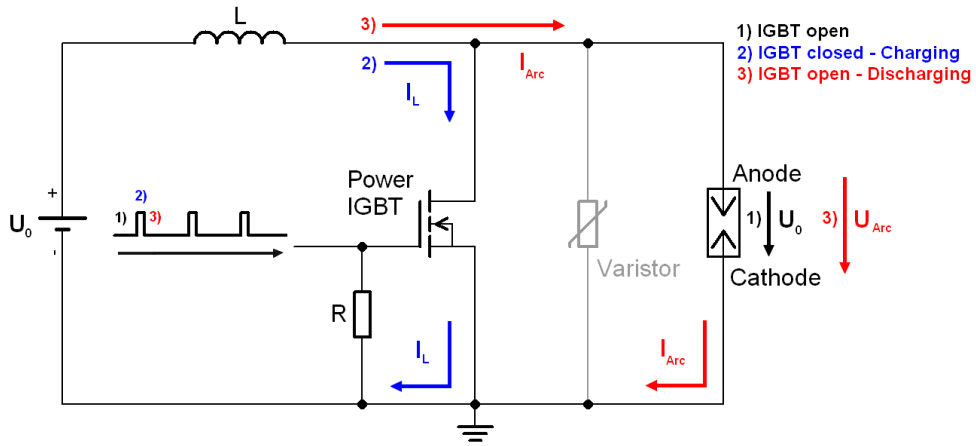

Figure 4.3: Schematic of the initial PPU concept with inductive energy storage by [Schein et al. 2002] where the inductor acts as ignition coil and as energy storage. 1) At an open circuit a potential difference U_0 is measured between anode and cathode. 2) The IGBT is activated and the inductor is charged by the current I_L. 3) The deactivation of the IGBT leads to a voltage pike and subsequently the initiation of a vacuum arc. This discharge is characterized by the arc voltage U_{Arc} and the arc current I_{Arc}.

of some 100 A, e. g. [Yushkov et al. 2000], [Roy et al. 2009]. In the latter system, one capacitor is charged with a voltage up to 1000 V to achieve the breakdown for the initiation of a vacuum arc, which is in the following sustained by the energy of a second capacitor, charged with up to 100 V [Sekerak 2005]. Both types of power supply are relatively space consuming and heavy. Moreover, high input voltages are necessary for the charging of the capacitors which are accordingly large in size. Due to the strict restrictions, both approaches are not suitable for CubeSat integration. Another method to generate a high voltage ignition peak and to supply the arc voltage was therefore developed by [Schein et al. 2002]. Instead of a capacitive energy storage and ignition method, an inductor was used for both tasks. Based on this PPU concept, a further improved system especially for 1U-CubeSats has been developed within this thesis.

4.2.1 Inductive Energy Storage and Ignition

The idea of [Schein et al. 2002] was to minimize the electric components and to improve the efficiency of the PPU. By using an inductor as energy storage (IES), a system with very few parts was developed which in principle is relatively small and very reliable. The only active part is an IGBT (insulated-gate bipolar transistor) as fast acting switch for the charging and discharging of the inductor (see figure 4.3). Initially, when the IGBT is open, the circuit consists of power source and inductor, i. e. only terminated by the VAT. Because of the high resistance between anode and cathode no current can flow. Thus, a potential difference equal to the input voltage can be measured between the electrodes. When the IGBT is activated by the gate driver, a current runs through the inductor which

increases with [Horowitz and Hill 1989]

$$I_L(t) = I_0 \left(1 - e^{-\frac{t}{\tau}}\right) = \frac{U_0}{R_L} \left(1 - e^{-\frac{tR_L}{L}}\right). \tag{4.4}$$

Accordingly the voltage in the circuit changes with

$$U_L(t) = U_0 e^{-\frac{t}{\tau}} = U_0 e^{-\frac{tR_L}{L}}. \tag{4.5}$$

Depending on the current I at the moment when the IGBT is deactivated again and the inductance L of the coil, the energy is given by

$$W = \frac{1}{2} L I^2 \tag{4.6}$$

This energy can be discharged over a load parallel to the now open IGBT. Starting with the maximum current which was accumulated during charging the current during **discharging** develops like

$$I_L(t) = I_0 e^{-\frac{t}{\tau}} = \frac{U_0}{R_L} e^{-\frac{tR_L}{L}}. \tag{4.7}$$

For corresponding voltage follows

$$U_L(t) = -U_0 e^{-\frac{t}{\tau}} = -U_0 e^{-\frac{tR_L}{L}}. \tag{4.8}$$

The energy stored in this circuit depends on the inductivity L. Thus, in reality there are some limitations of this process: L depends on the core material, the number of windings and the geometry of the coil [Plonus 1978]. Without special core materials, a high inductance usually leads to a big coil as illustrated in 4.4. In addition, every core material has a given saturation current at which the inductance decreases sharply [Plonus 1978]. As with high inductances the saturation current depends on volume and material of the coil. Another disadvantage are the high magnetic fields which are generated by the currents running through the coil. They can be a serious issue for surrounding subsystems in terms of EMI. In case of a disrupted discharge the stored field energy has to be released somewhere. Without any mechanical freedom this can only be achieved by heating up the coil, which may lead to a melting of the insulation material and a subsequent shortcut inside the coil.

Alternatively, an air coil can be used which does not saturate [Plonus 1978], although the resulting inductor has more windings than a coil with ferrite core and is therefore much bigger. On the other hand, a powerful laboratory supply is necessary to provide the required currents. If e. g. a current of 10 A needs to be supplied, an energy of 10 mJ can be stored within an inductance of 200 μH. A coil with that parameters is already too big and heavy for CubeSat application. Even at an inductance of 2 mH, only 100 mJ could be achieved. As shown in the example above, an energy of around 2 J is necessary for an impulse bit of 2.6 μNs. Moreover, the conversion from around 4 V to 40 V e. g. would result in a reduction of the effective current from 0.5 A to 50 mA. The resulting charging

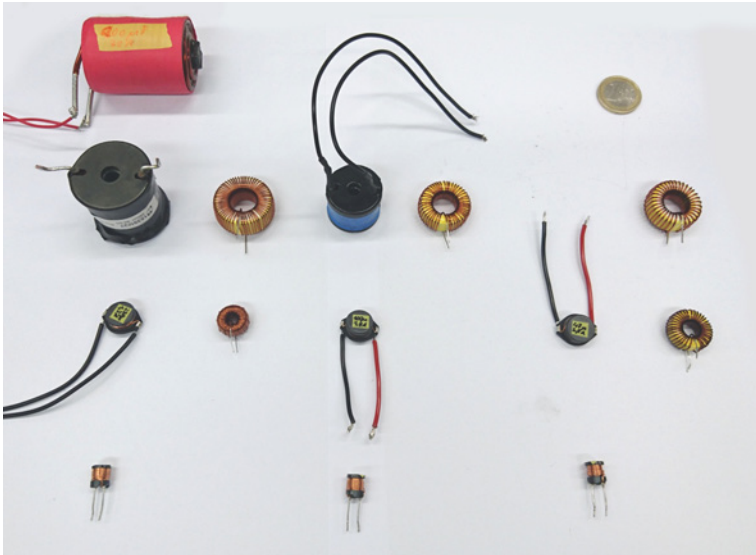

Figure 4.4: Selection of the inductors used for the PPU development. The dimensions of the coil are defined by the inductance and the saturation current. Both are depending on the number of wire windings, wire diameter and core material.

time permits reasonable repetition rates. Therefore, at the given conditions a pure IES is no option for a CubeSat PPU. Figure 4.5 shows a typical IES discharge with a pulse energy of approximately 50 mJ. A 500 μH coil with a saturation current of 15 A was used there.

However, the coil was initially not only intended as energy storage but also as source for the ignition voltage. Similar to the ignition coil in the control circuit of a spark plug, an inductor can be used to increase voltages for a very short period of time. If a charged inductance is switched off, a voltage peak occurs [Brown 2008]:

$$U(t) = L\frac{dI(t)}{dt} \tag{4.9}$$

The height of this peak depends on the inductance L and the temporal variation of the current $dI(t)/dt$ which is theoretically limited by the switching speed of the IGBT. Unfortunately, the switching and the relatively high power loads on the IGBT lead to thermal stress and aging inside the assembly [Lebeda 2015]. Therefore, the switching speed is a very uncertain parameter. In any case, with sufficiently high inductance and current, voltage peaks up to several kV can be generated. Although it is not possible to generate sufficient pulse energies under the given limitations, this very simply and reliable ignition concept is essential for the further PPU development.

Figure 4.6 shows an early laboratory prototype based on the concept of [Schein et al. 2002]. This IES PPU was additionally equipped with a capacitor which stabilizes the input voltage and acts as further energy storage. Similar enhanced PPUs have already been used in literature, e. g. [Sekerak 2005].

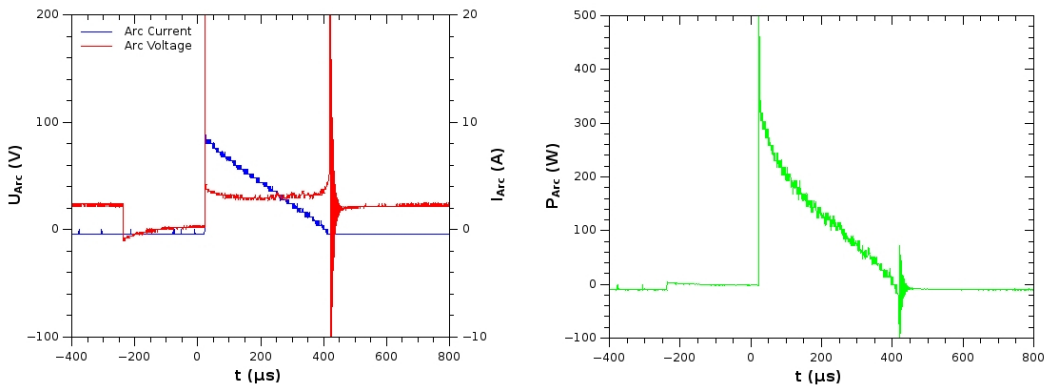

Figure 4.5: Electrical parameters for a typical discharge of a Cu cathode achieved with an reverse engineered PPU based on the concept of [Schein et al. 2001]. The inductor was charged for 250 μs at an input voltage of 24 V.

4.2.2 Capacitive Energy Storage

Classic vacuum arc experiments are often operated with pure capacitive energy storage (CES) systems which convert the voltage from the laboratory power supply to the required levels. This is usually achieved by charging one capacitor with a relatively low capacitance (some μF) to a voltage sufficiently high for arc initiation (around 1 kV). After ignition, a larger capacitor (some mF) charged with a lower voltage (100 – 200 V) takes over to maintain the arc plasma. The energy stored within a capacitor is given by [Horowitz and Hill 1989]

$$W = \frac{1}{2}CU^2 \tag{4.10}$$

Usually, around 20 to 30 V are used for typical VAT concepts [Schein et al. 2001]. As shown below, a typical capacitor of 4.7 mF and a working voltage of 63 V is approximately as big as the 200 μH inductor mentioned above but has only a mass of about 10 g. The energy content for an input voltage of 20 V is then 940 mJ, compared to the 10 mJ of the exemplary inductor above. Therefore, much higher energies can be applied to the VAT by using a capacitor of CubeSat conform dimensions as main energy storage, albeit long charging times have to be accepted. The time constant is defined by the capacitance and the resistance. If the current is limited by the power supply, the **charging** up to the maximum voltage at a given capacitance takes longer, following

$$U_c(t) = U_0\left(1 - e^{-\frac{t}{\tau}}\right) = U_0\left(1 - e^{-\frac{t}{R_C C}}\right). \tag{4.11}$$

Accordingly the current progression during charging is given by

$$I_c(t) = \frac{U_0}{R_C}e^{-\frac{t}{\tau}} = I_0 e^{-\frac{t}{R_C C}}, \tag{4.12}$$

This limits the pulse repetition rate drastically on a CubeSat. As explained above, the current limit lies after conversion to 40 V at around 50 mA, assuming that the conversion

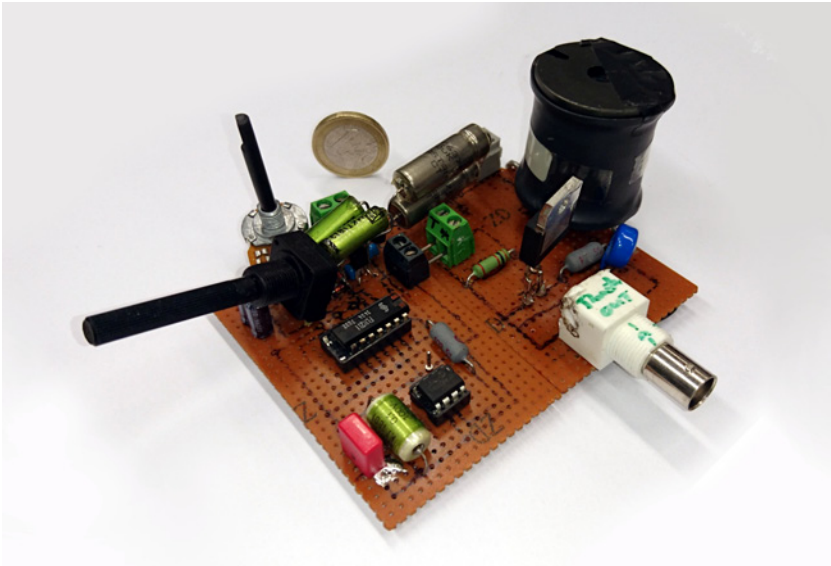

Figure 4.6: Early laboratory PPU prototype with a 220 μH / 9 A inductor and two 430 μF capacitors as energy storage. The two potentiometers allow the adjustment of inductor charging time and pulse repetition. The corresponding TTL signal is produced by a Schmitt trigger. For the amplification to 15 V, which is required by the IGBT, a TC1427 driver is used.

was ideally without loss. If the arc was initiated, the stored energy can be discharged with the vacuum arc plasma as load. Starting with a voltage U_0 the **discharging** can be expressed as

$$U_c(t) = U_0 e^{-\frac{t}{\tau}} = U_0 e^{-\frac{t}{R_C C}}. \tag{4.13}$$

The corresponding current progression is given by

$$I_c(t) = -\frac{U_0}{R_C} e^{-\frac{t}{\tau}} = -I_0 e^{-\frac{t}{R_C C}}. \tag{4.14}$$

Therefore, the discharge time constant $\tau = R \cdot C$ is depending on the resistance R of the circuit. The value of the capacitance and the applied voltage determine the electric charge Q of the pulse:

$$Q = CU. \tag{4.15}$$

Thus, by increasing voltage and capacitance the erosion rate and therefore the thrust can be raised. In contrast to an inductance where a switching to a load leads to a voltage peak, a capacitor drives a current when a shortcut occurs:

$$I(t) = \frac{dU(t)}{dt}. \tag{4.16}$$

Thus depending on the resistance of the arc circuit which influences the voltage variation with time $dU(t)/dt$ currents up to some hundred A can be driven. However, a large voltage leads to a lower efficiency, i. e. a lower current, since the EPS voltage has to be converted. The efficiency of typical conversion methods drops rapidly with higher amplification factors

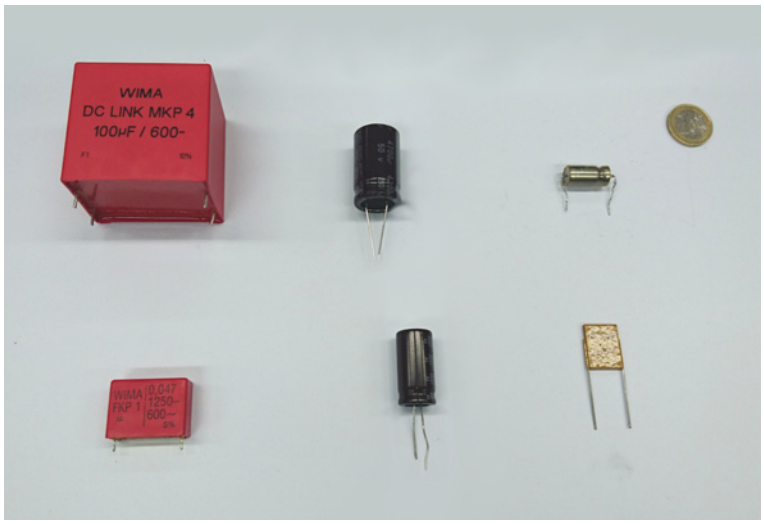

Figure 4.7: Capacitors of varying type with different capacitance and operation voltages. Foil capacitors are relatively big compared to electrolyte capacitors but can stand higher voltages and are bipolar.

($>$ 9 [Lebeda 2013]). This rules out the use of an ignition capacitor which would need a voltage in the kV region. A feasible alternative is the inductive ignition explained in the last subsection.

The use of a capacitor simply as storage device is limited by the dimensions, since space is very restricted within a CubeSat. The important factors hereby are the capacitance and the maximum voltage. According to NASA guidelines a voltage derating of 60% has to be respected [Sahu et al. 2008]. This means if a voltage of 40 V is needed, the capacitor has to stand at least 67 V. In principal this is no issue for an electrolyte capacitor, for which a large number of variable sizes are purchasable. Ceramic and film capacitors on the other hand can be ruled out. Ceramic capacitors are only available up to around 10 μF and film capacitors are very big at higher capacitances as can be seen in figure 4.7, although they have very high voltage limits.

A big advantage is the bipolarity of such capacitors. Depending on L and C (see figure 4.8), an oscillation may occur when the discharge expires, thereby interrupting the circuit. Similar to the deactivation of the IGBT, a voltage peak is generated from the remaining energy in the inductor. This energy is not sufficient to achieve a further discharge and again a disruption occurs. This process will be repeated as long as energy can be supplied by the inductor, which is further charged by the capacitor. Thus, a damped oscillation results with undershoots that can destroy the gate-emitter path of the IGBT and therefore lead to a permanent shortcut. This can be avoided if the capacitor works in both directions. Otherwise, the IGBT has to take the full negative voltage.

Since there are no bipolar capacitors which are applicable in terms of size and mass, a protection diode parallel to the unipolar capacitor is necessary. So, currently only electrolytic

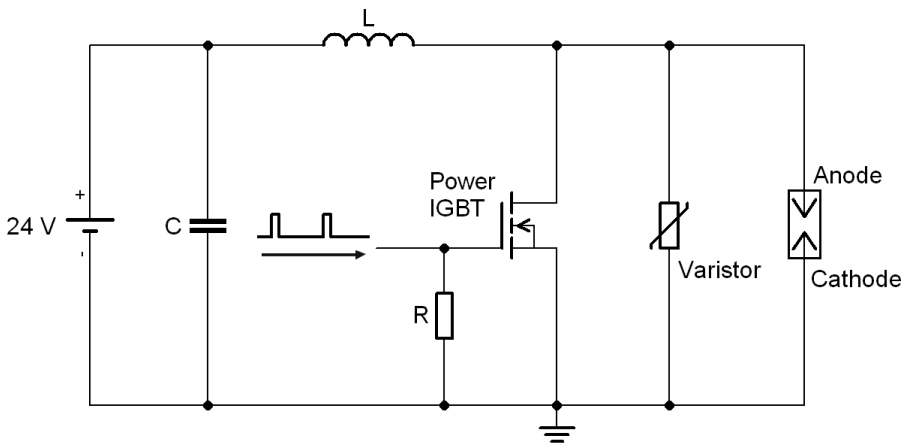

Figure 4.8: Schematic of the initial PPU concept with an additional capacitive energy storage. Thus, a very small inductor can be implemented which is used as ignition coil only. The capacitor and the inductor form a *L*-*C* circuit as long as the arc is maintained. Due to the resistance of the real circuit no oscillation occurs.

capacitors can be used because of their compact size. However, ordinary off-the-shelf capacitors have a serious out-gassing rate [Walter and Scialdone 1997]. Therefore, NASA and ESA only allow special electrolytic capacitors of Ta. To cope with these restrictions for the further development, Ta capacitors were used which are bigger than the corresponding Al capacitors but still fit into the scope of the CubeSat limitations. Figure 4.9 shows a laboratory prototype where all these considerations have been taken into account. Moreover, this PPU is already partially equipped with some auxiliary systems which will be described in the following section.

A further important advantage compared to the initial concept is the fact that the inductor is only needed for ignition and not anymore as storage device. Therefore, a smaller inductance is possible which is also an important asset in terms of a lower size, mass and circuit impedance. A detailed discussion of the PPU performance with all improvements as described in the next sections will be given at the end of this chapter. Yet the voltage conversion from satellite EPS to PPU, the process control and solutions for temporally higher pulse energies have to be integrated.

4.3 Auxiliary Systems

The integration of an additional unit into an already existing satellite raises several questions. Apart from the geometric compatibility, the main issues are the use of suitable interface components as well as a common communication protocol for operational information interchange and commands. Most of all, it is essential that none of the other subsystems of the CubeSat will be affected by EMI. This implies some though challenges, especially for a propulsion system which generally operates with high voltages and/or cur-

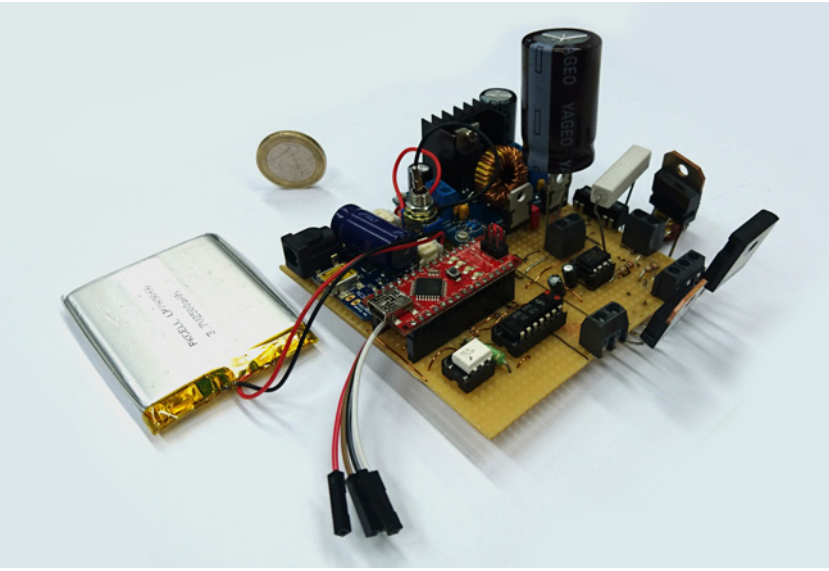

Figure 4.9: Final laboratory PPU prototype, equipped with an Arduino microcontroller and a Li-Po battery as additional energy storage. Note the bigger capacitor with 4700 μH and the very small ring inductor with 47 μH / 3 A hidden behind the IGBT. The whole assembly including battery has a mass of 200 g which can be reduced drastically by the use of optimized components.

rents. In case of the VAT pulsed operation and HV peaks are an additional issue.
As it was shown earlier, the EPS voltage of CubeSats lies in the region of 4 V while the optimal operating voltage of the PPU is in the range of 30 to 50 V. The voltage for the control of suitable IGBTs and MOSFETs on the other hand requires gate voltages from 12 to 16 V. Therefore, a highly efficient voltage conversion unit is necessary. The reliability and efficiency of VAT operation can be controlled by monitoring the electrical parameters of the PPU. These data are evaluated by a microcontroller, which controls the whole system of PPU and VAT.

4.3.1 CubeSat Interface

The connection to the satellite bus will be described by using the proposed successor of the 1U-CubeSat UWE-3 as an example. For the integration on other CubeSats, changes in hardware and software will possibly be necessary. The implementation of various subsystems and the need for a standardized interface lead to a complex connector layout. As figure 4.10 shows, up to 50 pins can be used for information and power transfer. For the control and power supply of the UWE-3 PPU, the following signals were designated initially:

- GND_SYS: System ground of the satellite
- VCC_3V3: Supply voltage for the microcontroller, 3.3 V
- V_UNREG_SW: Direct unregulated EPS voltage, 3.6 – 4.2 V

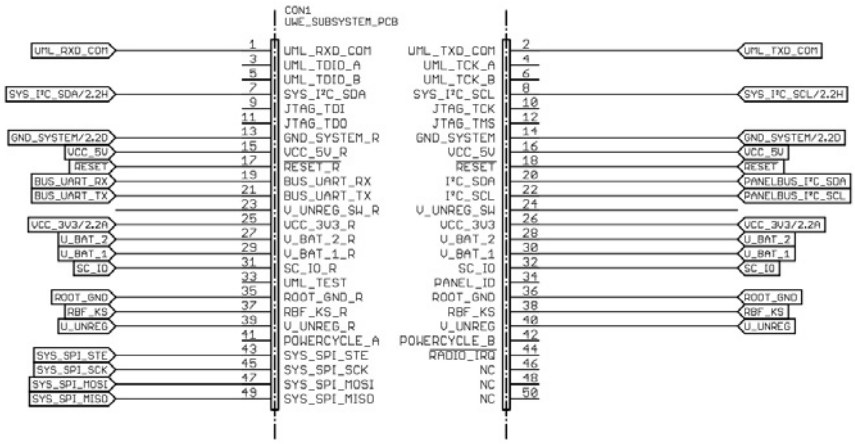

Figure 4.10: Schematic of the standardized interface between the UWE satellite bus and subsystems [Ziegler 2012]. For the supply and control of the PPU only GND_SYS, V_UNREG_SW $\overline{\text{RESET}}$, PANELBUS_I2C_SDA and PANELBUS_IC_SDL are used.

- $\overline{\text{RESET}}$: External reset for the microcontroller
- PANELBUS_I2C_SDA: Serial data connection for I^2C communication
- PANELBUS_IC_SDL: Serial clock connection for I^2C communication

As will be shown below in subsection 4.3.3, it was decided not to use VCC_3V3 which has a current limit of 100 mA. Instead, V_UNREG_SW is used for all PPU systems since peak voltages up to 4 A are allowed. To ensure that enough voltage is supplied and that no overvoltage and overcurrent damages occur, a dual hot swap controller (DHSC) is provided, using the basic layout specification for UWE-3 subsystem PCBs [Ziegler 2012]. The basic configuration of the controller block of the hereby used LTC4222UH is illustrated in figure 4.11.

A comprehensive description of the electrical dimensioning of the hot swap circuit for the PPU can be found in [Kramer 2014]. The resulting circuit design for the controlled connection to the unregulated EPS voltage is illustrated in figure 4.12.

For an additional protection of sensitive components like the microcontroller, corresponding lines are galvanically separated by opto-couplers. To avoid the creation of parasitic magnetic fields due to high currents, all power lines are split into several layers on the PCB prototypes. Possibly necessary further EMI measures have to be implemented in the final PPU.

For activation and control of thruster operation I^2C communication is used. Both the DHSC and the microcontroller are connected to PANELBUS_I2C_SDA and PANELBUS_IC_SDL. Via these signal connectors, the microcontroller receives the input commands for starting or ceasing thruster operation as well as information in which regime the thruster has to be operated, i. e. high thrust at low repetition rate or vice versa (of course a low thrust at low repetition rate is also possible).

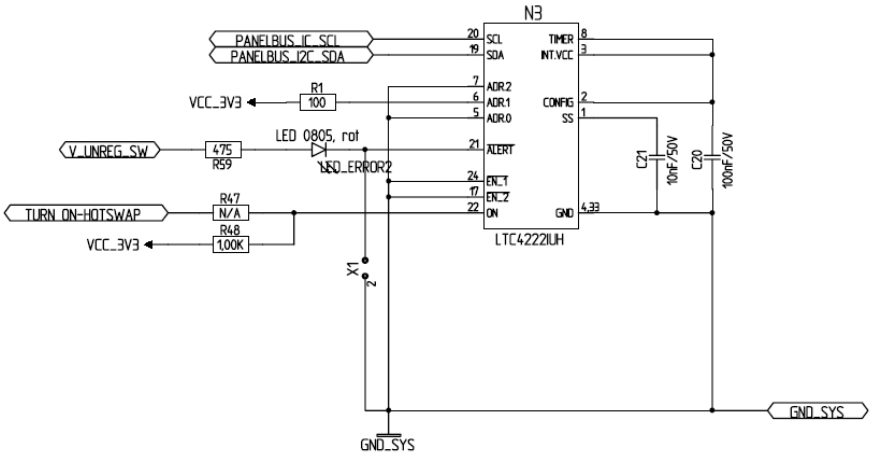

Figure 4.11: Schematic of the controller block of the dual hot swap controller LTC4222UH which is essential for UWE subsystems [Kramer 2014]. This controller allows the activation and deactivation of the PPU. Moreover, is is used as protection circuit in case of overvoltages or overcurrents.

4.3.2 Operating Voltage Conversion

Since the exemplary satellite can only provide around 4 V as PPU input voltage, a conversion to the required operation voltage is necessary which depends on the characteristic arc voltage of the given cathode material [Polk et al. 2008]. Higher voltages are recommended for a stable discharge, as it turned out as a result during PPU development since longer pulses and a higher pulse energy can be reached if a sufficiently large capacitor is used. Thus, an efficient voltage conversion is necessary. A simple yet reliable system is a boost converter [Brown 2008], [Tietze et al. 2008]. For the CubeSat PPU described here, a LM3488QMM switching controller has been chosen as core of the boost converter. The corresponding circuit for the conversion from the unregulated input voltage up to a maximum operation voltage of 50 V is shown in figure 4.13.

Five MOSFETs allow the microcontroller to switch between five operation voltages. This limits the possible number of different operation voltages but lowers the number of components and mass. On the other hand, a control voltage of 15 V is necessary for the microcontroller and the driver of the MOSFET which controls the ignition process. This MOSFET replaces the IGBT that was originally used for this task because of a lower current demand. As the circuit layout in figure 4.14 shows, the current is limited to 100 mA as additional protection of the sensitive parts.

The boost converters enable a relatively simple PPU with a very high efficiency, albeit it might be necessary to achieve higher pulse energies for certain position control maneuvers. Moreover, it may be necessary to maintain operation during eclipse periods. A CubeSat like UWE-3 in a circular LEO of around 600 km altitude needs around 90 minutes to circle once around Earth [Bangert et al. 2014]. The satellite spends half of this time within Earth's shadow. The solar arrays cannot provide energy within this so called

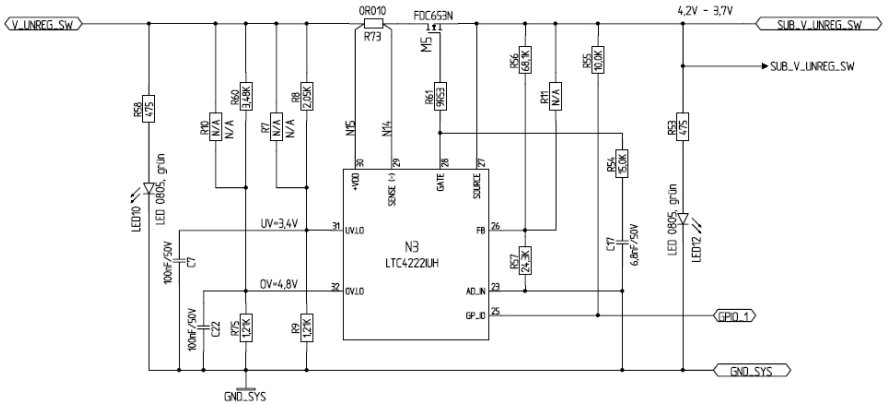

Figure 4.12: Schematic of the hot swap circuit of the UWE-4 PPU. The input voltage is the unregulated EPS voltage of the example satellite ranging from 3.7 to 4.2 V.

eclipse period. CubeSats are typical equipped with batteries to bypass this time, e. g. [Kronhaus et al. 2013]. As shown below, this solution can also be implemented into the PPU subsystem.

4.3.3 Process Control

For operation control it is necessary to monitor various parameters. In laboratory conditions it is no issue to monitor arc voltage, discharge current, thrust, ion current density, plume shape and so on. Aboard a very small satellite the selection of control parameters is very limited due to mass and space restrictions. Therefore, the PPU and VAT monitoring is reduced to EPS input voltage and current, CES charging voltage and a temperature sensor in the satellite structure near the thruster nozzle. The input parameters are directly monitored by the DHSC which will cease operation in case of deviations from the allowed range (3.6 – 4.2 V, 1 A).

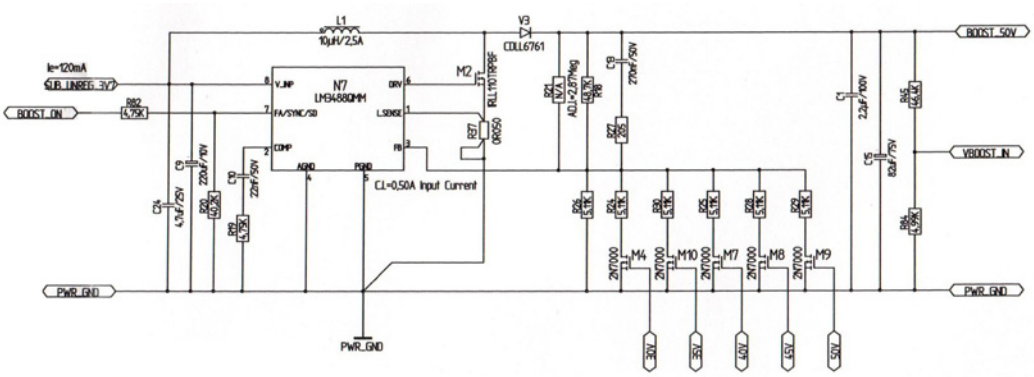

Figure 4.13: Schematic of the boost converter for an output voltage range of 30 to 50 V. The five MOSFETs on the lower right allow a change of the output voltage in steps of 5 V.

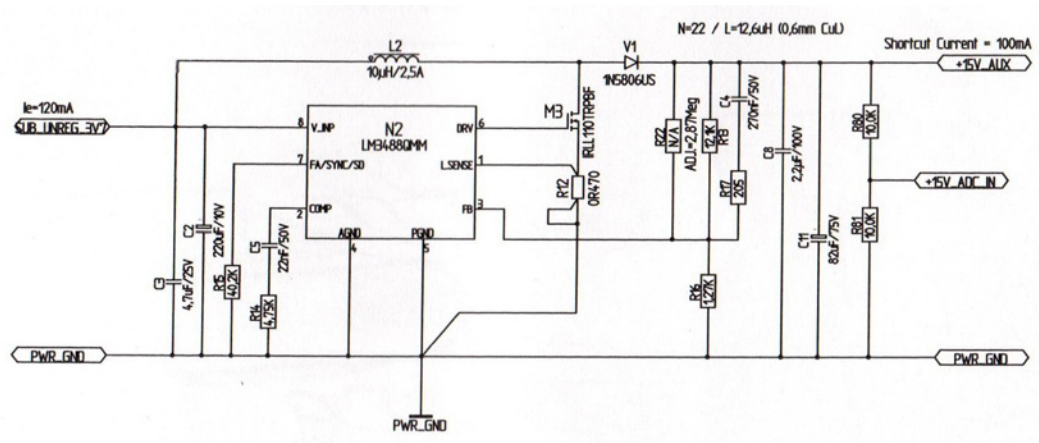

Figure 4.14: Schematic of the boost converter for n output voltage range of 15 V. This voltage level is required for the operation of the MOSFET driver and the microcontroller.

The output voltage from the boost converter which equates to the charging voltage of the capacitor provides a sufficient information about the functionality of the thruster. If the capacitor is not discharged to a voltage level corresponding to the arc voltage of the cathode material, a malfunction has occurred. A reason for this may be the consumption of the cathode. As described in chapter 2, the distance between anode and cathode is increased by this, which results in higher breakdown voltages. When the PPU cannot provide the necessary voltage anymore, no further arc can be initiated. The microcontroller should react by feeding of the cathode material, which will be described later in detail. If the capacitor voltage drops to zero, a welding of anode and cathode has occurred, which ultimately ceases thruster operation. In this case, the DHSC will also disconnect the system from the EPS interface because of a too high current demand.

Data collection and processing as well as process control will be achieved by an Arduino Nano microcontroller. Figure 4.15 shows the schematic of the Arduino Nano. The central component is an ATMEGA328 8-bit microcontroller which can be supplied directly by an input voltage of 3.3 V. However, within this operation scheme no current protection is implemented. The surrounding layout of the Arduino on the other had is equipped with a voltage converter with current protection circuit, which provides an input voltage of up to 16 V. Since 15 V are necessary for the ignition MOSFET, it was decided to use only the V_UNREG_SW for the power supply of the whole subsystem.

Figure 4.16 shows the implementation of the Arduino Nano as PPU microcontroller. The arc initiation is achieved by a TTL signal to the ignition circuit described in subsection 4.2.1. Usual charging periods for the inductor are below 100 μs, while the charging of the capacitor has a duration of one to ten seconds, corresponding to the desired pulse energy. The switching between more than one VAT is achieved by MOSFETs with so called "high side drivers" which allow safely to connect or separate each thruster with the PPU output. Due to the high voltage peaks for ignition and the high currents, this side of the PPU

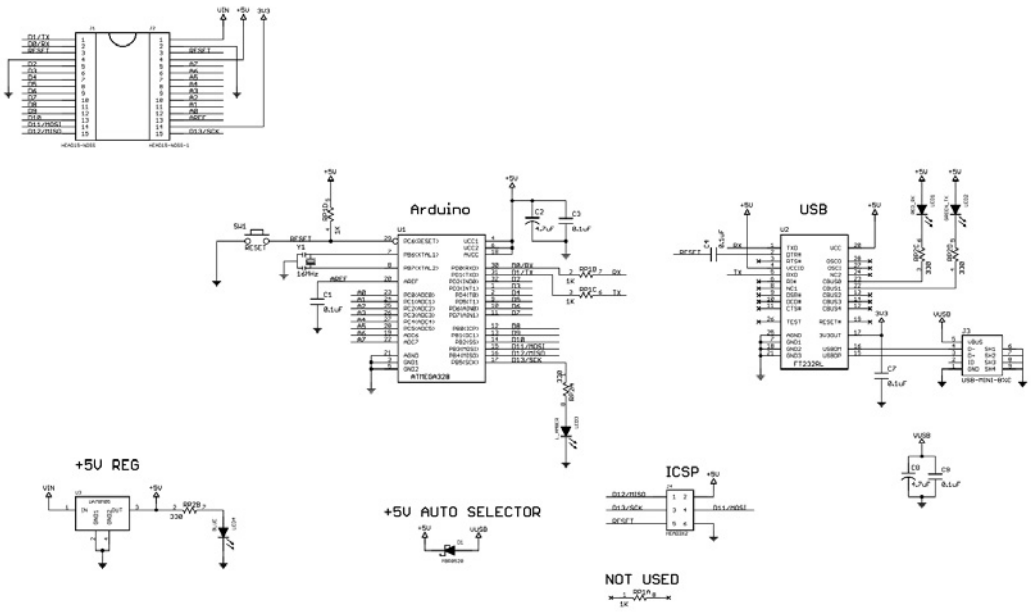

Figure 4.15: Schematic of the Arduino Nano microcontroller used for process control and monitoring [Arduino 2009]. The Arduino can be supplied with 3.3 to 16 V. For the PPU control the digital outputs D0 – D 13 are used. The analog inputs A0 – A7 allow the monitoring of the voltage signals from the PPU.

is referred to as "high side". Within the given example, four thrusters have been implemented which are firing all in the same direction. With the given EPS, operation of all four thrusters at the same time is not possible. Therefore, the thrusters are switched alternating in a circular pattern. A weak tumbling motion has therefore to be accepted. However, on bigger satellites more than one thruster can be operated at one time, depending on the available energy.

4.4 Improved PPU Design

Apart from the combination of IES and CES, while still using the inductive arc ignition and the implementation of several additional subsystems for process control and EPS connection, further improvements have been developed. This concerns the charging of the CES, an electrically enhanced arc initiation mechanism and the temporary supply of additional energy. The resulting design of the current state-of-art PPU is shown in figure 4.17.

The resulting PPU is (together with the already described auxiliary systems) much more complicated than the initial concept. However, all systems were successfully packed into a quadratic PCB of 90 mm side length, while the maximum thickness of the PPU is around 15 mm owed to the three Ta capacitors. For a first testing, a relatively small inductance of 120 μH and a saturation current of 3 A was chosen. The overall mass is in the region of

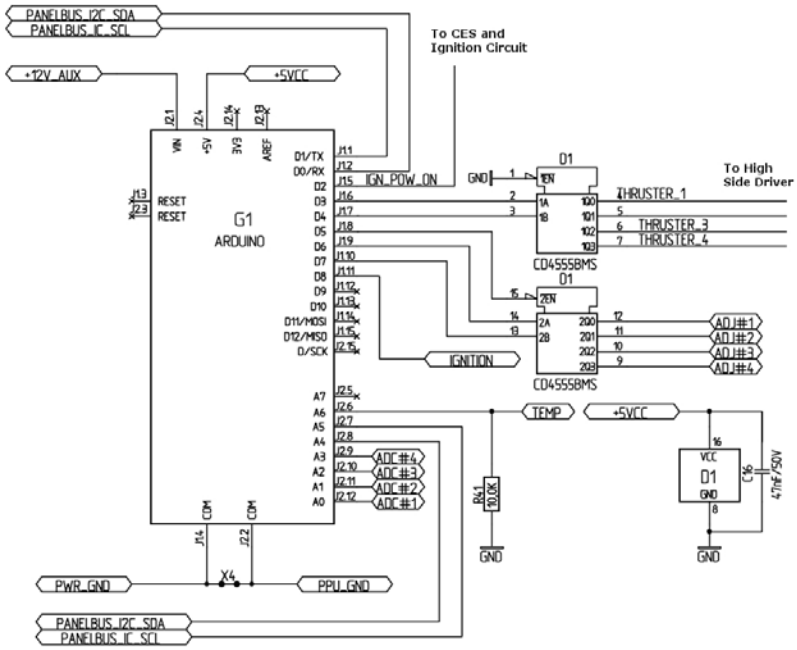

Figure 4.16: Schematic of the implementation of the Arduino Nano microcontroller for process control and monitoring.

150 g. Figure 4.18 shows the current PCB layout created by Apcon Aerospace & Defense GmbH.

As mentioned, all power lines are split on six different layers to avoid parasitic magnetic fields which could violate sensible satellite systems due to EMI. The additional subsystems will be described in the following.

4.4.1 Enhanced Ignition Mechanism

The core of the whole PPU system is still the inductive ignition. Compared to the initial setup equipped with an additional CES (see 4.9), three important components have been added. The first is a switch which disconnects the capacitor from the operation voltage converter during arc discharge. This is the additional MOSFET in the upper left of 4.17. The other insertion is a switch between inductor and anode which can be found on the bottom of 4.17, controlled by a high side driver. Moreover, a bypass switch was added parallel to the coil. All three components are illustrated in figure 4.17, labeled as Bus Separator, Ignition Switch and Coil Bypass, respectively.

The bus separator is intended to protect components on the low side from the voltage peak and arc current. This switch is opened just before the ignition, controlled by the microcontroller. Thus, only the energy stored within the capacitor can be drawn by the vacuum arc. The ignition switch on the other hand disconnects the thruster during the charging period between the pulses. Thereby, the capacitor can be charged even if the

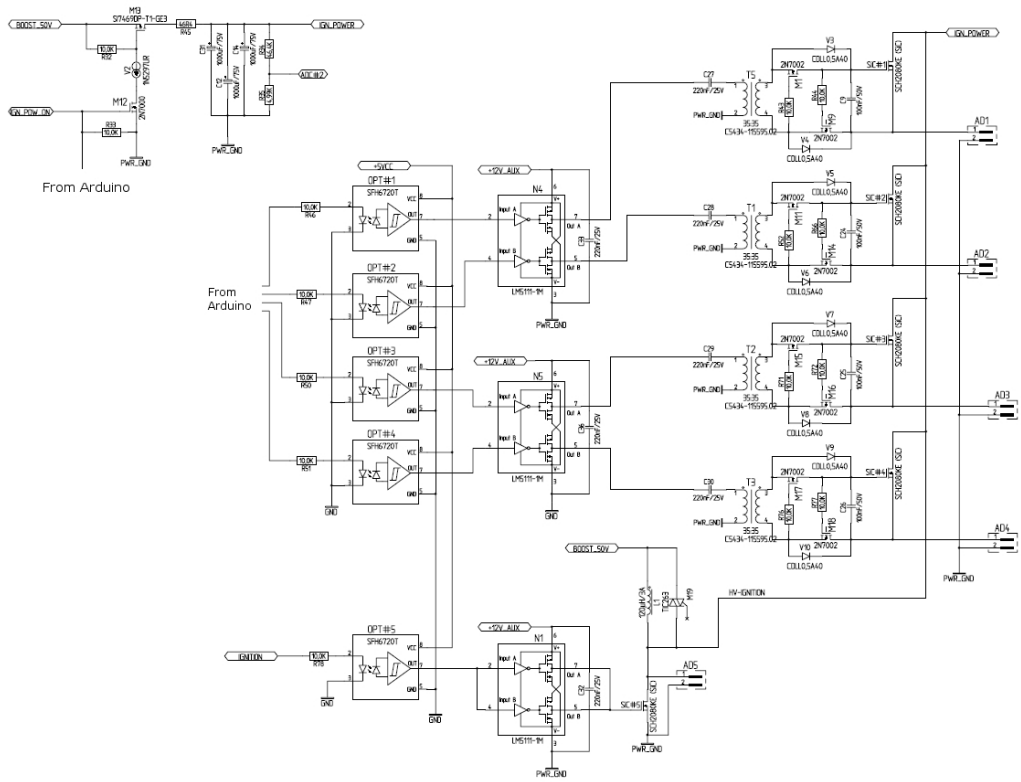

Figure 4.17: Circuit diagram of the final PPU, developed together with Apcon Aerospace & Defense GmbH. The four high side drivers in the center allow the switching between up to four thrusters. An enhanced ignition behavior is achieved by the high side driver at the bottom.

resistance between anode and cathode drops below some 100 Ω. However, as it turns out, this only works for resistances above ∼ 30 Ω. Therefore, a welding of both cathodes ultimately ceases thruster operation, which has to be prevented by geometrical measures on the electrode interface.

Within the lab prototype this electric trigger support mechanism is achieved by a TRIAC (Triode for Alternating Current). This is in principle a two-directional diode, which is usually controlled by an external gate signal. Without this signal both directions are blocked. If the gate is triggered, it becomes conducting in one of the two directions depending on the sign of the trigger signal. The TRIAC stays open as long as a current is running through the then closed circuit. However, the TRIAC becomes also conducting if voltage on one of the two sides increases too fast. This occurs if the arc is initiated by the voltage peak from the switching of the inductor ($U = \frac{dI}{dt}$). While this operation mode is not intended by the manufacturer, it allows a simple improvement of the arc initiation procedure.

Figure 4.20 shows the switching pattern of the improved PPU. For a better control of this mechanism, the TRIAC has been replaced by a MOSFET in the PCB layout. The TRIAC was rather unreliable and tended to stay conducting, especially at very low resistances. By applying a MOSFET, an exact separation of the thruster from the PPU is possible. The

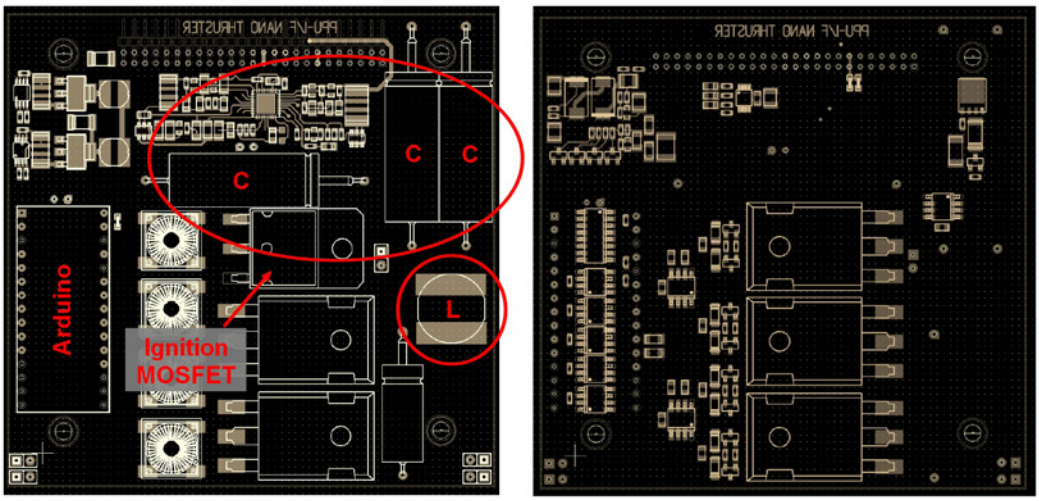

Figure 4.18: Top and bottom side of the PCB layout for the 1U-CubeSat PPU resulting from the considerations within this chapter. The Layout was created by Apcon Aerospace & Defence which was an industrial partner in a research project in connection with this thesis.

energy stored within the capacitor can thus be discharged into the vacuum arc plasma as long as current is running through the circuit. The impedance of the circuit which limits the output current is given by the wiring, the arc and by the inductor. To minimize the total impedance and to maximize the arc current, a TRIAC is also used to bypass the inductance.
The TRIAC is inserted parallel to the inductor and operated in the same way as the ignition switch. When the coil is discharged by opening the corresponding MOSFET, a high voltage peak arises, which as already explained leads to the initiation of a vacuum arc. On the other hand, the bypass TRIAC is activated and allows discharging the capacitor without a damping by the resistance of the inductor. Thus, a very smooth discharge is being generated which is shorter than without the bypass but starts at much higher voltage level. Therefore, the number of charges at the beginning of the pulse is higher than before, which leads to a higher thrust [Lun and Law 2015]. As it turned out, the TRIAC is a feasible component for coil bypassing.

4.4.2 Additional Energy Storage

Since the beginning of spaceflight, energy storage is a big issue. For the given EPS voltage range 3.7 V Lithium ion batteries have been developed to a very sophisticated, space qualified level [Frost et al. 2014]. Currently, research especially for small satellite solutions focuses on Li-Polymer batteries. This type of accumulator has a higher energy density compared to Li ion batteries, thus allowing smaller packaging [Zhang et al. 2014], although the capacity of Li-Po accumulators has a strong dependency on temperature variations. Especially low temperatures are a serious issue. Therefore, the developers of small satel-

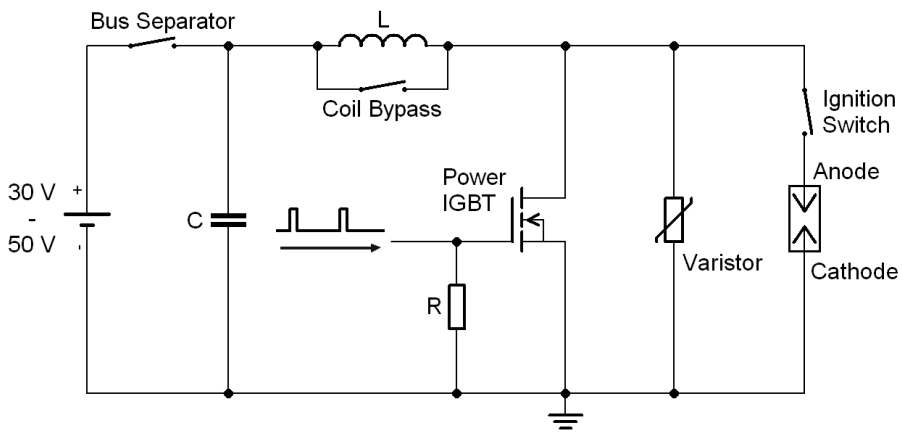

Figure 4.19: Simplified schematic of the final PPU concept with capacitive energy storage, inductive arc initiation, bus separation, coil bypass and ignition switch. The ignition switch is open as long as capacitor and inductor are being charged. Directly before arc initiation the PPU is circuit is disconnected from the EPS by the bus separator to protect sensitive parts of the satellite. The ignition voltage peak after deactivation of the IGBT occurs simultaneous with the closing of the ignition switch. Subsequently, the coil bypass is activated and allows a smooth discharging of the capacitor.

lites usually have to qualify each battery separately.

Figure 4.21 shows a selection of batteries used for PPU development. The large battery on the top is typically used for RC-cars and allows output currents of up to 76 A at a capacity of $C_N = 3.8$ Ah. The discharge current is limited by the so called $C\ factor$ (20C in the given example) that is given by the battery properties: $I_{max} = 20\text{C} \cdot C_N = 20\ \text{h}^{-1} \cdot 3.8\ \text{Ah} = 76\ \text{A}$, which can be sustained for $C = 20\ \text{h}^{-1} = 3$ min. Drawing a higher current will result in the chemical destruction of the battery. Therefore, a special protection circuit is necessary. This is required in any case, since some PPU components have also current limits.

A lower C factor is therefore reasonable. The center battery in figure 4.21 has a C factor of 0.5 from which a maximum discharge current of 1.25 A for 120 min follows [Sunping et al. 2015]. This is much more suitable for the electronic components of the PPU, although it increases the charging speed of the CES. This special product is already equipped with a protection circuit. The maximum charging current is given by the manufacturer with 1C which means that the battery is charged after one hour at an input current of 2.5 A. Since the average EPS current is 0.5 A, charging will take longer and a suitable charging circuit is necessary.

For this a MCP73833-AMI/UN Li-Po charge management controller has been implemented into the PPU layout, which is illustrated in figure 4.22. The additional mass amounts to 46 g while an extra volume of 61x47x8 mm is necessary. However, the battery used for PPU development is only tested for operation within 0 to +40°C. Therefore, the use of a space qualified battery may worsen the performance of this subsystem. On the

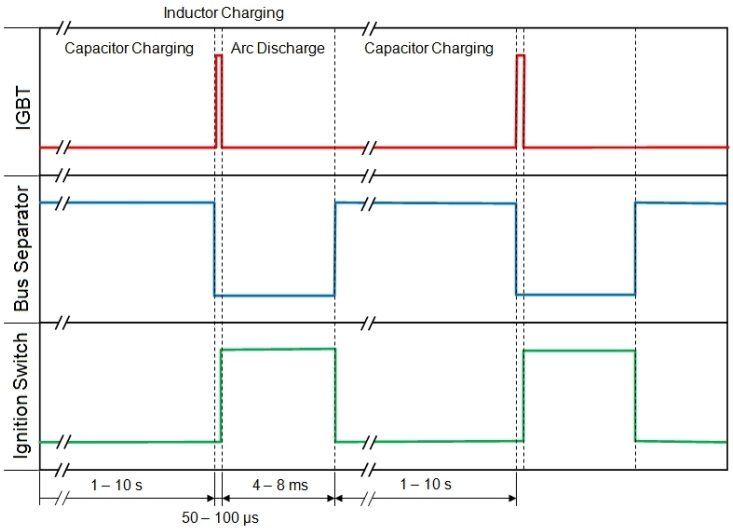

Figure 4.20: Schematic operation sequence of the IGBT, the bus separator and the ignition switch. The coil bypass is switched in the same pattern as the ignition switch.

1U-CubeSat e. g. a battery temperature variation between and +4.5 and +9.5° was measured [Bangert et al. 2014]. Therefore, the battery chosen for laboratory testing may be suitable for future CubeSats, although a proper mechanical implementation has still to be achieved.

4.5 Summary

The improved PPU has a slightly different operation scheme and performance than the original concept by [Schein et al. 2001]. Although the simplicity of the initial concept was barely conserved, it fits well within the space and mass limitations of a 1U-CubeSat, as it will become clear within the following discussion.

4.5.1 Operation Characteristics and Performance

To illustrate the differences between both PPU concepts, figure 4.23 shows current and voltage values of typical discharges. For the pulse shown in the left image an IES PPU with an inductance of 330 μH and 9 A saturation current was used. In addition, it was equipped with a buffer capacitor like in the improved concept with a capacity of 1000 μF. The released pulse energy is approximately 180 mJ. The right pulse was achieved by the improved PPU with a 47 μH / 3 A coil and a capacitance of 4700 μF. Since the achieved pulse length is longer than in the first case, a pulse energy of 0.76 J is reached despite a lower peak current.

As stated by [Lun and Law 2015], longer pulses lead to a higher thrust per pulse. The left diagram includes a damped oscillation at the end of the pulse which results from the

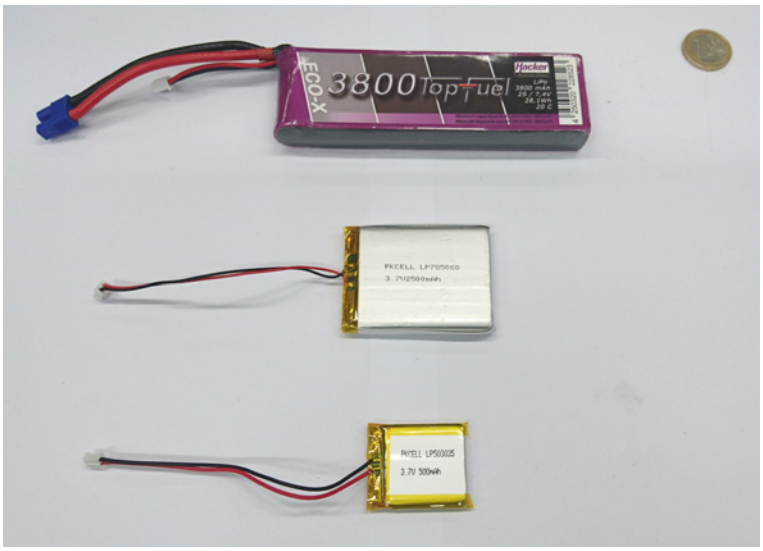

Figure 4.21: Different sizes of Li-Po batteries. The top one is a typical RC-car battery while the lower two are meant for power banks or quadrocopter.

passive switching of the inductance when the current converges to zero. This behavior has been eliminated by the coil bypass introduced above. However, without the throttling effect of the coil a further increase of current and pulse length is possible as figure 4.24 shows.

As it is visible, the voltage declines in a way that is typical for a capacitor discharge with a parallel load. The total impedance is caused by the electric circuit and by the vacuum arc. Plotting voltage versus current shows a linear behavior like it can be found in a gas discharge [Lieberman and Lichtenberg 2005]. The impedance can be determined from the gradient of a linear fit as illustrated in figure 4.25. The negative currents occur because of undershoot of the current at the end of the discharge which results from the circuit properties, e. g. the wire inductance.

This typical capacitor behavior shows that the ignition inductance is successfully bypassed

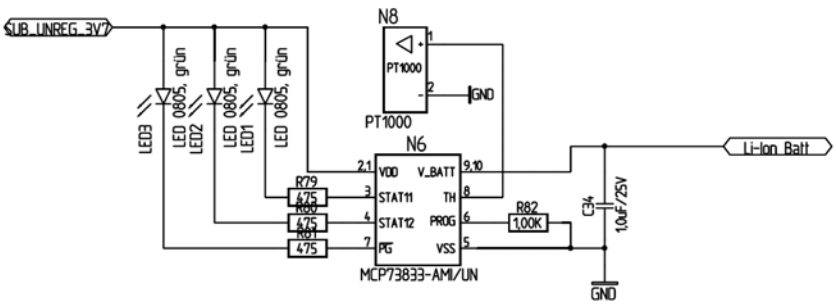

Figure 4.22: Charge management control system for 3.7 V Li-Po batteries.

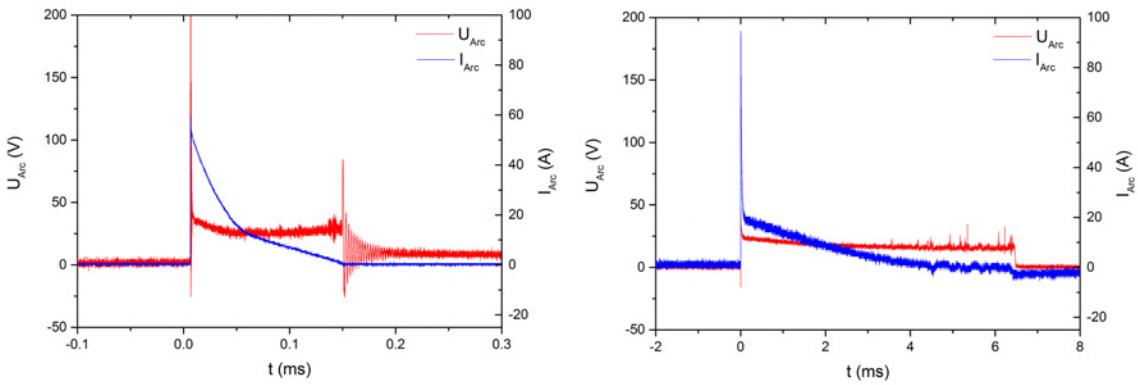

Figure 4.23: Comparison between a pulse from the initial PPU concept (left) and from the improved system (right). Both arcs operated at 30 V. The damped oscillation in the left diagram stems from the passive switching of the inductor.

by the included TRIAC. The pulse energies can be derived from the voltage and current measurements by $W = \int P(t)dt = \int U \cdot Idt$. The limitation of pulse energy and repetition rate is given by the EPS energy of a satellite like UWE-3, together with the temporal energy extension by a 2.5 Ah Li-Po battery and the efficiency of the voltage conversion. The charging pattern of the capacitor reveals the minimum pulse repetition rate as shown in figure 4.26.

For the lab prototype, a LM2577 step-up converter was used. The battery discharging current is limited to 1.25 A. The Output voltage is typically between 3.7 and 4.3 V. The output current can be calculated from the charging periods of the capacitor (4.7 mF) with $t \approx 5\tau = RC = U/I \cdot C$. At 30 V operation voltage a charging time of 0.71 s is measured while the corresponding average current is 66.19 mA. On the other end, at 50 V and a

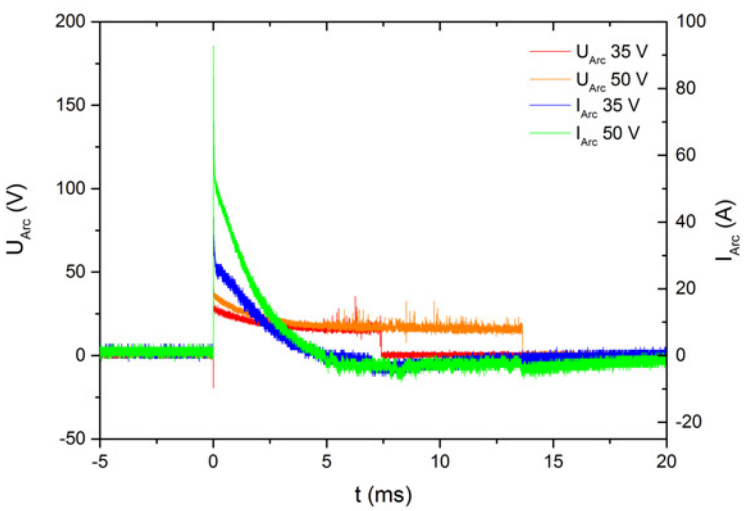

Figure 4.24: Progression of Voltage and Current for two different input voltages.

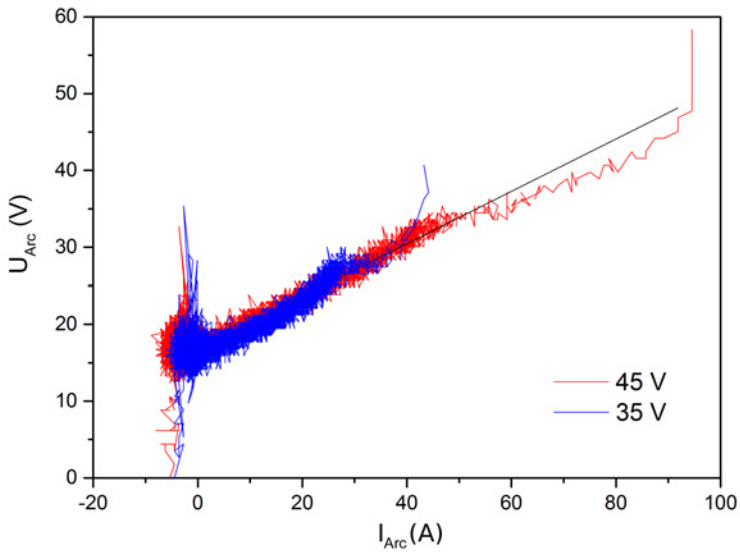

Figure 4.25: Characteristic U-I-Diagrams for Input Voltages of 35 V and 45 V. From the slope of the linear fit the circuit (PPU and arc) impedance can be determined (here 0.34 Ω).

charging time of 10 s an average current of 9.4 mA is supplied by the boost converter. This can be explained by the power dissipation of the LM2577 step-up converter which rises with increasing output voltage [Texas Instruments, Inc. 2013]. The efficiency η_{con} of the conversion is then given as

$$\eta_{con} = \frac{P_{Out}}{P_{In}} = \frac{U_{Out} I_{Out}}{U_{In} I_{In}}. \tag{4.17}$$

Accordingly, the efficiency drops from 0.40 at 30 V to 0.09 at 50 V. However, the most recent PCB built together by Apcon Aerospace & Defense GmbH is equipped with a much more efficient boost converter than described above. The lower energy dissipation should theoretically result in a better total efficiency. A characterization as just described has to be conducted when the PCB is delivered by Apcon Aerospace & Defense GmbH. Figure 4.27 shows the variation of the pulse energy for different operation voltages. An energy range from 0.75 to 2.7 J has been achieved within the given system.

The discharge can only be maintained as long as sufficient voltage and current can be supplied by the PPU. This is limited by the capacitor energy $W = 1/2CU^2$ since the PPU is separated from EPS and battery during discharge. Therefore, the voltage level necessary for the discharge can only be maintained as long as current flows. The possible peak energy supplied by the capacitor is therefore given by the difference of charging voltage and actually released voltage. For the 50 V discharge shown in figure 4.24 a difference of around 34 V has been observed, from which an applied energy of 2.88 J vs. a pulse energy of 2.69 J can be calculated. The efficiency η_{CES} of the CES branch of the PPU is given by

$$\eta_{CES} = \frac{W_{Arc}}{W_{CES}}. \tag{4.18}$$

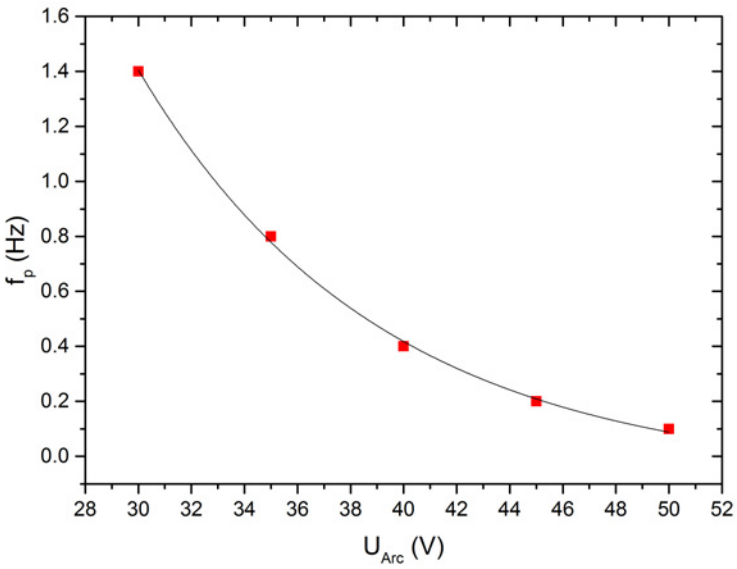

Figure 4.26: Variation of the maximum repetition rate for several input voltages. The exponential decay of the repetition rate is owed to the power dissipation of the boost converter and the current limitation of the Li-Po battery.

Thus, an efficiency of 0.94 can be calculated for the 50 V example. This is in the same region as the efficiency of a pure IES PPU as assumed by [Schein et al. 2001]. Together with the conversion efficiency η_{con} a PPU efficiency $\eta_{PPU} = \eta_{CES} \cdot \eta_{con} = 0.08$ follows in this case (respectively 0.38 at 30 V operation voltage). The corresponding thrusts will be investigated in the next chapter. Nevertheless, the actually required thrust depends on the mission design. Therefore, it remains up to the satellite developer to decide if the achieved performance is sufficient for the desired mission.

4.5.2 Viability for Spacecraft Integration

This chapter described the conversion of the initial PPU concept by [Schein et al. 2001] into a system ready for integration into a 1U-CubeSat. Some of the additional systems are adapted especially to the architecture of an example CubeSat (UWE-3 respectively its successor). This concerns in particular the interface between EPS and PPU. The implemented microcontroller on the other hand allows I^2C communication, which is a universal protocol. Therefore, the PPU should be compatible to most CubeSat architectures apart from the interface layout. However, the satellite developer may choose a 3.3 V microcontroller which consumes less current than the used Arduino Nano, e. g. a MSP430F543xA. This is used for most of the UWE-3 subsystems.
A topic which still needs to be addressed is the EMI compatibility of the PPU, since there are high voltage peaks as well as relatively high currents. The PPU microcontroller is decoupled and as it turns out it is not influenced by arc ignition and discharge. This

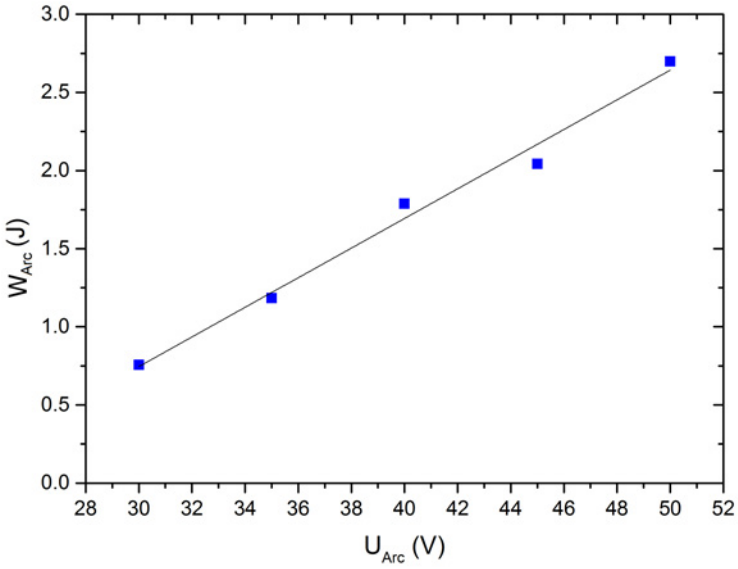

Figure 4.27: Variation of the energy per pulse and maximum repetition rate for several input voltages.

was a serious issue in earlier development stages, but not only the decoupling is the solution to this issue. The inductor, on the other hand, also generates EMI. Therefore, it was important to choose the right geometry, material and electrical dimension for this component. To avoid the generation of parasitic magnetic fields, a laminated toroidal core that splits the current into several layers was integrated. As described above, a relatively small inductance can be used in the improved PPU design. An additional reduction of EMI is achieved by the splitting of the power lines to six layers, by which further parasitic magnetic fields are decreased. Yet a thorough EMI testing by the satellite developer is still pending.

The energy consumption was also adapted to the capabilities of a 1U-CubeSat with an EPS voltage of around 4 V and an average current of 0.5 A. This limits the performance of the propulsion system, although the PPU already allows higher input power and can therefore be integrated into larger satellites without essential changes – apart from the interface. High pulse energies are already possible with the system described in this chapter, which on the other hand limits the repetition rate. To allow higher thrust at higher repetition rates on picosatellites, an additional energy storage needs to be implemented. This battery might be obsolete on bigger satellites with a stronger power supply. Higher pulse energies are not recommended with the thruster dimensions described in the next chapter, which limit the energy input of the electrodes. Therefore, the production of higher thrust requires not only a scaling of the PPU but also a redesign of the thruster geometry.

Chapter 5

Thruster Design

The reliable operation of a VAT based propulsion system depends not only on the PPU but primarily on the thruster itself. Within this chapter, the important aspects of VAT design will be explained. It starts with the geometric design and the material selection for anode and supporting structure. In the following, the cathode design will be introduced along with a calculation of the propellant demand for different materials. Several feeding methods for the cathode will be described as well as alternative geometries for anode and cathode. This chapter closes with an introduction of the final VAT design with a special focus on CubeSat integration.

5.1 Structural Design

The thruster design presented in the following is heavily influenced by the space restrictions given by the integration into an existing 1U-CubeSat. However, since an integration into other satellites is considered, a transferable design solution has to be found. As explained in chapter 2, a coaxial electrode setup was chosen for the further development of a CubeSat VAT system. The reasons for this decision were a very compact assembly, a well defined origin of thrust production and an accurate expansion direction. Moreover, various studies concerning this thruster type have already been conducted, e. g. [Schein et al. 2002], [Sekerak 2005], [Lun and Law 2013]. Therefore, a wide range of data and improvement ideas are available. The basic principle is shown again in figure 5.1.

However, only a few attempts have been made to integrate a VAT into a CubeSat, e. g. [Rysanek et al. 2002], [Hurley et al. 2015]. Therefore, not only the choice of a suitable cathode material as reaction mass but also the geometry and material of anode, insulator and additional elements like mounting adapter and feeding system have to be considered. This section focuses on the principle restrictions given by CubeSat Design Specifications as well as on the design of anode, insulation and CubeSat mounting.

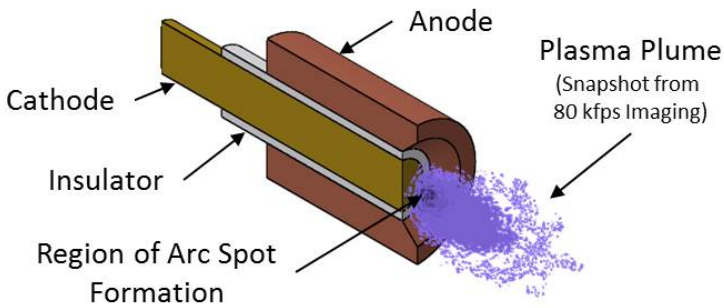

Figure 5.1: A coaxial electrode setup has been chosen for CubeSat integration. The cathode in the center is surrounded by a thin tube of insulating material like Al_2O_3 or BN and by the anode. This concept is space-saving, has a well defined location of thrust production and an accurate expansion direction.

5.1.1 Constraints

As described in chapter 4, the design rules have been determined by the restrictions and requirements of a possible successor of the 1U-CubeSat UWE-3. It was launched in November 2013 and turned out to be a very successful satellite construction, since it has still been operable in LEO at the date of this thesis [Bangert 2016]. This shows especially that the integrated hardware is feasible for space conditions, i. e. mechanical and thermal loads during launch as well as thermal variations and radiation in orbit. For the testing of a propulsion system, it is therefore intended to use an identical hardware architecture [Pietzka et al. 2013]. This affects not only the systems inside the satellite like on board computer, communication system, ADCS and energy storage but also the exterior systems. The side panels are equipped with solar panels, attitude sensors and magnetorquers. An integration of the thrusters into these panels would imply a complete redesign. Moreover, energy is one of the most important resources on a spacecraft, especially for the propulsion system. Therefore, it was decided that the thrusters should be implemented into the rail structure of the CubeSat [Pietzka et al. 2013]. The geometry and the material properties of this part are standardized by the CubeSat Design Specifications [Mehrparvar et al. 2014]. Thus, by integrating the thruster into the rail, a standard assembly procedure for a large number of different CubeSats could be achieved. Figure 5.2 shows the chosen location for the integration of the thruster into UWE-4 and an early mounting concept.

In the given example, all four thrusters are aligned along the length axis of the rails into the same direction. Thus, attitude control and fine positioning require the interaction of thrusters and magnetorquers respectively reaction wheels. Further constraints for the thrusters are given by the geometry of the rails. As illustrated in figure 5.2, only a square length of 8.5 mm is available for the outer dimensions of the thruster while the length (up to 100 mm) is more than sufficient, as shown above. However, to reduce mechanical loads

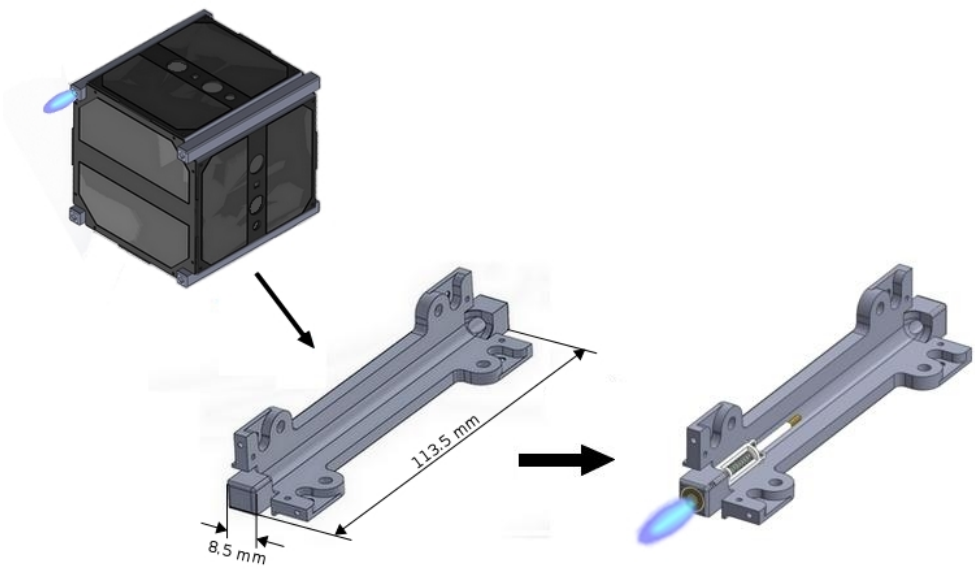

Figure 5.2: Concept for the VAT integration into an 1U-CubeSat like UWE-3. Only the four CubeSat rails can be used for this without bigger modifications. This limits the shape and the dimensions of the thruster. An early mounting concept is shown by the rail on the right.

during launch, four springs are placed between two CubeSats inside a P-POD (see chapter 1), which use the faces of the rails as bearing area [Mehrparvar et al. 2014]. Thus, the thruster has to be constructed in a way, that allows this setup. Moreover, to avoid electrostatic effects between the satellites and the P-POD, all contact surfaces have to be anodized, which also reduces friction issues during deployment.
Only the volume of the rails can be used for VAT integration, since the remaining space inside of the satellite is reserved for the electronic hardware. To conserve the structural integrity of the CubeSat, a minimum wall thickness of 1 mm is necessary [Rathinam et al. 2015]. The mass is restricted by the total mass of the VAT system which is limited to 250 g. Since around 200 g are already used by the PPU, only around 12 g are left for each thruster. However, as shown below, the propellant mass necessary amounts to only 1 g for an exemplary mission with a required Δv of 7.5 m/s. Thus, most of the remaining mass can be used for structural parts like mounting adapter and feeding system. For the choice of proper materials not only mechanical stability and thermal resistance have to be considered, but also aspects as out-gassing under vacuum conditions and aging effects due to heating and radiation [Walter and Scialdone 1997]. The size and geometry of the anode will be discussed in the following.

5.1.2 Anode Material and Geometry

Metals usually used in vacuum arc experiments like Al, Cu, Fe, Ti and W and their alloys are not significantly affected by the expected mechanical loads, out-gassing and radiation.

Material	Type	ρ (g/cm^3)	σ (MS/m)	T_m (°C)	λ_T (W/(m · K))
Ag	Metal	9.320	61.35	961.78	429
Cu	Metal	8.02	58.0	1084.62	401
Al	Metal	2.38	36.59	660.32	243
Fe	Metal	6.98	10.02	1538	80.2
Sn	Metal	6.99	8.69	231.93	66.6
Ms	Alloy	8.41 – 8.86	15 – 33	902 – 1065	120
Graphite	Semimetal	2.30 – 2.72	3.0	3825	119 – 165

Table 5.1: Density ρ, electric conductivity σ, melting point T and thermal conductivity λ_T for possible anode materials [Lide 2003]. Note that the temperature for carbon is not the melting point but the sublimation point since this element changes directly from solid to gaseous.

For thermal effects, only the heat loads due to thruster operation are important, since, as mentioned above, no significant temperature changes have to be expected in LEO. In principle, every electrically conductive material can be used as anode since thrust range and specific impulse are being influenced by the cathode material and the pulse power as shown in chapter 2. However, regarding mechanical stress, metals are superior to electrically conductive nonmetals like Graphite, Ge and Si which have a very low ductility and can easily break or crumble under mechanical loads. Since the anode has to handle part of the vibrations and g-forces during launch, only metals will be considered in the following.

As table 5.1 shows, the electric and thermal conductivity of selected elements is relatively similar, with a slight advantage for Ag, Cu and Al. The anode heats up during thruster operation due to the energy input by the vacuum arc. This energy input can be dissipated by conduction, i. e. to the anode body and subsequently to the satellite structure, radiation, melting or vaporization [Boxman et al. 1995]. However, radiation is only effective at high temperatures and the anode is thermally insulated by the surrounding space ($p \approx 10^{-5}$ Pa) and by the insulating material which separates it from the cathode and the satellite structure. The only effective way for heat conduction is the electric connection between anode and PPU. Thus, cooling between the pulses is very slow and may not be sufficient to dissipate the applied energy. Depending on the used anode material a melting or evaporation of the surface may occur in the worst case. Nonetheless, at experiments with Sn anodes of 7 mm diameter and a length of 18 mm no melting or evaporation was observed at pulse repetition rates of around 1 Hz and an arc current of around 40 A. According to [Boxman et al. 1995] repetition rates of several dozen Hz or DC arcs and currents of several hundred Ampere are necessary to exceed the melting temperature of Cu (1356 K) locally.

However, Sn was used only for laboratory testing with low operation times, since it can easily be casted into the desired shape. Further machining like drilling holes or thread cutting is also uncomplicated. For the implementation into a CubeSat Al was chosen for the further development, not only because of its better thermal stability than Sn but also

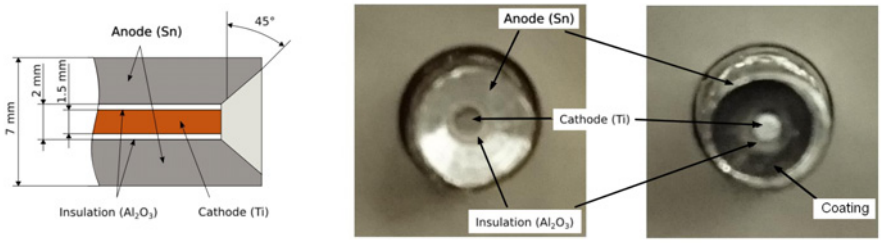

Figure 5.3: Comparison of two thrusters before (left) and after (right) several 100 pulses with an energy of 1.7 J. The anode is made from Sn and has a conical shape with an inverse phase angle of 45° while the cathode is of Ti. Visibly, a dark coating has been deposited on the anode and on the insulation during thruster operation.

because of its better machinability compared to Cu. Due to the limitations given by the integration into the CubeSat rails (see subsection 5.1.1), the dimensions of the anode were set to an outer diameter of 8.5 mm, a hole diameter of 2 mm for cathode and insulation and a length of 5 mm. The latter is determined by the overall length of the rail (113.5 mm) which is determined by the CubeSat Design Specifications [Mehrparvar et al. 2014]. As 8 mm of rail length can be removed without interfering with its functionality and some space is necessary for a mechanically stable mounting adapter, around 5 mm are left. However, bigger satellites with other geometrical structures may allow longer anode with a bigger cross section.

It has been shown by [Polk et al. 2008] and [Lun et al. 2010] that a slightly recessed cathode and insulation reduces contamination of the satellite structure. Depending on the length of the recession, macroparticles which leave the cathode under very flat angles to the surface normal ($< 30°$ [Boxman et al. 1995]) are captured on the inner wall of the anode. However, a loss of useful thrust has to be tolerated by this measure. As trade-off between a loss in thrust and contamination a conical shaped anode with an inverse phase angle was therefore tested. The deposition of cathode material on the anode may also be accompanied by a coating of the conductive layer. Figure 5.3 clearly shows that after several 100 pulses with a typical energy of 1.7 J a coating has been deposited on the thruster surface.

Figure 5.4 shows the ICDD for different cone angles, measured with the setup described in chapter 3. As it is visible, more shielding leads to a narrowing of the beam profile. From that, a reduction of thrust results, as mentioned in literature [Polk et al. 2008]. Within the tested configurations, an outlet angle of 45° to each side shows the best result with minimal loss due to the Cosine or Gauss shape of the beam profile.

The re-deposition or recovery of the conductive layer with cathode material has been already been described in literature for higher pulse energies [Anders et al. 2000]. At values achieved with an IES PPU (some 10 mJ) no sufficient deposition has been observed during a typical operational lifetime of several hundred pulses. The application of higher pulse energies by using a CES PPU as described in chapter 4 seems to support the ob-

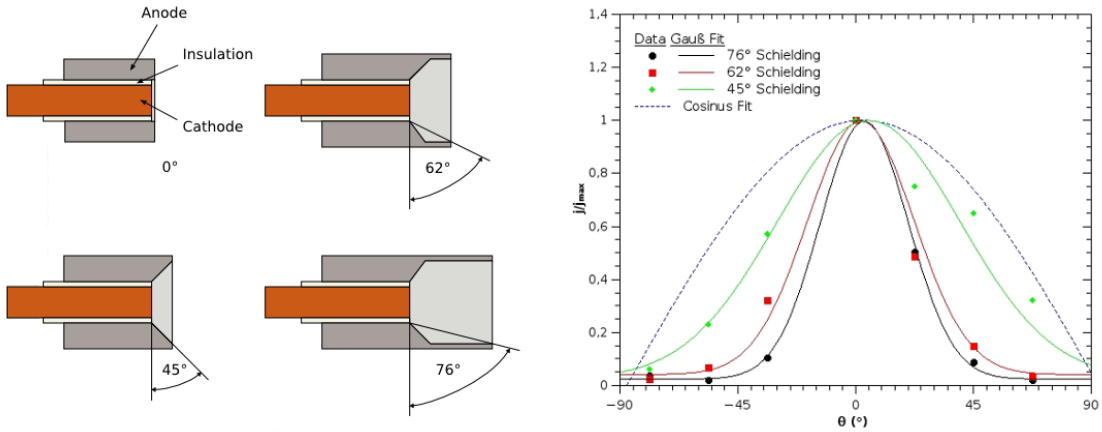

Figure 5.4: Left: Sketch of different tested shieldings. The marked angle was chosen as parameter for the further discussion. Right: Ion current density distribution for several shielding angles. As mentioned by [Polk et al. 2008] a narrowing of the ICDD is resulting from a bigger shielding angle.

servations of [Anders et al. 2000]. As an example, figure 5.5 shows two SEM (Scanning Electron Microscope) images from a thruster and especially the anode surface. It can be seen that a grey coating has been deposited on the surfaces of anode and insulation during thruster operation. This coating stems probably from the cathode material (Ti). The right SEM image shows that this coating consists partially of droplets as described by [Polk et al. 2008].

However, due to technical limitations of the SEM used thereby, only an estimation concerning the surface composition is possible. But based on literature it seems reasonable that the coating stems from the cathode material. As it is published, macroparticles, i. e. droplets from molten cathode material, are moving under a very flat angel ($< 30°$ to the surface normal) away from their origin. This explains the existence of droplets on the anode surface as it can be seen on the right image in figure 5.5. Yet, further research, probably with EDX (Energy Dispersive X-Ray), has to identify the composition of this layer.

By this, the geometrical specifications of the anode are set which will provide sufficient mechanical and thermal resistance for CubeSat operation (see table 5.2). However, the

Material	Al
Length	5 mm
Diameter	8.5 mm
Hole Diameter	2 mm
Mass	0.38 g

Table 5.2: Specification of an anode for the integration into CubeSat rails.

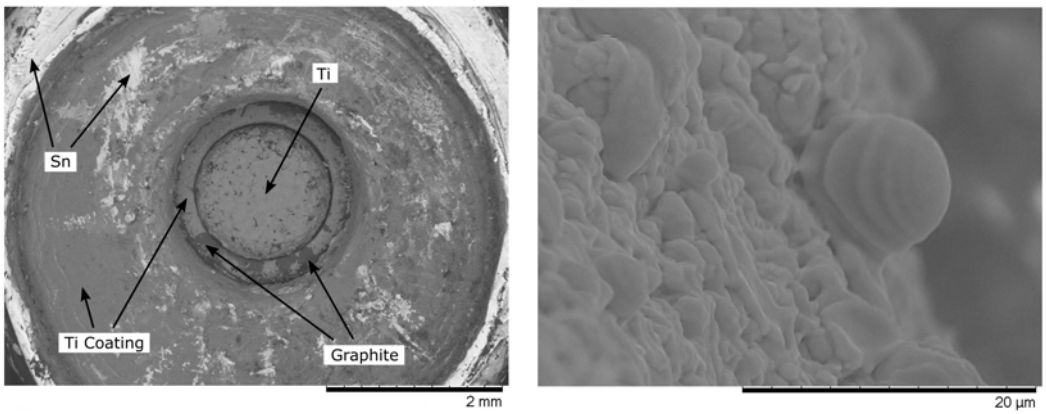

Figure 5.5: SEM images of the thruster surface after several 100 pulses with an energy of 1.7 J. The left image shows the surface composition. Anode and insulation are partly coated with material that is probably from the cathode. Right: Droplet probably from the Ti cathode on the anode surface.

overall durability of the VAT depends also on the structural elements as well as on the insulation between anode and cathode, which will be discussed in the following.

5.1.3 Insulation

As described in chapter 2, an insulation between anode and cathode is required for the electrical separation of both. This insulation is coated with a conductive layer, which is required for the so called "triggerless" arc initiation. Given by the concept of the coaxial electrode setup, the insulation has the shape of a tube. To prevent this tube from detaching from the thruster, e. g. due to mechanical loads during launch, a proper attachment is necessary, either by a tight fitting between insulation and anode or by a step at the end of the tube as illustrated in figure 5.6. Both solutions require a precise machining of anode and insulation which, at least for ceramics, is very complex.

The insulation material has not only the task to separate the two electrodes from each other, but it also has to withstand various loads: Heating due to the energy input into

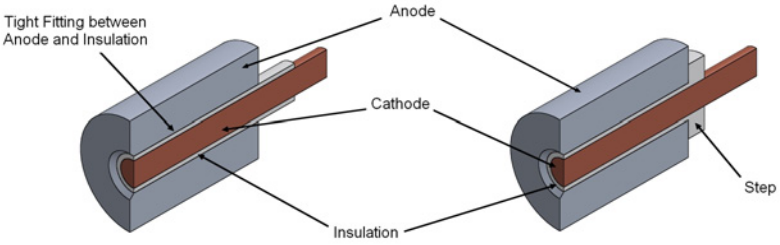

Figure 5.6: Integration of the insulation into the thruster structure. Left: Tight fitting between insulation and anode, i. e. the diameter of the anode hole and the outer diameter of the insulation have a very close tolerance. Right: Step at the end of the insulation.

Material	Type	T_{max} (°C)	λ_T (W/(m·K))	E_D (kV/mm)	Ref.
Kapton®	Polyimide	–	0.12	291	1
PEEK	Thermoplastic	$\sim$ 310	$\sim$ 0.25	24	2
Vespel®	Polyimide	$<$ 500	0.35 – 1.73	9.84 – 22	3
Al_2O_3	Oxidic Ceramic	1,000 – 1,500	20 – 30	17 – 30	4
BN	Nitridic Ceramic	1000 – 2000	11 – 130	10 – 88	5
Macor®	Glass Ceramic	1000	1.46	9.4 – 62.4	6

Table 5.3: Maximum operation Temperature T_{max}, thermal conductivity λ_T and dielectric strength E_D of possible insulation materials.

anode and cathode, erosion by ion bombardment, mechanical stress during launch and compressive force due to the different expansion coefficients of anode, insulation and cathode. While the first two issues call for a ceramic material, the latter two are more in the range of synthetic materials. Table 5.3 gives a selection of different materials used within development.

Further aspects which have to be considered for space qualification are the radiation resistance and out-gassing effects which both can change the microscopic structure of those materials. However, all materials mentioned in table 5.3 are qualified by NASA [Walter and Scialdone 1997]. In most publications alumina was used as insulation material which has shown a very good persistence under vacuum arc treatment. Unfortunately, as it turned out, off-the-shelf alumina tubes have a low production accuracy especially concerning the radial dimensions, therefore a careful post-processing is required. An alternative is the glass ceramic Macor, which has a very good machinability. On the other hand, like boron nitride, it is brittle and thus prone to breaking and crumbling during thruster operation.

The search for alternatives leads to synthetic materials with a high thermal resistance. Possible materials are Kapton and Vespel, both are Polyimides from DuPont, and PEEK (Polyether Ether Keton). All three have a very high maximum working temperature (up to 400°C) and very good insulation properties. Moreover, they can be milled very well and have a high mechanical load capacity. As shown above, the thermal loads from the contact with anode and cathode can be handled, but the Joule heating during arc initiation and the ion bombardment within the discharge are a serious issue. Thereby, the melting temperature can be easily reached locally and changes within the microscopic structure may occur. From this, a massive erosion can follow as observed with thin Kapton insulations of around 100 μm thickness.

At typical conditions, i. e. pulse energies between 1 and 2 J and a duration between 3 and

1 [DuPont High Performance Films 1996]
2 [Quadrant Engineering Plastic Products 2009]
3 [DuPont Engineering Polymers 2002]
4 [CeramTec GmbH 2015]
5 [Saint-Gobain Boron Nitride 2011]
6 [Corning Inc. Lighting & Materials 2001]

8 ms, two main cases occurred: In the first, a smooth erosion along the whole insulation edge occured. Due to the recession of the Kapton, arcs no longer developed at the front face of the cathode but at the lateral surface. Thus, the evolving plasma plume is limited by the walls of anode and cathode which leads to a reduction of thrust [Lun 2008] and more macroparticle deposition on the anode wall and on the insulation. By this, a fusing of both electrodes finally results. As shown below, the cathode spots have a very low mobility in the given setup and tend to stay at the same location during one discharge. This can lead to a very localized erosion of Kapton. In this case, a faster erosion in this area results while the remaining capton is largely unaffected. As in the first case a recessing of the insulation follows, but only in one spot and with a higher speed. Finally, anode and cathode are fused again.
However, erosion effects have also been found using alumina insulations with a wall thickness of around 250 μm. While Kapton and PEEK insulations are more or less evaporated at locations with high heat load, alumina seems to crack or to crumble due to the mechanical tension resulting from thermal loads. If erosion of Kapton or PEEK insulation can be controlled by the thickness of the material, it may be possible to condition the whole process in a way that insulation and cathode are consumed at the same rate. This may not only be beneficial due to the higher mechanical resistance, but also because it is not to be expected that cracks spread through the material, like it is the case in ceramics (see figure 5.7). The latter issue can lead to additional arc path inside the thruster, which will not lead to thrust production. However, this has to be left for further research.
The other important component of the interface between anode and cathode is the con-

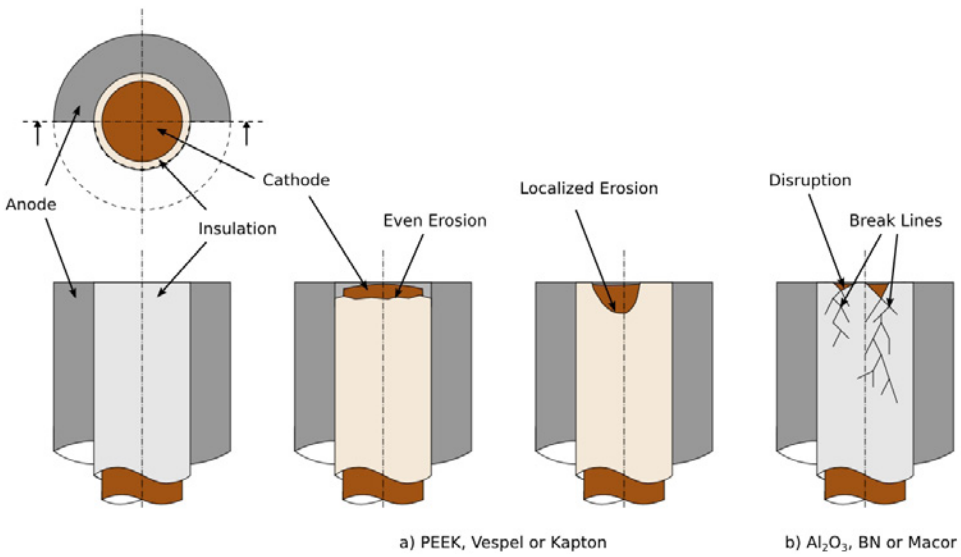

Figure 5.7: a) PEEK or Kapton are evaporated either evenly around the insulation surface or very localized if the vacuum arc has a preferred ignition area. b) The brittle material structure of ceramics can lead to cracking inside the thruster due to mechanic stress during launch or due to thermal loads.

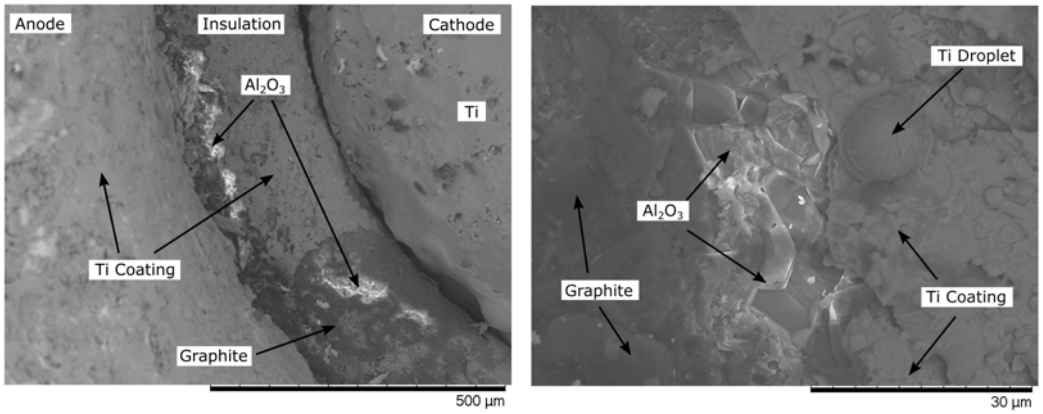

Figure 5.8: SEM images of the insulator surface after several 100 pulses with an energy of 1.7 J and a duration of around 4 ms. Left: The dark area on the insulator stems from the Graphite coating, while other parts of the insulator are coated probably with cathode material (Ti). The white areas are uncoated or eroded parts of the insulator made from alumina. This is supported by the image on the right where the crystalline structure of the ceramic becomes visible. There are also some droplets, probably from the Ti cathode, visible.

ductive layer which usually is simply made from Graphite that is applied with a pencil. However, the erosion of the conductive layer by explosive evaporation is essential for the functionality of the VAT. Thereby, a cloud of conducting vapor is produced between anode and cathode which acts as low-resistance path at the beginning of the arc discharge. Thus, for a long duration thruster operation it is necessary to replace this layer. As mentioned in the previous subsection, a deposition with cathode material can be observed within VAT operation with CubeSat parameters, i. e. for a maximum pulse energy of around 2.7 J and pulse repetition rates of 1.4 Hz at most.

Figure 5.8 shows images taken with a SEM. Thereby, three areas can be found at the insulator: The initial Graphite layer, uncoated alumina and a coating which may result from cathode material. In contrast to the initial issue of an interruption of thruster operation due to the erosion of the conductive layer, another issue evolved during VAT development: Due to the re-deposition, a fusing of the electrodes may occur which prevents further operation. Thus, an optimization of insulation thickness, cathode dimensions and thruster design is necessary. However, as mentioned in case of the anode, further investigations are necessary.

5.2 Cathode Properties

As explained in chapter 2, the cathode is used as propellant for thrust production. The performance of the VAT is not only determined by the power supply but also by the physical properties of the cathode material. Based on these, the propellant demand for a given Δv can be calculated. This is necessary for the choice of the most suitable cathode material

Element	M (AMU)	E_r (μg/C)	V_{arc} (V)	v_i (m/s)	I_{sp} (s)	η	T/P (μN/W)
C	12	17	29.6	17300	859	0.020	4.84
Al	2.71	28	23.6	15400	604	0.021	7.03
Ti	4.5	30	21.3	16700	924	0.058	12.77
Cu	8.94	35	23.4	12800	794	0.045	11.65
Mo	10.28	36	29.3	17400	1066	0.067	12.85
W	19.27	55	31.9	14300	1078	0.096	18.24

Table 5.4: Material properties and predicted performance of possible cathode materials [Polk et al. 2008].

and the decision if a feeding system should be integrated. Without such a propellant supply system, thruster operation is limited. A detailed description of possible realizations is given in section 5.3. Apart from the propellant demand and the material selection, the erosion behavior under the given conditions will be investigated in the following.

5.2.1 Propellant Demand

Widely used cathode materials in literature are Al, Cu, Ti, Mo and W. Moreover, Fe, C and CFRP (Carbon Fiber Reinforced Plastic) have been tested especially for thruster applications. The theoretical propellant demand can be calculated based on the data of [Polk et al. 2008]. As shown in chapter 2, there is a dependency of erosion rate E_r and ion velocity u_i respectively specific impulse I_{sp} on the ion mass M_i. Table 5.4 gives a summary on these parameters for cathode materials used in most studies.

The necessary propellant mass can be derived from the Δv, which is determined by the mission design for a given maneuver. Assuming that the exhaust velocity v_e remains constant, with the inital total mass m_0 and the final total mass after the end of the maneuver m_1, Δv is given as [Jahn 1968]

$$\Delta v = v_e \ln \frac{m_0}{m_1}. \tag{5.1}$$

The exhaust velocity is equal to the product of specific I_{sp} (given by the propellant properties) and gravitational acceleration g (= 9.81 m/s^2). With propellant mass $m_{prop} = m_0$ - m_1 equation 5.1 can be transposed into

$$m_{prop} = 1 - \frac{m_0}{e^{\frac{\Delta v}{v_e}}}. \tag{5.2}$$

With the density ρ of the propellant material, the necessary propellant volume can be determined from this. The geometry of the cathode is limited by the dimensions of anode and insulation. In the example at hand, the cathode has to be of cylindrical shape with a maximum diameter of 1.5 mm, while the length of the cathode is limited by the rail structure of the satellite to around 100 mm at most. At this, a smooth erosion of the full cross section of the cathode rod has been observed as shown below.

Element	ρ (g/cm^3)	m_{prop} (g)	m_{pulse} (μg)	l_{prop} (mm)	l_{pulse} (nm)	No. of Pulses
C	2.25	0.89	0.68	223.74	171.0	1,308,269
Al	2.71	1.26	1.12	264.14	233.9	1,129,438
Ti	4.50	0.83	1.20	104.01	150.9	689,222
Cu	8.94	0.96	1.40	60.92	88.6	687,440
Mo	10.28	0.72	1.44	39.47	79.3	497,871
W	19.27	0.71	2.20	20.82	64.6	322,253

Table 5.5: Predicted propellant demand for different cathode materials of 1.5 mm diameter at an exemplary Δv of 7.5 m/s, a peak pulse current of 40 A and a pulse length of 4.75 ms ($Q_{pulse} \approx 95$ mC). Density ρ according to [Lide 2003].

The VAT is a pulsed propulsion system. Hence, the total propellant demand is given by the sum over all pulses that were ignited during the maneuver. The mass per pulse m_{pulse} can be calculated with the erosion rate E_r and the electric charge per pulse Q_{Arc}. As shown in the previous chapter, this is given as

$$m_{pulse} = E_r \int_{t_0}^{t_1} I_{Arc}(t)dt. \tag{5.3}$$

The total number of pulses N required for the proposed maneuver is then given as the quotient of the total propellant mass m_{prop} and the mass per pulse m_{pulse}. Under the assumption of a smooth erosion over the whole cross section of the cathode, the length of the consumed propellant material per pulse l_{pulse} and the required total length l_{prop} can be calculated for a given diameter of cylindrical cathode (here 1.5 mm):

$$l_{pulse} = \frac{m_{pulse}}{\rho \pi r^2} \;\rightarrow\; l_{prop} = N l_{pulse} \tag{5.4}$$

Based on the example of section 4.1 ($Q_{Arc} = 95$ mC) and $\Delta v = 7.5$ m/s, table 5.5 gives values for m_{prop} and l_{prop} as well as for m_{pulse} and l_{pulse} for a cylindrical cathode of 1.5 mm diameter under inclusion of table 5.4. The mentioned Δv is obtained from the mission scenario for a proposed successor of the 1U-CubeSat UWE-3 [Kronhaus et al. 2013]. Based on the exemplary input data, theoretically a total propellant mass of 0.83 g and a total length of 104.1 mm of titanium (= four cathodes with a length of 26.03 mm) are necessary for this. Per pulse a mass of 1.2 μg and a cathode segment of 151 nm will be consumed. Analogously, 689,222 pulses have to be accomplished. At a pulse repetition rate of 0.5 Hz, it will take 382.9 h or around 16 d to execute the planed maneuver. This shows that not only a reliable, repeatable thruster operation is essential but also a suitable feeding mechanism is required to achieve the intended Δv.

5.2.2 Material Selection

Based on the considerations above, W is the most interesting material with regard to propellant efficiency and expected thrust-to-power ratio. However, it is very difficult to

Element	M (AMU)	E_r (μg/C)	v_i (m/s)	I_{sp} (s)	η	T/P (μN/W)	T_m (K)
In	114.82	-	5500	-	-	18.59	429.75
Sn	118.69	295	7500	139	0.016	22.95	505.08
Pb	207.2	510	5400	94	0.014	30.39	600.61

Table 5.6: Material properties and predicted performance of possible cathode materials with a low melting point [Polk et al. 2008].

mill and tends to break already during machining. This is owed to the low ductility of W, which is usually provided as a sintered product by the manufacturer. Testing shows that W cathodes tend to produce macroparticles which lower the performance. These macroparticles are probably produced because of the high heat load applied by the cathode spots. This leads to high tensions within the cathode which, in case of material with low ductility like W, leads to a cracking within the affected area. Mo, that has comparable properties, shows a similar behavior.

Better performance is predicted for Cr [Polk et al. 2008]. However, the database on this element regarding thruster applications is very small. Since its material properties (see table 5.4) are very similar to W and Mo, an equivalent behavior is assumed. An alternative with a relatively good performance prediction by [Polk et al. 2008] and with a big database in literature is Ti. To verify these predictions and the good experience made in literature, the thrust of a coaxial Ti thruster was measured with the balance described in chapter 3 for different pulse energies by [Kramer 2014]. The discharges were thereby produced with an IES PPU (L = 230 mH) with additional capacitor (C = 1000 μF) at different input voltages, ranging from 30 to 60 V. With pulse length up to 8 ms pulse energies between 1.3 and 1.7 J have been achieved.

Thereby, a thrust-to-power ratio for Ti of 13.49 μN/W was determined which is comparable to the 12.77 μN/W predicted by [Polk et al. 2008]. As shown in the next subsection, a relatively smooth erosion over the whole cathode cross section has been observed during testing. However, under the given circumstances an expansion of the cross section has been observed that probably results from the heat load. At longer operation times (some 100 pulses), this leads to a cracking of the thin ceramic insulation used for testing. Although it has been shown that the performance of Ti is in agreement with literature, a further optimization of cathode diameter and insulation thickness is necessary.

As predicted by [Polk et al. 2008], materials with a low melting point have a higher thrust-to-power-ratio than common cathode materials (e. g. 22.95 μN/W for Sn compared to 12.77 μN/W for Ti). Hence, the use of such materials has been investigated. Table 5.6 gives an overview on the properties of possible cathode materials with a low melting point.

Due to the small database of materials with a low melting point regarding VAT applications, the theoretical propellant demand will only be calculated for Sn and Pb. Based on the calculation method above, table 5.7 shows that compared to the values of

Element	ρ (g/cm^3)	m_{prop} (g)	m_{pulse} (μg)	l_{prop} (mm)	l_{pulse} (nm)	No. of Pulses
Sn	5.77	5.49	11.8	548.04	1157	464,838
Pb	11.34	8.10	20.4	404.22	1018	397,072

Table 5.7: Predicted propellant demand for Ti and Pb cathodes of 1.5 mm diameter at an exemplary Δv of 7.5 m/s, a peak pulse current of 40 A and a pulse length of 2 ms ($Q_{pulse} \approx 40$ mC). Density ρ according to [Lide 2003].

table 5.5 much more propellant is necessary for the exemplary Δv (e. g. 548 mm for Sn compared to 104 mm for Ti). This requires more space and mass than for common cathode materials like Al, Cu or Ti. Moreover, compared to these materials more droplets have been observed during testing. This, as already discussed, lowers the efficiency of the thruster (e. g. only 0.016 for Sn compared to 0.058 for Ti [Polk et al. 2008]) and may lead to more contamination of the surrounding satellite structure. The fusing of anode and cathode which was also observed for Ti cathodes can occur already after some dozen pulses at typical pulse energies in the range of 1 J, as experiments with an In cathode show. According to [Boxman et al. 1995] a heat flux of up to 10^{13} W/m^2 is to be expected which equals a heat load of around 785 W for a assumed cathode spot diameter of 10 μm. Depending on the depth of the affected cathode area a temperature variation of $122.5 \cdot 10^9$ K·m follows. Thereby, the melting point of In is easily reached within a few pulses.

Therefore, such materials are only interesting if only a few pulses with higher thrust are required. Regarding to the low predicted efficiency this is only reasonable if the actual measured thrust-to-power ratio is comparable to the theoretical value. To validate this and to gain data for comparable cathode materials, the thrust-to-power ratio of In was evaluated. Due to its physical properties a behavior similar to Pb and Sn is expected. [Polk et al. 2008] predicts a thrust-to-power ratio of 18.59 μN/W. However, it was thereby pointed out that macroparticles will probably further lower the predicted performance. Measurements with the setup described in chapter 3 showed a thrust-to-power ratio of only 9.72 μN/W [Kramer 2014]. A probable explanation might be the massive production of macroparticles observed during testing, which leave the thruster under very flat angles ($< 30°$ to the surface normal of the cathode) with very low velocities ($\sim 10^2$ m/s). Thus, due to their low thrust performance, their macroparticle production and their low propellant efficiency, materials with a low melting point are not suitable for the intended application.

5.2.3 Erosion Behavior

Up to now it was assumed that the cathode is eroded evenly over the whole cross section. An optimal erosion can be achieved if the arc moves to the cathode center. However,

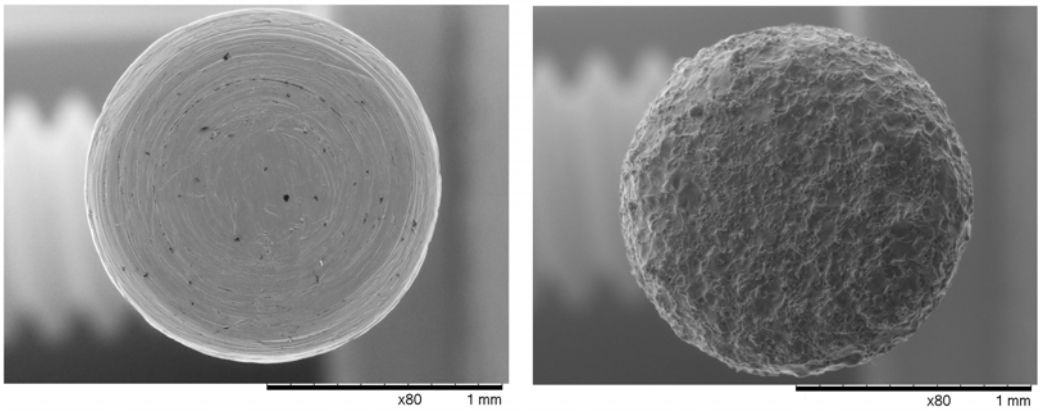

Figure 5.9: Ti cathode of 1.5 mm diameter before (left) and after 100 pulses with an energy of 1.7 J and a duration of 4 ms (right). As expected, the surface structure is massively influenced by the cathode spots. The whole cross section is covered with craters, which are formed by the erosion of the cathode spots. As visible, the whole cathode surface is affected.

experiments at the beginning of this thesis with an IES PPU and cathode diameters of around 4 mm showed that only a ring with a thickness of around half a millimeter was eroded. This is owed to the low pulse energies of only some mJ and the short pulse length of only some hundred μs (see chapter 4). The short residence time (up to 50 ns [Boxman et al. 1995]) prevents, together with the low energy input, the cathode spots from moving to the center of the cathode [Lun and Law 2015] showed that longer pulses (some ms) with higher pulse energies (some 100 mJ) lead to a higher heat load and thus to a even erosion of the whole cathode cross section. Pulse length of several ms and pulse energies in the range of 1 J are easily reached with the CES PPU developed within this thesis (see chapter 4) and lead, supported by the limited cathode diameter to 1.5 mm, to a smoother erosion than initially observed. Figure 5.9 shows a Ti cathode before and after 100 pulses with around 1.7 J pulse energy.

As visible the cathode surface was only roughly pre-conditioned by an Al_2O_3 cutoff wheel. Since thruster operation changes the surface condition rapidly, it is only interesting for the first few pulses. Essentially, once deployed in space, the thruster has to work under any circumstance. Therefore, no effort was set into determining the optimal surface condition for ignition, arc movement and erosion rate. However, as [Lun and Law 2013] pointed out, the shape of the cathode has an influence on the arc movement and erosion rate. Especially an inside conical cathode with a opening angle of 120° shows a higher arc mobility and an increase of 68 % for I_{sp}. However, under spacecraft conditions with up to a million pulses this cone will not exist for more than some 1,000 pulses. For a cathode diameter of 1.5 mm this cone would be 0.43 mm deep. The remaining volume of this part of the cathode would be $5.07 \cdot 10^{-10}$ m^3. From the calculation for the propellant demand (see subsection 5.2.1) follows that this amount of a Ti cathode would be consumed within around 3,200 pulses. Therefore, a modification of the cathode shape was not further investigated.

In general it appears that while the erosion, averaged over numerous pulses, is spread over the whole cathode, within a single pulse erosion is very localized, i. e. the cathode spots are stationary and concentrated at one area of the cathode. This is illustrated in figure 5.10. Thereby, the cathode spot movement within a period of around 230 μs has been observed with the high speed imaging setup described in chapter 3. The region of origin is almost constant over the acquisition time. A closer look with the SEM shows relatively big craters and also droplet-like structures (see figure 5.11). The edges of the

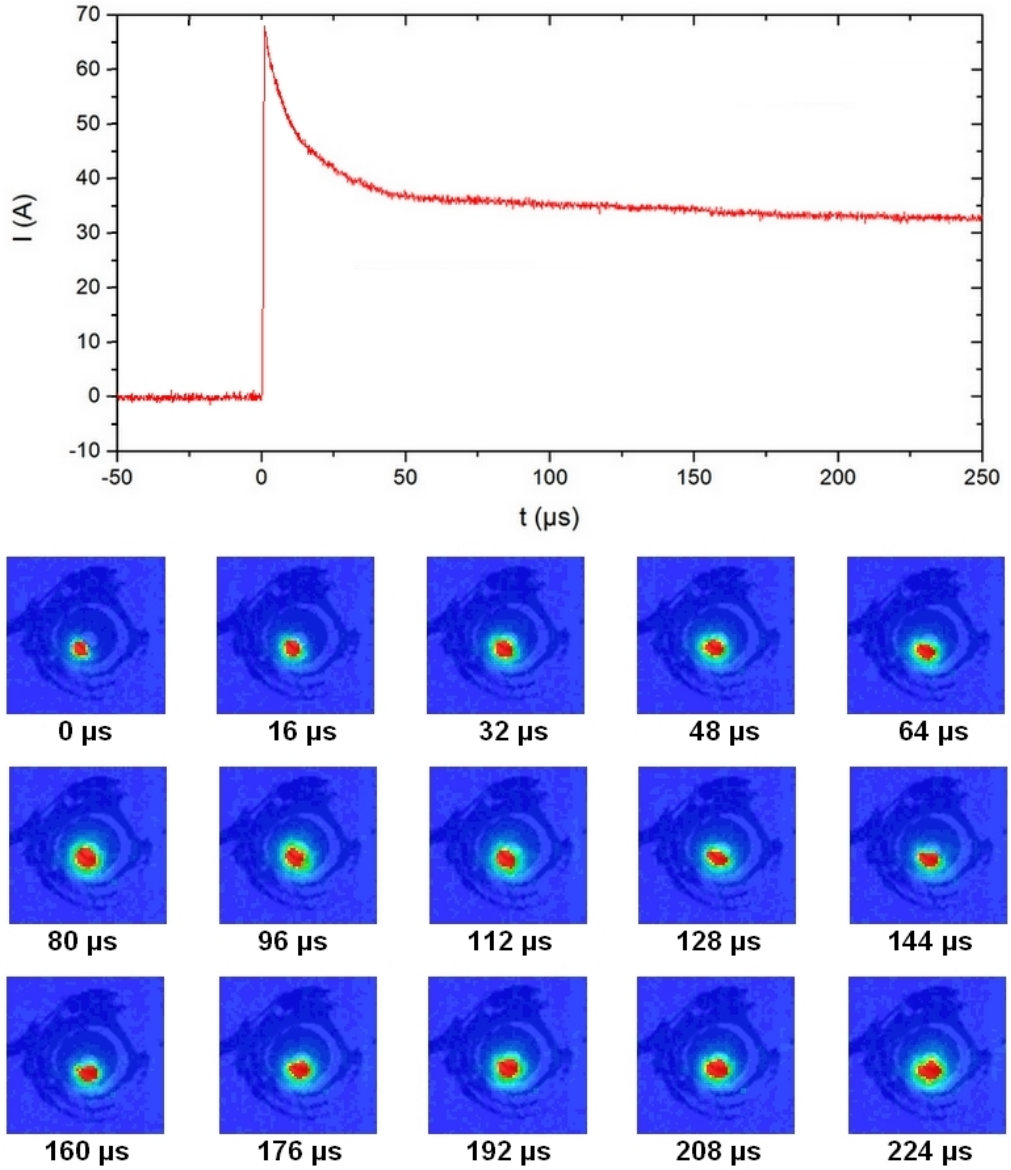

Figure 5.10: High speed imaging sequence taken at a Ti cathode of 1.5 mm diameter (U = 40 V). During the first 230 μs of the discharge no cathode spot movement is observed. This behavior dominates the further discharge apart from some erratic changes of the spot location.

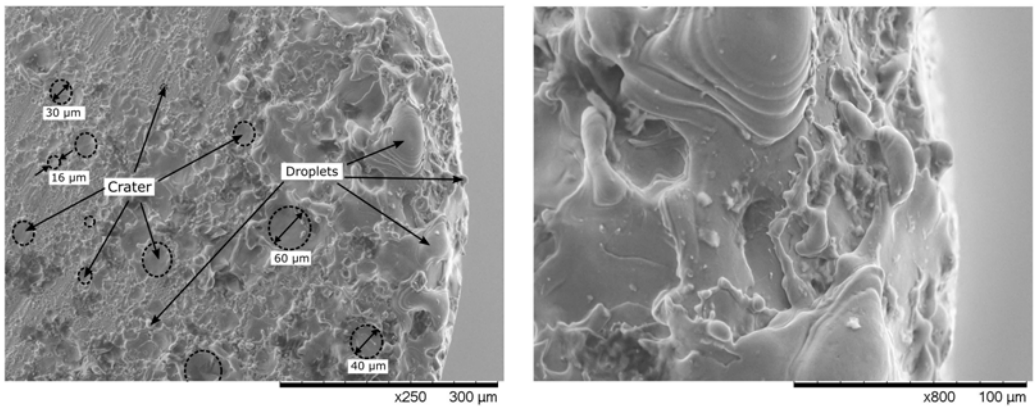

Figure 5.11: SEM images of a Ti cathode after one pulse with 1.7 J and a duration of 4 ms. Craters at the edge of the cathode are bigger than the distant craters (left). The crater edges show molten structures (left). This leads to the formation of droplets (right).

craters are not very well defined, which makes it difficult to determine the size of the cathode spots. However, it seems that due to their long presence in a given location, they are relatively big (10 – 100 μm). This behavior matches more with type 3 spots, which can be found on semiconductors than with type 1 or 2, spots which are expected due to the good conductivity of Ti (see chapter 2).

In the worst case, the cathode spots are concentrated at one location for several pulses. This results in a higher thermal load on the insulator, which finally cracks. Thus, the insulator is locally recessed and the vacuum arc evolves between the walls of anode and cathode. Anode wall and insulator surface are covered with macroparticles and a fusing of both electrodes may occur. One possible solution is the reduction of the peak current, which is simply achieved by a higher cable resistance or by an additional inductivity in the PPU circuit. However, this reduces also the pulse energy and therefore the thrust. Another approach is the use of a segmented anode [Lun and Law 2015]. As introduced by [Vergason et al. 2001] for vacuum arc deposition, this technique allows a significant reduction of the cathodes surface roughness and a decreased macroparticle production. This is realized by several discrete anodes with insulation in between. One after each other is then switched sequential to the power supply. The corresponding setup is illustrated in figure 5.12. Thus, the cathode spots have to move their location from one anode to another.

[Lun and Law 2015] adopted this approach for VAT application and observed a more even erosion and a reduced roughness of the cathode surface. The heat load is distributed over the whole surface and not concentrated on a single area. Thus, fewer macroparticles are produced which otherwise reduce the effective thrust. By this an increase in thrust of up to 20 % and in specific impulse of up to 27.9 % was shown. However, the switching requires additional MOSFETs and high side drivers. The portioning of the anode leads to very small anode segments (see figure 5.12) with additional wiring. Therefore, at current

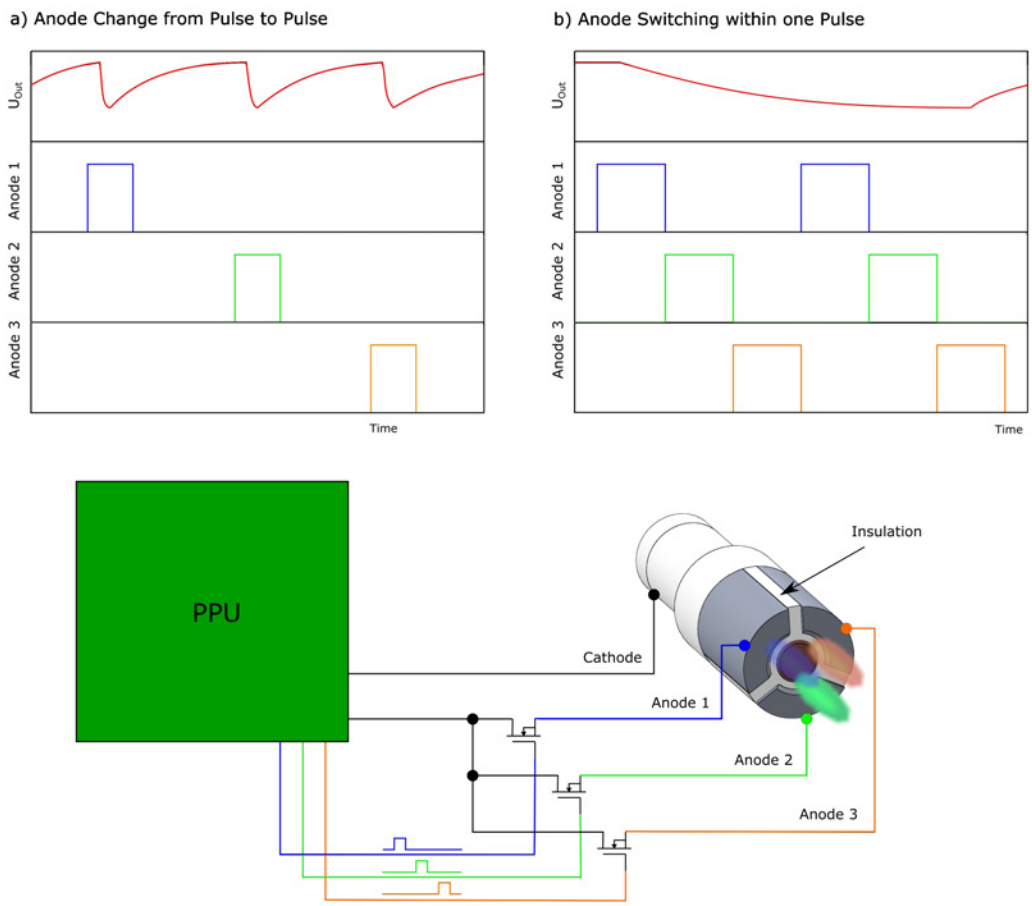

Figure 5.12: Thruster setup with a segmented anode. One segment after each other is switched sequential to the power supply. The cathode spots are thereby forced to change their location. Two possible switching patterns are possible: a) Anode change from pulse to pulse, i. e. the arc location is not enforced within one discharge. b) Anode switching within one pulse. This requires a fast switching logic and may lead to a noisy discharge [Lun and Law 2015].

state this approach is not reasonable under CubeSat limitations, although bigger satellites may benefit from this technique. Another solution for a higher cathode spot mobility and hence a better distribution of the heat load over the whole cathode surface is the application of magnetic fields as introduced by [Keidar and Schein 2004]. Earlier work, e. g. of [Smith 1957] and [Robson 1978], showed a significant influence of magnetic fields on the cathode spot movement. This approach will be further investigated in the next chapter. First, the solutions for the feeding of the reaction mass will be examined.

5.3 Propellant Supply System

Due to the consumption of the cathode material some kind of refill mechanism is necessary, similar to PPTs, where the PTFE (PolyTetraFluorEthylene) insulation is eroded.

Typically, PPT systems are equipped with a mechanical feeding simply based on a spring, e. g. [Hamidian and Dahlgren 1973], or they do not have any kind of feeding mechanism, e. g. [Ozaki et al. 2011]. This increases the simplicity and robustness of the thruster but drastically limits its operation time. Thus, it is still an important research subject with challenges similar to the VAT feeding system [Lau and Herdrich 2013]. As [Hamidian and Dahlgren 1973] did for PPTs, [Schein et al. 2002] proposed a simple spring mechanism for propellant feeding. However, as it becomes clear in the following, several issues prevent a realization of this approach for the use on CubeSats. Alternative solutions are electro-motors, piezoelectric actuators and shape memory alloy actuators. Unfortunately, the mass, space and power limitations of a 1U-CubeSat are a serious challenge for all these possible approaches.

5.3.1 Conventional Feeding Mechanisms

The idea behind a spring as actuator is that no control system is necessary, since the spring is expanded with the same rate as the cathode is consumed. Analogously, this expansion pushes the cathode forward, as it is illustrated in figure 5.13. However, this requires a step or alike at the end of the insulation to prevent the spring from pushing out the cathode completely [Schein et al. 2007]. This is a common solution for PPTs where the step is implemented into the electrode structure [Hamidian and Dahlgren 1973]. Thereby, the soft PTFE is pushed against the metallic electrodes. This works well, especially since the PTFE heats up and becomes softer during thruster operation. As shown above, in VAT design usually alumina is used as insulator. Thus, a hard but ductile metal is pushed against a hard and brittle ceramic. Both cathode and insulation are heated up from which a cracking of the insulation may occur. The erosion affects only some hundred nm per pulse. Therefore, the step has to be very thin to allow cathode erosion itself. Assuming that the

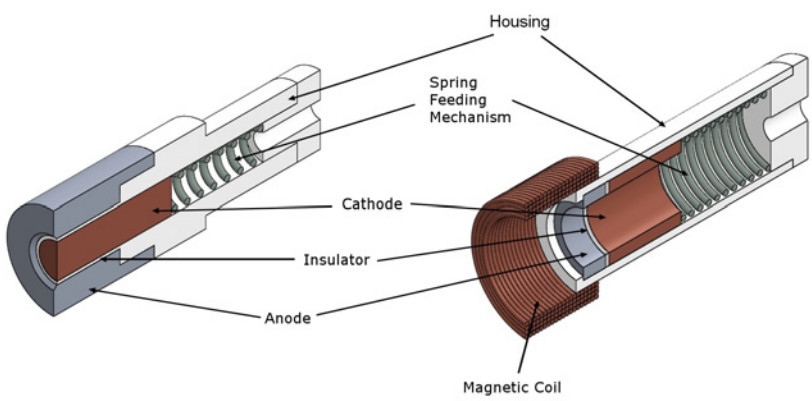

Figure 5.13: Schematic illustration of a coaxial (left) and a ring thruster (right) with spring feeding mechanism according to [Schein et al. 2001] and [Keidar et al. 2005]. The cathode is pushed forward by the spring with the same rate as it is consumed by the vacuum arc.

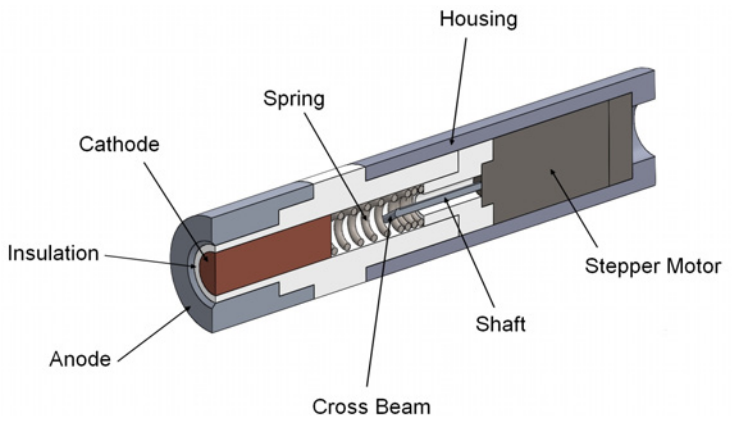

Figure 5.14: A possible combination of spring and stepping motor. The cross beam prevents the spring from expanding. A stepwise motion of the motor partially releases a winding of the spring, which can thus expand for some μm and pushes the cathode forward.

alumina is already weakened by the vibration and g-forces during launch, a destruction of this structure can be expected especially during thruster operation. Hence, this solution is no option for a coaxial thruster, although it works with the ring electrode setup of [Keidar et al. 2005] as shown in figure 5.13. However, for the work at hand it was chosen to use the coaxial setup. Thus, another approach is necessary.

A possible alternative is the use of a stepping motor for a precise cathode movement in the range of μm or even nm. Off-the-shelf motors can be purchased with a wide variation of torque and steps per rotation (e. g. [Dr. Fritz Faulhaber GmbH & Co. KG 2015a]). The size and mass of rotational steppers which can achieve the necessary motion force meet barely the restrictions for the intended CubeSat integration. The smallest stepper motor of [Dr. Fritz Faulhaber GmbH & Co. KG 2015a] e. g. has a length of 9.5 mm, a diameter of 6 mm and a mass of 1.1 g. An additional gear system is required for the transformation into a linear motion. Moreover, a driver unit is necessary, which has to be developed especially for this application since purchasable units are too big for that (e. g. controller board for maximal two motors: 68x47.5x13 mm and 22 g, peak current up to 1.6 A at 9 – 36 V [Dr. Fritz Faulhaber GmbH & Co. KG 2015a]). Thereby, the space, mass and power budget easily overshoots the limitations. Alternatively, the stepping motor can be used as stopping element of a spring.

As illustrated in figure 5.14, a shaft is attached to the motor, which is aligned with the longitudinal axis of the spring. At the end of the shaft, a cross beam is mounted which prevents the spring from expanding. Each incremental movement of the motor releases some μm of a winding which leads to a slight expansion of the spring. Since the direct rotational motion of the stepping motor can be used, no further gear mechanism is needed. However, the realization of this concept has to be left for future development.

5.3.2 Shape Memory Effect Spring

Due to the simplicity of the spring feeding mechanism, a realization has been further investigated. Since it is not possible to prevent the spring from expanding without a step in the insulation or a stepping motor, another solution is necessary. This has been found in a Nitinol (Nickel Titanium Naval Ordonnance Laboratory) spring which allows the realization of the concept by [Schein et al. 2002] without any stopping system [Schuster 2014]. Nitinol is a noncorrosive and highly-tensile shape memory alloy consisting of nickel ($\tilde{5}5\%$) and titanium which can easily be deformed at room temperature.[Buehler et al. 1963]. If it is heated over its transformation temperature of around 80°C it recaptures its original form which was set by annealing at around 500°C [Chen 2010]. Typical applications are actuators for valves. Within the field of CubeSat development, Nitinol actuators are planed as release switch for additional solar panels [Grulich et al. 2015].
The thermal expansion coefficient of Nitinol is similar to other metals and therefore very small. Thus, only short elongations are possible and subsequently other shapes are necessary for bigger traveling distances. For the integration into a CubeSat a spiral spring of 0.58 wire diameter, 4 mm winding diameter and an initial length of 12.22 mm was chosen. This spring allows a traveling distance of 5 mm [G. Rau Gmbh & Co. KG 2013]. Accordingly, the spring is compressed by this length before it is attached to the mounting structure of the VAT. The necessary temperature for the back transformation could be applied directly by the electrical current of the vacuum arc. The electrical resistivity of Nitinol ranges typically from $76 \cdot 10^{-6}\ \Omega \cdot \text{cm}$ and $82 \cdot 10^{-6}\ \Omega \cdot \text{cm}$ while its coefficient for thermal expansion α_{T_0} lies between $6.6 \cdot 10^{-6}\ /°\text{C}$ and $11 \cdot 10^{-6}\ /°\text{C}$. The exemplary spring of 12.22 mm length has a wire length of 31.31 mm and a resistance of 0.8 Ω at room temperature. From Ohm's law and [Serway and Jewett 2003]

$$R(T) = R(T_0)(1 + \alpha_{T_0} \cdot (T - T_0)) \tag{5.5}$$

it can be calculated that a current typical for VATs of 38 A at an arc voltage of 20 V is required to start the back transformation. If the current is guided through the spring only as long as an expansion is required, a stepwise feeding of the cathode is achieved. Otherwise, which is the normal case, the current is directly guided to the anode via a bypass connection. For the switching between these two cases a power MOSFET is used (see figure 5.15). As mentioned in chapter 4, the feeding mechanism is activated if the capacitor voltage, which is monitored by the microcontroller via ADC, is not discharged below a predefined threshold value which means that no proper discharge occurred. Subsequently, the spring expands due to the resistive heating by the applied current. If the ADC measurements show that the capacitor voltage falls again below the threshold, the feeding systems is deactivated.
The continuously changing electric resistance and variations in the heating process lead to a nonlinear expansion. Therefore, a frequent monitoring of this process is necessary. Moreover, as this process depends on a temperature change, a proper insulation against thermal influence from the outside is required. However, for thermal variations like they

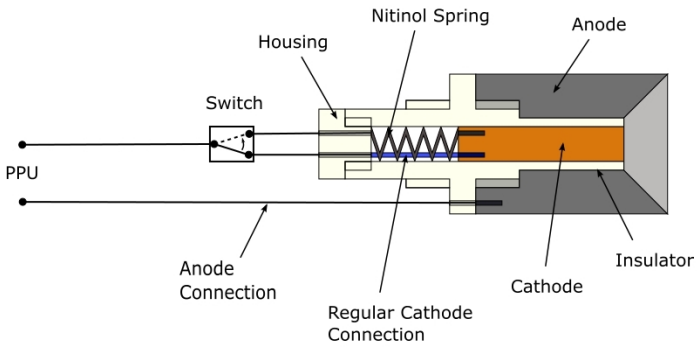

Figure 5.15: Schematic illustration of the cathode feeding with a shape memory alloy spring. If feeding is necessary a switch, e. g. a MOSFET, is activated which guides the arc current through the Nitinol spring.

were measured on UWE-3 (-25 – + 29°C [Rathinam et al. 2015]), a housing of PEEK is sufficient for thermal insulation. Since PEEK is good to mill, this housing can also be used as mounting element between thruster and satellite. The constructive realization is shown in the last section of this chapter.

5.3.3 Piezoelectric Cathode Feeding

Another form of an electrically supplied motion can be achieved by using the piezoelectric effect. The elastic deformation of certain crystals and ceramics like doped lead zirconate titanate (PZT) generates a voltage between the opposite ends of the element [Martin 1972]. This effect is widely used for sensors and filters. The *inverse* piezoelectric effect is the application of a voltage to such an element that leads to an expansion of the material of up to 100 μm. Therefore, this effect alone cannot achieve the necessary traveling length for a propellant feeding system.
However, due to the mechanically robust and small mounting options various linear and rotational systems have been developed for industrial applications, e. g. [Dr. Fritz Faulhaber GmbH & Co. KG 2015b]. Although they are smaller and lighter in comparison to stepper motors with similar performance data, the electrical components are of similar mass and dimension. Therefore, conventional piezoelectric motors are currently not suitable for CubeSat integration. For the linear motion of the cathode relatively small forces are necessary. Hence, much smaller piezoelectric motors can be used like the so called "squiggle" motor [New Scale Technologies, Inc. 2014]. At an input voltage of 3.3 V, which fits perfectly to a typical CubeSat EPS, and an input power below 340 mW a stall force of 0.3 N can be achieved.

In figure 5.16 a possible integration is illustrated [Eckert 2015]. As it is visible, the biggest part of the system is the motor controller which requires an additional space of 50x30 mm on the PPU board. However, at the current PPU layout a second "floor" would be necessary for implementation. But due to the small size of the motor itself and the fact

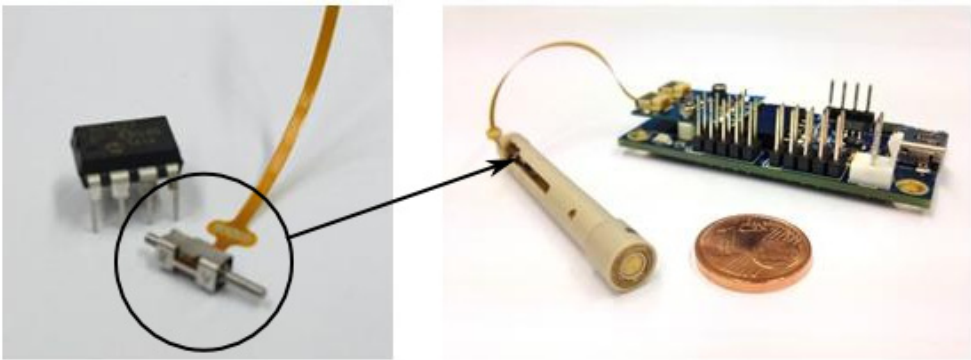

Figure 5.16: Left: Size comparison of a New Scale Technologies squiggle motor with a DIP-8 IC. Right: Prototype for a piezoelectric feeding system based on a squiggle motor. This motor allows a cathode feeding of 6 mm length at an input power below 340 mW.

that no additional mechanical gear system is required, the system can easily be integrated into the CubeSat structure. As shown by table 5.8, thermal range and shock resistance are also acceptable for CubeSat integration.

However, due to the thermally caused spread of the cathode cross section mentioned above and irregularities along the cylindrical surface, a seizing of the cathode may occur. If the resulting friction forces overstrain the capabilities of the motor, no further feeding is possible. To prevent a fusing of both electrodes, a constant motion of the cathode may be useful. This motion can be applied by a rotational piezoelectric motor with a low power consumption or maybe by a constantly knocking motion against the backplane of the cathode by a linear piezoelectric actuator. Yet, the simplest solution is the installation of a thruster with multiple cathodes.

Travel Range	6 mm
Housing Dimensions	2.8 x 2.8 x 6 mm
Resolution	0.5 μm
Stall Force (at 3.3 V input)	0.3 N
Speed (at 15 gram force load)	$>$ 7 mm/s
Input Power	$<$ 340 mW
Lifetime	$>$ 1 million cycles
Operating Temperature	-30 to +80°C
Shock Resistance	2500g
Mass	0.16 grams

Table 5.8: Relevant technical data of the SQL-RV-1.8 squiggle motor [New Scale Technologies, Inc. 2014].

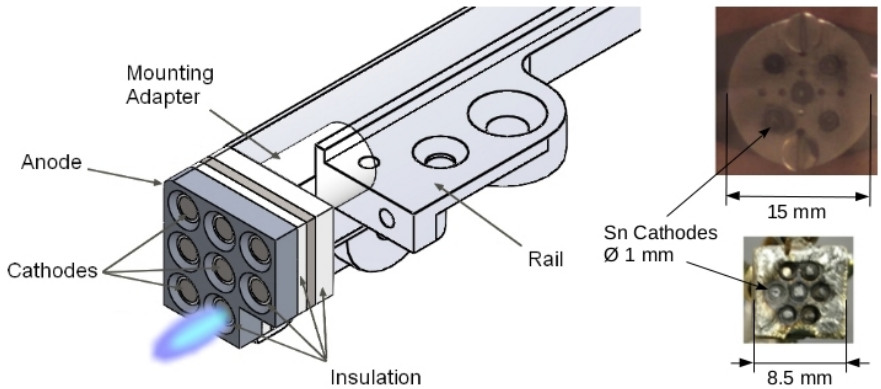

Figure 5.17: Design concept for a multi cathode array without feeding system adapted to CubeSat demands. The two pictures on the right show prototypes with Sn cathodes of which the lower one was operated for 10^4 pulses without disruption.

5.3.4 Multiple Cathodes

A thruster with multiple cathodes can be a feasible alternative if a feeding system can not be integrated. Apart from a possible electrode fusing, a multi-cathode thruster is more reliable since no additional mechanical or electronic parts can cause a failure of the VAT system. Moreover, a thinner VAT assembly is possible since the necessary reaction mass is split into several cathodes. This idea has been adopted by several concepts: [Osiander et al. 2006] mentioned a digital thruster design with different possible types of microthrusters based on MEMS. Moreover, it is suggested to use the material of the solar arrays for end-of-life maneuvers, i. e. de-orbiting [Slotten et al. 2013].
As in the previous developments, significant changes of the CubeSat design should be avoided. Especially the side panels with the solar arrays, ADS sensors and magnetorquers should ideally not be affected by the integration of a multi-cathode thruster. Therefore, a solution is necessary where only the rails are used for attachment and which allows to use the whole surface of the solar arrays for energy supply. However, in principle up to four cathodes with a diameter of 1.5 mm can be placed within the front plane of a rail. If again a Δv of 7.5 m/s is intended and the cathode consists of Ti, for each of the 16 cathodes (four rails with four thrusters) a length of 6.51 mm is required.
This is too long for operation without a feeding system. However, the exemplary CubeSat based on UWE-3 allows a bigger thruster surface due to the dimensions of the solar arrays. Without any affect on the power supply, a maximum side length of 12 mm is possible if the thruster has a square cross section. Since no changes to the side panels are desired, the thruster has to be mounted to rails without contact to the solar arrays. Thereby, the same mounting system as for a coaxial thruster can be used, which will be described in the final section of this chapter.

Figure 5.17 shows a possible realization with 12 cathodes on every rail. At an assumed cathode diameter of 1.5 m/s an individual length of 2.17 mm or a lifetime of 14,359 pulses

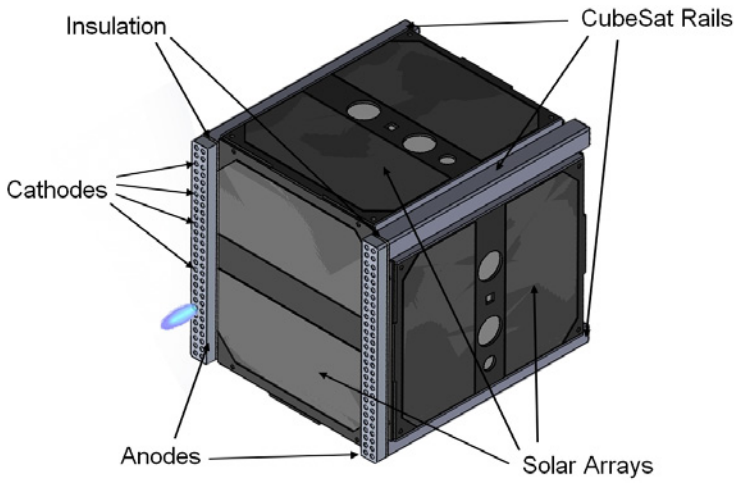

Figure 5.18: Another solution for the installation of a VAT system with multiple cathodes. All connections for the two anode bars and the cathodes are guided through the CubeSat rails. The reduction of the surface of the solar arrays is negligible.

will be necessary for the exemplary Δv. Bigger cathodes would reduce the necessary length and the number of pulses, but it has to be considered that due to thermal issues the anode volume should be maximized as mentioned above. This can be achieved if an aluminum bar of 100×8.5×5 mm is used as anode. Within this bar, numerous cathodes can be implemented. The thruster bar is then installed on the face plane of two CubeSat rails as shown in figure 5.18. A slice PEEK between thruster and satellite structure acts as insulation. Thereby, only a minimal fraction of the solar array is covered by the thruster assembly.

An individual control of every single cathode would require numerous additional electronic parts and cables. Thus, apart from the possible integration on bigger satellites it is necessary to renounce a corresponding system. If every cathode is connected to each other, ignition will occur at the location with the lowest resistance. This will change during thruster operation, so that every cathode will be used eventually. The location of thrust production on each thruster will therefore be rather indeterminable. Thus, a thorough monitoring of the resulting satellite motion by the ADCS is necessary.

As mentioned above, a prototype with seven Sn cathodes showed good operational behavior with a lifetime of around 10^5 pulses. The relatively thick alumina insulation (0.35 mm) required a reliable conductive film which was applied by a coating with macroparticles. Thereby, a total cathode length of 1.82 mm was measured. In case of Ti cathodes, the applied pulse energies of some mJ were not sufficient for a re-deposition of the conductive layer with cathode material. Since the development within this thesis concentrates on the coaxial VAT, further investigation has to show if under the influence of higher pulse energies a reliable operation of a multi-cathode is possible.

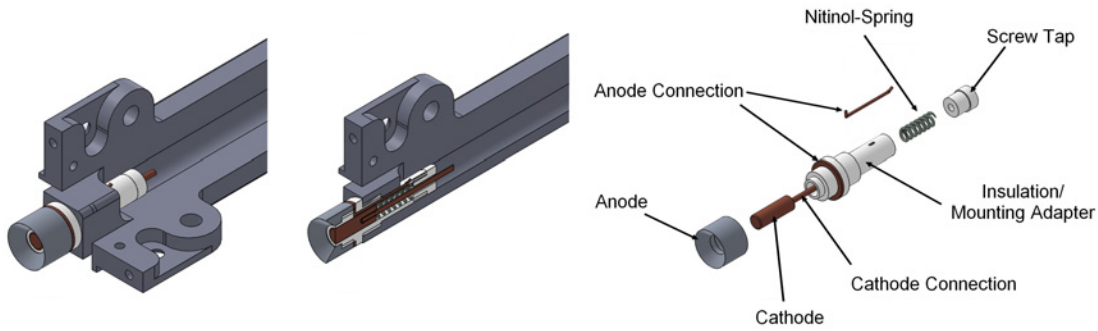

Figure 5.19: Integration of a VAT with shape memory effect spring feeding mechanism into the rail of an 1U-CubeSat. An exploded view shows the individual parts (right).

5.4 Roundup

From the findings of this chapter, a VAT design especially but not only for 1U-CubeSats has been developed. The individual design of anode, cathode and insulation has already been discussed. Now, additional structural elements which are necessary for the mounting onto the satellite and the housing of the feeding mechanism will be presented. Some issues regarding lifetime and reliability are still remaining yet. Possible approaches for future research will be shown at the end of this section.

5.4.1 CubeSat Integration

As mentioned at the beginning of this chapter, it is necessary to insulate the thruster from the satellite structure. This is, among other things, caused by the fact the rails are connected to satellite ground. Thus, the anode cannot directly be attached to the rail. For a reliable mechanical connection, PEEK was chosen as material for the mounting adapter which also comprises the feeding mechanism, e. g. the Nitinol spring. The adapter is attached to the rail with a metric M6 thread. Therefore, it is necessary to trim the rail by 6 mm and to tap the equivalent M6 thread centric into the face plane. For the reception of the feeding system, only some material from inside the rail has to be milled away. Thus, only a few changes of the rail are necessary.

Figure 5.19 shows an exploded view of the VAT assembly. As it is visible, the electric connection of the anode is integrated into the mounting adapter. Thereby, no additional holes in the rail are necessary. The anode is attached to the mounting adapter with an additional M6 thread. By screwing the anode tightly onto the adapter, an electric contact is achieved by a copper ring which is soldered to the PPU cable. The cathode connection is guided through the center of the Nitinol spring. Electrical contact is prevented by a Kapton insulation. The insulation between anode and cathode is made of alumina. As mentioned above, it is outfitted with a step which prevents it from slipping out of the

cathode.

Images of a prototype can be found in figure 5.20. To allow a view on the inner parts, the mounting adapter is made of acrylic glass. Moreover, it is equipped with a magnetic coil for the collimation of the plasma beam and the control of the cathode spot movement. These aspects will be discussed in detail in the following chapter. With this additional component, the geometric limits are definitely reached, especially with regard to the implementation of the coil cables into the mounting adapter. However, without significant changes, this mounting concept allows a fast adaption to other CubeSat structures like LibreCube (two units) or SNUSAT-2 (three units) [Scholz and Juang 2015], [Park et al. 2015]. Exemplary design concepts for these two satellites are illustrated in figure 5.21.

Yet, this concept is only one of many imaginable integration solutions. Based on the principle geometry and the considerations made within this chapter, it should be possible to scale this thruster concept to bigger cathode and anode diameters. Thereby, the integration to other satellite geometries with other design specifications should be viable.

5.4.2 Lifetime and Reliability

Ti was chosen as cathode material because of its good vacuum arc properties. Thrust measurements show a good compliance with theoretical predictions. Several solutions for common issues like the erosion of the conductive layer, the worsening of the arc initiation due to cathode consumption, an uneven cathode erosion and a fusing between anode and cathode have been evaluated:

- For a given cathode diameter and the available pulse energy of around 1 J, deposition of a conductive layer, possibly from the cathode material, has been observed. Unfortunately, a higher fusing probability comes along with this. Further research may find out how this process can be controlled.

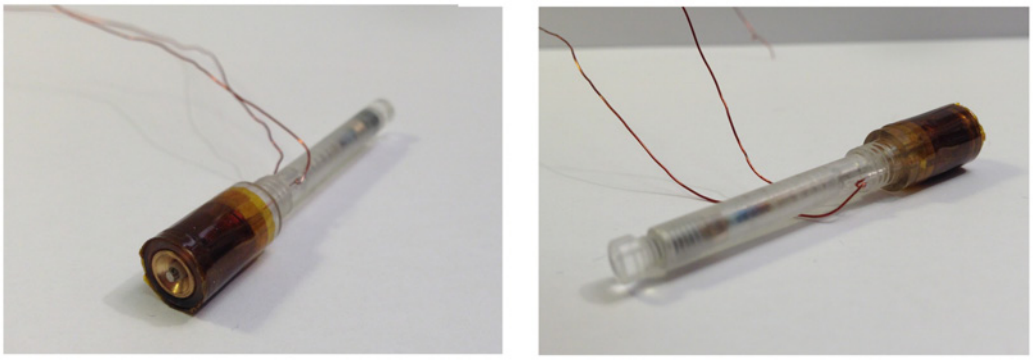

Figure 5.20: Images of a VAT prototype for the integration into a 1U-CubeSat. The mounting adapter is made of acrylic glass to allow a view on the inner parts.

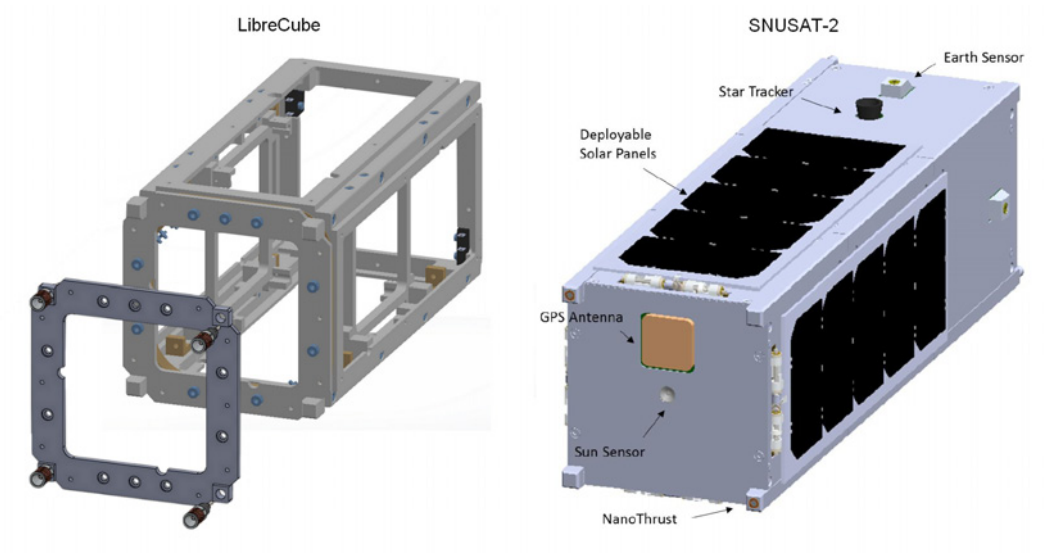

Figure 5.21: Possible implementation concepts for the equipment of LibreCube and SNUSAT-2 with a VAT system [Scholz and Juang 2015], [Park et al. 2015].

- The consumed cathode material can be replaced by using a feeding mechanism. However, due to a spreading of the cathode cross section by thermal effects, a seizing of the cathode can occur. This might be solved by a constant rotation of the cathode, which, on the other hand, consumes additional energy.

- Due to the size of the cathode and pulse energies in the range of 1 J, a relatively smooth erosion has been achieved. Yet, a very low mobility of the cathode spots has been observed which leads to a very rough surface and to a cracking or melting of the cathode material. A possible solution is the application of magnetic fields.

These issues limit the feasibility of the VAT massively. As described in earlier publications, only some 100 to 1,000 pulses have been achieved with Ti cathodes. Despite, the exemplary intended Δv requires a total lifetime of almost 700,000 pulses. Therefore, based on this work additional research is necessary. A further investigation of the surface composition with suitable methods like EDX can improve the knowledge of the re-deposition mechanism. The influence of magnetic fields under CubeSat conditions will be investigated in the following chapter.

Chapter 6

Application of Magnetic Fields

Within this chapter, the idea of improving the plasma beam geometry by means of a magnetic field is discussed. After a short overview on previous work on this topic, the various effects of magnetic fields on charged particles will be explained. Following that, a first attempt to influence the plasma plume with an axial magnetic field based on literature will be introduced. The actual realization for CubeSats is supported by field simulations which will show how an external field has to be positioned for the different effects. Finally, experimental results will show the feasibility for CubeSats.

6.1 Overview

As mentioned in chapters 2 and 3, the propagation of ions emitted by a VAT can be described by a Cosine or exponential distribution. According to this, [Polk et al. 2008] calculated a thrust correction factor of 0.64 respectively 0.67 for these two expansion patterns, i. e. only around two thirds of the ejected particles contribute to the effective thrust. The rest is not only useless for thrust production, it may even contaminate the satellite surface. The latter issue can be reduced by a geometrical shielding as shown in chapter 5. Unfortunately, a shadowing of the plasma plume leads to a further decrease in thrust. However, the quasi-neutral plasma of the vacuum arc can be influenced by magnetic and electric fields [Kimblin 1971], [Qi et al. 1998]. As shown by [Polk et al. 2008], electrical fields may enhance the performance of a VAT drastically e. g. a rise of I_{sp} from 924 s to 4689 s for Ti. However, this requires additional components like an acceleration grid and a neutralizer as well as the corresponding electronics. Bigger nanosatellites may allow the integration of a Vacuum Arc Ion Thruster (VAIT), but for 1U-CubeSats this is no option due to the already exhausted space and mass budget.
First experiments with magnetic fields have been conducted by [Kimblin 1971], who observes a reduction of the ion flux within an axial field. The directional control of the plasma plume and of the arc spot movement was investigated by [Gilmour and Lockwood 1972] and [Dolotov et al. 1974]. [Heberlein and Porto 1983] found out that a collimation

of the ion flux can be achieved by the application of magnetic fields and [Cohen et al. 1989] discovered that an axial magnetic field can lead to an increased ion flux. Further research by [Keidar et al. 1996], [Keidar et al. 1997] and [Anders and Yushkov 2002] supports this observation especially for thruster applications and shows that thrust and specific impulse can be improved. An actual application example for small satellites based on the initial PPU concept was introduced by [Tang et al. 2005]. Therefore, it seems appropriate to investigate the usage of a magnetically enhanced VAT within the limitations of a 1U-CubeSat.

6.2 Theoretical Background

As described in literature, both a reduction and an increase of ion flux respectively thrust can result from the influence of an external axial magnetic field. Hence, a short look on the physical background might be useful to define the actual desired focusing effect for CubeSat propulsion. A correct description of the particle motion within a plasma under the influence of a magnetic field is not trivial and requires magneto-hydrodynamics. Luckily, a simplified one-particle model is sufficient to explain how homogeneous and inhomogeneous axial magnetic fields may influence the path of electrons and ions in various ways.

6.2.1 Homogeneous Magnetic Fields

Initially, it is assumed that the magnetic field is homogeneous within the whole area of influence, i. e. the field strength and density is constant in time as well as in space. Moreover, the field lines are not diverging and remain parallel on an infinite scale. The equation of motion of a charged particle in a constant magnetic field is then given by the Lorentz force [Chen 1984]

$$m\dot{v} = \vec{F}_L = q\vec{v} \times \vec{B}. \tag{6.1}$$

The parallel component of $\vec{v}$ is zero since the Lorentz force acts only perpendicular to the magnetic field. However, due to collisional phenomena in the dense plasma right after ignition, it is rather unlikely that the particles are moving only parallel or perpendicular to the field lines. The most obvious proof of this is the Cosine or exponential distribution of the ion current distribution. Therefore, all particles will eventually be affected by the magnetic field. Charged particles are forced into a gyration around the field lines. The centripetal force is compensated by the Lorentz force and the corresponding cyclotron frequency is given by

$$m\omega_c^2 r = q\omega_c r B \rightarrow \omega_c = \frac{qB}{m}. \tag{6.2}$$

Thus, electrons and ions are gyrating in the opposite direction around the magnetic field lines as illustrated in figure 6.1.

The gyration leads to a current and subsequently to a magnetic field which acts against the original field. The result is a very small reduction of the effect of the magnetic field in

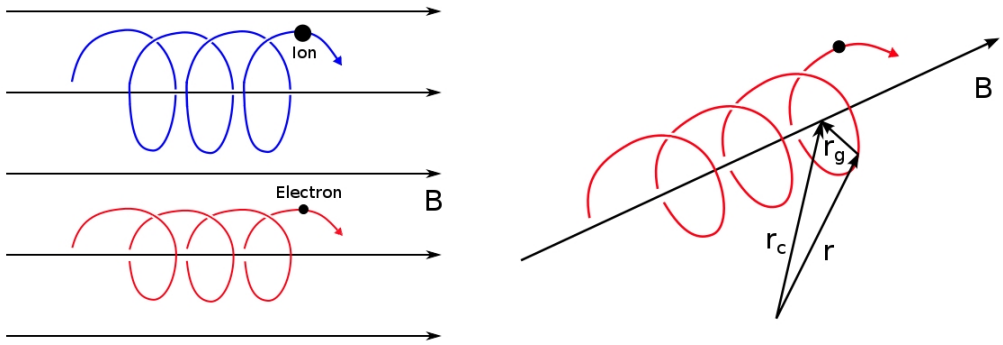

Figure 6.1: Left: Charged particles are forced into a gyration around the field lines of an axial magnetic field (based on [Chen 1984]). The direction depends on the charge of the particles, i. e. electrons and ions are gyrating in the opposite direction. Right: Particle motion under the influence of an additional external force. The resulting motion is a superposition of the gyrating motion and the external force.

general. Depending on the entrance angle into the field, charged particles will only gyrate stationary around the field lines or proceed along the field lines while gyrating. Thereby, it has been assumed that no further external forces have been applied and that the particles do not interact with each other. However, the expansion of the plasma plume due to Joule heating, electromagnetic forces and pressure can be seen as additional external force. Therefore, the general form of equation 6.1 is given as

$$m\dot{v} = \vec{F} + q\vec{v} \times \vec{B}. \tag{6.3}$$

Now, all particles are moving along open circular paths around the field lines, i. e. they describe a helical motion along the field lines. If B and F are constant over time the so called "guiding center" approach is valid: The resulting motion is a superposition of the gyrating motion and the external force F (see figure 6.1) [Chen 1984]. Thus, the particles are "trapped" by the magnetic field and guided along the field lines away from their origin. However, electrons and ions are moving with different velocities due to their different masses. This leads to an ambipolar diffusion of charged particles along or radial to the field lines, depending on the particular experimental setup. The solution of a given problem is not trivial and requires magneto-hydrodynamics [Chen 1984]. Apart from that, the field lines of a real magnetic field are not parallel on an infinite scale. Instead, they are diverging with increasing distance, which is also connected with a change of the field strength.

6.2.2 Inhomogeneous Magnetic Fields

In reality, magnetic fields are generated either by permanent magnetic materials or by the movement of electric charges [Plonus 1978]. The magnetic fields have in both cases an inhomogeneity in space. Depending on the shape and dimensions of the source, the field

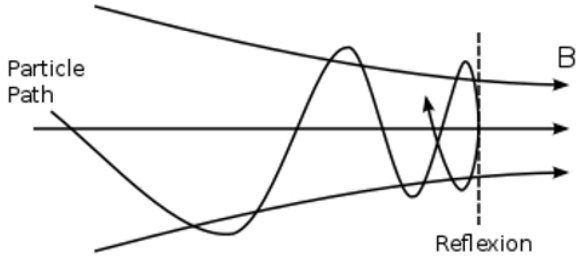

Figure 6.2: Magnetic mirror effect, based on [Plonus 1978]: Charged particles are reflected in a converging magnetic field.

strength is approximately homogeneous only within a limited part of the field domain. Therefore, the gyrating particles run through areas of different field strength. The force which is thereby acting on the charged particles is given by [Anders and Yushkov 2002]

$$F_{||} = -\mu \frac{dB}{ds}. \tag{6.4}$$

μ is the magnetic moment of a charged particle, which in absence of collisions is given as

$$\mu = \frac{mv_{\perp}^2}{2B} = const. \tag{6.5}$$

If the field strength increases, the particles are decelerated. This is known as magnetic mirror effect and was used in early fusion experiments to achieve a plasma confinement [Chen 1984]. From the invariance of the magnetic moment $\mu = const.$ follows that the perpendicular component of the kinetic energy of an affected particle has to increase with the same rate as the field strength B. However, the energy has to be conserved, i. e. $1/2m(v_{\perp}^2 + v_{||}^2) = 1/2mv^2$. Thus, $v_{||}$ has to be decreased up to the point where it becomes zero and its trajectory is reversed at the so called reflection plane. This is illustrated in figure 6.2. In nature this mirror effect leads to northern lights. Here, an additional effect can be seen: The converging field lines increase the probability of interaction and therefore more excitation and recombination processes occur, i. e. a visible plasma in the polar regions and a more intense laboratory plasma is the consequence. If the plasma is already almost fully ionized as is the case in an arc plasma, the electrically applied energy will no longer be useful for thrust production, but it will just lead to a brighter discharge due to the excitement to higher ion charge states. This is conform with the observed increase of the plasma impedance by [Anders 2008]. Consequently the thrust efficiency decreases. On the other hand, some of the particles reflected by the magnetic mirror will fly back to the electrodes.

If the particles are running into a decreasing magnetic field, the influence of the Lorentz force becomes weaker and the gyration radiuses become bigger. Due to the invariance of the magnetic moment the perpendicular component of the kinetic energy is converted into the parallel energy component. Since the particles are guided along diverging trajectories,

the probability of interaction is decreased. Subsequently, the energy loss owed to possible interactions is reduced. With this setup an influence on I_{sp} and thrust has been observed in literature. [Keidar et al. 2005] predicted an I_{sp} gain of factor three which could be verified by a lower mass flow.
However, as it will become important later, magnetic fields can also vary in time and not only in space. Thus, it is possible to control whether the particles are running into an area of decreasing or increasing field strength. This complicates the described behavior in spatial inhomogeneous fields, since it is now important to synchronize both effects for the desired result. As it was shown in chapter 3, a significant number of ions is only be generated within the first 200 μs of the pulse or below. Thus, a magnetic field has to be applied already before or directly with arc initiation, or it will lead to the mirror effect which thereby cannot only be achieved by the correct geometric positioning but also based on the time of its application.

6.3 Previous Approaches

A magnetic field which is constant in time can only be achieved with a permanent magnet or a field coil powered with DC current. The latter would be a big challenge within the energy restrictions of a CubeSat. As [Keidar et al. 2005] showed, a field strength of at least around 50 mT is necessary for an appreciable influence on the plasma plume. This would require a DC current of at least 15 A, as will be shown below in a FEM simulation which is absolutely beyond the possibilities of a CubeSat. From FEM simulation it can be derived that a corresponding permanent magnet needs a remanence of around 1 - 1.5 T, which is typical for Neodym magnets [Lide 2003].
The application of a ring shaped Neodym magnet would simplify the whole setup. No further power supply or control unit would be necessary. The ejected particles would automatically face a time-independent magnetic field. However, a situational on and off switching of the field is not possible. Therefore, either a decelerating or focusing effect can be achieved, depending on the position of the magnets. Furthermore, the magnets can be affected by temperature changes during launch and orbiting. Temperatures higher than the Curie temperature, which is around 300°C for Neodym magnets [Lide 2003], can lead to the loss of their ferromagnetic behavior.
Moreover, the constant existing field may interfere with field sensors and magnetorquer of the ADCS. Some launch providers have limitations for permanent magnetic fields aboard CubeSats. Because of this and due to possible complications during separation from the P-POD, the CubeSat Design Specifications recommend to limit magnetic fields outside the CubeSat to 50 μT above the Earth's magnetic field [Mehrparvar et al. 2014]. Typical values are between 25 to 65 μT on the Earth surface [Finlay et al. 2010] and around 15 to 50 μT in a typical CubeSat orbit (e. g. 600 km for UWE-3 [Bangert et al. 2014].

Thus, during launch and orbital deployment, a permanent field of around 100 μT should not be exceeded by magnets aboard a CubeSat. This limit is too low for the application of Neodym magnets outside the satellite which would generate a constant field of at least some mT at the edges of the CubeSat where the thrusters are installed. Therefore, the use of permanent magnetic fields can be ruled out.
Another option is the use of the arc current for field generation as in the so called Magnetically enhanced VAT (MVAT) introduced by [Keidar and Schein 2004] and [Tang et al. 2005]. Thereby, the inductor of the PPU which is used for IES and arc initiation is realized as air coil around the coaxial thruster (see figure 6.3). This adds another complication: In this arrangement the current running through the coil is not constant. Instead, it is decreasing during the pulse and so is the magnetic field strength. Consequently, the charged particles in the arc run automatically through a temporally weakening field.
In the end, both the geometric and the temporal inhomogeneity can be used for the manipulation of the plasma plume. In addition to the already experimentally demonstrated improvement of thrust and I_{sp}, the magnetic mirror effect can be utilized to reflect particles back to the electrodes, which may lead to a higher probability for the re-deposition of the conductive layer on the interface between anode and cathode. However, the used anode geometry improves the re-deposition of the layer already as shown in chapter 5. Unfortunately, this effect leads to a higher probability for a fusing of anode and cathode. Therefore, the mirror effect may only be reasonable for other geometries with bigger anode and cathode diameters as well as thicker insulations.

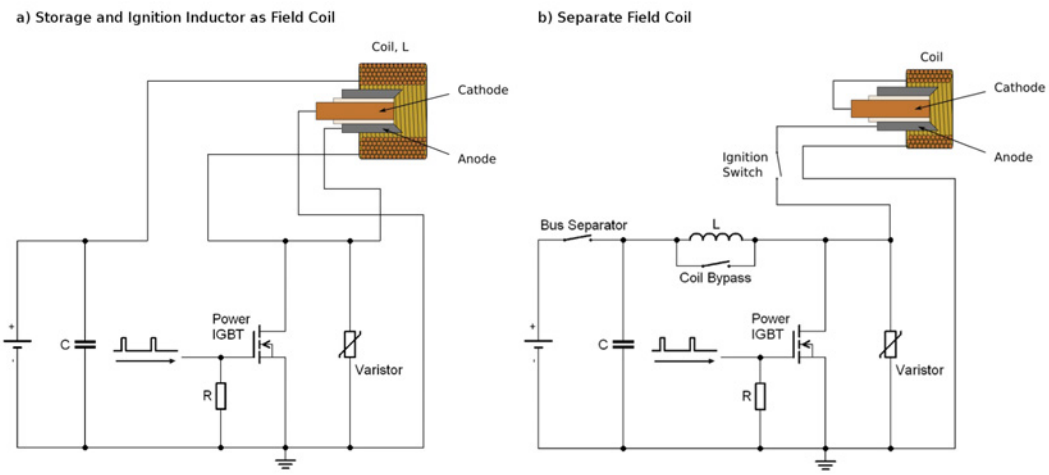

Figure 6.3: Left: The PPU inductor used as field coil for the generation of an axial magnetic field. This setup requires a big air coil to achieve a sufficient inductance for energy storage and ignition. Right: Implementation of an additional coil in the improved PPU described in chapter 4. The voltage peak for ignition is produced with a suitable inductor within the PPU while the second coil is only for the generation of the magnetic field. This coil does not need a high inductance and can therefore be smaller as in the first case.

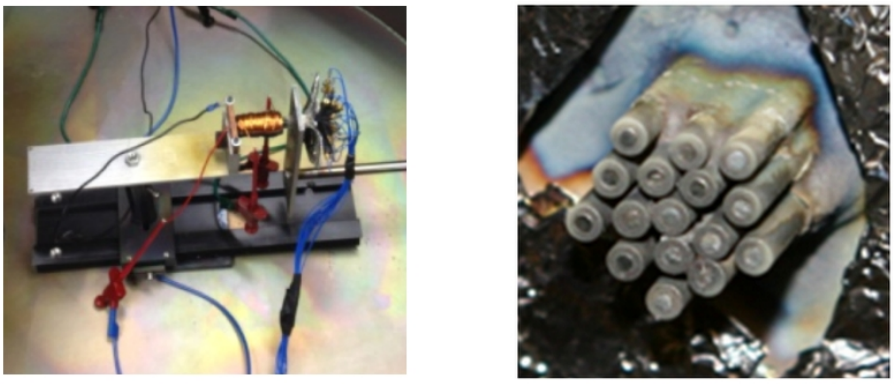

Figure 6.4: Setup for the current density measurement in front of a coil within an early attempt to use the PPU inductor for plume focusing (left). The right picture shows the probe array used thereby. The probe circuit was similar to the one described in chapter 3.

Considering the limitations of a CubeSat in matters of space, mass and power consumption the concept of [Tang et al. 2005] is an interesting option. By using the PPU inductor as field coil, no further components and circuits are necessary [Greisert and Heitz 2012]. However, the first approach within this work featuring the initial PPU concept with IES based on a inductance of 330 μH and a saturation current of around 10 A was quite unsatisfying – not in terms of the focusing effect which was suitable considering the PPU performance but with regard to space and mass demand. The mentioned original PPU inductor has a diameter and respectively a height of around 20 mm and a mass of nearly 50 g, which was one of the reasons for the changes in the PPU design described in chapter 4. Furthermore, the use as focusing element requires a hollow inductor core or an air coil.

[Tang et al. 2005] uses an air coil of 100 turns of copper wire with a diameter of 1 mm which was 25 mm long and had an inner diameter of around 40 mm. This is necessary for an inductance of sufficient value ($\sim$ 640 μH). At a peak current of 22 A, around 50 mT were achieved with this assembly. The result is an increase in thrust of about 50 %. Unfortunately, the dimensions of the coil made the adaption to CubeSats difficult. To accomplish a smaller construction, a ferrimagnetic ceramic tube was used as support for a coil with 200 turns of copper wire with a diameter of 0.5 mm. Measurements acquired with the setup in figure 6.4 show an inductance of 347 μH, a saturation current of 8.65 A and a magnetic field in the center of the coil of up to 15 mT. Figure 6.5 shows the resulting effect on the ion current distribution.

Even for this very small field strength a visible effect is present. A higher current would have resulted into a higher field strength, but unfortunately this was limited by the used core material. The coil had a length of 30 mm, an inner diameter of 11 mm and an outer diameter of 25 mm, which is no big improvement compared to the coil of [Tang et al. 2005] at the price of a much lower field strength and a worsening of the thruster performance. Taking all this together, this is no option for CubeSat application. However, for the improved PPU a different concept is necessary in any case.

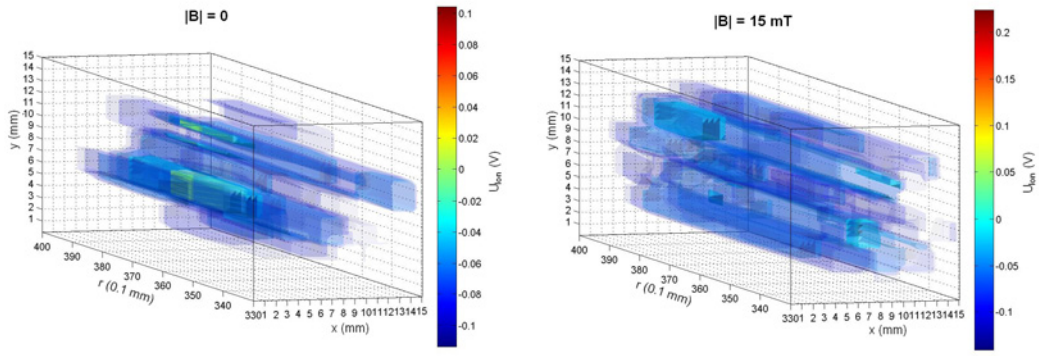

Figure 6.5: 3D illustration of the focusing effect of an axial magnetic field measured with an electric probe array 4 μs after arc initiation. With an external magnetic field a higher ion density is observed as in the case without magnetic field [Greisert and Heitz 2012].

6.4 MVAT for CubeSats

As described in the previous chapter, an improved PPU has been developed within this work to overcome the shortcomings of IES regarding CubeSat integration. The inductor is only used for ignition while the actually applied energy is stored within a capacitor. This allows a small inductance in the range of 50 – 100 μH and a low saturation current of up to 3 A. Consequently, the coil is very small and lightweight. To avoid saturation and damping effects during the discharge the inductor is bypassed after arc initiation. In chapter 4 it was shown that thereby a very smooth discharge with a peak current of up to 50 A and a pulse length of up to 8 ms, depending on capacity and input voltage, can be achieved. Thus, it seems not reasonable to insert an additional coil into the circuit. Fortunately, the required field strength of around 100 mT can also be achieved by a small, short air coil with only several dozen turns.

6.4.1 Electromagnetic Setup

Such a B-field coil cannot be used as ignition coil since its inductance would be to low, but it would have a relatively low resistance and could therefore be switched in series to the real ignition coil which in contrast to the field coil will still be bypassed after ignition. A first estimation of the achievable field strength B in the center of a coil with radius r and length l was done with a simple correlation given by [Plonus 1978]:

$$B = \frac{\mu_0 N I}{\sqrt{4r^2 + l^2}}. \tag{6.6}$$

N denominates the number of turns, I is the arc current and $\mu_0 = 4\pi \cdot 10^{-7}$ N/A^2 is the vacuum permeability. Assuming that given by the additional resistance a peak arc current of 20 A can be achieved, and that due to CubeSat dimensions the length is limited to 8 mm and the radius to 3.5 mm, 16 turns will be sufficient to achieve a magnetic

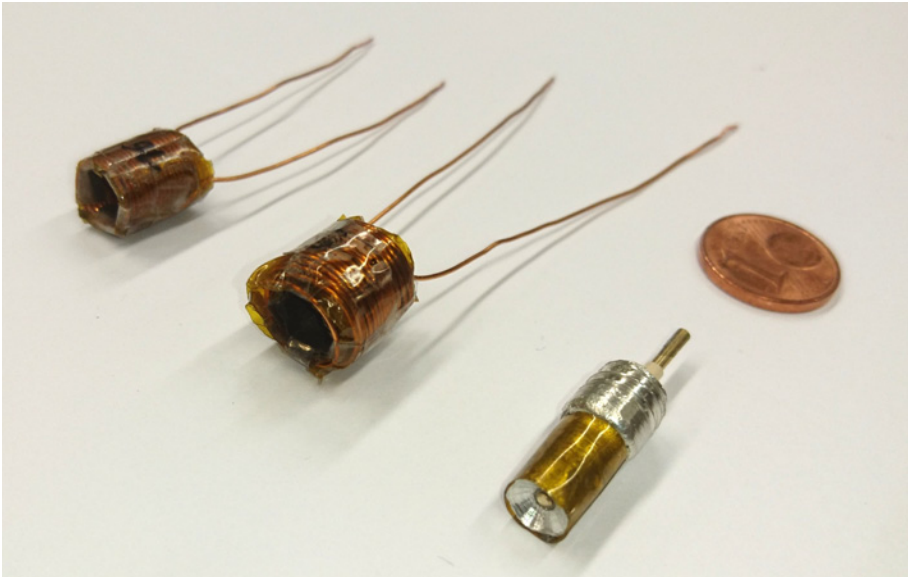

Figure 6.6: VAT with CubeSat conform dimensions and two coils which have been tested for thrust improvement and plume manipulation. The small coil has 16 turns of 0.5 mm copper wire and the big coil has 48 turns.

field of around 50 mT, which would be enough to see first weak effects as described by [Cohen et al. 1989]. As illustrated in figure 6.6, coils with a different number of turns have been used for the following investigations. However, only the small coil with 16 mm would fit into the current VAT design for a 1U-CubeSat. As before, a copper wire of 0.5 mm diameter was used which gives a length of 8 mm for a single layer coil with 16 turns. Based on the estimation above, an inner diameter of 7 mm has been chosen as trade-off between a preferably big anode and CubeSat limitations. The actual size of the coil is bigger than theoretically necessary. This is owed to the Kapton insulation between each layer which is necessary to avoid shortcuts due to melting caused by the relatively high currents.
By this configuration the overall mass and space demand of the VAT systems remains almost unchanged, while the concept of [Tang et al. 2005] results into a system mass of 1 kg. A coil geometry which is longer than its inner diameter was chosen to allow a preferably long homogeneous field domain with parallel field lines inside the coil.

6.4.2 Geometrical Aspects

For a better understanding of the field distribution, a simulation with FEMM 4.2 has been done accompanying to the experiments. FEMM is the abbreviation for an opensource program suit called "Finite Element Method Magnetics" which allows the solving of two-dimensional electromagnetic problems on the basis of classical electrodynamics and finite element analysis [Baltzis 2008], [Meeker 2015]. Several applications in the field of EP

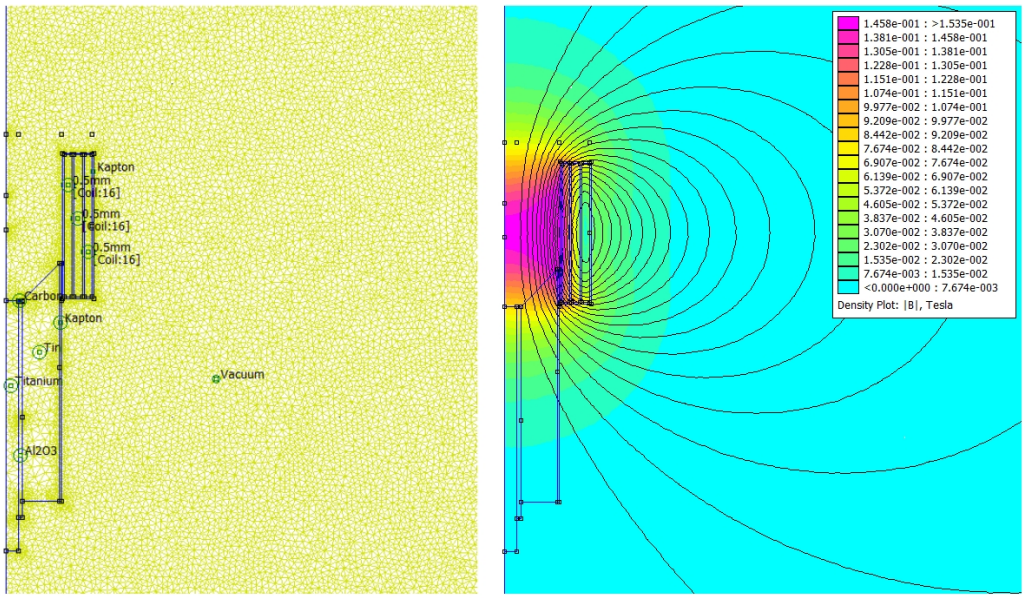

Figure 6.7: Illustration of the open boundary FEMM simulation domain of a VAT with a multi-layered coil (left) and of the result for 48 turns and 30 A (right). The mesh was automatically created by the program suit.

have shown the viability of this tool for the given task, e. g. by [Boniface et al. 2005] for the computation of magnetic fields inside a Hall Effect Thruster. Moreover, it has already been used for the visualization of the field lines of an magnetically enhanced VAT by [Zhuang et al. 2009]. Therefore, FEMM seems to be appropriate for this work despite the existence of various more powerful yet commercial FEM tools.

The program is able to divide a given number of turns inside a wound coil into several layers if the length of the coil is determined [Meeker 2010], although for the simulated geometry every layer of wire was defined separately together with an accompanying insulation layer to take the influence of a non-ideal wound coil with additional Kapton layers into account and to allow an easy on and off switching of the different layers. Up to three layers with 16 turns of copper wire with a diameter of 0.5 mm have been simulated according to the geometrical circumstances explained above. The magnetic field of such a coil calculated with FEMM is visualized in figure 6.7.

The influence of the diamagnetic materials of the VAT (Al, Ti, Graphite) is very weak. On the other hand, the magnetic field created by the current running through the electrodes and the vacuum arc has also a certain effect on the whole picture. However, for simplicity this matter has been neglected for further considerations. The two diagrams in figure 6.8 show the axial and radial variation of the field strength of the simulated coil at different positions. From figures 6.8 and 6.9 it becomes clear that the axial position of the coil around the thruster is important. Putting the coil front even with the cathode surface would possibly lead to a diverging plasma plume, since the charged particles run into

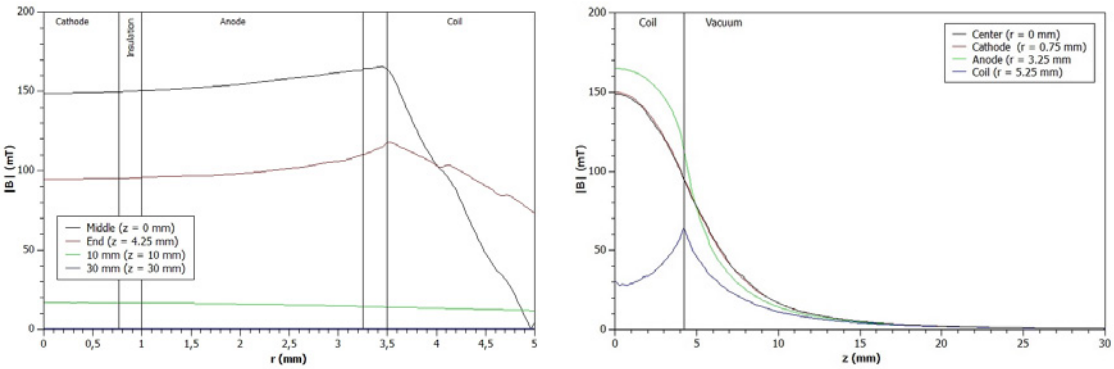

Figure 6.8: Radial (left) and axial (right) variation of the field strength of an air coil with 48 turns and a current of 30 A from FEMM simulation.

an attenuating field. If the coil is positioned in front of the thruster, the particles will be decelerated and possibly reflected due to an increasing field strength and the mirror effect discussed above. However, the magnetic field is not strong enough to achieve a complete reflection of the ions. Instead, a deceleration is more likely to happen. Moreover, a significant part of the plasma plume will be shadowed by the walls of the coil which is also not intended. The most reasonable arrangement is to put the axial center of the coil even with the cathode face (figure 6.9 b)). Thereby, the particles run through a decreasing magnetic field with parallel field lines which leads to a collimation of the plasma plume. Figure 6.9 illustrates the influence of different coil positions.

Another aspect which has been mentioned above is the time dependency of the magnetic field due to the decay of the electric current. Depending on the supplied energy and voltage, different current levels will be found at the beginning of the discharge. Furthermore, the decay constant and the pulse length are also influenced by these parameters. The effect of different current values of the magnetic field strength starting from the coil center is illustrated in figure 6.10.

With the knowledge of the temporal variation of the arc current, the time dependent variation of the magnetic field can easily be determined from the simulation results (see figure 6.11).

Based on these considerations, measurements with thrust balance, ICDD setup and high speed imaging system have been conducted. As will become clear in the following section, the application of an external magnetic field is feasible even under the limitations of a 1U-CubeSat.

6.5 Results

Several effects have been observed with the described realization of a MVAT for CubeSats. Apart from a narrowing of the beam profile, an increase of the ion current density has been measured with the ICDD setup as well as a decrease of the ICD, depending on the

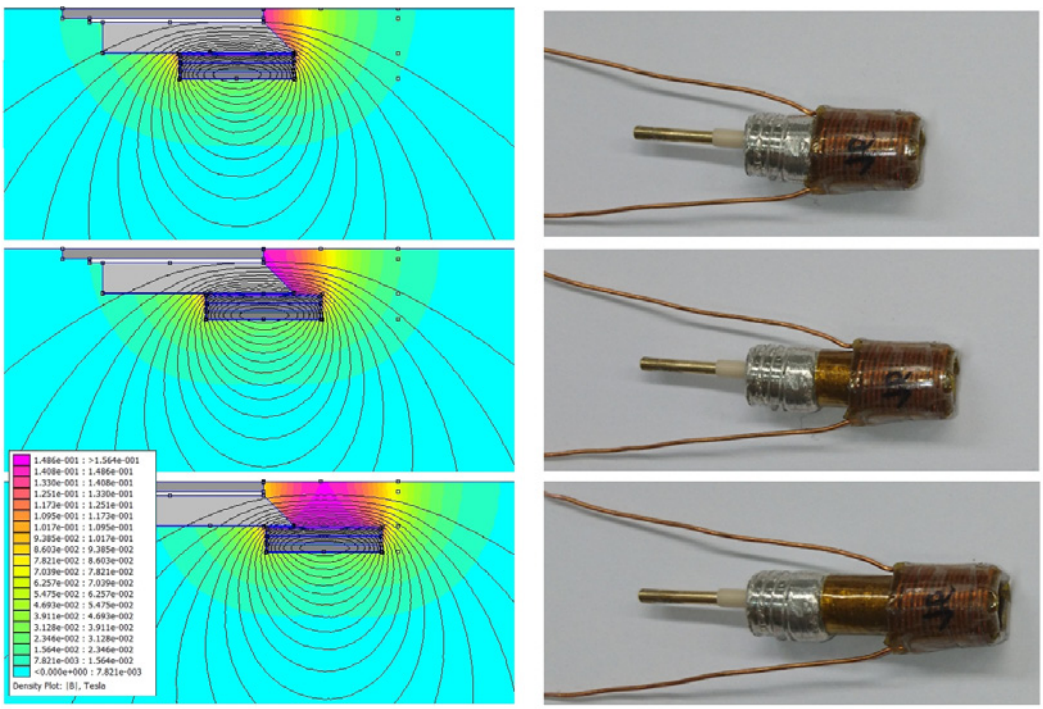

Figure 6.9: Computational illustration of the field lines and field density within three different coil configurations. The third setup leads to a deceleration of the ions since they are running in an area of converging field lines.

position of the field coil. The thrust has shown a corresponding behavior. As required by theory, the application of an additional coil in the PPU circuit leads to an increase of pulse length and a decrease of arc current (see figure 6.12). Thus, the power load onto the thruster materials and therefore the thermal load could thereby be reduced. However, without the effect of the magnetic field, e. g. if the coil is placed away from the thruster somewhere else in the PPU circuit, pulse energy and thrust are reduced. Three effects have been further investigated: The influence on the beam profile, the reduction and increase of thrust and the movement of the cathode spots.

6.5.1 Thrust and ICDD

The resulting effect on the plasma plume has been investigated especially for a coil with 48 turns. At first, an optical inspection of a tungsten thruster with and without magnetic field is illustrated in figure 6.13. The images were shot with an ordinary digital camera. Therefore, only a qualitative interpretation is suitable. Three cases have been observed: The first image shows a totally unaffected plasma plume since the coil was not connected to the PPU circuit. When an identical coil has been implemented outside the chamber, a slight reduction of the luminosity is visible (middle image). The last image

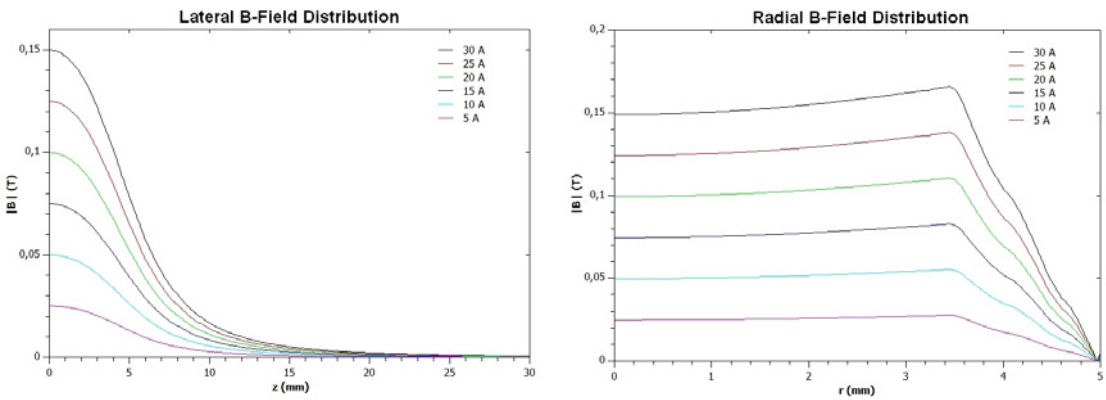

Figure 6.10: Variation of the magnetic field for different electric currents. Zero position is in both diagrams the center of the coil.

clearly illustrates the influence of a magnetic coil onto the plasma plume. However, these images give only a rough, subjective overview on the possible effects. Hence, further investigations with ICDD detector and high speed imaging system are necessary. Within this context, only the effects seen in the left and in the right image are of interest, since it should be primarily investigated if a coil will improve thrust and plume shape compared to the totally unaffected system. The case in the middle image affects the pulse energy and the thrust in an undesired way due to the additional resistance of the unnecessary coil in the PPU circuit. Hence, if a MVAT should be installed on a CubeSat, circuit design is necessary which allows the total separation of the field if the described effects are not needed.

Figure 6.14 shows the ion current density distribution measured with the apparatus introduced in chapter 3. The case in the left diagram is the same as already discussed for the different shadowing angles which were tested in chapter 5 to avoid contamination.

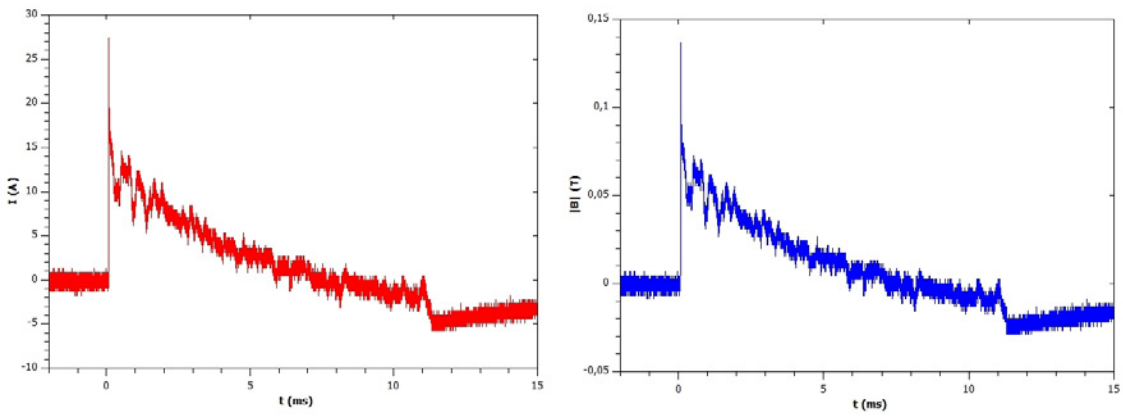

Figure 6.11: Variation of the magnetic field in the center of the coil with time (right). The corresponding current profile (left) was measured with an operation voltage of 40 V at a Ti cathode.

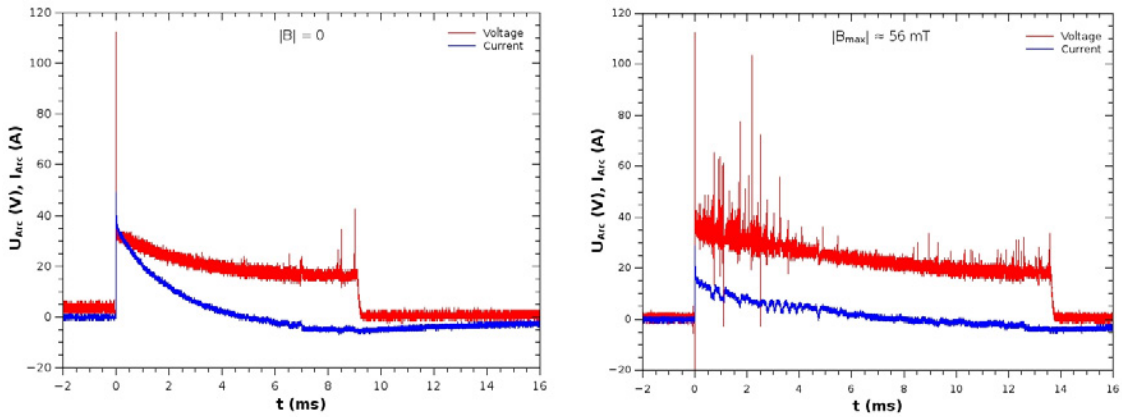

Figure 6.12: Voltage and Current of a Ti thruster without (left) and with (right) external axial magnetic field.

Compared to the right diagram it is clearly visible that the application of a magnetic field increases the peak ion current density and narrows the ICDD if the center of the coil is even with the cathode surface or if the end of the coil is even with the end of the anode. In contrast to that, it can be seen that the positioning of the coil in front of the thruster leads to a reduction of the peak ion current density and a slight broadening of the ICDD. It has to be pointed out, that due to the damping effect of the coil, the peak arc current was smaller than in the unaffected case.

The effect of beam collimation by a magnetic field is also visible in 6.15. Thereby, high speed images have been acquired with 62,500 fps. Thus, one image has been taken every 16 μs. This is not sufficient for the investigation of processes within or directly after arc initiation, but it is fast enough for the observation of the interesting magnetic field effects.

As it is visible, the image intensity is lower than in the unaffected case. Again a

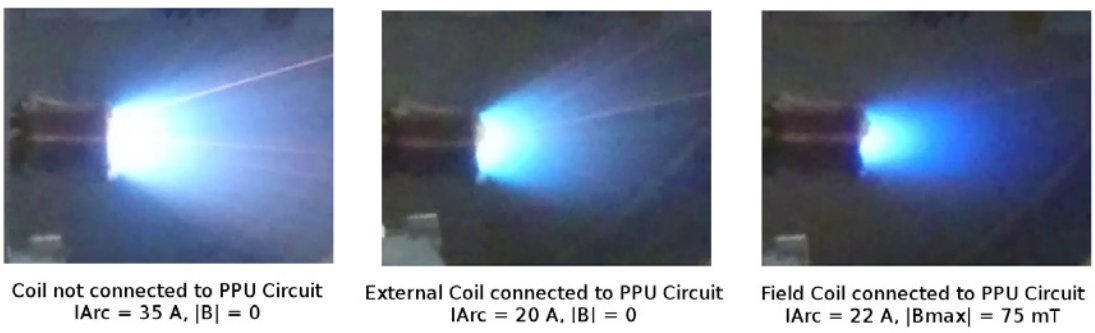

Figure 6.13: Influence of a magnetic field on a Ti thruster. The coil center is even with the surface of the cathode. Only the right thruster is affected by an external magnetic field. The coils in the center and left image are not connected to the PPU. However, in the center a second coil within the PPU circuit with same inductance as the field coil is used to simulate the damping effect.

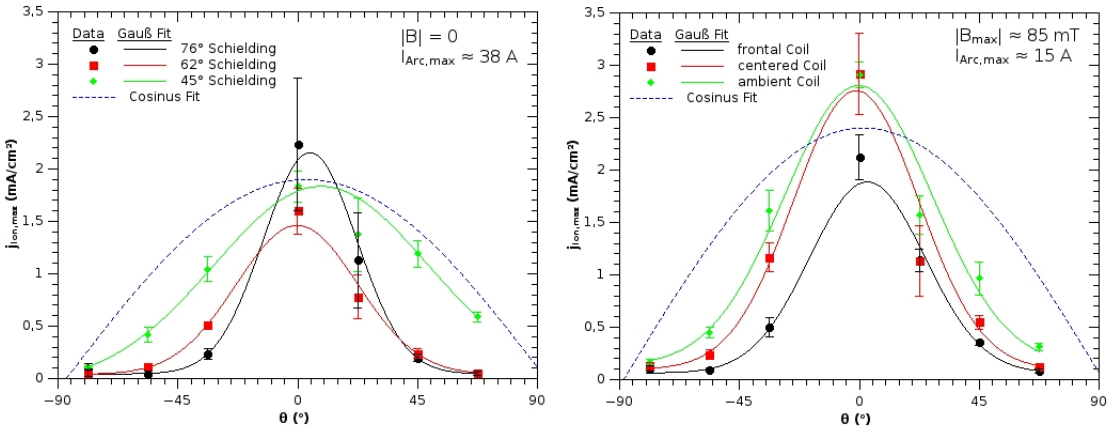

Figure 6.14: Peak Ion Current Density at different angles in front of the thruster at a distance of 150 mm. The left diagram shows the unaffected thruster and the right diagram illustrates the influence of an axial magnetic field created by the arc current, running through a coil with 48 turns and 3 layers at different relative positions to the cathode surface. Note that in both configurations the presence of the coil leads to a geometrical shadowing effect as described earlier in this chapter and that the resistance of the coil leads to a reduction of the arc current.

collimation respectively an elongation and narrowing of the plasma plume occurs. The lower intensity can be explained with a lower electric current. In the case of an additional coil in the circuit which does not produce a magnetic field in front of the VAT (see figure 6.13), almost no discharge is visible for the given camera parameter set (exposure time 10 μs, 62.500 fps). The rise of intensity could be explained with an increase of charge states due to the influence of the magnetic field [Anders 2008].

The thrust has been measured simultaneously with the ICDD. Therefore, again the three configurations as investigated above will be examined. In the first case, the coil end is even with the anode edge. This implies a shadowing angle of 45° to the surface normal of the cathode. The second setup is given if the coil center is even with the cathode surface and in the third case, the coil is placed in front of the thruster. The behavior for the different coil positions is the same as in the ICDD measurements (see figure 6.16).

Within the limits of the used measurement equipment, a relative improvement between 20 % and 50 % was determined, which is in good agreement with [Tang et al. 2005] who measured a relative improvement of the thrust of about 50 %. The third configuration on the other hand shows a reduction of thrust of around 45 %. This is also conform with the results of ICDD measurements. Moreover, this approves the theoretical considerations above. However, a total reflection of the charged particles like in a magnetic mirror has not been observed, since the velocity of the particles is too high and the strength of the magnetic field too low.

By this, the predicted effects have been observed under the circumstances of CubeSat application. If a continuous focusing is not possible due to satellite limitations, the application of a coil as decelerating device may be a solution for the ignition issues.

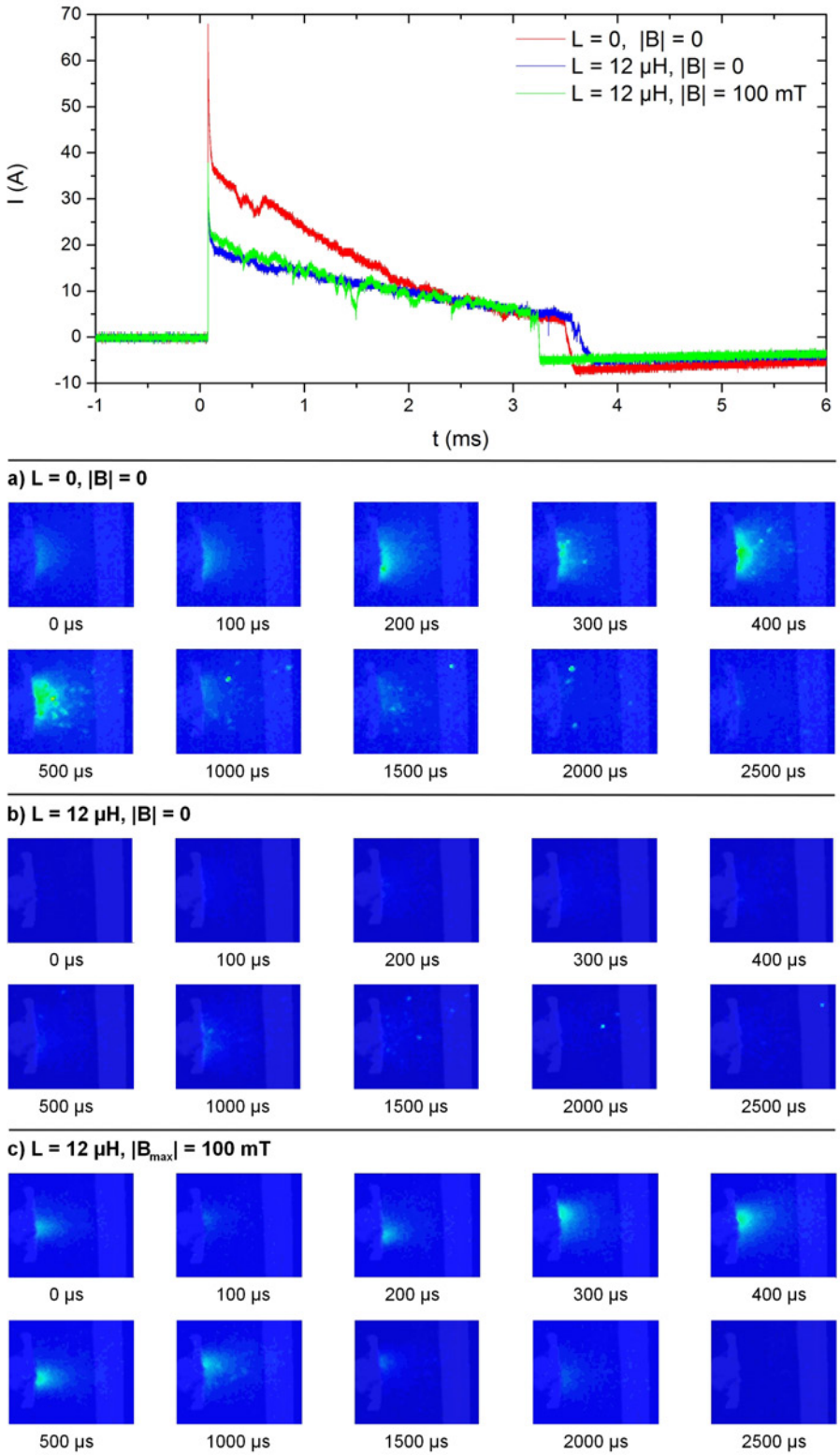

Figure 6.15: Lateral high speed image sequence of a Ti cathode without (a) and b)) and with magnetic field (c)). In the second case an additional coil in the PPU circuit was used which does not create a field near the thruster. The resulting plasma plume is much weaker as in case a). An external magnetic field leads to a brighter plume than in case b) and a narrower plume than in case a). $U_{Arc} = 40$ V, $I_{Arc,max} = 30$ A, $|B_{max}| = 100$ mT.

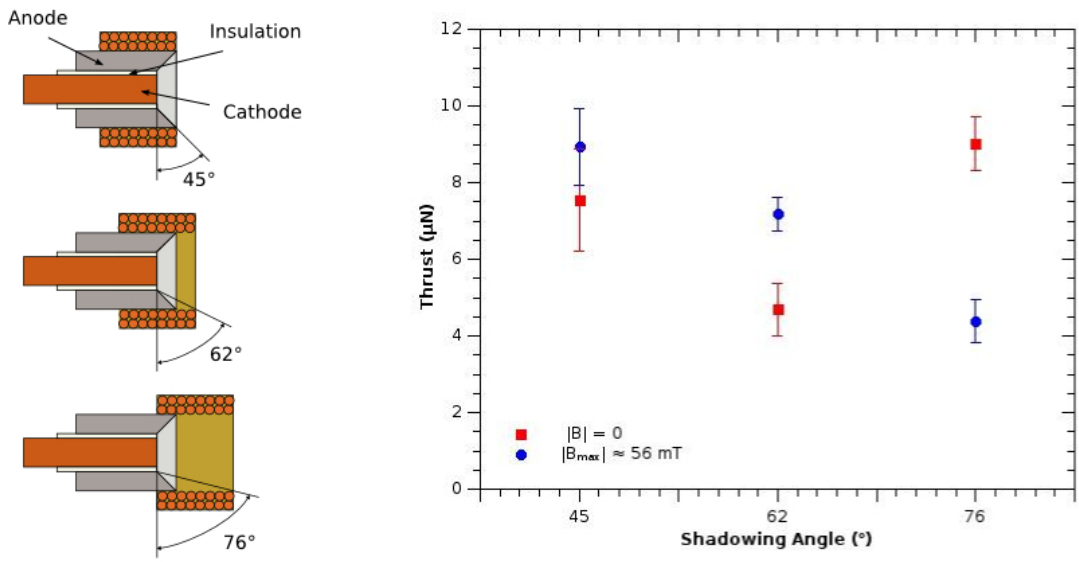

Figure 6.16: Variation of the measured thrust for different coil positions with and without axial magnetic field. Depending on the coil position an improvement of 20 % or 50 % in thrust is observed. An increasing magnetic field as in the third coil position leads to a thrust reduction of around 45 %.

However, apart from the beam collimation a movement of the cathode spots has been observed as predicted by literature.

6.5.2 Cathode Spot Movement

Figure 6.17 shows a SEM image of the cathode surface after thruster operation without (left) and with (right) axial magnetic field. Visibly, the craters have no sharp edges on the first image as it is the case at the cathode where the magnetic field was applied. This may be owed to the higher local heat load due to a low cathode spot mobility without magnetic field.

In case of the application of an axial magnetic field there are also molten edges around the craters, but not as clear as in the left image. In addition, the cathode spots have lower diameter if a magnetic field is applied, which may be explained with a higher mobility. For further investigation, the high speed imaging setup described in chapter 3 has been applied. The exposure time has been set to 10 μs and the acquisition rate to 62,500 fps. As visible in figure 6.18, the cathode spot in the unaffected thruster stays in the same location within the illustrated period. For longer observation times only an erratical jumping from one side to the other has been found. In contrast to that, a clockwise motion of the vacuum arc is visible at the image sequence connected with the MVAT. This is also conform with literature [Anders 2008].

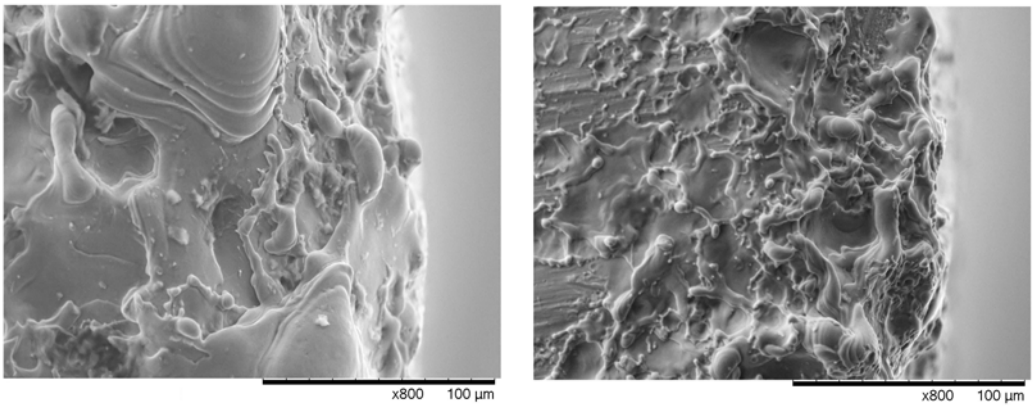

Figure 6.17: The application of a magnetic field leads to smaller cathode spots as these two REM images show. Left: The high energy input and the tendency of the cathode spots to stay at one location during the whole pulse leads to very rough erosion where single spots are hard to define. Right: The higher mobility of the cathode spots lead to a lower energy input and thus to smaller crater which can clearly be determined.

As it turns out, the cathode spots are moving in the opposite direction as the electric current in the coil. This was already observed by [Smith 1957] and [Robson 1978] and can be explained with the right-hand rule: If the current is running counterclockwise through the coil, the magnetic field is orientated inwards, i. e. from the anode plane towards the CubeSat rail. The arc current is running from anode to cathode, i. e. towards the center of the thruster. Thus, a Lorentz force moves the arc clockwise around the cathode.
The cathode spot velocity can be calculated from the rotation time and the cathode geometry. With a period of $t \approx 220$ μs, an angular velocity of $omega = \Delta\phi/\Delta t = 2\pi/220\mu$s $= 28{,}559.93$ rad/s follows. Hence, the arc is moving with a velocity of $v = \pi d \ / \ t = \pi \cdot 1.5$ mm / 220 μs = 21.42 m/s along the cathode-insulator interface (distance from the center of the thruster $r = 0.75$ mm). This shows that an external magnetic field improves arc motion and decreases the local heat load on the cathode surface. Subsequently, a more even erosion with a lower surface roughness is achieved and the production of macroparticles may be reduced.

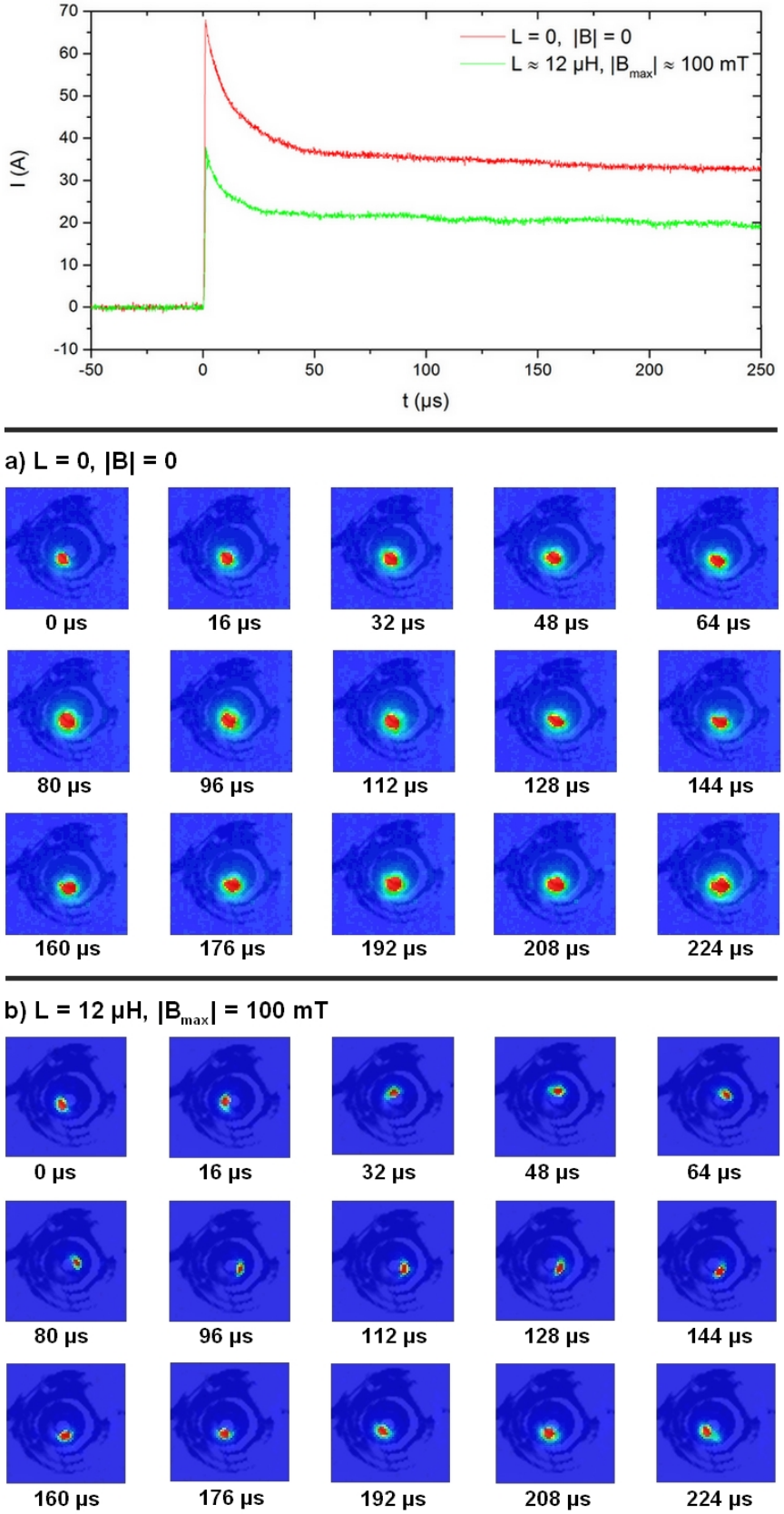

Figure 6.18: Frontal high speed image of a Ti cathode without (a)) and with (b)) magnetic field. Given by the orientation of the magnetic field the cathode spots move clockwise around the cathode. $U_{Arc} = 40$ V, $I_{Arc,max} = 30$ A, $|B_{max}| = 100$ mT.

Chapter 7

Discussion

In this chapter, the findings of the different development areas, i. e. PPU, VAT design and the application of magnetic fields are merged together. Based on this, the feasibility of the developed VAT system for CubeSats will be discussed with a special emphasis on performance and reliability. Subsequently, an outlook on further research will be given. This comprises alternative geometries which may improve VAT performance and reliability, the use of other propellant materials as well as a discussion on the improvement of arc initiation and a possible alternative for thrust production. Finally, the use of VATs as de-orbiting system will be discussed.

7.1 VAT as CubeSat Propulsion System

The scope of this work was the integration of a VAT system into an 1U-CubeSat, although the results are also feasible for bigger satellites. The mechanical limitations of an example satellite have been successfully incorporated, as presented in chapters 4 and 5. The PCB and thruster design described therein is also applicable to any other CubeSat with a similar structure. Although the electrical design of the PPU is based on the power supply capabilities of a 1U-CubeSat, it can also be used in CubeSats with up to three units without significant changes. The efficiency of a VAT system aboard such a satellite will therefore be higher than in the given example, which will be discussed in the following.

7.1.1 Performance

The EPS power of a satellite like UWE-3 is limited to around 2 W or a constant average energy of 2 J per second. This restricts the capabilities of the VAT system drastically. While the efficiency of the CES and ignition circuit is around 0.94, the total PPU efficiency is limited by the conversion unit between EPS and CES. The efficiency of step-up converter used for laboratory testing drops from 0.40 at 30 V operation voltage to 0.09 at 50 V. For the final PCB layout attention has been focused on the choice of a more efficient boost

converter. By the use of an additional energy storage, i. e. an Li-Po battery, pulse energies up to 2.7 J have been achieved which allow a thrust of up to around 20 μN per pulse both for Ti and In. The corresponding thrust-to-power ratio was measured with 13.49 μN/W and 9.72 μN/W, respectively. While the value for Ti matches the 12.77 μN/W predicted by [Polk et al. 2008], In shows a worse behavior (9.72 vs. 18.59 μN/W). This may be owed to the massive production of macroparticles which leave the cathode under a very flat angle to the surface normal ($< 30°$ [Kutzner and Miller 1989]). Therefore, these macroparticles have only minor contribution on the produced thrust.
With the step-up-converter used for the laboratory prototype, only low repetition rates can be achieved if higher thrust is desired. At a pulse energy of 0.7 J (30 V) a repetition rate of 1.4 Hz is possible. With that, a thrust of around 4 μN per pulse can be achieved which, at this repetition rate, is similar to an impulse bit of 5.6 μNs. However, for better arc initiation it has been shown to be beneficial to use higher operation voltages of at least 40 V, with which currently a repetition rate of only 0.4 Hz is possible. Thereby, a pulse energy of around 2.7 J and a thrust of up to 17 μN can be achieved per pulse. This correlates with an impulse bit of 6.8 μNs. Therefore, depending on the mission design, the CubeSat developer has to choose between high thrust at low repetition rate or low thrust at higher frequencies. However, the reduced efficiency of the PPU has also to be considered. Table 7.1 shows the technical data of VAT system for 1U-CubeSats which was developed within this thesis.

The possible Δv depends on the amount and the properties of the propellant material. As was shown, only around 0,83 g of Ti are necessary for a Δv of 7.5 m/s which was the required value at the beginning of this thesis. However, at the given cathode geometry with a diameter of 1.5 mm, four thrusters with a cathode length each of 26 mm are necessary for this desired mission. This is only possible with a reliable propellant feeding mechanism like the two systems presented in chapter 5, which are based on a piezoelectric actuator and a shape memory alloy spring. In has been tested as alternative propellant materials with a higher thrust-to-power ratio. Unfortunately, the thrust-to-ratio of In was only half

Total Mass	200 g
PPU Mass	150 g
PPU Size	90×90×15 mm
Input Power	2 W
Pulse Energy	0.7 – 2.7 J
Repetition Rate	1.4 – 0.1 Hz
Thrust	< 17 μN
T/P	~ 13 μ/W (Ti)
η_{PPU}	0.38 – 0.08

Table 7.1: Technical data of the VAT system, developed for an 1U-CubeSat.

of the predicted value and the I_{sp} is assumed to be in the same range as of Sn (139 s). Therefore, the propellant efficiency is very low. For Sn a propellant demand of around 5.5 g was calculated which corresponds to a cathode length of 137 mm for four thrusters. Under the given dimensional restrictions of a CubeSat this is not suitable for satellite propulsion.

7.1.2 Reliability

The reliability of the VAT is still an issue. In earlier research it was found that the conductive layer deteriorates with ongoing thruster operation, e. g. [Lun 2008]. On the other hand, this process is essential for arc initiation as pointed out in chapter 2. In the literature it was mentioned that a "healing" of the layer has been observed at higher arc currents (some 100 A) and high repetition rates (some 100 Hz) [Anders et al. 2000]. However, both is not possible under the given limitations. Therefore, other measures have been tested. The improved PPU allows the use of insulations with a minimal thickness of 0.35 mm. Thinner insulations have a tendency to break under high thermal loads, thus creating additional possible discharge paths. However, it has been shown that an insulation of high-temperature synthetics like PEEK or Vespel can be designed so that they erode with the same rate as the cathode. This is also beneficial in terms of the mechanical resistance of the VAT against vibrations and acceleration forces during launch, since synthetics have a much higher ductility than ceramic materials.
Another method which was tested to improve the reliability and lifetime of the thruster was the application of an axial magnetic field. The magnetic field leads to a collimation of the plasma plume and probably to a reduced contamination of the satellite surface. When the magnetic field is applied in a way that the particles fly through a reducing field strength, an increase in ion current density and thrust has been observed. However, the use as a magnetic mirror, i. e. the particles fly into a increasing magnetic field, seems to lead to a deposition of cathode material on the thruster surface. This was concluded from the fact that a higher probability for a fusing of both electrodes occurred. Yet, further investigation has to proof this observation. In addition it was observed that an axial magnetic field leads to a forced movement of the cathode spots along the cathode edge. This leads to a smoother erosion of the cathode and may reduce fusing issues.
For the PPU only components allowed by MIL-SPEC and NASA regulations will be used. The downsizing of the inductor and the use of a toroidal core have reduced the production of parasitic magnetic fields. All power lines have either been split into six layers, thus reducing the current density, or by the use of shielded, interlaced cables. Further measures for EMI reduction have to be applied if necessary. Therefore, a thorough testing of the PPU is still pending. Moreover, it has to be tested, if the Li-Po battery is suitable under the given temperature variations.

7.2 Further Development

Apart from the investigated measures for the implementation of a VAT into a CubeSat and for the improvement of the reliability, several other solutions are thinkable. This concerns the investigation of alternative geometries as well as the use of new propellant materials. In the following section several different measures will be discussed. Moreover, a rather unconventional approach will be introduced: The use of an α-emitter as anode for an improved arc initiation. Finally, the use of a VAT as propulsion system for de-orbiting will be reviewed.

7.2.1 Alternative Geometries

This work focused on the coaxial arrangement of anode and cathode. Additionally, a planar and a ring shaped electrode geometry were introduced in chapter 2. These basic VAT types can be combined and extended with additional components. One possible arrangement is the feeding of the cathode material sideways into a planar thruster. This concept was already tested with a PPT by [Ciaralli et al. 2013]. As was observed in chapter 5, the cathode material can be eroded at least up to 1 mm before no further arc initiation is possible. Therefore, an exact arrangement of anode, insulation and a cathode shaped like a bar of 1 mm thickness should work. This allows also the application of a simple spring as feeding system as attempted in the original VAT concept by [Schein et al. 2001]. Figure 7.1 shows how this concept could be realized.

However, the integration into a CubeSat is not as obvious as with coaxial or ring shaped

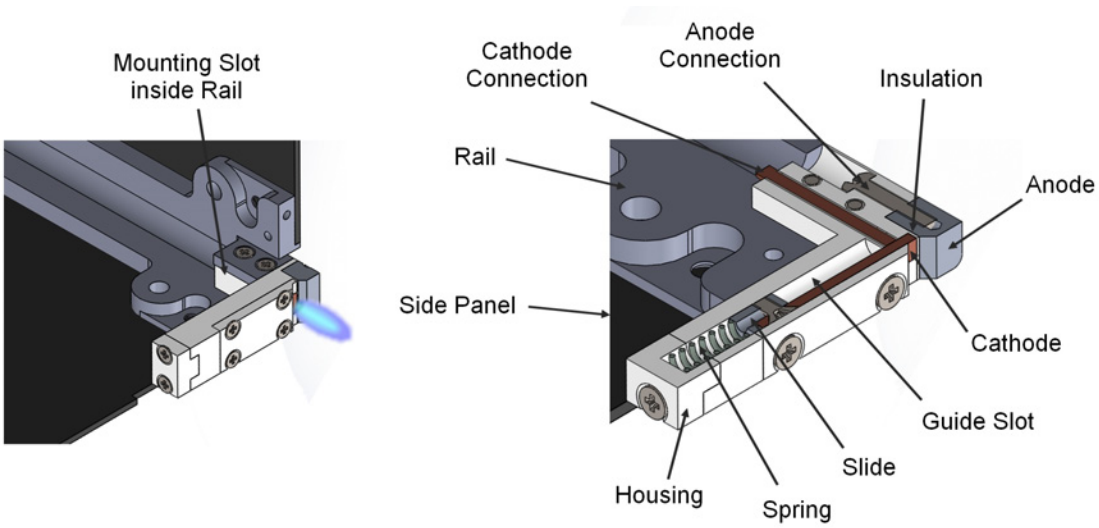

Figure 7.1: Possible design of a planar thruster with a sideways feeding system. The spring is pushing the cathode bar permanently against a wall which acts as insulation between anode and cathode. The thickness of the cathode has to be chosen that a sufficient stiffness of the bar and a complete erosion of the material is achieved.

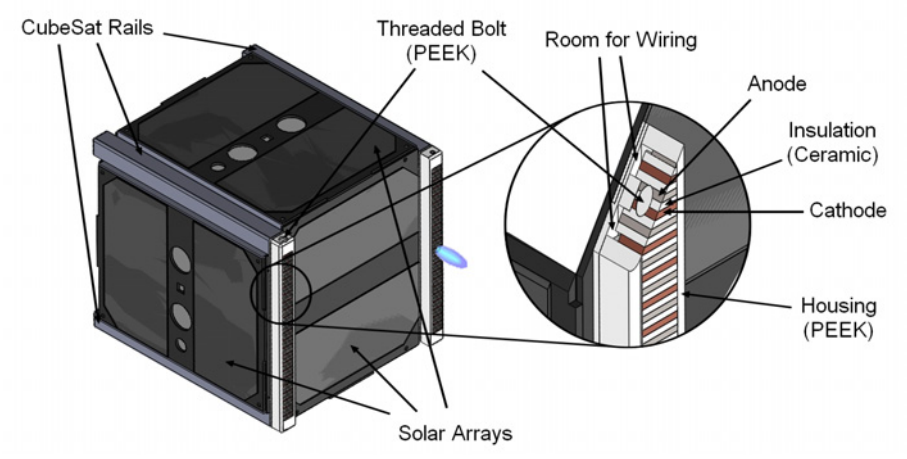

Figure 7.2: Top: Concept for the integration of a VAT consisting of multiple disks which can be connected as anode or cathode.

electrodes. Another concept which is based on the planar thruster is the use of a stack of electrodes and insulating disks. With a more complicated switching electronics, each disk can be used as anode or cathode. Thus, if two electrodes are fused together, a switch will separate them from the other electrodes and converts an anode into a cathode or vice versa. This can also be used if a cathode is exhausted. Figures 7.2 7.3 show a possible realization.

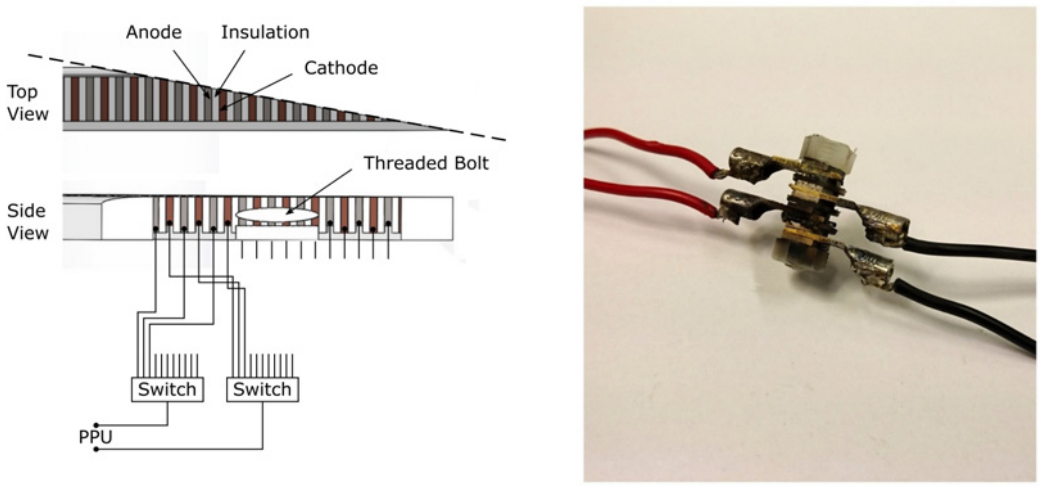

Figure 7.3: Left: Working principle of the disk VAT. If two disks are fused together they can be separated from the PPU by a electric switching system and replaced by another pair of electrodes. Thereby an exhausted cathode can also be bypassed. Right: Early prototype consisting of ring terminals for cables and Nylon washers.

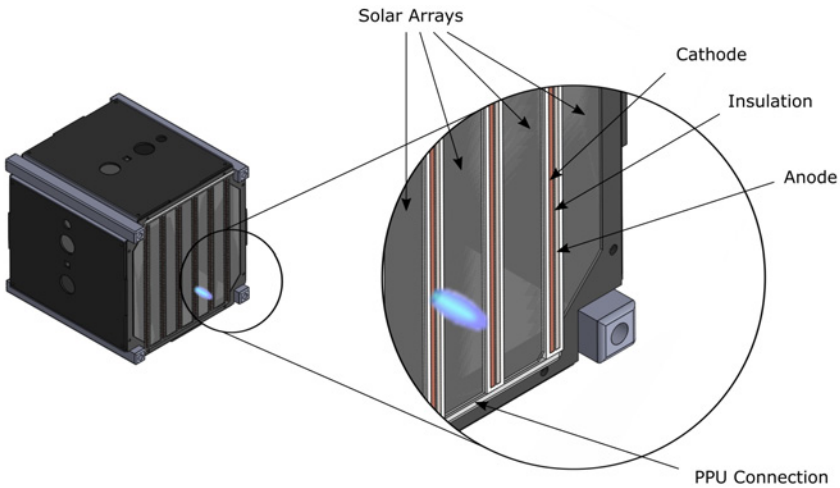

Figure 7.4: Concept of a laminar thruster setup where the electrodes are positioned between the solar arrays. This option is primarily interesting for de-orbiting since thruster operation will lead to a contamination of the solar arrays.

This concept allows the integration into an usual CubeSat structure. However, the origin of the plasma plume is located in a much bigger area than in a coaxial thruster which complicates mission control. This is also an issue with a laminar thruster design as illustrated in figure 7.4, which may occupy one whole side plane of a CubeSat. A more detailed explanation will be given in the last subsection.

However, all potential geometries are prone to a fusing of the electrodes. A possible solution could be to move the cathode permanently. Thereby, the risk of sticking together with the anode could be decreased. This requires a mechanism with a very low power consumption, e. g. a piezoelectric element which produces an oscillating movement of the cathode or a permanent rotation of the cathode applied by an electro-motor or again a piezoelectric actuator (see figure 7.5).

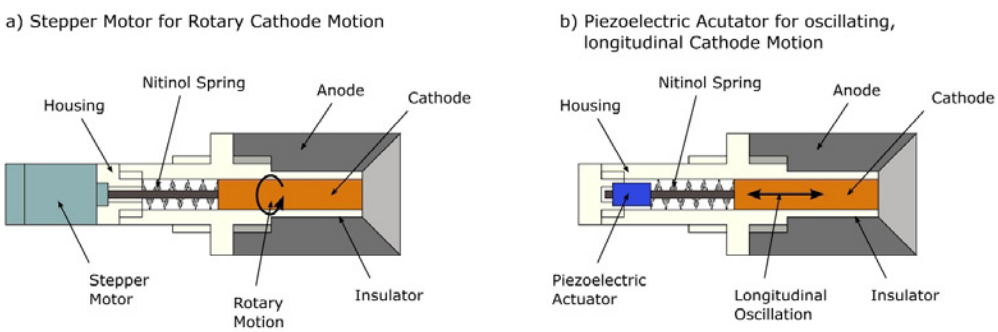

Figure 7.5: Left: A stepper motor provides a constant rotation of the cathode. Thereby a fusing of anode and cathode may be prevented. Right: Another option is the implementation of a piezoelectric actuator for a permanent oscillation of the cathode.

7.2.2 Other Materials

Most literature source have concentrated on cathodes of Al, Cu, Ti, W, Bi, Fe and Y. [Polk et al. 2008] suggested a much larger selection of possible materials. Very interesting in terms of T/P are elements with a high atomic mass like Pb, Pt and U, although the I_{sp} is assumed to be very low. On the lower side of the periodic table Cr might be a good choice in terms of high I_{sp}. Alloys and doped materials have also not been investigated sufficiently. First experiments with carbon fiber reinforced plastics (CFRP) have shown very good results [Fuchikami et al. 2013], [Lun and Law 2015]. Moreover, the use of materials with a low melting point like Sn, In or Pb should be reconsidered. As it was shown, I_{sp} and thrust can be improved by axial magnetic fields. The influence of this method on the mentioned cathode materials may lead to a better feasibility for thruster applications. This would be an interesting option, since due to the better re-deposition Sn and In showed a longer thruster lifetime than Ti or Cu even without feeding.
Especially the insulation material has not been investigated thoroughly up to now. An interesting option is the use of diamonds which is a very good insulator, although they have a very high thermal conductivity. If a thin diamond layer is surrounded by a good thermal insulator like Al_2O_3 a massive heating due to the high thermal load during thruster operation will occur. [Evans and James 1964] showed that a heating above 1,500°C for 45 minutes leads to slight transformation from diamond to graphite. The diamond specimens used thereby were circular with a diameter of up to 1.17 μm. Graphite spots were detected in regions where the thickness of the diamond was below 10 nm. Temperatures of around 1900°C lead to conversion of almost the whole diamond structure into carbon after 5 to 10 minutes. Synthetic diamond layers or layers with diamond-like properties, e. g. hydrogenated amorphous carbon (a-C:H) films, can be produced by chemical vapor deposition (CVD) [Pietzka 2010]. The thereby possible layer thickness ranges from some nm to μm. If the layer thickness is optimally adjusted to the heat load of a given thruster setup it should be possible to use a diamond or a-C:H layer as insulator with self-regenerating conductive layer.
Since arc initiation is still an issue, other solutions have to be found. Formerly, thoriated W electrodes have been used for TIG welding. This was based on the improved ignition behavior and higher ampacity compared to normal W electrodes. Thoriated W electrodes are usually doped with around 1 to 4 % of Thorium Dioxide (ThO_2) [Davies 1992]. If the electrode is used as cathode, a monoatomic layer of Th develops at the surface of the electrode. Thereby the work function of W ($\sim$ 4.6 eV [Lide 2003]) is reduced to around 2.6 eV if the surface is completely covered with Th atoms [Redwitz 2004]. The evaporating layer is replaced continuously by diffusion of Th from the electrode volume. Experiments have to show, if the reduction of the work function is sufficient for an improved arc initiation.
However, since Th is radioactive, thoriated electrodes should nowadays be avoided for welding. The natural isotope ^{232}Th decays with an half-life of $1.405 \cdot 10^{10}$ years to ^{228}Ra

under the emission of α-particles [Pfennig et al. 1998]:

$$^{232}\mathrm{Th} \xrightarrow{\alpha,\gamma} {}^{228}\mathrm{Ra} \xrightarrow{\beta^-} {}^{228}\mathrm{Ac} \xrightarrow{\beta^-} {}^{228}\mathrm{Th} \xrightarrow{\alpha} {}^{224}\mathrm{Ra} \xrightarrow{\alpha} {}^{220}\mathrm{Rn} \xrightarrow{\alpha} \ldots \xrightarrow{\beta^-} {}^{208}\mathrm{Pb}$$

An α-particle consists of two protons and two neutrons, i. e. it has the same structure as a helium nucleus ($^4_2\mathrm{He}^{2+}$) [Krane 1987]. In other words, it is an ion with a mass of 4.002 u and a characteristic energy, e. g. 4.084 MeV in the case of ^{232}Th. The particle velocity ranges between 10,000 and 20,000 km/s. Hence, a permanent ion flux is present if an α-emitter is used as anode. 1 g of ^{232}Th e. g. constantly emits $2.26 \cdot 10^{-12}$ μg/s of ions. Unfortunately, the emission is omnidirectional, i. e. the ions are distributed over the whole surrounding space. The risk of an interference with spacecraft electronics is low due to the short penetration depth of α-particles – even a slice of paper is sufficient for shielding. But the omnidirectional distribution reduces the useful ion flux in front of the thruster. Thus, the effective ion flux may not be sufficient to improve arc initiation.
Another technically established α-emitter which has already been used in space applications is ^{210}Po. Because of its high power density (141 W/g) it was used in early space probes as fuel for RTGs (Radioisotope Thermoelectric Generator) [Larson and Wertz 1999]. However, its half-life is very short (138 d) and already half a gram of ^{210}Po reaches temperatures of over 500°C [Argonne National Laboratory, EVS 2005]. Therefore a thermal shielding is necessary to avoid a heating of satellite components. The corresponding ion flow is around $4.2 \cdot 10^{-5}$ μg/s which is much higher than for ^{232}Th. This may not only be sufficient for an improvement of arc initiation but it may also be possible to use this for thrust production itself. If e. g. only 1 % of the mass flow is focused with a magnetic field a constant thrust of around 6.3 μN results at an estimated ion velocity of 15,000 km/s. This is in the region which can be obtained with a VAT and may therefore be an interesting alternative. However, the ground handling of α-emitters requires safety measures since an accidentally incorporation leads to radiation injuries.

7.2.3 De-Orbiting with VAT

Apart from attitude and position control it is also thinkable to use the VAT as de-orbiting method [Schein et al. 2001]. For de-orbiting from LEO as it is usually mentioned by satellite developers, a Δv in the range of 100 m/s is required [Larson and Wertz 1999]. Thinking about the necessary propellant this is not possible with a VAT or any other propulsion system in the CubeSat range. However, ESA allows a stay of 20 years in LEO for small satellites. This gives much more room for CubeSat de-orbiting. A possible propellant source can be the satellite by itself since much of the structural mass is made from aluminum. Since a precisely controlled thrust production is no longer required, a planar thruster geometry is possible in this case which will avoid a feeding system. A simple approach has been tested within this thesis.
This prototype consists simply of a circuit board material on which two conducting lines of

Cu have been applied by etching. One line is used as anode and the other one as cathode. The board material acts as insulation on which graphite has been deposited as conductive layer. This simple setup shows a very good ignition behavior, although the lifetime is rather short due to the very limited amount of cathode material. In practice, this concept could be applied between the solar arrays on the CubeSat side planes. However, this will reduce the surface of the solar arrays. Moreover, the thrust generation in direct proximity of the solar arrays will result in coating and reduction of the available power. Figure 7.4 shows a possible implementation on a CubeSat.

Another approach has been made by [Slotten et al. 2013]. Thereby, the material of the solar arrays itself is used as cathode material. Thus, an optimal usage of the solar arrays could be achieved for the whole mission duration. However, without further measures, the cathode spots are immobile and remain in a single region of the solar array [Slotten et al. 2015]. This is in agreement with the behavior of type 3 cathode spots as mentioned in chapter 2. This could be improved by the magnetic fields or by the directional control of the electric current. The application of magnetic fields may be an issue under the given geometric constraints, though.

Conclusion

Within the scope of this thesis, an innovative propulsion system for the fine positioning and attitude control of small satellites was developed. Based on the concepts of [Gilmour 1966], [Schein et al. 2001] and [Keidar et al. 2005], a so called Vacuum Arc Thruster has been adopted to fulfill the special requirements of a Cube Satellite (CubeSat). The small size and mass budget limits the capabilities of a potential propulsion system drastically. Within a typical CubeSat with a side length of 100 mm and an maximum mass of 1.3 kg, only around a fifth of the volume and a mass of 250 g is left for the implementation of a VAT based propulsion system. Furthermore, the power supply output is limited to around 2 W, which has to suffice for the generation of impulse bits in the range of some μNs. Up to the date of this thesis only one 1.5U-CubeSat has been equipped with a propulsion system [Hurley et al. 2015]. The fact that a VAT based system has been chosen for this supports the feasibility of this concept.
At the beginning of this thesis, several issues have been identified, not only in terms of a possible CubeSat integration but also concerning a reliable function over a long lifetime (at least 10^6 pulses within laboratory conditions). For ignition the so called "triggerless" arc initiation introduced by [Anders et al. 1998] has been applied. However, the reliability of this mechanism depends on a thin layer of conductive material which is eroded during thruster operation. Another issue typical for VAT systems is the consumption of the cathode material which is used as propellant. The special requirements of a CubeSat in terms of mass, size and power as well as of mechanical and thermal resistance call for an innovative mechanism with a small number of moving parts. Moreover, EMI has to be taken into account and a contamination of the satellite structure, especially the solar arrays, has to be prevented.
For the development of a suitable VAT based propulsion, system several diagnostic systems were built within this thesis. The thrust has been investigated with a torsional thrust balance and compared to results already published. To proof the viability of this balance, an ion current detector array has been constructed, which allows a real-time measurement of the ion current density distribution (ICDD) within an angle of 170° in front of the thruster. With this, an estimation of thrust, a measurement of the ion velocity and an investigation of the beam geometry have been made possible. A high speed imaging system has been applied to visualize the movement of the cathode spots and the influence of external magnetic fields on the plasma plume. All experiments had been accomplished within a special

built vacuum chamber, which allows the simulation of the conditions at an 400 km LEO. The first challenge was the adaption of the Power Processing Unit (PPU) to CubeSat requirements. A power budget of only 2 W and bus voltage of around 4 V have led to complete redesign of the PPU concept of [Schein et al. 2002] which was based on Inductive Energy Storage (IES). The new PPU system features Capacitive Energy Storage (CES), while a small inductor is still used for arc initiation like in the original concept. Moreover, a simple electric switch has been implemented to support "triggerless" arc initiation. The whole system is electrically separated from the satellite EPS during the arc discharges to avoid the backflow of voltage peaks and high currents into the satellite hardware. The prototype allows the application of up to four thrusters in an alternating pattern. EMI concerns have been addressed by the use of suitable parts, shielded cables and a splitting of power lines into six layers on the print circuit board. The conversion from EPS voltage to operation voltage is achieved by a highly efficient boost converter. For the laboratory prototype a simple step-up converter was used which limits the maximum pulse repetition rate at higher operation voltages drastically (< 0.2 Hz). A Li-Po-battery has been implemented, which allows higher pulse energies for a short time. Thus, a PPU with a mass of only around 150 g and a size of 90×90×15 mm has been realized.
The spatial limitations of the CubeSat required a new thruster design. Based on [Polk et al. 2008], Ti was chosen as most suitable cathode material. Apart from this, In has also been tested because of a predicted higher thrust-to-power ratio. Ti showed performance values conform to literature (~ 13 μN/W), while with In only half of the predicted thrust-to-power ratio was achieved. A possible explanation is the massive production of macroparticles due to its low melting point. Therefore, In has been ruled out as alternative with higher thrust. A contamination of the satellite structure was reduced by the use of an anode with a conical transition phase to the insulation. Thereby, the solar panels are shielded against the plasma plume and the path between anode and cathode is reduced. This results in lower ignition voltages and a re-deposition of cathode material onto the thruster surface. For the feeding of the consumed cathode material, two mechanisms have been integrated: A highly precise piezoelectric actuator for systems with less limiting space and mass restrictions and a spring mechanic based on the shape memory alloy effect. In the latter system the arc current is used to expand a Nitinol spring due to resistance heating. The whole assembly has been designed for a space-saving installation aboard a CubeSat. Special emphasis has been laid onto the compatibility to other CubeSat geometries.
Furthermore, the application of magnetic fields for the improvement of thrust and specific impulse has been investigated based on the work of [Keidar et al. 2005]. Again, this has been accomplished with respect to the limitations of a CubeSat. Owed to the new PPU concept, a B-field coil has been successfully implemented into the electric circuit. This coil is only used for the generation of an axial magnetic field and not for arc ignition or energy storage. Thus, only a very small coil, conforming with CubeSat limitations, is necessary to achieve a sufficient field strength. Depending on the position of the coil, a reduction

or an increase of thrust and ion current density has been observed. Overall, it has been found that a magnetically enhanced VAT is suitable for CubeSat integration. Moreover, a movement of the cathode spots around the cathode edge has been observed. Thereby, a rotational period of around 230 μs at an cathode with circular cross section ($d = 1.5$ mm) respectively a angular velocity of around 28,500 rad/s was measured.
However, not all issues have been solved sufficiently under the given circumstances. The reliability of the ignition mechanism requires further effort. In connection with the new PPU concept, an improvement has been achieved by the use of different insulation materials and dimensions. Moreover, the chosen anode geometry leads to a higher deposition probability of conductive material on the thruster surface and thus to a regeneration of the conductive layer. A similar effect has been observed under the influence of a decelerating magnetic field. However, as it turns out, a higher fusing probability resulted from these measures. If both electrodes are fused together no ignition can be initiated and no thrust can be produced. Thus, further research regarding the optimal insulation material is necessary. Another possible solution could be a permanent motion of the cathode, which, on the other hand, would consume additional energy.
The power budget of a picosatellite limits the capabilities of the VAT drastically. By the use of a Li-Po battery as additional energy storage, a temporally higher pulse energy respectively thrust can be obtained. However, the necessary charging periods may not be suitable for the mission design. Since not only the PPU battery has to be charged by the solar arrays of the satellite but also the EPS battery, it will take several hours respectively several orbits before the VAT system can be used again in high thrust mode. Satellites with a bigger power budget, on the other hand, allow constantly high pulse energies (up to 2.7 J) without further changes of the PPU design. A big limitation is the bus voltage of 4 V, which is typical for most CubeSats of any size due to the use of 3.3 V ICs. The conversion to the necessary operation voltage is the most limiting factor for the PPU efficiency. Due to the low efficiency of the step-up converter used for laboratory testing up to 92 % of the supplied energy is lost during voltage conversion and pulse generation.
Taking all this together, the described solutions allow an integration of an improved VAT system into a 1U-CubeSat under certain limitations in terms of pulse repetition rate, thrust level and operation time. The developed diagnostic platform allows a thorough investigation of different design solutions and permits to gain a deeper knowledge of the physical processes at the cathode surface and in the plasma plume.

Appendix A

Technical Drawings

This appendix shows the technical drawings for a coaxial VAT with an optional B-field coil (see chapters 5 and 6).

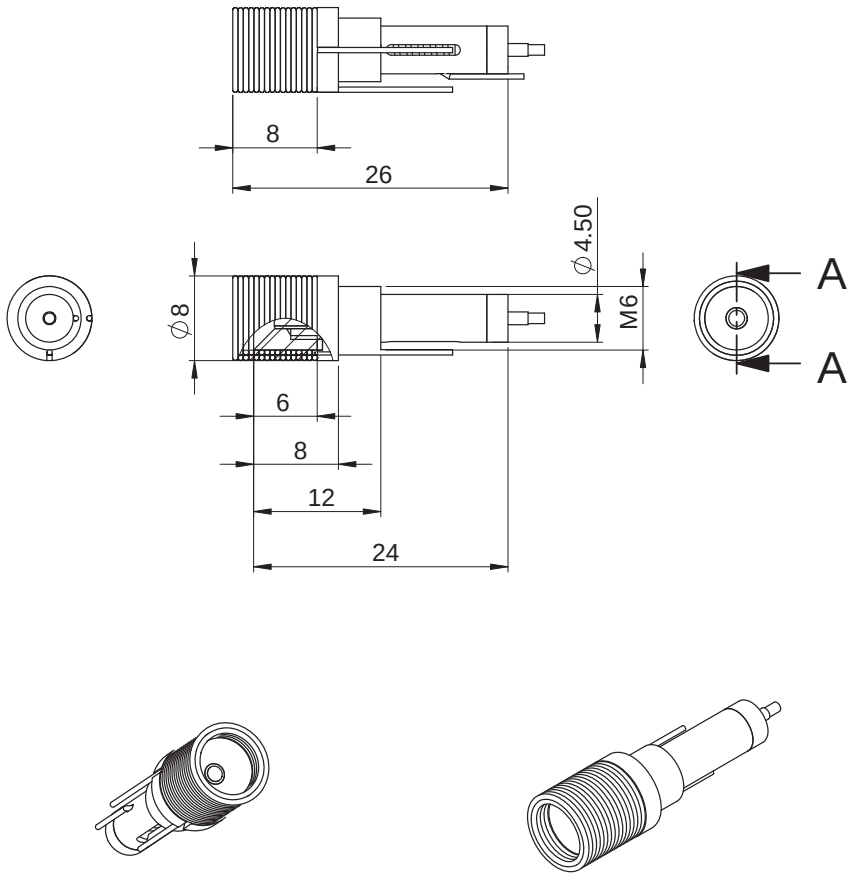

WENN NICHT ANDERS DEFINIERT: BEMASSUNGEN SIND IN MILLIMETER OBERFLÄCHENBESCHAFFENHEIT: TOLERANZEN: LINEAR: WINKEL:	OBERFLÄCHENGÜTE:			ENTGRATEN UND SCHARFE KANTEN BRECHEN	ZEICHNUNG NICHT SKALIEREN	ÄNDERUNG
	NAME	SIGNATUR	DATUM		BENENNUNG: MVAT for CubeSats	
GEZEICHNET						
GEPRÜFT						
GENEHMIGT						
PRODUKTION						
QUALITÄT				WERKSTOFF:	ZEICHNUNGSNR General Plan	A4
				GEWICHT:	MASSSTAB:2:1	BLATT 1 VON 3

SCHNITT A-A

MAßSTAB 5 : 1

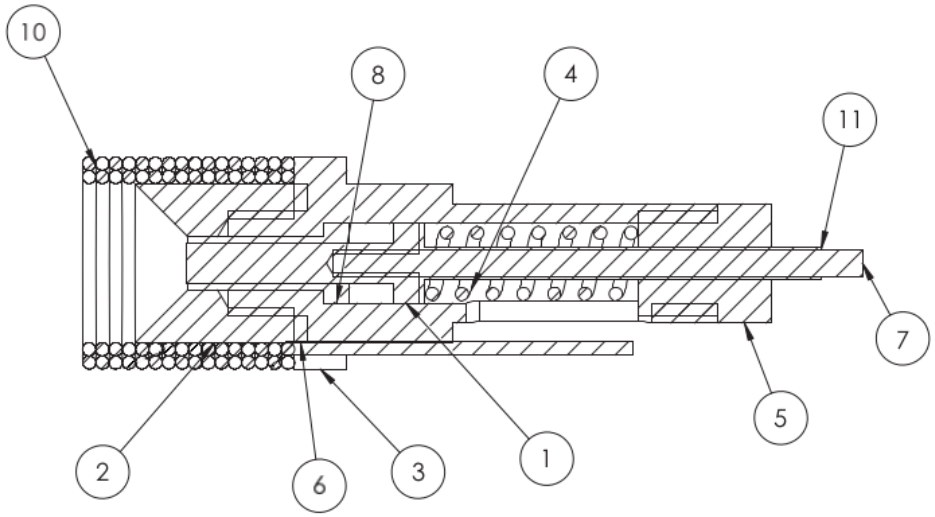

POS-NR.	BENENNUNG	MATERIAL	MENGE
1	Cathode	Ti	1
2	Anode	Al	1
3	Housing	PEEK	1
4	Nitinol Spring	Ni-Ti	1
5	Screw Tap	PEEK	1
6	Contact Ring	Cu	1
7	Cathode Connection	Cu	1
8	Insulation	Al2O3	1
9	Anode Connection	Cu	1
10	Coil	Cu	1
11	Shrinking Tubing	PVC	1

WENN NICHT ANDERS DEFINIERT:
BEMASSUNGEN SIND IN MILLIMETER
OBERFLÄCHENBESCHAFFENHEIT:
TOLERANZEN:
LINEAR:
WINKEL:

OBERFLÄCHENGÜTE:

ENTGRATEN UND SCHARFE KANTEN BRECHEN

ZEICHNUNG NICHT SKALIEREN

ÄNDERUNG

	NAME	SIGNATUR	DATUM
GEZEICHNET			
GEPRÜFT			
GENEHMIGT			
PRODUKTION			
QUALITÄT			

WERKSTOFF:

GEWICHT:

BENENNUNG:

MVAT for CubeSats

ZEICHNUNGSNR.

Sectional View

A4

MASSSTAB:5:1

BLATT 2 VON 3

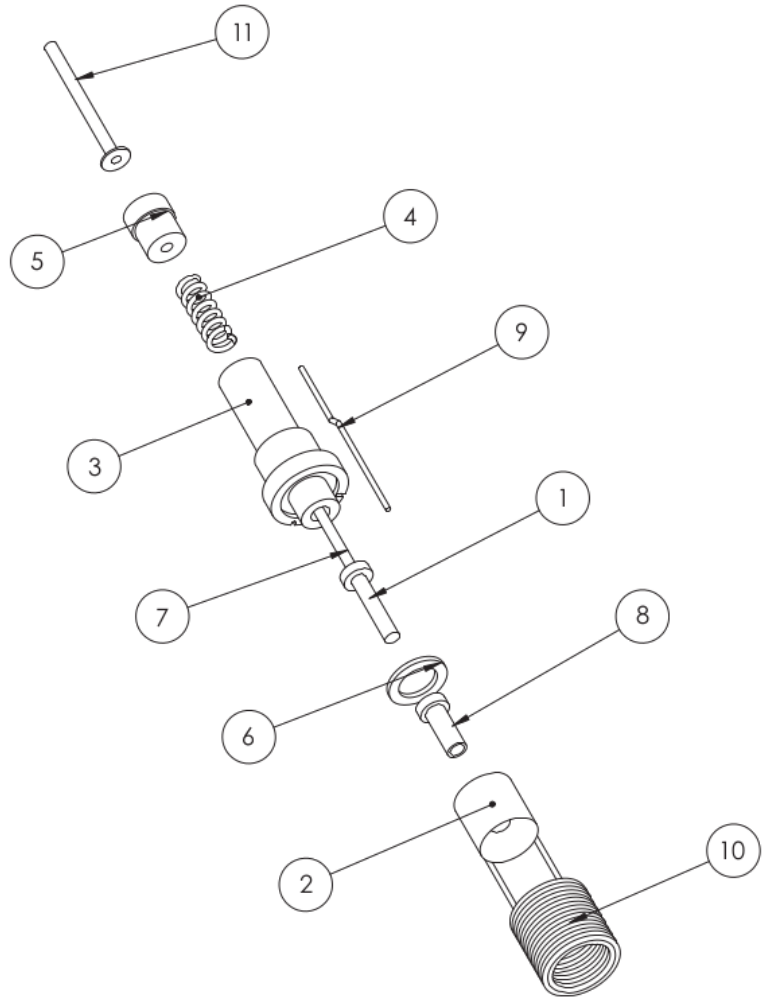

WENN NICHT ANDERS DEFINIERT: BEMASSUNGEN SIND IN MILLIMETER OBERFLÄCHENBESCHAFFENHEIT: TOLERANZEN: LINEAR: WINKEL:	OBERFLÄCHENGÜTE:				ENTGRATEN UND SCHARFE KANTEN BRECHEN	ZEICHNUNG NICHT SKALIEREN	ÄNDERUNG
	NAME	SIGNATUR	DATUM			BENENNUNG: MVAT for CubeSats	
GEZEICHNET							
GEPRÜFT							
GENEHMIGT							
PRODUKTION							
QUALITÄT				WERKSTOFF:		ZEICHNUNGSNR. Exploded View	A4
				GEWICHT:		MASSSTAB:2:1	BLATT 3 VON 3

Appendix B

Circuit Diagrams

The following two pages contain the circuit diagrams of the PPU systems as designed by Apcon Aerospace & Defense GmbH according to the findings of this work (see chapter 4). These diagrams are published by kind permission of Apcon Aerospace & Defense GmbH.

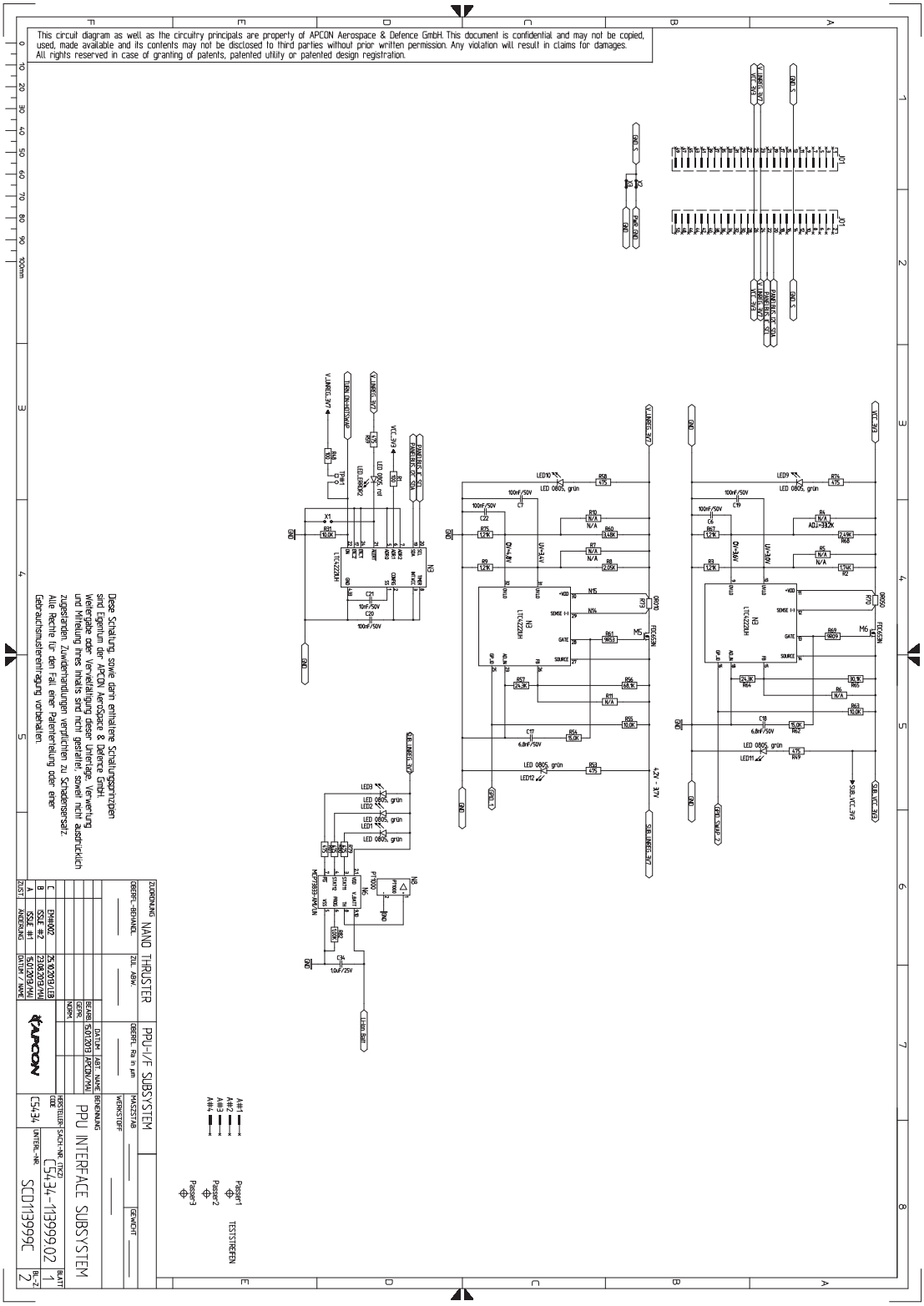
This circuit diagram as well as the circuitry principals are property of APCON Aerospace & Defence GmbH. This document is confidential and may not be copied, used, made available and its contents may not be disclosed to third parties without prior written permission. Any violation will result in claims for damages. All rights reserved in case of granting of patents, patented utility or patented design registration.
Diese Schaltung sowie darin enthaltene Schaltungsprinzipien sind Eigentum der APCON AerroSpace & Defence GmbH. Weitergabe oder Verwertung dieser Unterlage, Verwertung und Mitteilung ihres Inhalts sind nicht gestattet, soweit nicht ausdrücklich zugestanden. Zuwiderhandlungen verpflichten zu Schadensersatz. Alle Rechte für den Fall einer Patenterteilung oder einer Gebrauchsmusterentragung vorbehalten.
ZEICHNUNG NAND THRUSTER
PPU-I/F SUBSYSTEM
PPU INTERFACE SUBSYSTEM
C5434-113999.02
SCD113999C
APCON
DATUM
NAME
BENENNUNG
MASSSTAB
GEWICHT
WERKSTOFF
ZUSTAND
ANDERUNG
DATUM / NAME
BLATT
TESTSTREFEN

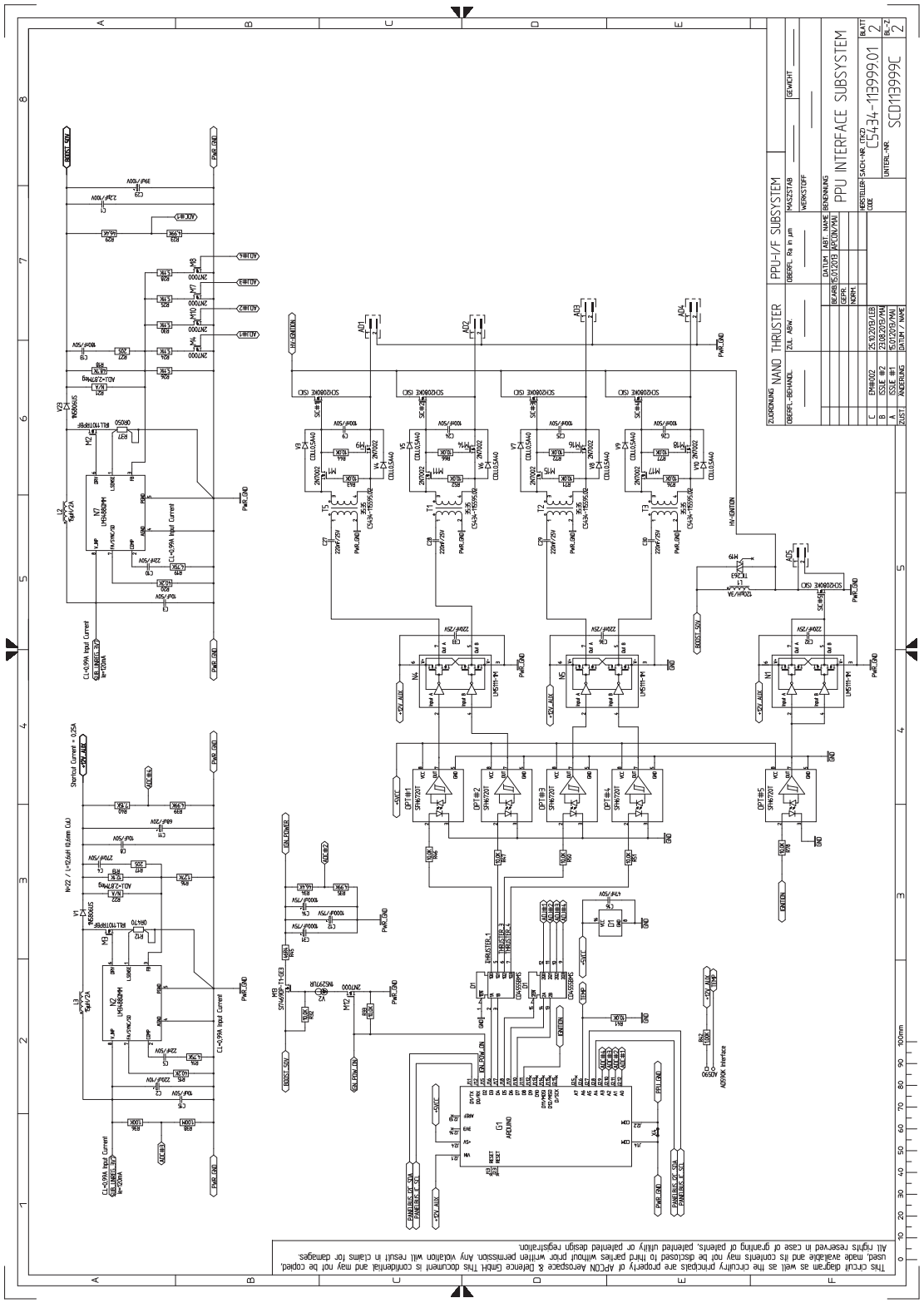

Appendix C

Experimental Setup

Within this work a test environment for low thrust propulsion systems was developed. For the characterization and testing of the VAT the following components and diagnostic systems where used:

Vacuum System (see figure C.1)

Recipient: Pfeiffer Vacuum TrinosLine 0.248 m^3

Vacuum Pumps

- Turbomolecular Pump Pfeiffer Vacuum HiPace 700 (685 l/s)
- Rotary Vane Pump Pfeiffer Vacuum Duo 20 M (20 m^3/h)

Pressure Gauges

- Balzers Compact Cold Cathode Gauge Type IKR 251
- Balzers Compact Full Range Gauge Type PKR 250
- Pfeiffer Vacuum Compact Full Range Gauge Typ PKR 251

Diagnostics

ARC Thrust Balance, Revision 2, October 2008

- Improved Thrust Balance with Liquid Metal Rotating Power Connection
- Thrust Balance Software 1.2.0

Rotatable Ion Current Densitiy Detector Array

- Rotatable 170° Arc with 9 Probes
- Measurement Box with RC-Measurment Curcuit

High Speed Imaging

- PCO dimax HS4
- PCO CamWare 64

Data Acquision Systems

- LeCroy SDA 11000 Serial Data Analyser 6 GHz, 20 GS/s
- LeCroy WaveSurfer 104MXs-A Oscilloscope 1 GHz, 5 GS/s
- LeCroy WaveAce 222 Oscilloscope 200 MHz, 2 GS/s
- LeCroy ADP 305 High Voltage Differential Probe
- LeCroy CP 150 Current Probe
- Pearson Coil Model 301
- PicoScope 4824 High Resolution 8 Channel Oscilloscope

Laboratory Power Supplies

- Hameg Triple Power Supply HM7042-S
- Voltcraft VLP-1302A Power Supply
- Picotest LXI G5100A, 50 MHz Function/Arbitrary Waveform Generator

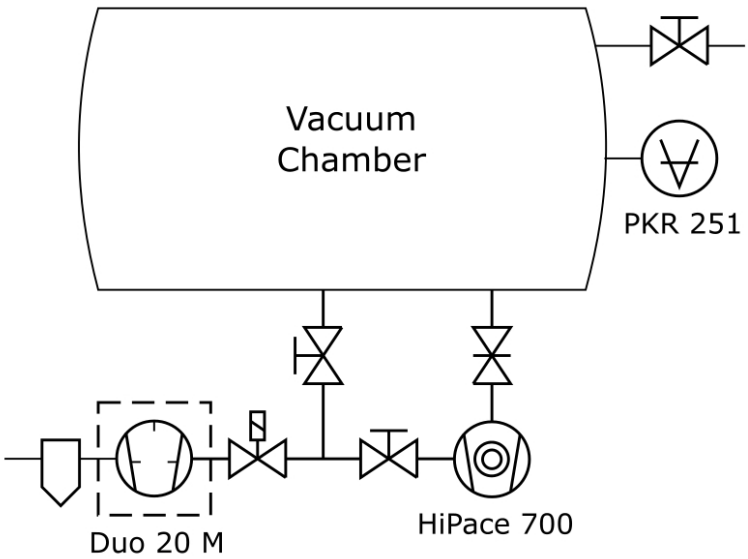

Figure C.1: Schematic of the used vacuum system.

Appendix D

Nomenclature

Acronyms

ADC	Analog-to-Digital Converter
ADCS	Attitude Determination and Control System
AASC	Alameda Applied Sciences Corporation
ADS	Attitude Determination System
ARC	Austrian Research Centers
CalPoly	California Polytechnic State University
CES	Capacitive Energy Storage
CFRP	Carbon Fiber Reinforced Plastic
CP	Chemical Propulsion
CVD	Chemical Vapor Deposition
DC	Direct Current
DHSC	Dual Hot Swap Controller
EP	Electric Propulsion
EPS	Electrical Power System
EMI	Electro-Magnetic Interference
EDX	Energy-Dispersive X-Ray Spectroscopy
ESA	European Space Agency
EEE	Explosive Electrone Emission
FFT	Fast Fourier Transformation
FEEP	Field Electric Emission Propulsion
FEM	Field Element Method
FEMM	Field Element Method Magnetics
fps	Frames per Second
GPS	Global Positioning System
HET	Hall Effect Thruster
HV	High Voltage

HOBAS	Hochgeschwindigkeitsbildaufnahmesystem
IES	Inductive Energy Storage
IGBT	Insulated-Gate Bipolar Transistor
IC	Integrated Circuit
I^2C	Inter-Integrated Circuit
ICDD	Ion Current Density Distribution
JPL	Jet Propulsion Laboratory
PZT	Lead Zirconate Titanate
kS/s	kilo Samples per Second
Li-Po	Lithium Polymere
LEO	Low Earth Orbit
MVAT	Magnetically enhanced Vacuum Arc Thruster
MPD	Magnetoplasmadynamic Thruster
MOSFET	Metal Oxide Semicondcutor Field-Effect Transistor
NASA	National Aeronautics and Space Administration
Nitinol	Nickel Titanium Naval Ordonance Laboratory
PVD	Physical Vapor Deposition
P-POD	Poly-Picosatellite Orbital Deployer
PEEK	Polyether Ether Ketone
PTFE	Polytetrafluorethylene
PPU	Power Processing Unit
PCB	Printed Circuit Board
PFN	Pulse Forming Network
PPT	Pulsed Plasma Thruster
RIT	Radiofrequency Ion Thruster
RTG	Radioisotope Thermoelectric Generator
RMS	Root Mean Square
SEM	Scanning Electron Microscope
TTP	Thrust-to-Power Ratio
TTL	Transistor-Transistor Logic
TRIAC	Triode for Alternating Current
TIG	Tungsten Inert Gas Welding
MIL-SPEC	United States Military Standard
UWE	Universitaet Wuerzburg Experimentalsatellit
VAIT	Vacuum Arc Ion Thruster
VAT	Vacuum Arc Thruster
VASIMR	Variable Specific Impuls Magnetoplasma Rocket

Constants

c	Speed of Light in Vacuum	(299,272,458 m/s)
e	Elementary Charge	($1.602 \cdot 10^{-19}$ C)
E_{solar}	Solar Constant	(1.367 kW/m^2)
g_0	Standard Gravity	(9.82 m/s^2)
k_B	Boltzmann Constant	($1.381 \cdot 10^{-23}$ J/K)
μ_0	Vacuum Permeability	($4\pi \cdot 10^{-7}$ H/m)

Symbols

a	Magnitude of the applied Thrust	(N)
A	Area	(m^2)
α	Specific PPU Mass	(kg)
α_{T_0}	Thermal Expansion Coefficient	(K^{-1})
B	Magnetic Field	(T)
C	Capacitance	(F)
C_P	Probe Correction Factor	
C_T	Thrust Correction Factor	
d	Diameter	(m)
E_D	Dielectric Strength	(kV/mm)
E_r	Erosion Rate	(μg/C)
η	Efficiency	
η_{CES}	Efficiency of the CES Circuit	
η_{con}	Efficiency of the Voltage Conversion Unit	
f_{Ion}	Ion Fraction	
f_Z	$= I_Z/I_{Ion}$	
F	Force	(N)
F_{Ion}	Fraction of total Ion Mass Loss	
F_L	Lorentz Force	(N)
γ	Damping Coefficient	(N $\cdot$ s/m)
I	Impulse	(kg $\cdot$ m/s)
I	Electric Current	(A)
I_{Arc}	Discharge Current	(A)
I_{bit}	Impulse Bit	(Ns)
I_{Ion}	Ion Current	(A)
I_{sp}	Specific Impulse	(s)
I_Z	Ion Current for a given Charge State Z	(A)
j	Current Density	(A/m^2)

j_{Arc}	Discharge Current Density	(A/m^2)
$j_{Ion,C}$	Ion Current Density on the Cathode Surface	(A/m^2)
$j_{Ion,max}$	Measured Peak Ion Current Density	(A/m^2)
$j_{Ion,P}$	Ion Current Density within Plasma Plume	(A/m^2)
J	Moment of Inertia	(kg $\cdot$ m^2)
k	Spring Constant	(kg/s^2)
κ	Constant Factor	
l	Length	(m)
l_{prop}	Total Cathode Demand	(m)
l_{Pulse}	Cathode Erosion per Pulse	(m)
L	Inductance	(H)
λ	Mean Free Path	(m)
λ_T	Thermal Conductivity	(W/m·K)
m	Mass	(kg)
m_0	Initial total mass	(kg)
m_1	Final total mass	(kg)
m_{Ion}	Ion Mass	(kg)
m_{PPU}	Mass of the PPU	(kg)
m_{prop}	Total Propellant Mass	(kg)
m_{Pulse}	Propellant Mass per Pulse	(kg)
$\dot{m}$	Mass flow Rate	(kg/s)
$\dot{m}_{Ion,P}$	Ion Mass Flow Rate within Plasma	(kg/s)
$\dot{m}_{Ion}$	Ion Mass Flow Rate	(kg/s)
$\dot{m}_T$	Propellant Mass Flow Rate	(kg/s)
μ	Magnetic Moment of a charged Paricle	(A·m^2)
M	Torque	(N·m)
N	Number of Particles	
ν	Frequency	(Hz)
ω_0	Natural Frequency	(1/s)
ω_c	Cyclotron Frequency	(1/s)
p	Pressure	(Pa)
p_{rad}	Solar Radiation Pressure	(μN/m^2)
P_{in}	Input Power	(W)
P_{out}	Output Power	(W)
ϕ	Angle	(rad)
q	Electric Charge of a Particle	(C)
q_L	Leakage Rate of the Vacuum System	(mbar·l/s)
q_P	Throughput of the Pumping System	(mbar·l/s)
q_T	Virtual Leakage Rate for the VAT Pulse	(mbar·l/s)
Q	Electric Charge	(C)
Q_{Arc}	Electric Charge per Pulse	(C)

Q_{Ion}	Ion Charge per Pulse	(C)
r	Radius, Distance	(m)
R	Resistance	(Ω)
R_S	Shunt Resistance	(Ω)
ρ	Density	(g/cm^{-3})
s_d	Drift Length	(m)
σ	Electric Conductivity	(S/m)
t	Time	(s)
t_d	Drift Time	(s)
T	Thrust	(N)
T	Temperature	(K)
T_m	Melting Point	(K)
T/P	Thrust-to-Power Ratio	(N/W)
τ	Time Constant	(s)
Θ	Angle	($^\circ$)
U	Voltage	(V)
U_{Arc}	Discharge Voltage	(V)
U_P	Probe Voltage	(V)
v_e	Exhaust Velocity	(m/s)
v_{Ion}	Ion Velocity	(m/s)
Δv	Velocity Change for a certain maneuver in space	(m/s)
V	Volume	(m^3)
W	Energy	(J)
W_{Arc}	Discharge Energy	(J)
W_{PPU}	Energy supplied by the PPU	(J)
x	Displacement	(m)
Z	Charge State	

Bibliography

[Alameda Applied Sciences Corporation 2011] Alameda Applied Sciences Corporation (2011). *Vacuum Arc Thruster*. http://www.aasc.net/micropropulsion/vat. Online, accessed 2015-12-14.

[Aldrin 1963] E. Aldrin. *Line-of-sigth guidance Techniques for manned orbital rendezvous*. PhD thesis, Massachusetts Institute of Technology (1963).

[Alfriend et al. 2009] K. Alfriend, S. Vadali, P. Gurfil, J. How and L. Breger. *Spacecraft Formation Flying: Dynamics, control and navigation*. Elsevier Astrodynamics Series. Elsevier Science (2009).

[Anders 2008] A. Anders. *Cathodic Arcs*. Springer New York (2008).

[Anders et al. 1998] A. Anders, I. G. Brown, R. A. MacGill and M. R. Dickinson. *'Triggerless' triggering of vacuum arcs*. Journal of Physics D: Applied Physics, 31(5), 584–587 (1998).

[Anders et al. 2005] A. Anders, E. Oks, G. Yushkov, K. Savkin, I. Brown and A. Nikolaev. *Measurements of the total ion flux from vacuum arc cathode spots*. IEEE Trans. Plasma Sci., 33(5), 1532–1536 (2005).

[Anders et al. 2000] A. Anders, J. Schein and N. Qi. *Pulsed vacuum-arc ion source operated with a "triggerless" arc initiation method*. Review of Scientific Instruments, 71(2), 827 (2000).

[Anders and Yushkov 2002] A. Anders and G. Y. Yushkov. *Ion flux from vacuum arc cathode spots in the absence and presence of a magnetic field*. Journal of Applied Physics, 91(8), 4824 (2002).

[Arduino 2009] Arduino (2009). *Arduino Nano*. Circuit Diagram. Rev. 3.0.

[Arestie et al. 2012] S. Arestie, E. G. Lightsey and B. Hudson. *Development of A Modular, Cold Gas Propulsion System for Small Satellite Applications*. Journal of Small Satellites, 1(2) (2012).

[Argonne National Laboratory, EVS 2005] Argonne National Laboratory, EVS (2005). *Polonium*. Human Health Fact Sheet.

[Auweter-Kurtz et al. 1996] M. Auweter-Kurtz, B. Glocker, T. Goelz, H. Kurtz, E. Messerschmid, M. Riehle and D. Zube. *Arcjet thruster development*. Journal of propulsion and power, 12(6), 1077–1083 (1996).

[Bachmann 2013] B.-L. Bachmann. *Development of Innovative thermal plasma and particle diagnostics*. PhD thesis, Universitaet der Bundeswehr Muenchen (2013).

[Baertling 2015] Y. Baertling. *SOMP2, a 2U CubeSat – Where is it now?*. In *8th Pico- and Nano-Satellite Workshop on "Technologies for Small Satellite Research"*, Wuerzburg, Germany (2015).

[Baltzis 2008] K. B. Baltzis. *The FEMM Package: A Simple, Fast, and Accurate Open Source Electromagnetic Tool in Science and Engineering*. Journal of Engineering Science and Technology Review, 1, 83–89 (2008).

[Bangert 2015] P. Bangert (2015). *Private Communication*.

[Bangert 2016] P. Bangert (2016). *Private Communication*.

[Bangert et al. 2014] P. Bangert, S. Busch and K. Schilling. *Performance Characteristics of the UWE-3 Miniature Attitude Determination and Control system*. In *2nd IAA Conference on Dynamics and Control of Space Systems (DYCOSS)* (2014).

[Barral et al. 2014] S. Barral, J. Kurzyna, Rachubiński, A. Szelecka, E. Remírez, R. Martin, P. Ortiz, J. Alonso, S. Bottinelli, Y. Mabillard et al. *First Experimental Characterization of a Pulsed Plasma Thruster with Non-Volatile Liquid Propellant*. In *Space Propulsion*, Cologne, Germany (2014).

[Beasley 2009] C. Beasley (2009). *The satellite payload sits fully assembled, covered in shiny solar panels.*. http://www.nasa.gov/mission_pages/smallsats/pharmasat/main/index.html. Online, accessed 2015-11-26.

[Biddy and Svitek 2012] C. Biddy and T. Svitek. *LightSail-1 Solar Sail Design and Qualification*. In *Proceedings of the 41st Aerospace Mechanisms Symposium*, Pasadena, California. Jet Propulsion Laboratory (2012).

[Bock et al. 2014] D. Bock, M. Bethge and M. Tajmar. *Highly Miniaturized FEEP Thrusters for CubeSat Applications*. In *Proceedings of the 4th Spacecraft Propulsion Conference*, Cologne, Germany (2014).

[Boniface et al. 2005] C. Boniface, G. J. M. Hagelaar, L. Garrigues, J. P. Boeuf and M. Prioul. *A Monte-Carlo study of ionization processes in Double Stage Hall Effect Thruster*. In *XXVIIth ICPIG*, Eindhoven, The Netherlands (2005).

[Boxman et al. 1995] , eds. R. L. Boxman, D. M. Sanders and P. J. Martin. *Handbook of Vacuum Arc Science and Technology*. Noyes Publications, New Jersey (1995).

[Brown 2008] M. Brown. *Power sources and supplies: World class designs*. Newnes/Elsevier, Amsterdam and Boston (2008).

[Buehler et al. 1963] W. J. Buehler, J. V. Gilfrich and R. C. Wiley. *Effect of Low-Temperature Phase Changes on the Mechanical Properties of Alloys near Composition TiNi*. Journal of Applied Physics, 34(5), 1475–1477 (1963).

[Busch et al. 2015] S. Busch, P. Bangert, S. Dombrovski and K. Schilling. *UWE-3, in-orbit performance and lessons learned of a modular and flexible satellite bus for future pico-satellite formations*. Acta Astronautica, 117, 73–89 (2015).

[Busch and Schilling 2012] S. Busch and K. Schilling. *UWE-3: a modular system design for the next generation of very small satellites*. In *Proceedings of Small Satellites Systems and Services–The 4S Symposium, Slovenia* (2012).

[Byon and Anders 2003] E. Byon and A. Anders. *Ion energy distribution functions of vacuum arc plasmas*. Journal of Applied Physics, 93(4), 1899 (2003).

[Cardin et al. 2003] J. M. Cardin, K. Coste, D. Williamson and P. Gloyer. *A Cold Gas Micro-Propulsion System for CubeSats*. In *17 th Annual AIAA/USU Conference on Small Satellites* (2003).

[Carl Zeiss AG 2015] Carl Zeiss AG (2015). *Makro-Planar T'2/100 ZF*. Data Sheet, Jena, Germany.

[CeramTec GmbH 2015] CeramTec GmbH (2015). *Ceramic Materials. Advanced Ceramics for Mechanical Engineering*. Data Sheet, Plochingen, Germany.

[Chang-Díaz 2001] F. R. Chang-Díaz. *An overview of the VASIMR engine: High power space propulsion with RF plasma generation and heating*. AIP Conference Proceedings, 595(1), 3–15 (2001).

[Chen 1984] F. F. Chen. *Introduction to Plasma Physics and ConControl Fusion*. Plenum Press, Second Edition ed. (1984).

[Chen 2010] H. R. Chen. *Shape memory alloys: Manufacture, properties and applications*. Materials science and technologies series. Nova Science Publishers, New York (2010).

[Choueiri 2004] E. Y. Choueiri. *A Critical History of Electric Propulsion: The First 50 Years (1906–1956)*. Journal of Propulsion and Power, 20(2), 193–203 (2004).

[Ciaralli et al. 2013] S. Ciaralli, M. Coletti, F. Guarducci and S. Gabriel. *PPTCUP lifetime test results*. In *33rd International Electric Propulsion Conference, Washington DC, USA* (2013).

[Cohen et al. 1989] Y. Cohen, R. Boxman and S. Goldsmith. *Angular distribution of ion current emerging from an aperture anode in a vacuum arc*. IEEE Trans. Plasma Sci., 17(5), 713–716 (1989).

[Corning Inc. Lighting & Materials 2001] Corning Inc. Lighting & Materials (2001). *Macor®*. Data Sheet, Corning, NY.

[Coulombe and Meunier 1997] S. Coulombe and J.-L. Meunier. *Arc-cold cathode interactions: parametric dependence on local pressure*. Plasma Sources Science and Technology, 6(4), 508 (1997).

[Cybulski et al. 1965] R. J. Cybulski, E. J. Domino, J. T. Kotnik, R. R. Lovell and D. M. Shellhammer (1965). *Results from SERT I ion rocket flight test*. Technical Report NASA TN D-2718, NASA.

[Davies 1992] A. Davies. *The Science and Practice of Welding:*. The Science and Practice of Welding. Cambridge University Press (1992).

[Dethlefsen 1968] R. Dethlefsen. *Performance measurements on a pulsed vacuum arc thruster: AIAA Journal*. AIAA Journal, 6(6), 1197–1199 (1968).

[Dolotov et al. 1974] J. Dolotov, L. Getman, E. Goldiner, V. Gorbunov, K. Krishfeld, L. Sablev and V. Usov (1974). *Apparatus for vacuum-evaporation of metals under the action of an electric arc*. US Patent 3,783,231.

[Dr. Fritz Faulhaber GmbH & Co. KG 2015a] Dr. Fritz Faulhaber GmbH & Co. KG (2015a). *FDM0620-ww-ee*. Data Sheet. Data Sheet.

[Dr. Fritz Faulhaber GmbH & Co. KG 2015b] Dr. Fritz Faulhaber GmbH & Co. KG (2015b). *Piezo LEGS Rotary 30 mNm*. Data Sheet. Data Sheet.

[DuPont Engineering Polymers 2002] DuPont Engineering Polymers (2002). *Vespel® S Line Design Handbook*. Newark.

[DuPont High Performance Films 1996] DuPont High Performance Films (1996). *High Performance Films: Kapton® polyimide film*. Data Sheet, Circleville, Ohio.

[Dyke and Trolan 1953] W. P. Dyke and J. K. Trolan. *Field Emission: Large Current Densities, Space Charge, and the Vacuum Arc*. Phys. Rev., 89, 799–808 (1953).

[Easton and Votaw 1959] R. L. Easton and M. J. Votaw. *Vanguard I IGY Satellite (1958 Beta)*. Review of Scientific Instruments, 30(2), 70–75 (1959).

[Eckert 2015] K. Eckert. *Konstruktion einer Treibstoffnachfuehrung fuer Plasmaantriebe zur Verwendung in einem Kleinstsatelliten*. Bachelor's Thesis, Universitaet der Bundeswehr Muenchen (2015).

[Edmund Optics Inc. 2015] Edmund Optics Inc. (2015). *1.5 OD 50mm Sq, Absorptive ND Filter*. Data Sheet.

[Evans and James 1964] T. Evans and P. F. James. *A Study of the Transformation of Diamond to Graphite*. In *Proceedings of the Royal Society of London. Series A, Mathematical and Physical Sciences*, vol. 277, pp. 260–269. Royal Society, Royal Society Publishing (1964).

[Feili et al. 2009] D. Feili, B. Lotz, B. St Bonnet, H. Loeb and N. Puetmann. *μNRIT-2.5-A New Optimized Microthruster Of Giessen University*. In *International Electric Propulsion Conference* (2009).

[Finlay et al. 2010] C. C. Finlay, S. Maus, C. D. Beggan, T. N. Bondar, A. Chambodut, T. A. Chernova, A. Chulliat, V. P. Golovkov, B. Hamilton, M. Hamoudi et al. *International Geomagnetic Reference Field: the eleventh generation*. Geophysical Journal International, 183, 1216–1230 (2010).

[Frost et al. 2014] C. Frost, E. Agasid and N. M. D. D. Staff (2014). *Small Spacecraft Technology. State of the Art*. Technical Publication, NASA Ames Research Center. NASA/TP-2014-216648/REV1.

[Fuchikami et al. 2013] S. Fuchikami, M. Nakamoto, K. Toyoda and M. Cho. *Development of Vacuum arc thruster for nano satellite*. In *Proceedings of the 33rd IEPC 2013*. Electric Rocket Propulsion Society (2013).

[G. Rau Gmbh & Co. KG 2013] G. Rau Gmbh & Co. KG (2013). *Quotation*.

[Gerhardt and Palo 2010] D. T. Gerhardt and S. E. Palo. *Passive Magnetic Attitude Control for CubeSat Spacecraft*. In *24th Annual AIAA/USU Conference on Small Satellites*, Logan, Utah (2010).

[GG Phase A Study Team 2000] GG Phase A Study Team (2000). *Galileo Galilei (GG) Phase A Report*. Technical Report, Agenzia Spaziale Italiana. 2n Edition.

[Gilmour and Lockwood 1972] A. Gilmour and D. Lockwood. *Pulsed metallic-plasma generators*. Proceedings of the IEEE, 60(8), 977–991 (1972).

[Gilmour 1966] A. S. Gilmour. *Concerning the Feasibility of a Vacuum-Arc Thrustor*. In *AIAA 5th Electric Propulsion Conference*, San Diego, CA (1966).

[Goebel and Katz 2008] D. M. Goebel and I. Katz. *Fundamentals of electric propulsion: Ion and Hall thrusters*, vol. 1 of *JPL space science and technology series*. Wiley, Hoboken, N.J. (2008).

[Greisert and Heitz 2012] S. Greisert and S. Heitz. *Beeinflussung der Strahlcharakteristik eines VAT mithilfe eines externen Magnetfeldes*. Master's thesis, Universitaet der Bundeswehr Muenchen (2012).

[Grulich et al. 2015] M. Grulich, A. Koop, P. Ludewig, J. Gutsmiedl, J. Kugele and T. Ruck. *SMARD-REXUS-18: Development and Verification of an SMA Based CubeSat Solar Panel Deployment Mechanism*. In *22nd ESA Symposium European Rocket & Balloon Programmes and Related Research*, Tromso (2015).

[Haag et al. 2007] D. Haag, G. Herdrich, H. Kurtz, M. Winter and M. Auweter-Kurtz. *Experimental investigations of magnetoplasmadynamic thrusters with coaxial applied magnetic field*. In *30th International Electric Propulsion Conference* (2007).

[Hamidian and Dahlgren 1973] J. P. Hamidian and J. B. Dahlgren (1973). *Testing and evaluation of the LES-6 pulsed plasma thruster by means of a torsion pendulum system*. Technical Report NASA-CR-135940, JPL-TM-33-630, Jet Propulsion Laboratory, Pasadena, California.

[Harmann et al. 2013] H.-P. Harmann, S. Rothaus and G. Wanot. *μFCU – A Miniaturized Flow Control Unit for Xenon*. In *33rd International Electric Propulsion Conference*, Washington, D.C. (2013).

[Heberlein and Porto 1983] J. V. R. Heberlein and D. R. Porto. *The Interaction of Vacuum Arc Ion Currents with AxiaI Magnetic Fields*. IEEE Trans. Plasma Sci., 11(3), 152–159 (1983).

[Heidt et al. 2000] H. Heidt, A. S. Puig-SuariPuig-Suari, J., S. Nakasuka and R. J. Twiggs. *CubeSat: A new Generation of Picosatellite for Education and Industry Low - Cost Space Experimentation*. In *14th Annual/USU Conference on Small Satellites* (2000).

[Hey et al. 2015] F. G. Hey, A. Keller, C. Braxmaier, M. Tajmar, U. Johann and D. Weise. *Development of a Highly Precise Micronewton Thrust Balance*. Plasma Science, IEEE Transactions on, 43(1), 234–239 (2015).

[Horowitz and Hill 1989] P. Horowitz and W. Hill. *The Art of Electronics*. Cambridge University Press, New York, NY, USA (1989).

[Hurley et al. 2015] S. Hurley, G. Teel, J. Lukas, S. Haque, M. Keidar, C. Dinelli and J. Kang. *Thruster Subsystem for the United States Naval Academy's (USNA) Ballistically Reinforced Communication Satellite (BRICSat-P)*. In *34th International Electric Propulsion Conference*, Hyogo-Kobe, Japan (2015).

[Jahn 1968] R. G. Jahn. *Physics of Electric Propulsion*. McGraw-Hill, Inc. Republished 2006 by Dover Publications, Inc. Mineola, New York (1968).

[Jousten 2008] K. Jousten. *Handbook of Vacuum Technology*. John Wiley & Sons (2008).

[Karcher et al. 2003] C. Karcher, V. Kocourek and D. Schulze. *Experimental Investigations of Electromagnetic Instabilities of Free Surfaces in a Liquid Metal Drop*. In *International Scientific Colloquium. Modelling for Electromagnetic Processing* (2003).

[Katan and Lanning 2012] C. Katan and D. Lanning. *NASA's Next Solar Sail: Lessons Learned from NanoSail - D2*. In *26th Annual AIAA/USU Conference on Small Satellites*, Logan, Utah (2012).

[Kauffeldt 2010] M. Kauffeldt. *Measurements of Dense Plasma Generated in a Strong Magnetic Solenoid Field*. Diploma Thesis, University of the Federal Armed Forces (2010).

[Kauffeldt et al. 2012] M. Kauffeldt, M. Pflaum, J. Schein, B. Wiegmann and A. Haverich. *Triggerless pulsed vacuum cathodic arc plasma deposition of thin titanium oxide coatings on PMP-foils as a functional coating for medical applications*. In *Discharges and Electrical Insulation in Vacuum (ISDEIV), 2012 25th International Symposium on*, pp. 533–536. IEEE (2012).

[Kaufman 1961] H. Kaufman (1961). *AN ION ROCKET WITH AN ELECTRON-BOMBARDMENT ION SOURCE*. Technical Report NASA-TN-D-585, NASA, Lewis Research Center, Cleveland, Ohio.

[Keidar et al. 1996] M. Keidar, I. Beilis, R. Boxman and S. Goldsmith. *2D expansion of the low-density interelectrode vacuum arc plasma jet in an axial magnetic field*. Journal of Physics D: Applied Physics, 29(7), 1973 (1996).

[Keidar et al. 1997] M. Keidar, I. Beilis, R. Boxman and S. Goldsmith. *Voltage of the vacuum arc with a ring anode in an axial magnetic field*. Plasma Science, IEEE Transactions on, 25(4), 580–585 (1997).

[Keidar and Schein 2004] M. Keidar and J. Schein. *Modeling of a magnetically enhanced vacuum arc thruster*. In *40th AIAA/ASME/SAE/ASEE Joint Propulsion Conference and Exhibit*, Fort Lauderdale, Florida (2004).

[Keidar et al. 2005] M. Keidar, J. Schein, K. Wilson, A. Gerhan, M. Au, B. Tang, L. Idzkowski, M. Krishnan and I. I. Beilis. *Magnetically enhanced vacuum arc thruster*. Plasma Sources Sci. Technol., 14(4), 661–669 (2005).

[Kimblin 1971] C. W. Kimblin. *The effect of axial magnetic fields on vacuum arcs*. In *Proc. 10th Int. Conf Phenom. Ion. Gases* (1971).

[Kimblin 1974] C. W. Kimblin. *Cathode spot erosion and ionization phenomena in the transition from vacuum to atmospheric pressure arcs*. Journal of Applied Physics, 45(12), 5235–5244 (1974).

[Kirner 2011] S. Kirner. *HOBAS: Ein innovatives Hochgeschwindigkeits-Bildaufnahmesystem – Fertigstellung des Prototypen und erste messtechnische Anwendungen*. Diploma Thesis, Technische Universitaet Muenchen (2011).

[Kitts and Twiggs 1998] C. A. Kitts and R. J. Twiggs. *Low Cost Space Missions for Education and Technology Research*. In *1st International Symposium on Space Technology and Science*, Omiya, Japan (1998).

[Kramer 2014] A. Kramer. *Integration and Testing of Vacuum Arc Thrusters for the University Wuerzburg Experimental Satellite (UWE-4)*. Master's thesis, Julius-Maximilians-Universitaet Wuerzburg (2014).

[Krane 1987] K. Krane. *Introductory Nuclear Physics*. Wiley (1987).

[Kronhaus and Scharnowski 2015] I. Kronhaus and S. Scharnowski. *Investigation of Cathodic-Arc-Jet Influence on Cross Flow using Particle Image Velocimetry*. In *46th AIAA Plasmadynamics and Lasers Conference* (2015).

[Kronhaus et al. 2013] I. Kronhaus, K. Schilling, S. Jayakumar, A. Kramer, M. Pietzka and J. Schein. *Design of the UWE-4 Picosatellite Orbit Control System using Vacuum-Arc-Thrusters*. In *Proceedings of the 33rd IEPC 2013*. Electric Rocket Propulsion Society (2013).

[Kuninaka et al. 2007] H. Kuninaka, K. Nishiyama, I. Funaki, T. Yamada, Y. Shimizu and J. Kawaguchi. *Powered flight of electron cyclotron resonance ion engines on Hayabusa explorer*. Journal of propulsion and power, 23(3), 544–551 (2007).

[Kutzner and Miller 1989] J. Kutzner and H. Miller. *Ion flux from the cathode region of a vacuum arc*. Plasma Science, IEEE Transactions on, 17(5), 688–694 (1989).

[Kvell et al. 2014] U. Kvell, M. Puusepp, F. Kaminiski, J.-E. Past, K. Palmer, T.-A. Groenland and M. Noorma. *Nanosatellite orbit control using MEMS cold gas thrusters*. In *Proceedings of the Estonian Academy of Sciences*, vol. 63, pp. 279–285 (2014).

[Lafferty et al. 1980] J. Lafferty, J. Cobine, G. E. C. Research and D. Center. *Vacuum Arcs: Theory and Applications*. A Wiley-Interscience publication. Wiley (1980).

[Larson and Wertz 1999] , eds. W. J. Larson and J. R. Wertz. *Space Mission Analysis and Design*. Space Technology. Microcosm Press and Kluwer Academic Publishers, Third Edition ed. (1999).

[Lau and Herdrich 2013] M. Lau and G. Herdrich. *Pulsed Plasma Thruster Endurance Operation Stress Testing at IRS*. In *33rd International Electric Propulsion Conference*, Washington, D. C. Electric Rocket Propulsion Society (2013).

[Lebeda 2013] A. Lebeda (2013). *Private Communication*.

[Lebeda 2015] A. Lebeda (2015). *Private Communication*.

[Li et al. 2013] J. Li, M. Post, T. Wright and R. Lee. *Design of Attitude Control Systems for CubeSat-Class Nanosatellite*. Journal of Control Science and Engineering, 2013(Article ID 657182) (2013).

[Lide 2003] , ed. D. Lide. *CRC Handbook of Chemistry and Physics*. CRC HANDBOOK OF CHEMISTRY AND PHYSICS. Taylor & Francis, 84th Edition ed. (2003).

[Lieberman and Lichtenberg 2005] M. A. Lieberman and A. J. Lichtenberg. *Principles of Plasma Discharges and Materials Processing*. John Wiley & Sons, Inc., New Jersey, 2nd ed. (2005).

[LISA Mission Science Office 2007] LISA Mission Science Office. *LISA: Probing the Universe with Gravitational Waves*. LISA-LIST-RP-436, 1.0, 1–117 (2007).

[Long et al. 2002] M. Long, A. Lorenz, G. Rodgers, E. Tapio, G. Tran, K. Jackson, R. Twiggs and T. Bleier. *A CubeSat Derived Design for a unique Academic Research Mission in Earthquake Signature Detection*. In *Proceedings of the 16th Annual/USU Conference on Small Satellites*, Logan, Utah (2002).

[Lun 2008] J. Lun. *Development of a vacuum arc thruster for nanosatellite propulsion*. Master's thesis, Stellenbosch University (2008).

[Lun et al. 2010] J. Lun, R. T. Dobson and W. H. Steyn. *Determining Vacuum-Arc Thruster Performance Using a Cathode-Spot Model*. Journal of Propulsion and Power, 26(4), 663–672 (2010).

[Lun and Law 2013] J. Lun and C. Law. *Influence of Cathode Shape on Vacuum Arc Thruster Performance and Operation*. In *33th International Electric Propulsion Conference* (2013).

[Lun and Law 2015] J. Lun and C. Law. *High Specific Impulse Vacuum Arc Thrusters with Novel Electrode Designs and Arc Operation*. In *34th International Electric Propulsion Conference* (2015).

[Luna et al. 2011] P. Luna, C. Edwards, J. G. Del Amo and B. Hughes. *Development Status of the ESA Micro-Newton Thrust Balance*. In *31th International Electric Propulsion Conference* (2011).

[Marhold and Tajmar 2005] K. Marhold and M. Tajmar. *Micronewton thrust balance for indium FEEP thrusters*. AIAA Paper, 4387 (2005).

[Martin et al. 2001] M. Martin, P. Klupar, S. Kilberg and J. Winter. *TechSat 21 and revolutionizing space missions using microsatellites*. In *15th AIAA/USU Conference on Small Satellites* (2001).

[Martin et al. 1999] M. Martin, H. Schlossberger, J. Mitola, D. Weidow, A. Peffer, R. Blomquist, M. Campbell, C. Hall, E. Hansen, S. Horan et al. *University Nanosatellite Program*. In *IAF Symposium* (1999).

[Martin 1972] R. M. Martin. *Piezoelectricity*. Phys. Rev. B, 5, 1607–1613 (1972).

[Meeker 2010] D. Meeker (2010). *Continuum Representation of Wound Coils via an Equivalent Foil Approach*. Internet.

[Meeker 2015] D. Meeker (2015). *Finite Element Method Magnetics Version 4.2 User's Manual*, Version 4.2 ed.

[Mehrparvar et al. 2014] A. Mehrparvar, D. Pignatelli, J. Carnahan, R. Munakata, W. Lan, A. Toorian, A. Hutputanasin and S. Lee (2014). *CubeSat Design Specification*. California Polytechnic State University, Rev 13 ed.

[Mesyats 1998] G. A. Mesyats. *Explosive Electron Emission*. URO-Press (1998).

[Mueller et al. 2010] J. Mueller, R. Hofer and J. Ziemer (2010). *Survey of Propulsion Technologies applicable to CubeSats*. Technical Report, California Insitute of Technology, Jet Propulsion Laboratory.

[Nakaya et al. 2003] K. Nakaya, K. Konoue, H. Sawada, K. Ui, H. Okada, N. Miyashita, M. Iai, T. Urabe, N. Yamaguchi, M. Kashiwa et al. *Tokyo Tech CubeSat: CUTE-I - Design & Development of Flight Model and Future Plan*. In *AIAA 21st International Communications Satellite Systems Conference and Exhibit*, Yokohama, Japan (2003).

[NASA 2013] NASA (2013). *GENERAL ENVIRONMENTAL VERIFICATION STANDARD (GEVS) For GSFC Flight Programs and Projects*. NASA Technical Standards Program.

[New Scale Technologies, Inc. 2014] New Scale Technologies, Inc. (2014). *SQUIGGLE RV. SQL-RV-1.8 SQUIGGLE Reduced Voltage Linear Motor and Drive ASIC*. Internet. Technical Bulletin.

[Newton et al. 1729] I. Newton, A. Motte and J. Machin. *The Mathematical Principles of Natural Philosophy*. No. Bd. 1 in *The Mathematical Principles of Natural Philosophy*. B. Motte (1729).

[NorComp 2005] NorComp (2005). *D-Sub Standard Connector. Male - Solder Cup. Drawing No. 172-EYY-10YRYY1*. Technical Drawing.

[Nugent et al. 2008] R. Nugent, R. Munakata, A. Chin, R. Coelho and J. Puig-Suari. *The CubeSat: The Picosatellite Standard for Research and Education*. In *AIAA SPACE 2008 Conference and Exposition*. American Institute of Aeronautics and Astronautics (2008).

[Oland and Schlanbusch 2009] E. Oland and R. Schlanbusch. *Reaction wheel design for CubeSats*. In *Recent Advances in Space Technologies, 2009. RAST '09. 4th International Conference on*, pp. 778–783 (2009).

[Osiander et al. 2006] , eds. R. Osiander, M. A. Garrison Darrin and J. L. Champion. *MEMS and Microstructures in Aerospace Applications*. CRC Press, Taylor & Francis Group, Florida (2006).

[Ozaki et al. 2011] J.-i. Ozaki, T. Ikeda, T. Fujiwara, M. Nishizawa, S. Araki, H. Tahara and Y. Watanabe. *Development of Osaka Institute of Technology Nano-Satellite "PROITERES" with Electrothermal Pulsed Plasma Thrusters*. In *32nd International Electric Propulsion Conference*, Wiesbaden, Germany. Electric Rocket Propulsion Society (2011).

[Park et al. 2015] J. H. Park, A. Maskey and I.-S. Jeung. *Early Point-Of-Interest Scanning mission*. In *8th Pico and Nano Satellite Workshop*, Wuerzburg (2015).

[PCO AG 2015] PCO AG (2015). *pco.dimax HS. High speed CMOS cameras*. Data Sheet, Kehlheim, Germany.

[Pellegrino et al. 2015] A. Pellegrino, L. Arena, F. Curianó, F. Piergentili and F. Santoni. *Design, Manufacturing and Test of the CubeSat URSA MAIOR*. In *8th Pico and Nano Satellite Workshop*, Wuerzburg, Germany (2015).

[Pfeiffer Vacuum GmbH 2011a] Pfeiffer Vacuum GmbH (2011a). *Duo 20 M. Dual-stage rotary vane pumps with a pumping speed up to 24 m^3/h*. Data Sheet, Asslar, Germany.

[Pfeiffer Vacuum GmbH 2011b] Pfeiffer Vacuum GmbH (2011b). *HiPace(R) 700. Maximum vacuum performance in a compact design with a pumping speed of 685 l/s for N_2*. Data Sheet, Asslar, Germany.

[Pfeiffer Vacuum GmbH 2011c] Pfeiffer Vacuum GmbH (2011c). *IKR 261, metal sealed, long case, DN 40 CF-F*. Data Sheet, Asslar, Germany.

[Pfeiffer Vacuum GmbH 2011d] Pfeiffer Vacuum GmbH (2011d). *PKR 251, FPM sealed, DN 40 CF-F*. Data Sheet, Asslar, Germany.

[Pfennig et al. 1998] G. Pfennig, H. Klewe-Nebenius and W. Seelmann-Eggebert. *Karlsruher Nuklidkarte*. Marktdienste Haberbeck GmbH, Lage, 6. ed. (1998).

[Pietzka 2010] M. Pietzka. *Zeitaufgeloeste massenspektrometrische Untersuchung von gepulsten Methanplasmen*. Diploma Thesis, Ludwig-Maximilians-Universitaet Muenchen (2010).

[Pietzka et al. 2011] M. Pietzka, S. Kirner, M. Kauffeldt, C. A. J.-L. Marques-Lopez, G. Forster and J. Schein. *Development of Vacuum Arc Thrusters and Diagnostic Tools*. In *Proceedings of the thirty-second international electric propulsion conference, Electric Rocket Propulsion Society, Wiesbaden, Germany* (2011).

[Pietzka et al. 2013] M. Pietzka, M. Kuehn-Kauffeldt, J. Schein, I. Kronhaus, J. Schilling, T. Mai and A. Lebeda. *Innovative Vacuum Arc Thruster for extremely small Satellites*. In *33rd International Electric Propulsion Conference*, Washington, D.C. (2013).

[Plonus 1978] M. A. Plonus. *Applied Electromagnetics*. McGraw-Hill, Inc. (1978).

[Polk et al. 2008] J. Polk, M. Sekerak, J. Ziemer, J. Schein, N. Qi and A. Anders. *A Theoretical Analysis of Vacuum Arc Thruster and Vacuum Arc Ion Thruster Performance*. IEEE Trans. Plasma Sci., 36(5), 2167–2179 (2008).

[Puig-Suari et al. 2001] J. Puig-Suari, C. Turner and W. Ahlgren. *Development of the standard CubeSat deployer and a CubeSat class PicoSatellite*. In *Aerospace Conference, 2001, IEEE Proceedings.*, vol. 1, pp. 1/347–1/353 vol.1 (2001).

[Qi et al. 1997] N. Qi, S. Gensler, R. Prasad, M. Krishnan, F. Liu and I. Brown. *A high current vacuum arc ion source for heavy ion fusion*. In *Plasma Science, 1997. IEEE Conference Record-Abstracts., 1997 IEEE International Conference on*, p. 328. IEEE (1997).

[Qi et al. 1998] N. Qi, S. Gensler, R. R. Prasad, M. Krishnan, A. Vizir and I. Brown. *A pulsed Vacuum Arc Ion Thruster for distributed Small Satellite Systems*. In *34nd AIAA/ASME/SAE/ASEE Joint Propulsion Conference & Exhibit*, Cleveland, Ohio (1998).

[Quadrant Engineering Plastic Products 2009] Quadrant Engineering Plastic Products (2009). *Ketron® 1000 PEEK*. Data Sheet, Reading, PA.

[Rathinam et al. 2015] A. Rathinam, P. Bangert, D. Bock, M. Pietzka, M. Tajmar and J. Schilling. *Structural Design, Integration of Micro Propulsion units and Thermal Analysis of UWE Platform*. In *6th European Conference for Aeronautics and Space Science (EUCASS)*, Krakòw, Poland (2015).

[Redwitz 2004] M. Redwitz. *Charakterisierung des Plasmas nahe der Elektroden für Hochdruck-Plasmalampen durch spektroskopische Messungen*. Berichte aus der Elektrodenforschung. Tenea (2004).

[Robertson et al. 2013] G. A. Robertson, D. Young, K. Tony and M. Houts. *Massively Clustered CubeSats Nuclear Cryogenic Propulsion Stage (NCPS) Demo Missio*. In *Nuclear and Emerging Technologies for Space*, Albuquerque, New Mexico (2013).

[Robson 1978] A. E. Robson. *The motion of a low-pressure arc in a strong magnetic field*. Journal of Physics D: Applied Physics, 11(13), 1917 (1978).

[Rotteveel 2014] J. Rotteveel. *Launch results from the QB50 pre-cursor launch campaign flight qualification of the QB50 launch system*. In *28th Annual AIAA/USU Conference on Small Satellites – CubeSat Workshop* (2014).

[Roy et al. 2009] P. Roy, P. Seidl, A. Anders, F. Bieniosek, J. Coleman, E. Gilson, W. Greenway, D. Grote, J. Jung, M. Leitner et al. *A space-charge-neutralizing plasma for beam drift compression*. Nuclear Instruments and Methods in Physics Research Section A: Accelerators, Spectrometers, Detectors and Associated Equipment, 606(1), 22–30 (2009).

[Rycroft and Crosby 2002] , eds. M. J. Rycroft and N. Crosby. *Smaller Satellites: Bigger Business?*, vol. 6 of *Space Studies*. Springer Netherlands, 1 ed. (2002).

[Rysanek et al. 2002] F. Rysanek, J. W. Hartmann, J. Schein and R. Binder. *MicroVacuum Arc Thruster Design for a CubeSat Class Satellite*. In *16th Annual/USU Conference on Small Satellites* (2002).

[Sahu et al. 2008] K. Sahu, H. Leidecker and D. Lakins (2008). *EEE-INST-002: Instructions for EEE Parts Selection, Screening, Qualification, and Derating*. Technical Report NASA/TP–2003–212242, NASA, Goddard Space Flight Center.

[Saint-Gobain Boron Nitride 2011] Saint-Gobain Boron Nitride (2011). *Combat®*. Data Sheet, Amherst, NY.

[Saylor and France 2008] W. W. Saylor and M. E. France (2008). *Test and On-Orbit Experiences of FalconSAT-3*. Technical Report, DTIC Document.

[Scharlemann et al. 2011] C. Scharlemann, M. Tajmar, I. Vasiljevich, N. Buldrini, D. Krejci and B. Seifert. *Propulsion for Nanosatellites*. In *32nd International Electric Propulsion Conference*, Wiesbaden, Germany (2011).

[Schein et al. 2007] J. Schein, A. Gerhan, R. Woo, M. Au and M. Krishnan (2007). *Vacuum arc plasma thrusters with inductive energy storage driver*. US Patent App. 11/417,366.

[Schein et al. 2001] J. Schein, N. Qi, R. Binder, M. Krishnan, J. Polk, J. Ziemer and R. Shotwell (2001). *Vacuum Arc Thruster for Small Satellite Applications*. Final Contractor Report, NASA. NASA CR-2001-211323.

[Schein et al. 2002] J. Schein, N. Qi, R. Binder, M. Krishnan, J. K. Ziemer, J. E. Polk and A. Anders. *Inductive energy storage driven vacuum arc thruster*. Review of Scientific Instruments, 73(2), 925 (2002).

[Scholz and Juang 2015] A. Scholz and J.-N. Juang. *Toward open source CubeSat design*. Acta Astronautica, 115, 384 – 392 (2015).

[Schuster 2014] N. Schuster. *Innovativer Treibstoffnachfuehrmechanismus fuer einen Vacuum Arc Thruster*. Bachelor's Thesis, Universitaet der Bundeswehr Muenchen (2014).

[Seifert 2008] B. Seifert (2008). *Handbuch zur μN-Schubmesswaage*. Austrian Research Centers GmbH, Wiener Neustadt.

[Seifert et al. 2013] B. Seifert, A. Reissner, N. Buldrini, F. Plesescu and C. Scharlemann. *Development and Verification of a μN Thrust Balance for High Voltage Electric Propulsion Systems*. In *33rd International Electric Propulsion Conference*, Washington, D. C. (2013).

[Sekerak 2005] M. J. Sekerak. *Plasma Plume Characterization of a Vacuum Arc Thruster*. Master's thesis, California Insitute of Technology (2005).

[Serway and Jewett 2003] R. Serway and J. Jewett. *Physics for Scientists and Engineers*. Brooks/Cole (2003).

[Siemroth and Scheibe 1991] P. Siemroth and H.-J. Scheibe. *The method of laser-sustained arc ignition*. IEEE Transactions on Plasma Science, 18, 911–916 (1991).

[Slotten et al. 2015] J. Slotten, G. Teel, D. Chiu and M. Keidar. *Analysis of Vacuum Arc using Solar Array Materials*. In *34th International Electric Propulsion Conference* (2015).

[Slotten et al. 2013] J. D. Slotten, G. Teel, D. Chui and M. Keidar. *Cathode Spot Movement in Vacuum Arc Using Silicon Cathode*. In *33th International Electric Propulsion Conference* (2013).

[Smith 1957] C. G. Smith. *Motion of an Arc in a Magnetic Field*. Journal of Applied Physics, 28(11), 1328–1331 (1957).

[Sovey et al. 2001] J. S. Sovey, V. K. Rawlin and M. J. Patterson. *Ion Propulsion Development Projects in U.S.: Space Electric Rocket Test I to Deep Space 1*. Journal of Propulsion and Power, 17(3) (2001).

[Spanjers et al. 2002] G. Spanjers, D. Bromaghim, J. Lake, M. Dulligan, D. White, J. Schilling and S. Bushman. *AFRL MicroPPT Development for Small Spacecraft Propulsion*. 38th AIAA/ASME/SAE/ASEE Joint Propulsion Conference & Exhibit (2002).

[Sunping et al. 2015] Sunping, Z. Qi and J. Gang (2015). *Polymer Lithium-ion Battery. Product Specification. Model: 785060 2500 mAh*. Data Sheet, Xiangtan City, China.

[Tajmar 1999] M. Tajmar. *3D Numerical plasmasplasmasi and backflow contamination of a cesium field-emission-electric-propulsion (FEEP) emitter and thermionic neutralizer*. PhD thesis, Technische Universitaet Wien (1999).

[Tang et al. 2005] B. Tang, L. Idzkowski, M. Au, D. Parks, M. Krishnan and J. Ziemer. *Thrust Improvement of the Magnetically Enhanced Vacuum Arc Thruster (MVAT)*. In *29th International Electric Propulsion Conference*, Princeton (2005).

[Texas Instruments, Inc. 2013] Texas Instruments, Inc. (2013). *LM1577/LM2577 SIMPLE SWITCHER Step-Up Voltage Regulator*. Data Sheet, Dallas, Texas.

[Tietze et al. 2008] U. Tietze, C. Schenk and E. Gamm. *Electronic circuits: Handbook for design and application*. Springer-Verlag Berlin Heidelberg, New York, 2nd ed. ed. (2008).

[Trowitzsch 2008] S. Trowitzsch (2008). *BEESAT flight model after acceptance testing.*. https://commons.wikimedia.org/wiki/File:BeeSat-FM_Post-Acceptance-Test-Checkout_2008-09.JPG. Online, accessed 2015-11-26.

[Tsiolkovsky 1903] K. E. Tsiolkovsky. *The Exploration of Cosmic Space by Means of Rocket Devices*. The Science Review, 5 (1903).

[Tuma et al. 1978] D. T. Tuma, C. L. Chen and D. K. Davies. *Erosion products from the cathode spot region of a copper vacuum arc*. Journal of Applied Physics, 49(7), 3821–3831 (1978).

[Vergason et al. 2001] G. Vergason, M. Lunger and S. Gaur. *Advances in Arc Spot Travel Speed to Improve Film Characteristics*. In *Society of Vacuum Coaters 44th Annual Technical Conference Proceedings*, pp. 136–140 (2001).

[Walter and Scialdone 1997] N. A. Walter and J. J. Scialdone (1997). *Outgassing Data for Selecting Spacecraft Materials*. Technical Report 1124, NASA, Goddard Space Flight Center.

[Williams 2012] D. Williams. *Propulsion Solutions for CubeSats and Applications*. In *CubeSat Developers Workshop*, Logan, Utah (2012).

[Yoshida 2012] K. Yoshida (2012). *Raiko. Mission Completed!*. http://www.astro.mech.tohoku.ac.jp/RAIKO/. Online, accessed 2015-11-26.

[Yushkov et al. 2000] G. Y. Yushkov, A. Anders, E. M. Oks and I. G. Brown. *Ion velocities in vacuum arc plasmas*. Journal of Applied Physics, 88(10), 5618 (2000).

[Zhang et al. 2014] H. Zhang, C. Liu, L. Zheng, F. Xu, W. Feng, H. Li, X. Huang, M. Armand, J. Nie and Z. Zhou. *Lithium bis(fluorosulfonyl)imide/poly(ethylene oxide) polymer electrolyte*. Electrochimica Acta, 133, 529 – 538 (2014).

[Zhuang et al. 2012] T. Zhuang, A. Shashurin, I. Beilis and M. Keidar. *Ion velocities in a micro-cathode arc thruster*. Phys. Plasmas, 19(6), 063501 (2012).

[Zhuang et al. 2009] T. Zhuang, A. Shashurin, T. Denz, D. Chichka and M. Keidar. *Micro-vacuum arc thruster with extended lifetime*. In *Proc. 45th AIAA/ASME/SAE/ASEE Joint Propulsion Conf. Exhib* (2009).

[Ziegler 2012] D. Ziegler (2012). *Thruster Subsystem*. Julius-Maximilians-Universitaet Wuerzburg. Julius-Maximilians-Universitaet Wuerzburg.

[Ziemer 2001] J. K. Ziemer. *Performance Measurements Using a Sub-Micronewton Resolution Thrust Stand*. In *27th International Electric Propulsion Conference*, Pasadena, CA (2001).